2014-07-01

Passive Force on Skewed Bridge Abutments with Reinforced Concrete Wingwalls Based on Large-Scale Tests

Kyle Mark Smith
Brigham Young University - Provo

Passive Force on Skewed Bridge Abutments with Reinforced Concrete Wingwalls

Based on Large-Scale Tests

Kyle Mark Smith

A thesis submitted to the faculty of
Brigham Young University
in partial fulfillment of the requirements for the degree of

Master of Science

Kyle M. Rollins, Chair
Kevin W. Franke
Fernando S. Fonseca

Department of Civil and Environmental Engineering

Brigham Young University

July 2014

ABSTRACT

Passive Force on Skewed Bridge Abutments with Reinforced Concrete Wingwalls Based on Large-Scale Tests

Kyle Mark Smith
Department of Civil and Environmental Engineering, BYU
Master of Science

Skewed bridges have exhibited poorer performance during lateral earthquake loading when compared to non-skewed bridges (Apirakvorapinit et al. 2012; Elnashai et al. 2010). Results from small-scale laboratory tests by Rollins and Jessee (2012) and numerical modeling by Shamsabadi et al. (2006) suggest that skewed bridge abutments may provide only 35% of the non-skewed peak passive resistance when a bridge is skewed 45°. This reduction in peak passive force is of particular importance as 40% of the 600,000 bridges in the United States are skewed (Nichols 2012).

Passive force-deflection results based on large-scale testing for this study largely confirm the significant reduction in peak passive resistance for abutments with longitudinal reinforced concrete wingwalls. Large-scale lateral load tests were performed on a non-skewed and 45° skewed abutment with densely compacted sand backfill. The 45° skewed abutment experienced a 54% reduction in peak passive resistance compared to the non-skewed abutment. The peak passive force for the 45° skewed abutment was estimated to occur at 5.0% of the backwall height compared to 2.2% of the backwall height for the non-skewed abutment. The 45° skewed abutment displayed evidence of rotation, primarily pushing the obtuse side of the abutment into the backfill, significantly more than the non-skewed abutment as it was loaded into the backfill.

The structural and geotechnical response of the wingwalls was also monitored during large-scale testing. The wingwall on the obtuse side of the 45° skewed abutment experienced nearly 6 times the amount of horizontal soil pressure and 7 times the amount of bending moment compared to the non-skewed abutment. Pressure and bending moment distributions are provided along the height of the wingwall and indicate that the maximum moment occurs approximately 20 in (50.8 cm) below the top of the wingwall.

A comparison of passive force per unit width suggests that MSE wall abutments provide 60% more passive resistance per unit width compared to reinforced concrete wingwall and unconfined abutment geometries at zero skew. These findings suggest that changes should be made to current codes and practices to properly account for skew angle in bridge design.

Keywords: passive force, bridge abutment, backfill, large-scale, skew, pile cap, lateral resistance, reinforced concrete wingwalls, bending moment, pressure, PYCAP, earthquake, seismic

ACKNOWLEDGEMENTS

I would like to thank Dr. Kyle M. Rollins, my graduate advisor, for allowing me to be involved in this research. This research was the highlight of academic career and it was an honor to learn from and work with him. When interviewing for jobs after completing much of this research, some engineers were willing to speak with me only because they respected Dr. Rollins.

I'm grateful for my wife Katelyn for letting me spend long hours at times away from home to complete this research. It was a memorable experience working in the hot Utah sun with fellow students Amy Fredrickson, Arthur Guo, Cole Washburn, Quinton Taylor, John Cazier, Sam Mineer, and Ian Oxborrow. Dave Anderson and Rodney Mayo, our field technicians, were invaluable in performing the large-scale field tests.

I would like to especially thank Dr. Fernando S. Fonseca who individually taught me how to design reinforced concrete wingwalls before I took his Reinforced Concrete Design class. I also express my gratitude to Dr. Kevin W. Franke who is responsible for my interest in geotechnical engineering.

Funding for this study was provided by FHWA pooled fund study TPF-5(264), which was supported by Departments of Transportation from the states of California, Minnesota, Montana, New York, Oregon and Utah along with FHWA. Utah served as the lead agency, with David Stevens as the project manager. This support is gratefully acknowledged; however, the opinions, conclusions and recommendations in this paper do not necessarily represent those of the sponsoring organizations. I also express appreciation to the Salt Lake City Airport Department, who provided access to the test site used in this study.

TABLE OF CONTENTS

LIST OF TABLES

LIST OF FIGURES

1 INTRODUCTION

Background, objectives, and scope of research are provided in this chapter.

1.1 Background

Several large-scale field tests have been conducted investigate passive force-deflection behavior with densely compacted granular backfills (Cole and Rollins 2006; Duncan and Mokwa 2001; Lemnitzer et al. 2009; Rollins and Sparks 2002). Results from numerous field studies indicate that peak passive force is adequately predicted using the log-spiral method, typically achieved at displacements approximately 3% to 5% of the backwall height (Cole and Rollins 2006; Lemnitzer et al. 2009). Methods of approximating passive force-deflection curves with a hyperbola have been developed by Duncan and Mokwa (2001) and Shamsabadi et al. (2006, 2007). However, for simplicity in design, most bridge design specifications recommend a bilinear relationship (AASHTO 2011; Caltrans 2010).

Until recently, no large-scale experiments have been conducted to determine the passive force-deflection relationships for skewed bridge abutments. Furthermore, current bridge design practices assume the peak passive force is the same for skewed bridges as for non-skewed bridges (AASHTO 2011). However, field evidence clearly indicates poorer performance of skewed abutments during seismic events (Apirakyorapinit et al. 2012; Elnashai et al. 2010; Shamsabadi et al. 2006; Unjohn 2012) and distress to skewed abutments due to thermal

expansion (Steinberg et al. 2010). This topic is particularly relevant as 40% of the 600,000 bridges in the United States are skewed (Nichols 2012).

Laboratory tests performed by Rollins and Jessee (2012) and numerical analyses performed by Shamsabadi et al. (2006) both found that there is a significant reduction in passive force as skew angle increases. Using data obtained from these studies, Rollins and Jessee (2012) proposed the correction factor (R_{skew}) given by Equation (1-1), which defines the ratio between the peak passive force for a skewed abutment ($P_{P\text{-}skew}$) and the peak passive force for a non-skewed abutment ($P_{P\text{-}no\ skew}$) as a function of skew angle (θ).

$$R_{skew} = \frac{P_{p-skew}}{P_{p-no\ skew}} = 8.0 \times 10^{-5}\theta^2 - 0.018\theta + 1.0 \qquad (1\text{-}1)$$

Because Equation (1-1) is based only on small-scale tests and computer models with plane-strain conditions, the need for additional large-scale testing with more realistic boundary conditions was apparent. Large-scale testing for this study was a continuation of a test series that began in summer 2012 and involved a variety of different backfill materials and abutment geometries. Previous testing evaluated the failure mechanism and passive force development for abutments with wingwalls oriented transverse to the abutment and MSE wingwall oriented longitudinally with the abutment. For this thesis, the focus was on the behavior of an abutment with reinforced concrete wingwalls oriented longitudinally with the abutment. Two large-scale field tests were performed with skew angles of 0° and 45° using an existing pile cap and reinforced concrete wingwalls connected to the pile cap with concrete wedge anchors. Concrete wedges were attached to the face of the pile cap to create the skewed geometry necessary for testing.

Although passive force-deflection behavior for non-skewed abutments with reinforced concrete wingwalls has been investigated previously (Bozorgzadeh et al. 2008; Romstad et al.

1996), little information on the structural and geotechnical response of the wingwalls are available. In addition, no skewed abutments with reinforced concrete wingwalls have been tested previously. Therefore, these tests provide the first results for this abutment geometry.

1.2 Research Objectives

The research objectives for this study were:

1. Develop passive force-deflection relationships for abutments with longitudinal reinforced concrete wingwalls and a densely compacted sand backfill.

2. Investigate the effects of skew angle for abutments with reinforced concrete wingwall geometry and evaluate the applicability of the skew reduction factor (R_{skew}) proposed by Rollins and Jessee (2012).

3. Measure the structural and geotechnical response of the wingwalls to lateral earthquake type loading.

4. Compare passive force-deflection curves for abutments with reinforced concrete wingwalls to abutments with unconfined and MSE wingwall geometries.

1.3 Scope of Research

Similar to testing in summer 2012, large-scale lateral load tests were performed on a 15-ft (4.6-m) long, 11-ft (3.4-m) wide and 5.5-ft (1.7-m) high pile cap at a test site near the Salt Lake International Airport. Concrete wedges were attached to the pile cap to simulate a skewed abutment. For this study, longitudinal reinforced concrete (RC) wingwalls were secured to a non-skewed and 45° skewed abutment using ASTM A307 threaded rod and Redhead® wedge anchors. Pouring a new 45° concrete wedge with monolithic wingwalls was not within the scope of this research as multiple abutment types were tested at a 45° skew including unconfined sand and gravel backfill, MSE walls with sand backfill, and GRS gravel backfill. The wingwall connection to the pile cap was designed to simulate the moment capacity that would be expected from a monolithic wingwall. The test abutment with RC wingwalls was loaded by two 600-kip

hydraulic actuators into a densely compacted sand backfill with a deflection equal to 5 to 6% of the abutment backwall height. Larger deflections were outside the scope of this research as plastic deformation of the piles was undesirable in maintaining test repeatability. The geotechnical and structural response of wingwalls are presented in this thesis along with passive force-deflection and shear failure surface results.

Until this study, large-scale tests on abutments with RC wingwall geometry have not been conducted with densely compacted granular backfill. In addition, this study was the first to investigate the effects of skew angle on abutments with RC wingwalls. Finally, this thesis presents results regarding the structural and geotechnical response of the RC wingwalls to longitudinal earthquake loading. Results for bending moment, deflection, soil pressure, and lateral earth pressure coefficients are provided in this thesis.

2 LITERATURE REVIEW

2.1 Passive Earth Pressure Theories

Three widely used passive earth pressure theories have been developed to estimate the ultimate lateral compressive strength of a soil and are known as the Coulomb (1776), Rankine (1857), and Logarithmic Spiral (Log Spiral) theories. The theories differ in the method used to approximate the shear plane of the soil. Shear plane geometry defines the boundaries of a soil mass that is mobilized from a lateral load, which is directly related to the soil's ultimate passive resistance (P_P) using a passive earth pressure coefficient (K_P), as shown in Equation (2-1).

$$P_P = \frac{1}{2} K_P \gamma H^2 + 2\sqrt{K_P} c' H \qquad (2\text{-}1)$$

where,

$P_P = Ultimate\ passive\ force\ per\ unit\ width$

$K_p = Passive\ earth\ pressure\ coefficient$

$\gamma = Moist\ unit\ weight\ of\ the\ soil$

$H = Wall\ height$

$c' = Soil\ cohesion$

The form of Equation (2-1) is approximated using a uniform pressure distribution attributed to cohesion and triangular pressure distribution attributed to the weight and friction angle of the soil, as shown in Figure 2.1.

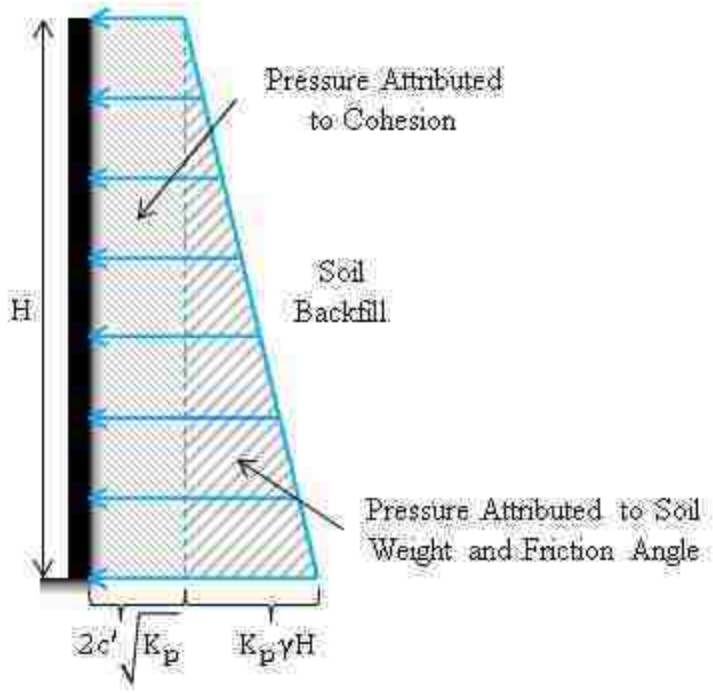

Figure 2.1. Lateral pressure distribution for soil.

The value for K_p differs depending on which passive earth pressure theory is employed.

2.1.1 Coulomb (1776)

The earliest recorded analytical method of estimating passive earth pressures was by Coulomb in 1776. Coulomb mathematically defined the geometry of the mobilized soil mass using the friction angle of the soil (φ), the slope of the wall being pushed into soil (θ), the embankment inclination (α), and the friction angle at interface between the wall and the soil (δ) (see Figure 2.2).

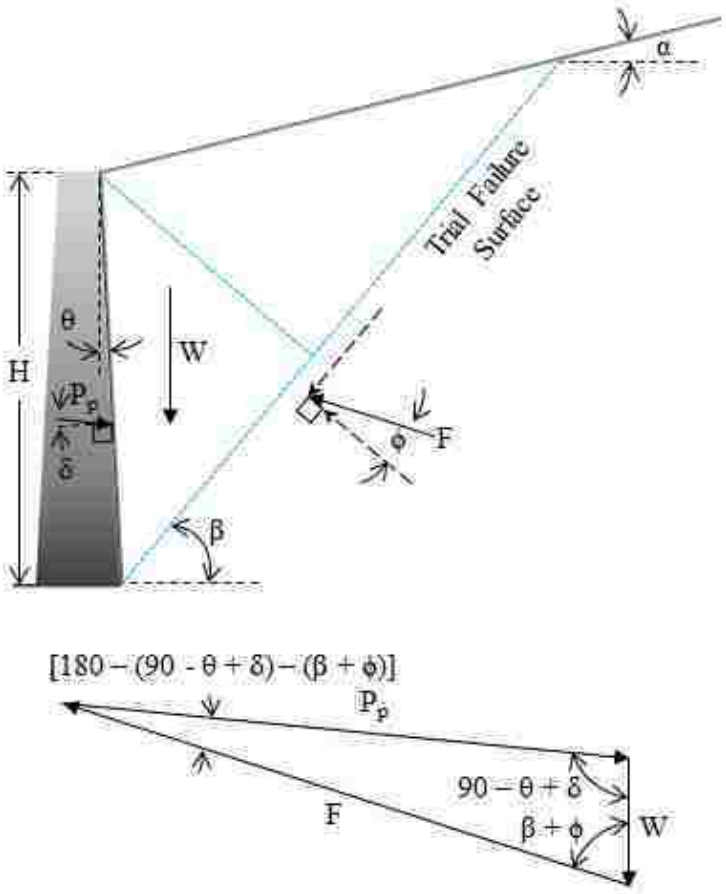

Figure 2.2. Shear failure surface geometry and direction of resultant force.

Coulomb approximated the mobilized soil mass using a linear shear plane but did consider wall friction at the soil-wall interface. The value for K_p is calculated based on the geometry of the mobilized soil mass predicted by φ, θ, α, and δ. A solution is obtained by using a series of trial failure wedges and finding the critical wedge which provides the lowest passive force. Although Coulomb's theory gives a closed form solution for ultimate passive force, experimental and field observations indicate that his theory predicts erroneously high values for K_p when $\delta > 0.4\varphi$, which would lead to an unconservative design. Engineers are discouraged from using Coulomb's

theory for predicting ultimate passive forces because typical construction materials that induce passive forces in soil have a $\delta > 0.4\varphi$, as shown in Table 2.1.

Table 2.1. Typical Values for δ_{max}/φ, adapted from Potyondy (1961)

Soil type	δ_{max}/φ		
	Steel	Concrete	Wood
Sand	0.54	0.76	0.76
Silt and clay	0.54	0.5	0.55

2.1.2 Rankine (1857)

Rankine developed a mathematical theory to describe the stability of a loose granular mass based only on the mutual friction of the soil grains (Rankine 1857). Because the Rankine K_p only depends on φ and c', the passive earth pressure $\left(K_p\sigma_v'\right)$ can be plotted in τ, σ' space as the pressure corresponding with enlarging Mohr's circle to shear failure, as shown in Figure 2.3. Rankine K_p generally predicts a steeper shear plane compared with observed shear planes, resulting in a smaller mobilized soil mass than what natural occurs. Although Rankine theory does not consider wall friction or complex backfill geometries as does Coulomb theory, Rankine passive earth pressures are conservative in design and are widely used in engineering practice.

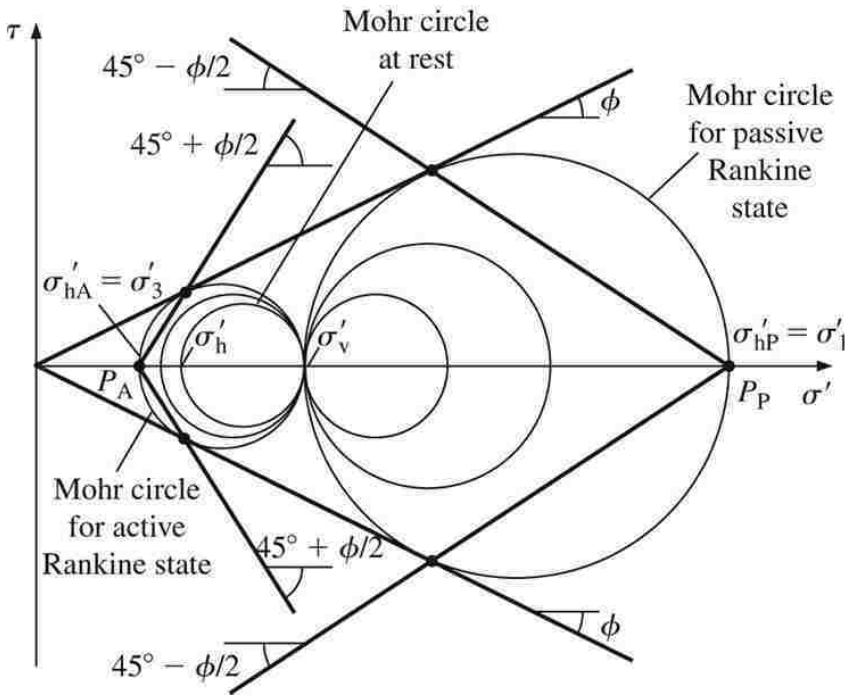

Figure 2.3. Passive and active failure states in Mohr-Coulomb (τ, σ) space.

2.1.3 Log Spiral

The log spiral method was developed by Terzaghi (1943) and provides the best agreement for the geometry of the predicted mobilized soil mass compared with the actual mobilized soil mass (Duncan and Mokwa 2001; Rollins and Cole 2006). The shear plane is modeled using an initial curved log spiral segment followed by a linear Rankine portion, illustrated in Figure 2.4. The non-linear shear plane leads to more accurate estimates of K_p for $\delta > 0.4\varphi$, rendering the log spiral method more appropriate for predicting passive forces induced by concrete, steel, or wooden walls (Duncan and Mokwa 2001). Log spiral theory can be employed with charts and tables, graphically, or numerically.

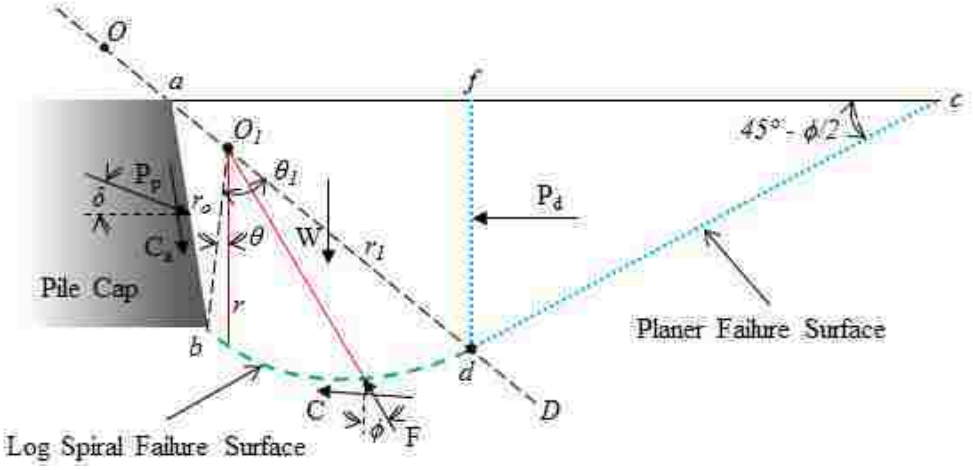

Figure 2.4. Log spiral shear failure surface geometry.

A general comparison of shear plane geometries from the three different passive earth theories is illustrated in Figure 2.5. A wall friction angle (δ) of approximately 0.75φ for concrete was used to generate the shear planes.

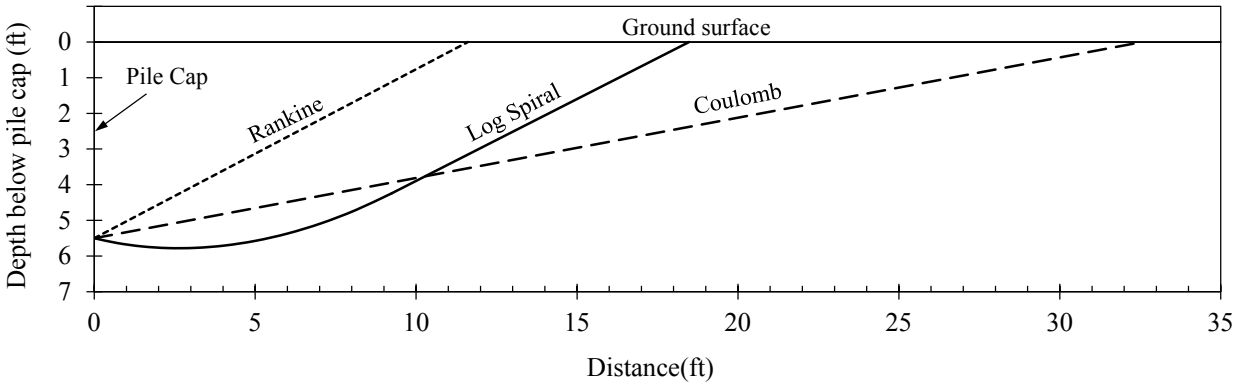

Figure 2.5. Comparison of Coulomb, Rankine, and Log Spiral failure surfaces.

Figure 2.5 helps illustrate that the difference in K_p from the different methods can be portrayed in the geometry and size of the predicted mobilized soil masses that provide passive resistance.

2.2 Passive Force-Deflection Relationships

Because a certain amount of displacement must be achieved before the ultimate passive resistance is mobilized, passive force-deflection curves have been developed based on large-scale testing to approximate intermediate values of passive resistance before the peak displacement is achieved. Passive force-deflection relationships are especially useful in bridge abutment design, where the passive resistance of the abutment backfill is considered in the total lateral resistance of the abutment. Displacements required to mobilize full passive resistance (Δ_{max}) are typically normalized to abutment backwall height (H) and expressed as $\frac{\Delta_{max}}{H}$. Values of $\frac{\Delta_{max}}{H}$ obtained by Cole and Rollins (2006) and three other sources are shown in Table 2.2. In general, it is believed that more movement is required to achieve the peak passive resistance for loose soils than for dense soils.

Table 2.2. Values of Δ_{max}/H for Different Backfill Types, adapted from Cole and Rollins (2006)

	Values of Δ_{max}/H			
Type of backill	Sowers and Sowers (1961)	Canadian Geotechnical Society (1992)	Clough and Duncan (1991)	Cole and Rollins (2006)
Coarse gravel	-	-	-	0.04
Fine gravel	-	-	-	0.03
Dense sand	0.002	0.02	0.01	0.03
Medium-dense sand	-	-	0.02	-
Loose sand	0.006	0.06	0.04	-
Silty sand	-	-	-	0.052
Stiff cohesive	-	0.02	-	-
Soft cohesive	-	0.04	-	-
Compacted silt	-	-	0.02	-
Compacted lean clay	-	-	0.05	-
Compacted fat clay	-	-	0.05	-

The relative density of a soil (loose or dense) has been addressed by assigning a stiffness value (K) to the soil. Currently in practice, two main approaches are employed to predict soil passive resistance at displacements below (Δ_{max}): bilinear and hyperbolic relationships. Common bilinear approximations include the Caltrans and AASHTO methods. More accurate hyperbolic approximations have been developed by Duncan and Mokwa (2001) method and Shamsabadi et al. (2007). Currently, the skew angle of the bridge is not considered in any of these approaches.

2.2.1 Caltrans Method

The Caltrans Seismic Design Criteria v1.6 (2010) approximates the non-linear passive force-deflection behavior using a bilinear model illustrated in Figure 2.6, based on large-scale abutment testing at BYU, UC Davis and UCLA.

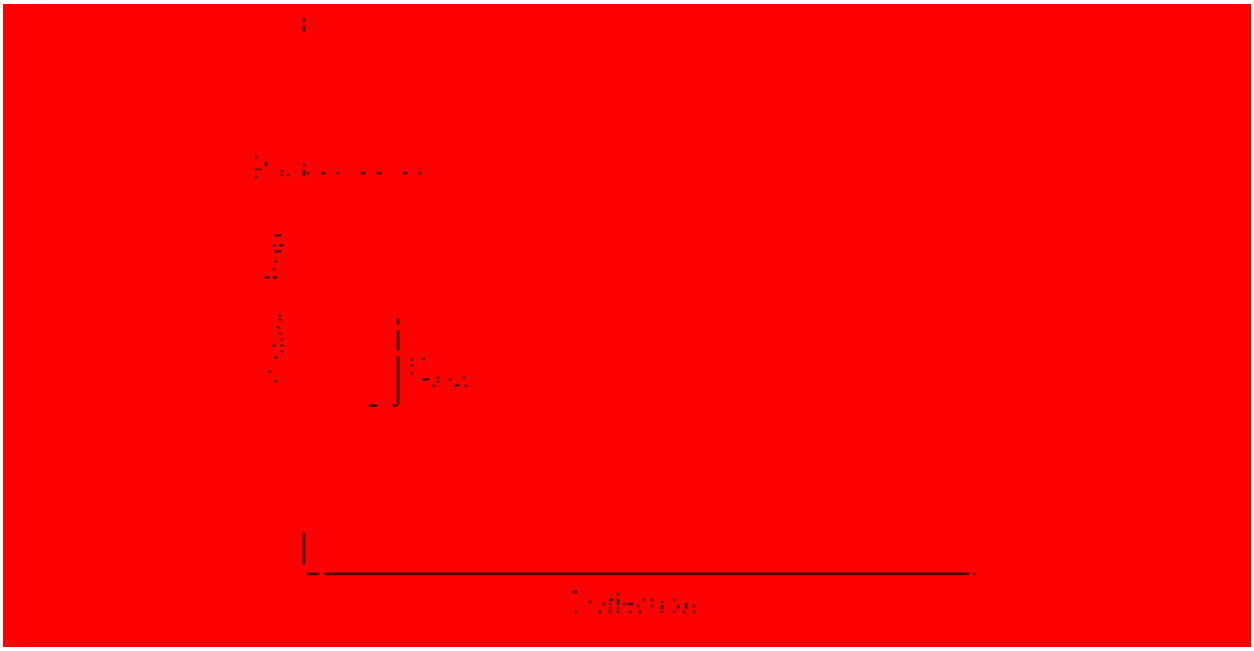

Figure 2.6. Caltrans bilinear passive force-deflection design curve.

The initial stiffness of backfill material that meets Caltrans Standard Specifications for fine-grained material is computed using Equation (2-2), and Equation (2-3) is used for computing initial stiffness when the backfill material does not meet specifications. Caltrans Standard Specifications typically include (Caltrans 2010):

- Standard penetration, upper layer [0 to 10 ft (0 to 3 m)] $N = 20$ (Granular soils)
- Standard penetration, lower layer [10 to 30 ft (3 to 9 m)] $N = 30$ (Granular soils)
- Undrained shear strength, $s_u > 1500psf \quad (72KPa)$ (Cohesive soils)
- Shear wave velocity, $v_s > 600\ ft/sec \quad (180\ m/sec)$
- Low potential for liquefaction, lateral spreading, or scour

NOTE: $N =$ The uncorrected blow count from the Standard Penetration Test (SPT)

Initial stiffness is adjusted proportional to the abutment backwall height in Equation (2-4) and used to construct the passive force-deflection curve.

$$K_i = \frac{50\ kip/in}{ft} \quad \left(\frac{28.70\ kN/mm}{m}\right) \tag{2-2}$$

$$K_i = \frac{25\ kip/in}{ft} \quad \left(\frac{14.35\ kN/mm}{m}\right) \tag{2-3}$$

$$K_{abut} = \begin{cases} K_i \times w \times \left(\frac{h}{5.5ft}\right) & \text{U.S. Units} \\ K_i \times w \times \left(\frac{h}{1.7m}\right) & \text{S.I. Units} \end{cases} \tag{2-4}$$

where,

$K_i = Initial\ soil\ stiffness$

$w = Projected\ abutment\ width$

$h = Abutment\ height$

Ultimate passive force (P_{ult}) is calculated using Equation (2-5) and is used as the constant value in the second segment of the bilinear curve.

$$P_{ult} = \begin{cases} A_e \times 5.0ksf \times \left(\frac{h}{5.5}\right) & (ft, kip) \quad \text{U.S. Units} \\ A_e \times 239kPa \times \left(\frac{h}{1.7}\right) & (m, kN) \quad \text{S.I. Units} \end{cases} \tag{2-5}$$

where,

$A_e = Effective\ abutment\ area\ (h \times w)$

$h = Abutment\ height$

The Caltrans bilinear model does not capture the continuous reduction in soil stiffness and is also limited by only dividing soils into two categories: those that meet Caltrans Standard Specifications and those that do not. This model does not allow the flexibility to accurately predict passive forces for soils outside of Caltrans Standard Specifications.

2.2.2 AASHTO Method

A different bilinear passive force-deflection approximation is provided by the American Association of State Highways and Transportation Officials (AASHTO) and is illustrated in Figure 2.7. Instead of directly calculating a soil stiffness, the curve is defined by $\frac{\Delta_{max}}{H}$ and P_{ult}. The value of $\frac{\Delta_{max}}{H}$ is obtained from estimates by Clough and Duncan (1991) in Table 2.2 and P_{ult} is calculated using a graphical log spiral method in section 3.11.5.4—Passive Lateral Earth Pressure Coefficient, k_p (p. 3-105) of *AASHTO LRFD Bridge Design Specifications* (2010). AASHTO (2010) recommends using $\frac{\Delta_{max}}{H} = 0.05$ for conservative design, which is in good agreement with observations from several field studies (Cole and Rollins 2006; Lemnitzer et al. 2009; Rollins and Sparks 2002).

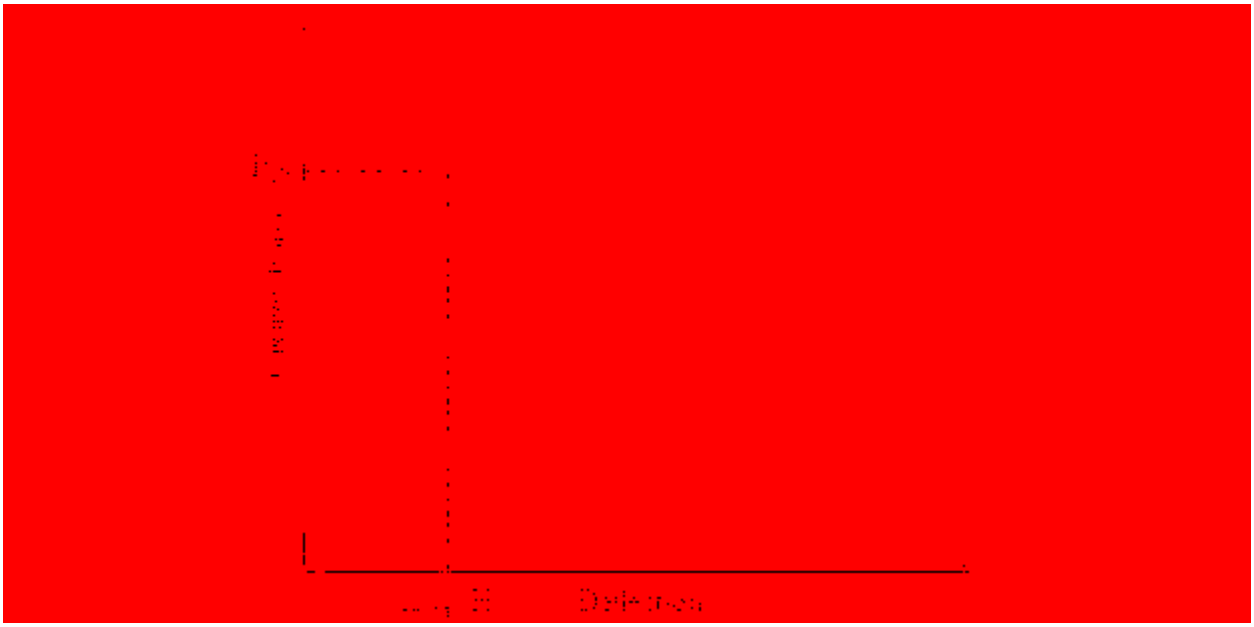

Figure 2.7. AASHTO bilinear passive force-deflection design curve.

Because P_{ult} is calculated using the log spiral method, the AASHTO method can more accurately model a wider range of backfill material compared with the Caltrans method; however, this method is still limited in modeling the continuous non-linear force-deflection behavior.

2.2.3 Duncan and Mokwa (2001) Method

Duncan and Mokwa (2001) approximated the variation of passive resistance with deflection using a hyperbola (shown in Figure 2.8) based on the hyperbolic stress-strain relationship by Duncan and Chang (1970). Similar to the Caltrans method, an initial stiffness (K_{max}) is used to define the initial slope of the curve and, similar to the AASHTO method, P_{ult} is computed using the log spiral method. However, the calculation of P_{ult} in the Duncan and

Mokwa (2001) method differs in that a correction factor is used to account for a 3D failure surface, which contributes additional resistance to P_{ult}.

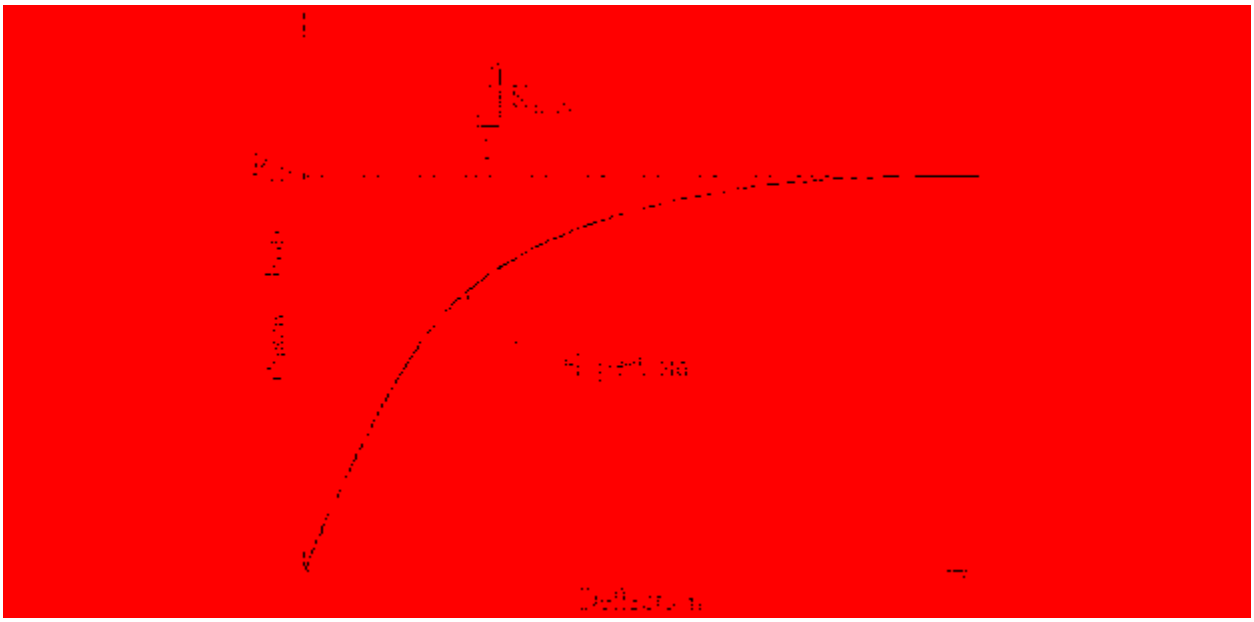

Figure 2.8. Duncan and Mokwa (2001) hyperbolic passive force-deflection curve.

The hyperbolic curve in Figure 2.8 is defined by Equation (2-6).

$$P = \frac{y}{\left[\frac{1}{K_{max}} + R_f \frac{y}{P_{ult}}\right]} \tag{2-6}$$

where,

$y = Pile\ cap\ deflection$

$K_{max} = Maximum\ soil\ stiffness$

$R_f = Failure\ ratio = 0.75\ to\ 0.95$

$P_{ult} = Maximum\ passive\ soil\ resistance$

K_{max} is estimated using the approach by Douglas and Davis (1964), which is based on elastic theory and depends on the soil's Young's modulus (E) and Poisson's ratio (v). The values of E and v are combined with the applied force (P), pile cap dimensions, and influence factors to approximate an average deflection (y_{avg}). Maximum stiffness is computed as $K_{max} = \frac{P}{y_{avg}}$. The failure ratio (R_f) is the ratio of ultimate passive pressure load to the asymptotic value of passive resistance. If no test data is available, values of R_f are estimated based on observations and experience. Values of $0.75 < R_f < 0.95$ were suggested by Duncan and Chang (1970) for hyperbolic stress-strain curves and can produce reasonable results for load-deflection curves as well. The value for P_{ult} defines the maximum value, or asymptote, of the hyperbola and is computed using the log spiral method in a spreadsheet (PYCAP) developed by Duncan and Mokwa (2001). The equation for P_{ult} can be written as Equation (2-7).

$$P_{ult} = E_p b M \tag{2-7}$$

where,

$E_p = Passive\ resistance\ per\ unit\ width$

$b = Pile\ cap\ width$

$M = Brinch\ Hansen\ 3D\ correction\ factor$

The Brinch-Hansen 3D correction factor (M) ranges from 1 to 2 in the PYCAP spreadsheet and essentially increases the effective width of the soil failure mass that provides passive resistance against the structure. The 3D correction factor (M) is appropriate for unconfined soils that allow the shear plane to extend beyond the width of the structure that applies the force.

The PYCAP spreadsheet generates passive force-deflection curves based on 12 input parameters: cap width (b), cap height (H), embedment depth (z), surcharge (q_s), cohesion (c), soil friction angle (φ), wall friction angle (δ), initial soil modulus (E_i), Poisson's ratio (v), soil unit weight (γ), adhesion factor (α), and Δ_{max}/H.

Predicted passive force-deflection curves were in good agreement with two large-scale lateral load tests on partially saturated stiff sandy silt and drained well-graded gravel at the Kentland Farms field test site.

The hyperbolic force-deflection relationship by Duncan and Mokwa (2001) more accurately estimates the continuous increase in passive resistance with increasing deflection when compared to the Caltrans and AASHTO methods (Cole and Rollins 2006). Because a 3D correction factor and the log spiral method are used to compute P_{ult}, the ultimate passive resistance can be predicted more accurately for unconfined backfills (in addition to confined backfills) of a wide variety of soil types.

2.2.4 Shamsabadi et al. (2007) Method

The hyperbolic passive force-deflection curve by Shamsabadi et al. (2007), see Figure 2.9, is also based on the hyperbolic stress-strain relationship by Duncan and Chang (1970). The hyperbolic curves are generated by a numerical model and have accurately modeled passive force-deflection relationships of several large-scale tests.

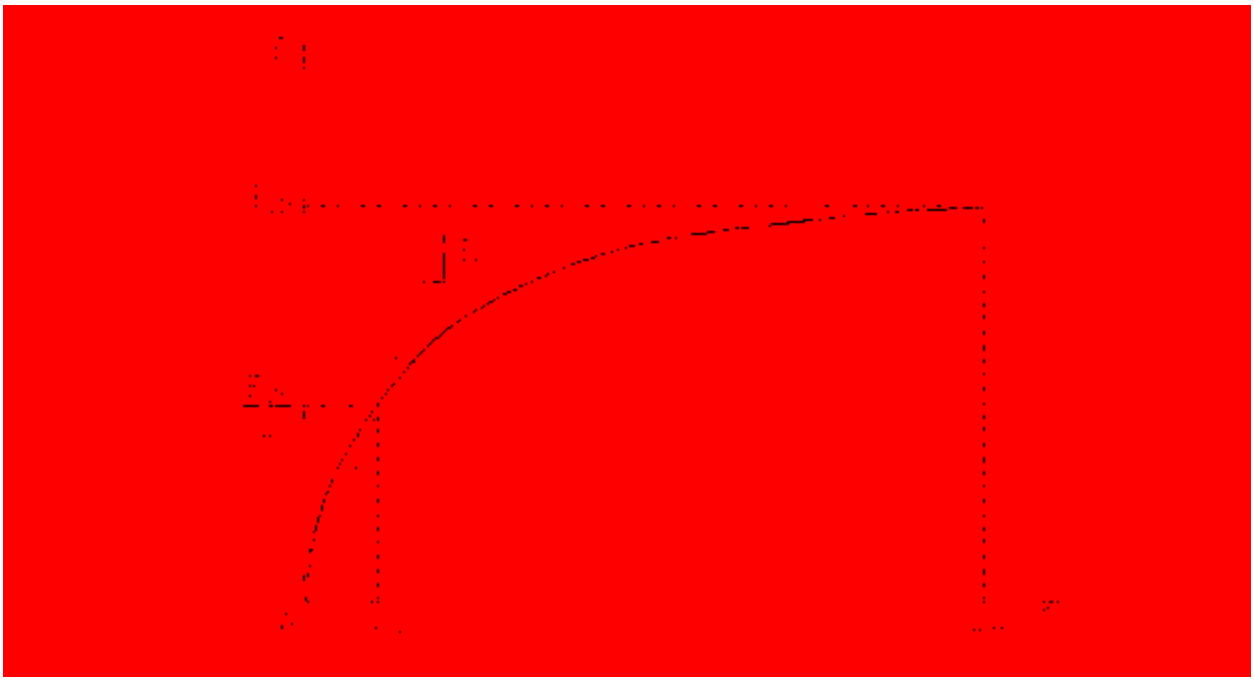

Figure 2.9. Shamsabadi et al. (2007) hyperbolic passive force-deflection curve.

The hyperbolic curve in Figure 2.9 is expressed by Equation (2-8).

$$F(y) = \frac{y}{\frac{y_{max}}{2Ky_{max} - F_{ult}} + \frac{2(Ky_{max} - F_{ult})}{F_{ult}(2Ky_{max} - F_{ult})}y} \tag{2-8}$$

where,

$y = Abutment\ displacement$

$y_{max} = Maximum\ displacement$

$K = Average\ soil\ stiffness$

$F_{ult} = Maximum\ abutment\ force$

Equation (2-8) is set up to accommodate K (average soil stiffness), F_{ult}, and y_{max}, which are typically the three parameters provided by the geotechnical engineer for seismic bridge design. While the force-deflection relationship by Shamsabadi et al. (2007) [see Equation (2-8)]

employs the same general hyperbolic form $\left[F(y) = \frac{y}{A+By}\ , where\ A\ and\ B\ are\ constants\right]$ as the Duncan and Mokwa (2001) method, the average stiffness is used, instead of maximum stiffness, and Condition II of the three boundary conditions gives the general hyperbolic curve a different shape compared to the general hyperbola by Duncan and Mokwa (2001). The three boundary conditions employed by Shamsabadi et al. (2006) are

- Condition I $FL = 0\ at\ y = 0$
- Condition II $FL = \frac{F_{ult}}{2}\ at\ y = y_{ave}$
- Condition III $FL = F_{ult}\ at\ y = y_{max}$

The average stiffness is not based on elastic theory but rather computed as $K = \frac{1}{2}F_{ult}/y_{ave}$. Suggested values for K and y_{max}/H are provided for granular and cohesive soils, and shown in Table 2.3.

Table 2.3. Suggested Values for K and y_{max}/H (Shamsabadi et al. 2007)

Abutment backfill type	K kN/cm/m (kip/in/ft)	y_{max}/H
Granular	290 (50)	0.05
Cohesive	145 (25)	0.10

Predictions of passive force-deflection behavior from the Shamsabadi et al. (2007) method are in good agreement with large-scale static load tests by Brigham Young University (Cole and Rollins 2006), centrifuge tests with a seat-type abutment and pile cap (Gadre and Dobry 1998), and large-scale cyclic loading tests by the University of California Davis (Romstad et al. 1996). Based on field test data, passive force-deflection curves were accurately modeled for

clean sand, silty sand, Nevada sand, fine- and coarse-grained gravel, and Yolo Loam clay. Adjustment factors, based on surface crack patterns in Cole and Rollins' (2006) field tests, were used to account for 3D effects in unconfined backfills. The 3D factors by Cole and Rollins (2006) were in good agreement with the Brinch-Hansen correction factors (Ovesen 1964).

Passive force-deflection curves are generated from seven input parameters in a program entitled Abutment. Similar to PYCAP (Duncan and Mokwa 2001), values of φ, δ, c, γ, and v are required to describe the soil and wall surface. The value of R_f is selected independently of the ultimate passive resistance and maximum deflection (unlike PYCAP), and a value of $R_f = 0.97$ is recommended by the author. Lastly a parameter ε_{50} is required, which estimates the strain at a 50% of the failure stress. Values for ε_{50} should be obtained from laboratory testing when possible. Where laboratory testing is not available, the author recommends $\varepsilon_{50} = 0.0035$ for granular soils and $\varepsilon_{50} = 0.007$ for cohesive soils.

The hyperbolic method by Shamsabadi et al. (2007) has similar advantages to Duncan and Mokwa's (2001) hyperbolic method as it more accurately estimates the continuous non-linear increase in passive resistance with increasing deflection and the model can be used for a wide variety of soil types. There are also significant differences between the two approaches. Duncan and Mokwa's (2001) approach for computing initial soil stiffness is more fundamentally based on soil mechanics theory than the approach of estimating an average soil stiffness. Shamsabadi et al. (2007) provides a suggested value of y_{max}/H for clay (0.10) which is more than twice the value of Duncan and Mokwa's (2001) recommended value of 0.04 for all soil types. It has been observed by the author that the 3D correction factor is dealt with more systematically in Duncan and Mokwa's (2001) PYCAP spreadsheet than the approach by Shamsabadi et al. (2007) described in their paper. Lastly, based on the two papers read by the

author, it appears that accuracy of passive force-deflection predictions by Shamsabadi et al. (2007) have been verified by more independent large-scale tests when compared to predictions reported by Duncan and Mokwa (2001).

2.3 Skewed Bridges vs. Non-skewed Bridges

A poorer response to lateral loads has been observed with skewed bridges in comparison to non-skewed bridges. Inspections following large seismic events in Northridge, California (1994), Chi Chi, Taiwan (1999), and Maule, Chile (2010) report significantly more damage experienced by skewed bridges compared to non-skewed bridges (Apirakvorapinit et al. 2012; Elnashai et al. 2010; Shamsabadi et al. 2006) Skewed bridges experienced nearly twice the damage rate of non-skewed bridges in the M8.8 Maule, Chile (2010) earthquake (Toro et al. 2013). Even before these seismic events, concern was expressed regarding poor performance of skewed bridges due to rotation from thermal expansion. Addressing this concern, pressures behind a skewed integral abutment in Maine were monitored for 33 months and a nonuniform lateral pressure distribution was measured as the superstructure expanded from temperature increases into the soil backfill (Sandford and Elgaaly 1993). Pressures near the obtuse end of the abutment increased 4 to 6 times the cold weather value compared to pressures near the acute end increasing only 2 to 3 times. A design lateral pressure distribution was developed that assigned the Rankine active pressure to the acute corner and the Rankine passive pressure to the obtuse corner of the abutment (see Figure 2.10). The higher pressure at the obtuse end indicated that the obtuse end of the abutment rotated into the backfill, while the acute corner rotated away from the backfill.

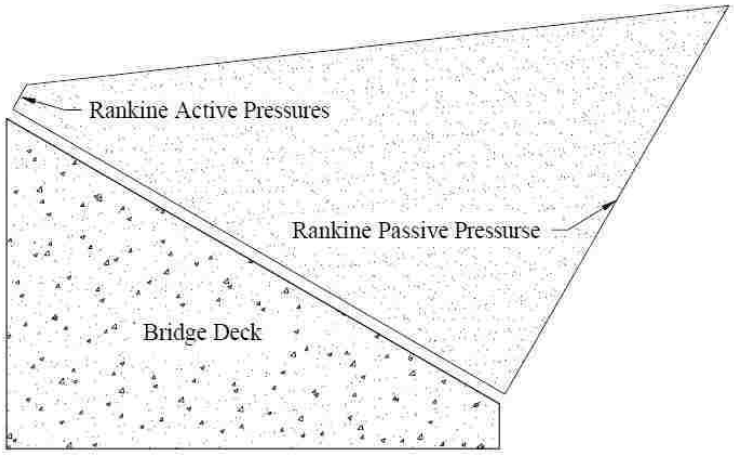

Figure 2.10. Nonuniform lateral pressure distribution, adapted from Sandford and Elgaaly (1993).

The rotation mechanism can be explained using Figure 2.11, which shows the typical distribution of forces on a skewed bridge in response to longitudinal loading (P_L) from either thermal expansion or earthquake ground motions (Burke Jr. 1994). In Figure 2.11, and in the remainder of this paper, lateral loading is only considered in the direction parallel to the bridge deck.

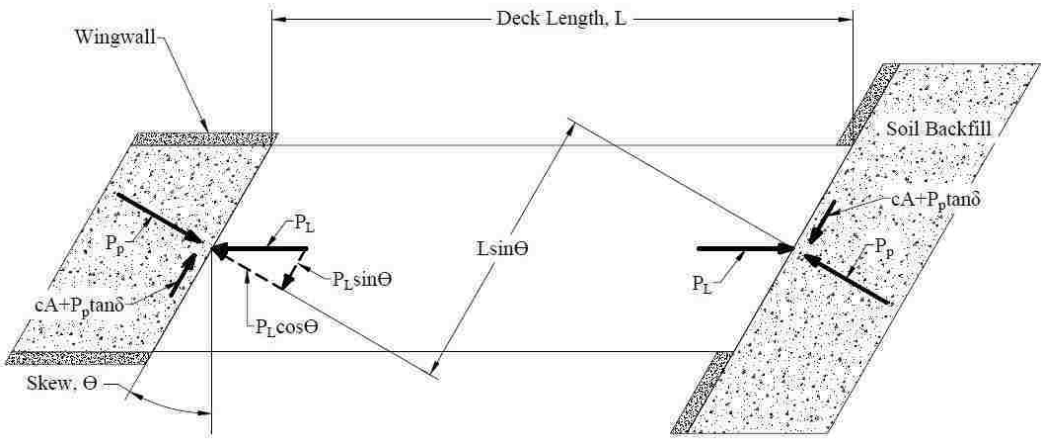

Figure 2.11. Typical forces on skewed bridge from lateral loading, adapted from Burke Jr. (1994).

The component of the earthquake load normal to the abutment ($P_L cos\theta$) is resisted by the soil passive resistance (P_p), while the transverse component ($P_L sin\theta$) is resisted by the soil shear resistance ($cA + P_L tan\delta$). For a bridge with non-skewed abutments, P_L acts normal to the abutment backwall and is only resisted by P_p, which is directed in the same line of action on both abutments at either end of the bridge, resulting in no moment. In contrast, P_p forces for skewed abutments are offset at opposite ends of the bridge (see Figure 2.11), resulting in a moment couple $\left(moment\ couple = P_p L sin\theta\right)$. Rotation of the entire bridge can occur if Equation (2-9) is not satisfied.

$$\frac{(cA + P_P tan\delta)L\ cos\theta}{FS} \geq P_P L\ sin\theta \tag{2-9}$$

where,

$c = cohesion$

$A = contact\ area\ of\ abutment\ and\ backfill$

$\delta = wall\ friction\ angle$

$FS = factor\ of\ safety$

$\theta = skew\ angle$

Because the skew angle introduces transverse loading ($P_L sin\theta$), the abutment may slide against the backfill if the transverse loading exceeds the shear resistance of the backfill. Sliding of the abutment can occur if Equation (2-10) is not satisfied.

$$\frac{cA + P_P tan\delta}{FS} \geq P_L sin\theta \tag{2-10}$$

2.3.1 Poor Performance of Skewed Bridges

Field investigations from the Northridge, California (1994), Chi Chi, Taiwan (1999), and Maule, Chile (2010) earthquakes indicate poor performance of skewed bridges in comparison to non-skewed bridges.

Significant damage was experienced by the Pico Lyons Bridge (40° skew) in the 1994 Northridge earthquake in California (Apirakvorapinit et al. 2012). Finite element analyses by Apirakvorapinit et al. (2012) suggest that end girders on a 40° skewed bridge can experience a 50% stress increase compared with non-skewed bridges. The skewed Wushi highway bridge in Taiwan was severely damaged in the Chi Chi earthquake (Shamsabadi et al. 2006). Asymmetric heave patterns were observed behind the abutments, which indicated reduced contact between the abutment wall and backfill. Figure 2.12 shows greater backfill heave at the obtuse corner of the abutment and less heave at the acute corner. Greater heave near the obtuse corner of the abutment was attributed to larger pressures at the obtuse corner from rotation of the bridge. Observations of asymmetric heave patterns behind skewed abutments are in good agreement with the asymmetric pressure distribution observed by Sandford and Elgaaly (1993) (see Figure 2.10).

Figure 2.12. Asymmetric backfill heave pattern at Wushi highway bridge abutment in Taiwan, adapted from Shamsabadi et al. (2006).

Unseating of bridge decks from abutments was observed, particularly for skewed bridges, during the field reconnaissance following the 2010 Maule, Chile M8.8 earthquake (Elnashai et al. 2010). Significant damage was reported for the Las Mercedes Bridge (10° skew), the Paso Cladio Arrau Bridge (50° skew), and the Route 5 overpass near Chillan (highly skewed). Evidence of bridge rotation was observed, which was attributed to the center of mass and the center of rigidity becoming misaligned during the earthquake. In general, it appeared that rotation of the bridge deck caused the shear keys to fail, which resulted in unseating of the bridge deck from the abutment. It was estimated that skewed bridges experienced twice the damage rate compared to non-skewed bridges (Toro et al. 2013).

2.3.2 Shamsabadi et al. (2006) 3D Models

Results from 3D PLAXIS modeling by Shamsabadi et al. (2006) indicate a significant reduction in passive resistance of backfill against the abutment wall as the abutment skew angle increases. Passive force-deflection curves in Figure 2.13 illustrate the reduction of passive resistance with increasing skew angle. The variation of passive resistance with deflection was plotted for abutments at skew angles of 0°, 30°, 45°, and 60°.

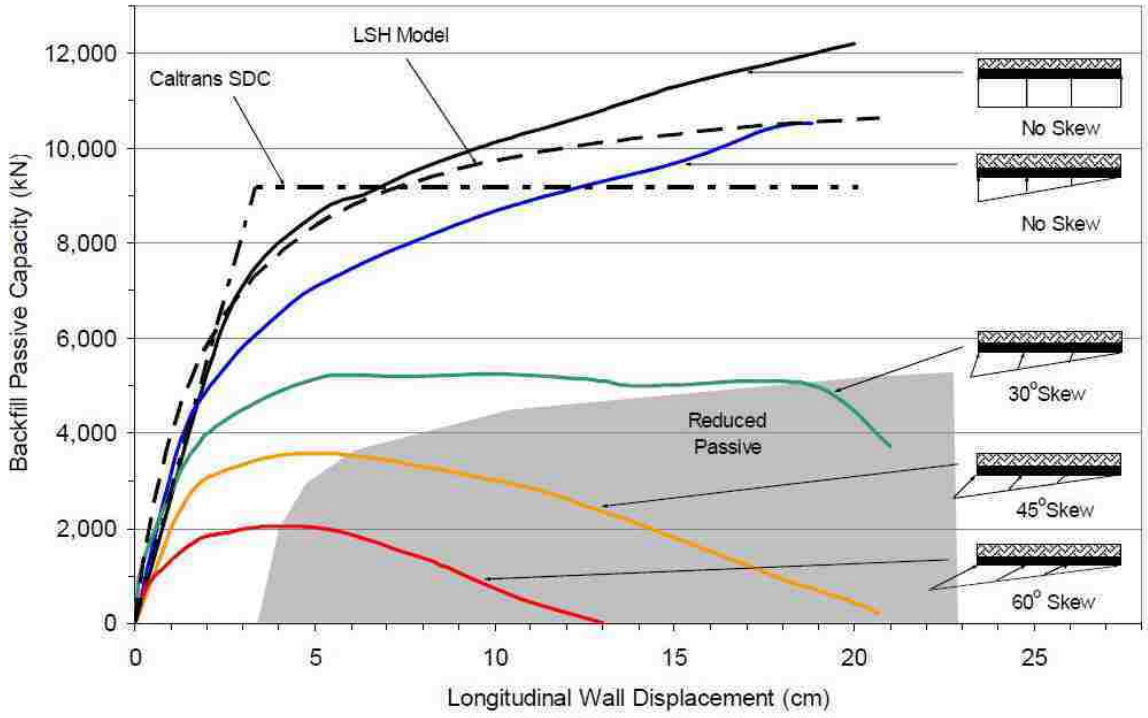

Figure 2.13. 3D PLAXIS results demonstrating reduction in passive resistance with increasing skew angle, adapted from Shamsabadi et al. (2006).

Cole and Rollins (2006) suggest that the passive resistance from the abutment backfill contributes 40% of the total lateral resistance of the abutment, with the other 60% attributed to the pile foundation. Results from PLAXIS 3D modeling suggest that poor performance of

skewed bridges is likely attributed to the reduction in passive resistance of the backfill against the abutment wall.

In the PLAXIS model, a 75-ft (22.8-m) wide and 5.5-ft (1.68-m) high abutment with longitudinal wingwalls was loaded monotonically into backfill with soil parameters listed in Table 2.4. Pressures along the abutment backwall were developed using a triangular lateral pressure distribution with the largest pressure at the obtuse end of the abutment (similar to Sandford and Elgaaly (1993)).

Table 2.4. Model Soil Parameters (Shamsabadi et al. 2006)

Soil Type	ɣ, pcf [kN/m^3]	ϕ	c, psf [kPa]	δ
Silty Sand	119.7 [18.8]	34°	522 [25]	23°

In Shamsabadi's (2006) study, the effect from wingwalls is considered small because of the large abutment width (75 ft). For narrow skewed bridges (such as the bridge abutment in the author's study) wingwalls can be expected to restrict the formation of the full passive wedge in the backfill. The restricted passive wedge would be expected to engage the wingwall on the obtuse side of the abutment, resulting in increased pressure on that wingwall.

Because of the rotation associated with skewed bridges, skewed abutments tend to develop a passive wedge near the obtuse corner that is less wide than the abutment width. Soil resistance decreases with increasing skew angle despite the wider contact surface normal to the abutment wall. Shamsabadi et al. (2006) suggest that more research is needed to evaluate the observed trends in the development of passive soil resistance as a function of skew angle

2.3.3 Rollins and Jessee (2012) Laboratory Tests

Rollins and Jessee (2012) also reported a reduction in soil passive resistance as skew angle increased. Nine small-scale laboratory tests were performed where a 1.26-m (4.1-ft) wide and 0.61-m (2-ft) high concrete wall was pushed longitudinally into a densely compacted sand backfill. Tests were conducted at skew angles of 0°, 15°, 30°, and 45°. Backfill extended 3 to 4 m (10 to 13 ft) behind the backwall and 0.3 m (1 ft) below the base of the wall to allow for the formation of a log-spiral failure surface. The backfill was confined by sidewalls to approximate plain-strain (2D) conditions. A plan and profile view of the test setup is provided in Figure 2.14.

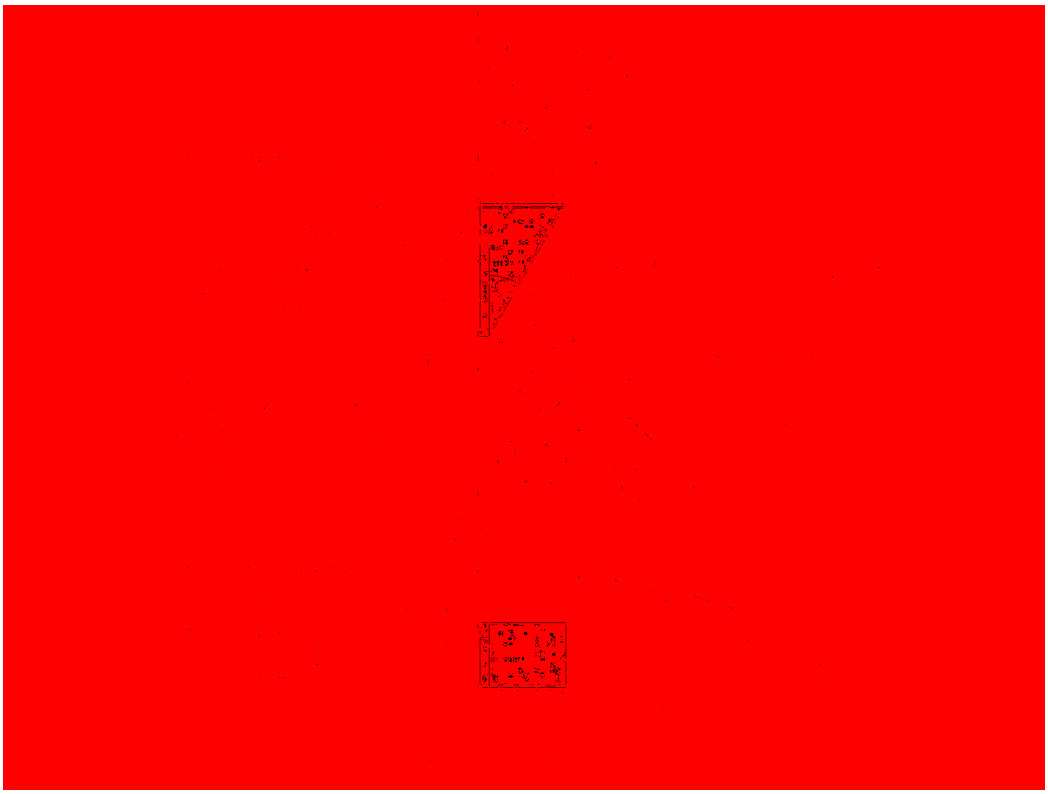

Figure 2.14. Small-scale lab test configuration (Jessee 2012).

Passive force-deflection curves at varying skew angles from the laboratory tests are shown in Figure 2.15. Similar to passive force-deflection curves by Shamsabadi et al. (2006) (see

Figure 2.13), a significant reduction in peak passive resistance was measured as skew angle increased. The dilative behavior of the passive resistance dropping off after reaching a peak is attributed to the high relative density of the backfill.

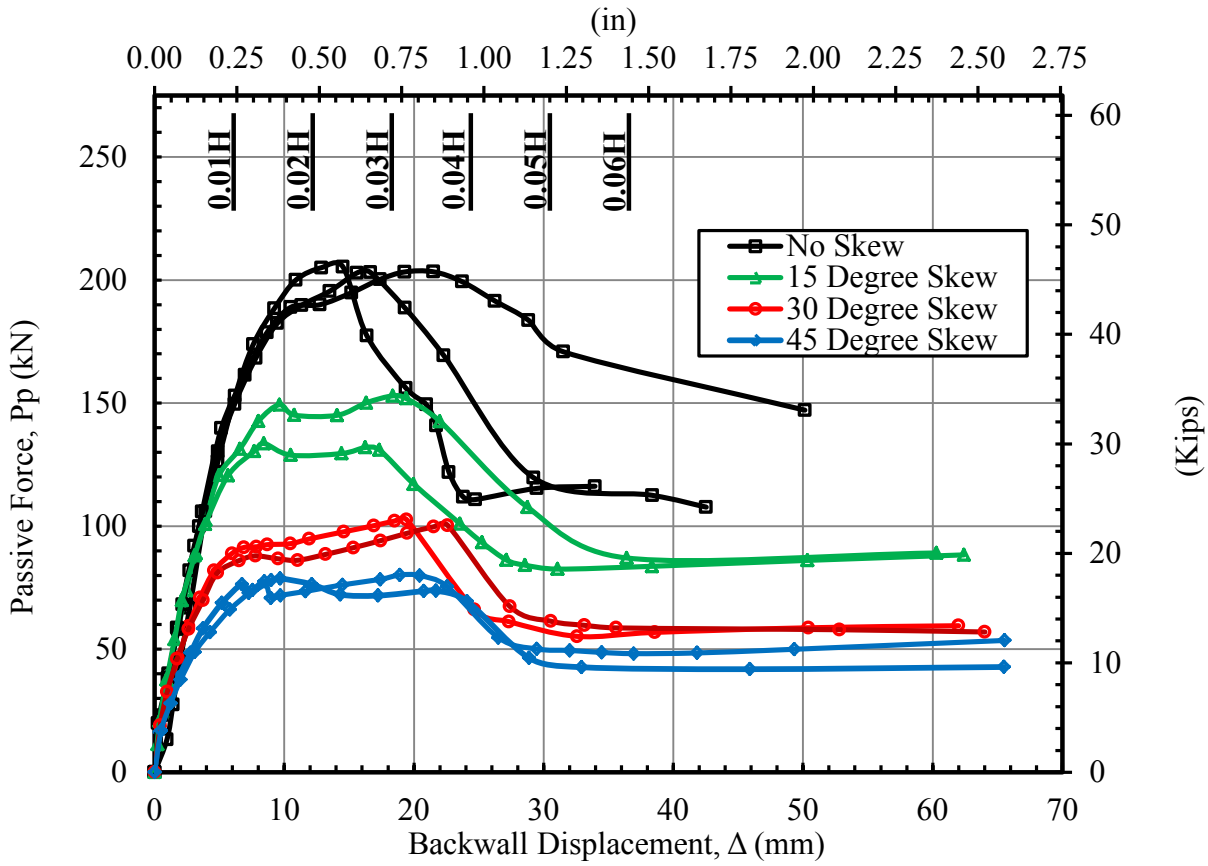

Figure 2.15. Reduction in passive resistance with increasing skew angle (Jessee 2012).

Based on the results from the small-scale tests, Rollins and Jessee (2012) developed a reduction factor (R_{skew}) as a function a skew angle (θ), and given in Equation (2-11).

$$R_{skew} = \frac{P_{p-skew}}{P_{p-no\ skew}} = 8.0 * 10^{-5}\theta^2 - 0.018\theta + 1.0 \qquad (2\text{-}11)$$

The reduction factor (R_{skew}) can be used to reduce the peak passive resistance in any passive force-deflection design method. Equation (2-11) is plotted in Figure 2.16 with results from the laboratory test data and is in remarkably good agreement with numerical model results from Shamsabadi et al. (2006).

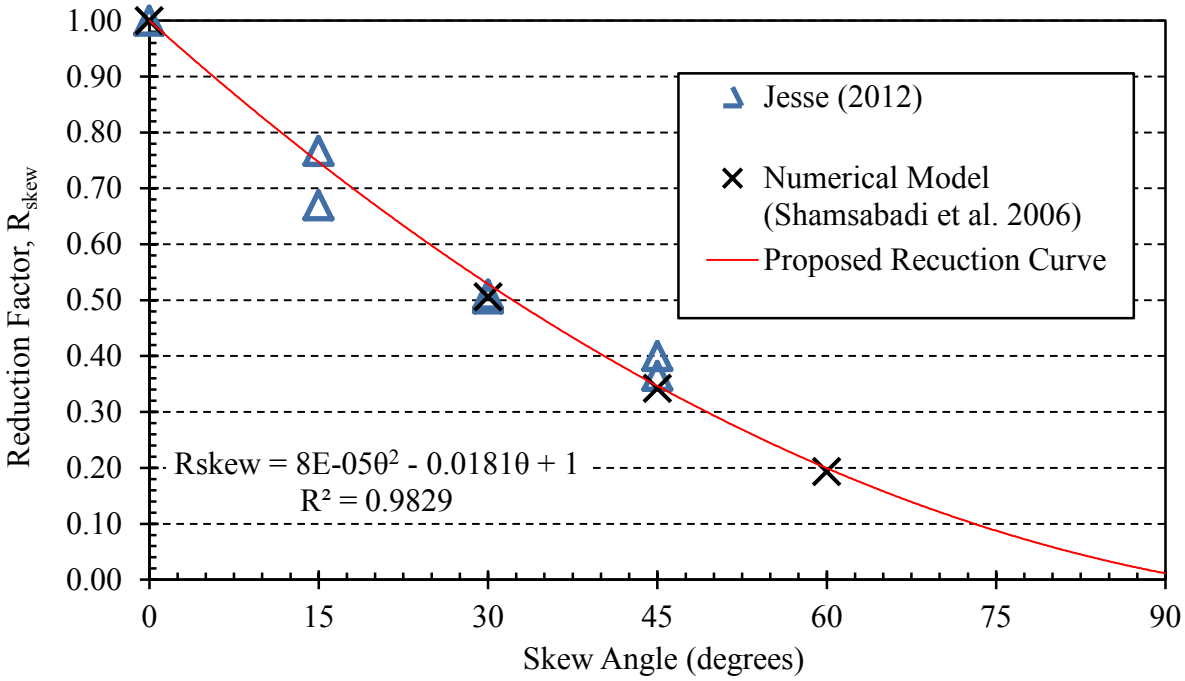

Figure 2.16. Proposed reduction curve by Rollins and Jessee (2012).

Results from Rollins and Jessee (2012) confirm the notion of a reduction in soil passive resistance with increasing skew angle proposed by Shamsabadi et al. (2006).

2.4 Reinforced Concrete Wingwalls

Longitudinal reinforced concrete wingwalls are commonly used on bridge abutments to provide lateral (transverse) resistance against seismic forces. Two previous studies investigated passive force-deflection behavior of abutments with longitudinal reinforced concrete wingwalls.

2.4.1 Romstad et al. (1996) UC Davis

Romstad et al. (1996) performed large-scale cyclic load-displacement tests on a non-skewed abutment with monolithic wingwalls. The abutment backwall was 10-ft wide (including wingwalls), 5.5-ft high, and 1.5-ft thick and was placed on 9-in-diameter CIDH piles. Wingwalls were 9-inches thick and extended 8 ft from the center of the backwall into the backfill. Structural backfill consisted of well-graded silty sand and embankment material was Yolo Loam (clayey silt). The structural backfill did not extend beyond the edge of the wingwalls and was so much stiffer and stronger than the embankment material that it experienced much less deformation compared to the embankment material. The general consensus for this study was that the silty sand backfill acted as a rigid body and transferred a large percentage of the abutment wall load to the Yolo Loam embankment (Romstad et al. 1996). Abutment and wingwall dimensions are illustrated in Figure 2.17.

Figure 2.17. Plan and profile view of longitudinal wingwalls (Romstad et al. 1996).

Romstad et al. (1996) reported passive force-deflection and stiffness-displacement results with the peak passive force (P_{peak}) mobilizing at displacements approximately 8% of the backwall height (0.08H). Peak displacements of 8% of the backwall height are larger than those reported for densely compacted granular backfills. The larger deflection required to mobilize the peak passive resistance suggests that shear failure occurred in the more compressible Yolo Loam embankment material as opposed to the stiffer silty sand used in the structural backfill.

2.4.2 Bozorgzadeh et al. (2008) UC San Diego

A similar study was done by Bozorgzadeh et al. (2008) with silty sand as both the embankment and backfill material. The silty sand had a drained friction angle of $\varphi' = 34°$ and a drained cohesion value of $c' = 600\ psf$. Measurements of P_{peak}were achieved at deflections approximately 2% to 3% of the backwall height (0.02H to 0.03H), in contrast to 8% of the backwall height observed by Romstand et al. (1996). The difference in the amount of deflection required to mobilized the P_{peak} can be attributed to the soil types used as embankment materials. The silty sand used by Bozorgzadeh et al. (2008) was likely less compressible than the Yolo Loam used by Romstand et al. (1996), resulting in lower peak deflection values. Abutment and wingwall dimensions used by Bozorgzadeh et al. (2008) are shown in Figure 2.18.

To the author's knowledge, no results were reported from either study regarding pressures or moments that developed normal to wingwalls. Steinberg et al. (2010) measured forces in transverse wingwalls on bridges in Ohio, but no results from longitudinal wingwalls were reported in the study. Load cells were instrumented at the wingwall-soil interface and changes in force were monitored with temperature variances.

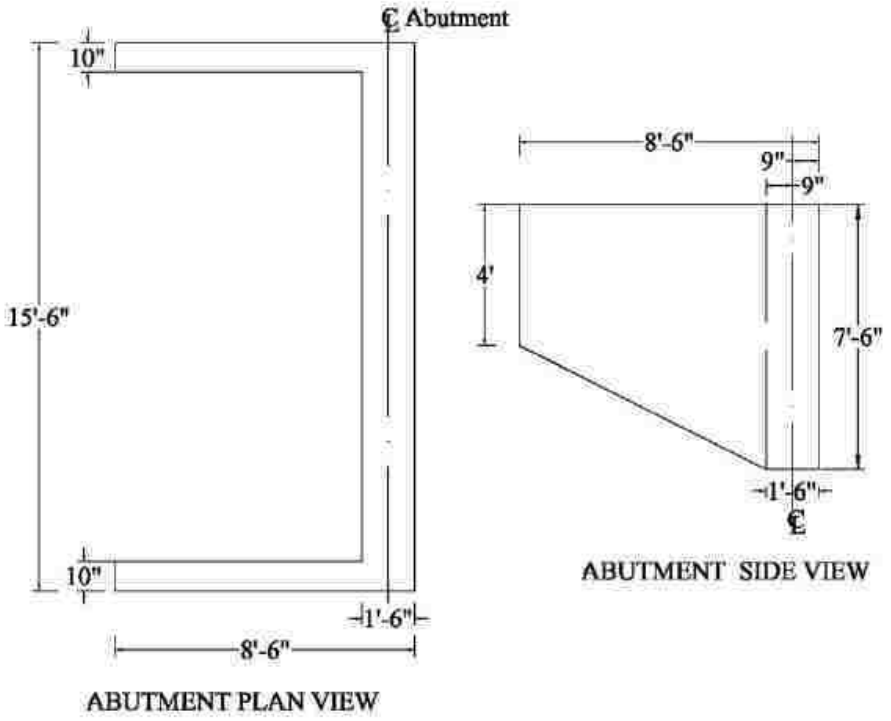

Figure 2.18. Plan and profile view of longitudinal wingwalls (Bozorgzadeh et al. 2008).

Results in this thesis aid in filling gaps in knowledge regarding the structural and geotechnical response of longitudinal RC wingwalls including wingwall deflection, bending moment and pressure distributions along the height of the wingwalls, lateral earth pressure coefficients, and the effect of a 45° abutment skew angle. In addition, until this study no large-scale tests with RC wingwall abutment geometry have been performed with densely compacted sand backfill or at a skew angle. The passive force-deflection results from this study provide useful information for bridge abutment design that involves RC wingwall geometry and/or skew angle.

3 FIELD TESTING METHODS

3.1 Site Description

The test site is located approximately 1,000 ft north of the air traffic control tower at the Salt Lake City International Airport. The site has been used for several series of tests, including those conducted by Rollins and Sparks (2002), Johnson (2003), Christensen (2006), Taylor (2006), and Rollins et al. (2010). Conditions at the site are ideal for conducting long-term field tests for several reasons including the absence of overhead obstructions, site security, available soil stratigraphic information, and the ease of maneuvering heavy equipment in and around the test site. An aerial view of the test site location relative to the air traffic control tower is shown in Figure 3.1.

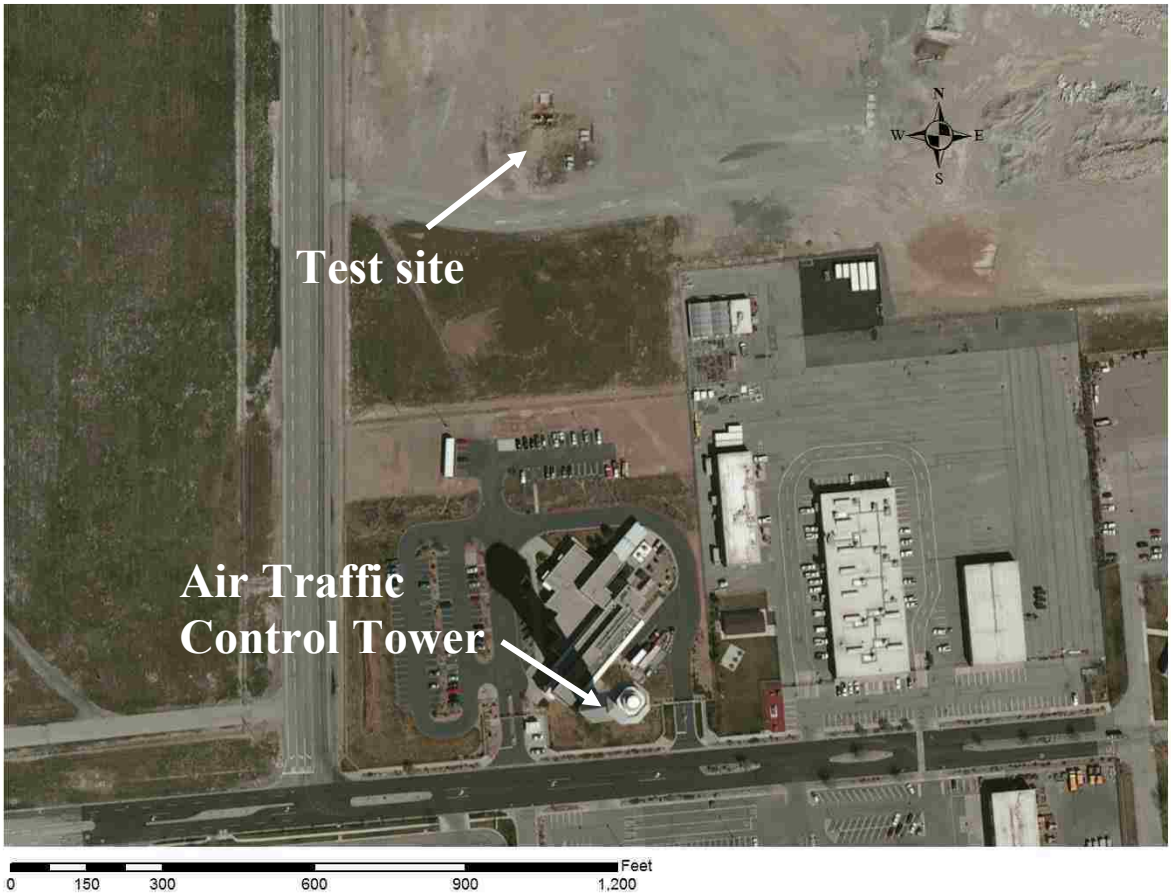

Figure 3.1. Large-scale field test site near Salt Lake City air traffic control tower.

3.2 Geotechnical Site Characterization

Drilled holes, hand augers, cone penetration tests (CPT), and dynamic cone penetration tests (DCPT) have been conducted at the test site during previous studies. The location of these subsurface tests is depicted in Figure 3.2. The pile cap for this study is located at CPT-06-M. Data for the idealized soil profile from CPT-06-M are available in Figure 3.3 and Figure 3.4. Below the densely compacted fill, the soil profile consists of interbedded silt and clay to a 15-ft-

depth, followed by interbedded silt and sand to a 50-ft-depth. The regional water table is located at approximately 5.5-ft-depth.

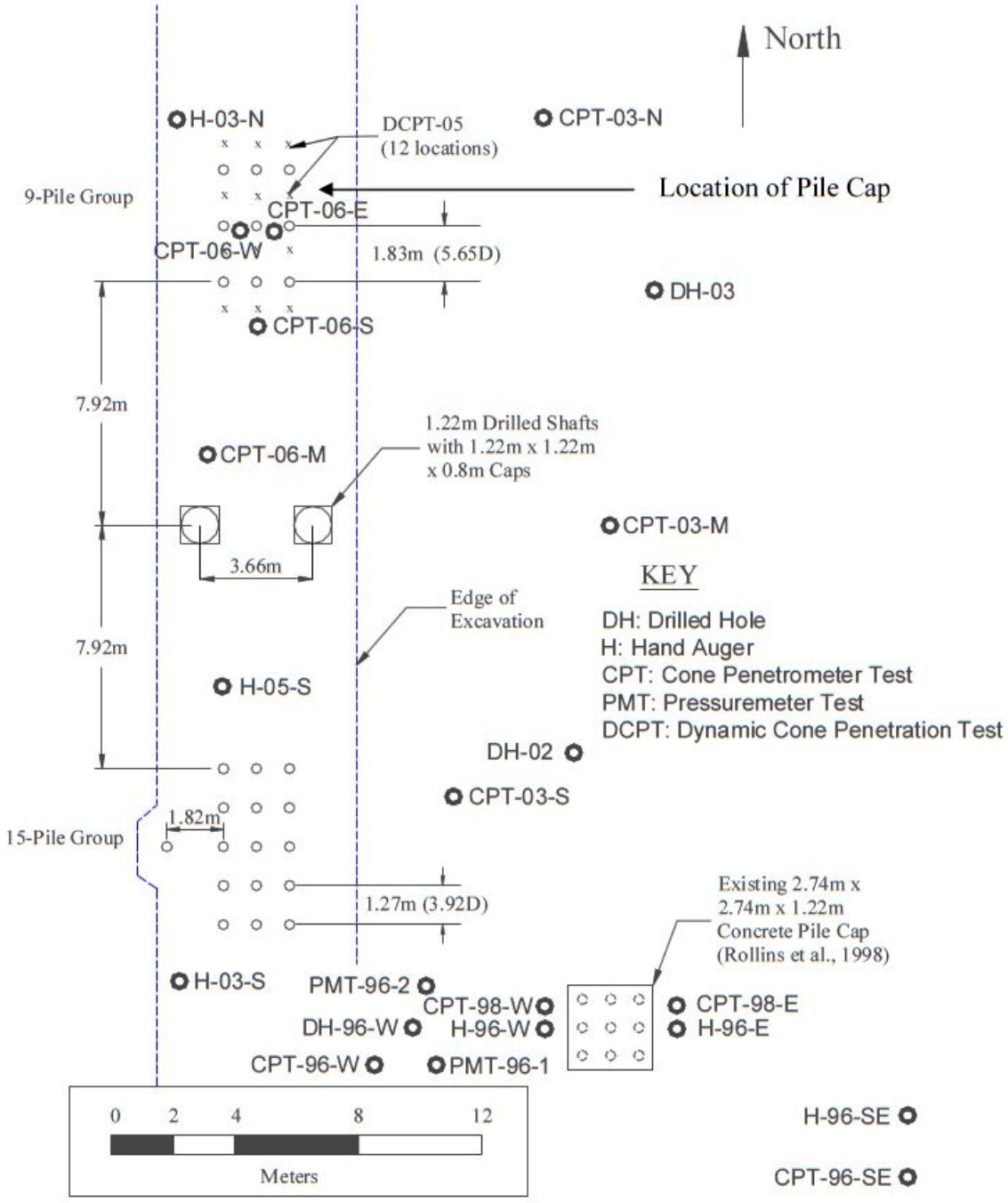

Figure 3.2. In-situ test history at Salt Lake City airport site (Rollins et al. 2010).

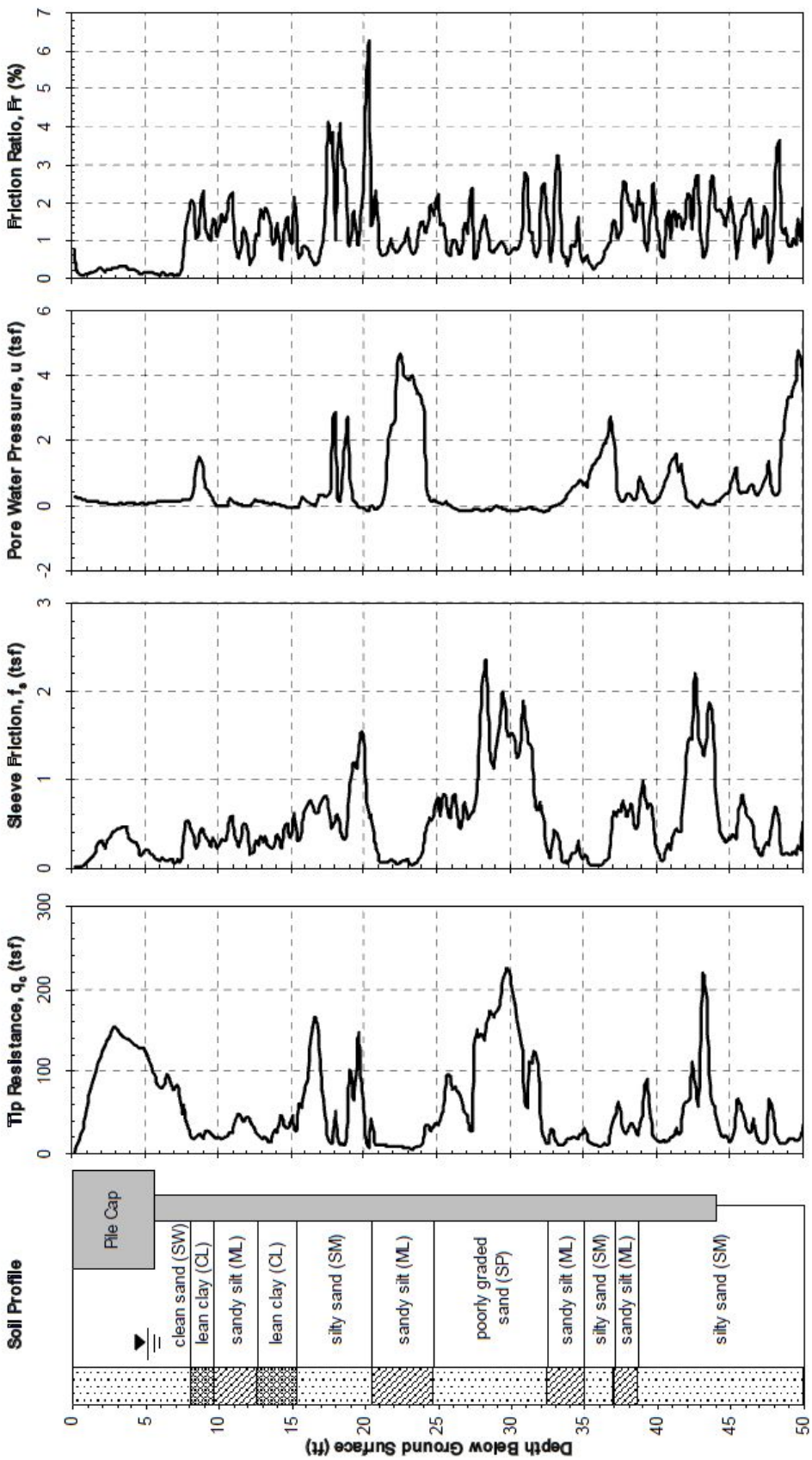

Figure 3.3. Idealized Soil Profile From CPT Test (Rollins et al. 2010)

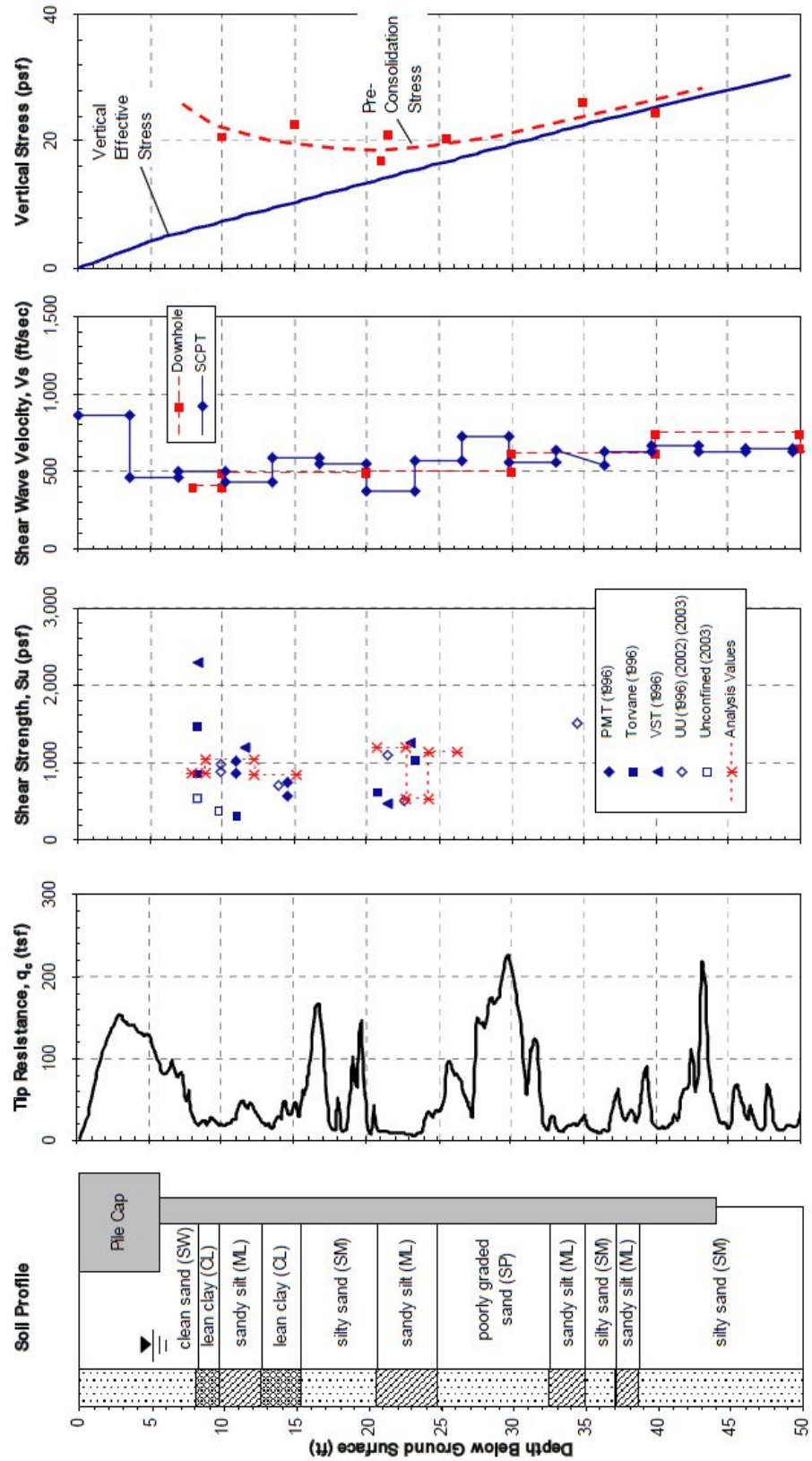

Figure 3.4. Idealized Soil Profile From CPT Data (Rollins et al. 2010)

Further details concerning the geotechnical characterization of the site may be found in previous publications (Christensen 2006; Rollins et al. 2010; Strassburg 2010).

3.3 Test Layout

Two large-scale lateral load tests were performed on 0° and 45° skewed abutments with reinforced concrete wingwalls. Two 600 kip hydraulic actuators reacted against a drilled shaft and sheet pile foundation to load the pile cap configuration into the backfill. The 45° skew angle was achieved by attaching two concrete wedges to the backside of the pile cap; reinforced concrete wingwalls were secured to the pile cap and concrete wedges. The reaction foundation, pile cap, and 15° skew wedge were available from previous testing. Plan and profile views of the complete test setup are illustrated in Figure 3.5. Individual components for large-scale field tests are described in detail in this section.

3.3.1 Reaction Foundation

The reaction foundation consisted of two 4-foot (1.22-m) diameter drilled shafts spaced 12 feet (3.66 m) center to center on an east-west line with a sheet-pile wall spanning the north side of the drilled shafts. Additionally, two deep I-beams with the strong axis oriented in the north-south direction spanned both the north and south sides of the drilled-shaft/sheet-pile wall group to provide the foundation with additional lateral rigidity.

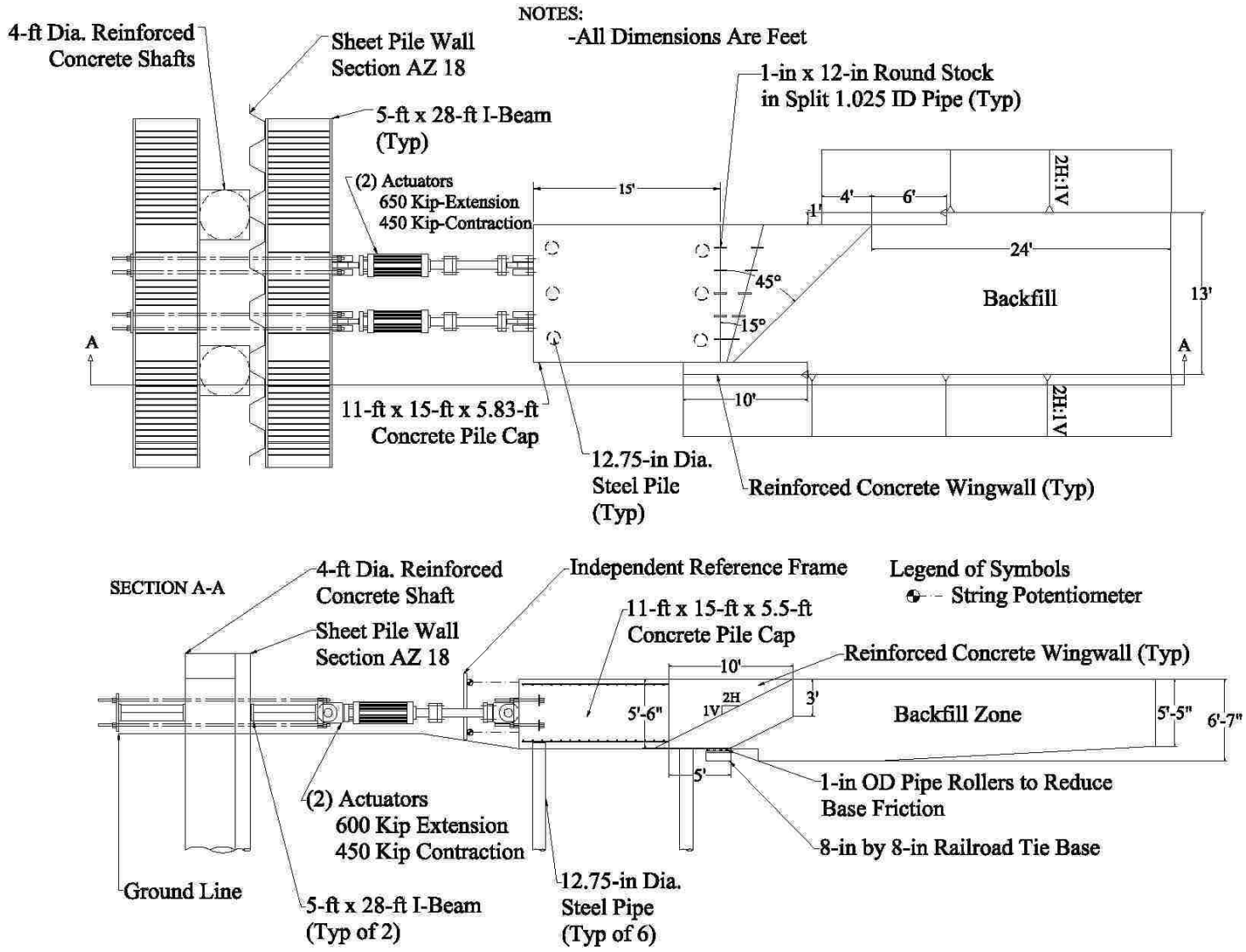

Figure 3.5. Schematic drawing of test layout for abutment with reinforced concrete wingwalls.

The east and west drilled shafts extend to depths of 70.0 feet (21.35 m) and 55.2 feet (16.82 m), respectively. Four-foot square by two-foot thick caps were installed at the top of each drilled shaft. Reinforcement of the top 35 feet (10.67 m) of each drilled shaft consisted of 18 #11 (#36) vertical bars with a #5 (#16) bar spiral at a pitch of 3 inches (75 mm). Below 35 feet, vertical reinforcement consisted of 9 #11 (#36) vertical bars with spiral reinforcement at a pitch of 12 inches (300 mm). Concrete cover throughout the length of the shaft was approximately 4.75 inches (120 mm). The specified compressive strength of the concrete in the drilled shafts was 6,000 psi (41 MPa).

AZ-18 sheet piling made of ASTM A-572 Grade 50 steel was used for the sheet pile wall on the north side of the two drilled shafts. A vibratory hammer was used to install the wall as close to the drilled shafts as possible and to depths ranging from 33.6 feet to 35.6 feet (10.24 m to 10.85 m) below the excavated ground surface.

The steel I-beams were 28 feet (8.53 m) long, 64 inches (1,626 mm) deep, and 16 inches (406 mm) wide. Numerous additional web stiffeners were installed between the flanges to prevent web buckling during loading. Eight 1.75 inch (44 mm) DYWIDAGs with minimal post-tensioning were used to tie the I-beams, drilled shafts, and sheet pile wall together. The reaction foundation is shown in Figure 3.6.

Figure 3.6. Reaction foundation for large-scale testing.

3.3.2 Pile Cap and Piles

The south edge of the pile cap was located 16.4 feet (5.0 m) to the north of the reaction foundation and was constructed on a six-pile group with two rows of three steel piles oriented in the east-west direction. Each pile had an outside diameter of 12.75 inches (324 mm), a wall thickness of 0.75 inches (9.5 mm) and was constructed with ASTM A252 Grade 3 steel pipe with an average yield strength of 57 ksi (393 MPa). All piles were driven closed-ended to a depth of approximately 43 feet (13.1 m) below the ground surface.

The tops of the piles were embedded a minimum of 6 inches (150 mm) into the base of the pile cap. 18-foot long (5.49 m) rebar cages consisting of 6 #8 (#25) vertical bars and a #4 (#13) spiral at a pitch of 6 inches (152 mm) were lowered 13.2 feet (4.02 m) into the steel piles with the remaining 4.8 feet (1.47 m) extending into the pile cap and supporting the upper horizontal reinforcing grid. The upper and lower reinforcing mats consisted of #5 (#19) bars in the longitudinal and transverse direction at 8 inches (203 mm) on center. Concrete with a compressive strength of 6,000 psi (41.37 MPa) was used to fill the steel piles and to construct the pile cap. Pile cap dimensions are 15 feet (4.57 m) long (north-south direction), 11 feet (3.35 m) wide, and 5.7 feet (1.74 m) high. Inclinometer and shape array tubes were also cast into the center pile of each row. Eight DYWIDAGs with plate anchors were cast horizontally into the pile cap to provide a connection point for the loading apparatus. The placement of these DYWIDAGS positioned the two actuators on the vertical center of the pile cap but offset 2.25 feet (0.69 m) on either side of the horizontal centerline.

3.3.3 Concrete Wedges

To test the effect of a 45° bridge skew angle, concrete wedges constructed with 6,000 psi specified compressive strength were attached to the pile cap face. A larger concrete wedge was attached to an existing 15° skew wedge to form a total skew of 45°. Both wedges were placed on steel rollers, as shown in Figure 3.7, to minimize friction resistance beneath the wedges and isolate the backfill as the primary source of passive resistance, in addition to the piles.

Figure 3.7. Rollers underneath 45° skew wedge.

Reinforcement requirements for each wedge were calculated assuming worst-case load assumptions: vertical and horizontal triangular pressure distribution with the maximum force occurring at the bottom acute corner of the wedge. The reinforcement cage and form for the 45° skew wedge can be seen in Figure 3.8, which shows the concrete pour.

To eliminate the potential for lateral or vertical movement of either wedge relative to each other or the existing pile cap, interface connections were designed that provided transverse and vertical rigidity but also provided means for removing the 45° wedge without damaging the 15° wedge. For this purpose a 1-inch (25.40 mm) diameter by 11-inch (279 mm) long piece of round stock was inserted into 1.0625-inch (26.987 mm) inside-diameter pipe at the interface of the 15° and 45° skew wedges. A similar setup was used for the connection between the existing pile cap and the 15° wedge except the round stock was placed in 1-1/8-inch (28.58 mm) diameter, 6-inch (152 mm) deep holes that were drilled into the face of the existing pile cap. Five

round stock connection elements were used for both the pile cap-wedge interface and the wedge-wedge interface. To ensure that the entire connection acted as a unit, ¾-in (1.90 cm) angle iron stiffeners were welded to the ends of the pipes.

Figure 3.8. Concrete pour for 45° skew wedge.

Wingwalls were not poured monolithically with the 45° skew wedge because 45° skew unconfined abutment tests were also performed as part of the test series; consequently, precast wingwalls were secured afterward. The 45° skew test abutment, without wingwalls, is shown in Figure 3.9. On both sides of the 45° skew test abutment, two lines of (5) 7/8-in-diameter ASTM

A307 steel threaded rod were cast in the abutment for securing the reinforced concrete wingwalls. Threaded rods were embedded 7 inches and extended out at least 14 inches to accommodate 12-in-thick wingwalls. Steel plates were also attached to the top and sides of concrete wedges to minimize movement relative to each other.

Figure 3.9. 45° skewed test abutment with threaded rod for securing wingwalls.

3.3.4 Reinforced Concrete Wingwalls

The reinforced concrete wingwalls were designed in general accordance with the Wingwall 'C' and 'D' guidelines provided by Jan Six (2013) from the Oregon Department of Transportation (ODOT) Bridge Engineering Section. Wingwalls 'C' and 'D' are longitudinal RC wingwalls and the design guidelines are identical with the exception of 'C' being the wingwall at the obtuse corner of the abutment and 'D' at the acute corner. Similar RC wingwall designs are implemented in California (Bozorgzadeh et al. 2008; Romstad et al. 1994; Shamsabadi et al. 2007) Plan and elevation details of the ODOT Wingwall 'C' design are illustrated in Figure 3.10 and a section view is provided in Figure 3.11.

The wingwall reinforcement and connection to pile cap was designed to match the moment capacity of the ODOT Wingwall 'C' design. The failure mode considered for design was bending moment failure of the wingwalls at the pile cap interface caused by bending of the wingwall about the weak axis due to soil pressures from lateral seismic loads. Based on the wingwall reinforcement at the center line labeled 'Bent 2' in Figure 3.10, a factored moment capacity of 47.6 kip-ft/ft (65.0 kN-m/m) was calculated using traditional reinforced concrete design equations (3-1) and (3-2).

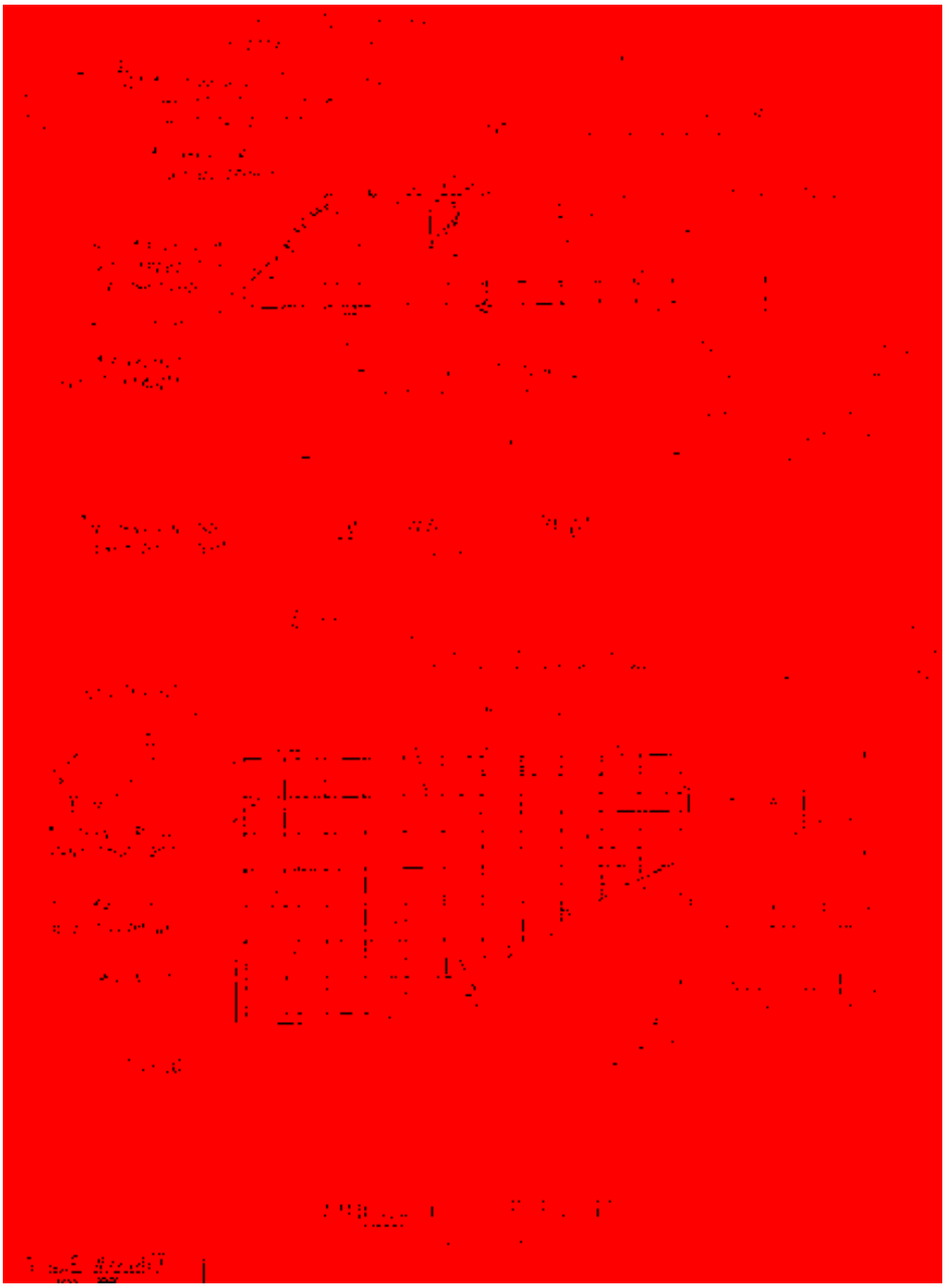

Figure 3.10. Wingwall 'C' detail from Oregon Department of Transportation (Six 2013).

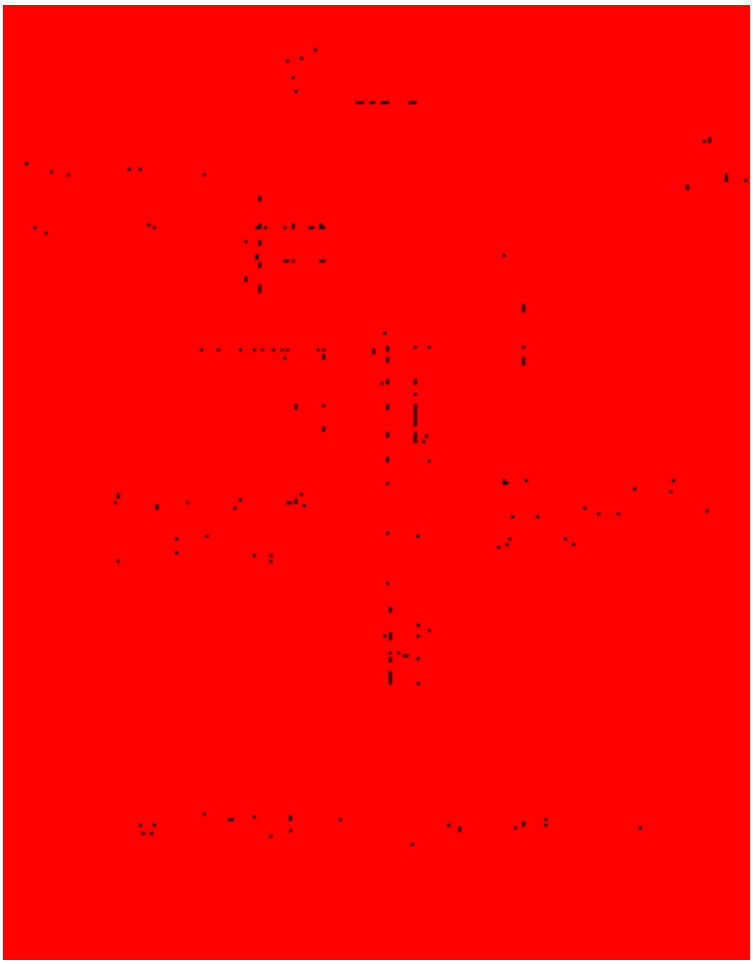

Figure 3.11. Typical section view for Wingwall 'C' design from Oregon Department of Transportation (Six 2013).

$$\varphi M_N = \frac{\varphi A_s f_y \left(d - {}^{a}/_{2}\right)}{12 \frac{in}{ft}} \tag{3-1}$$

where,

$$a = \frac{A_s f_y}{0.85 f_c' b} \tag{3-2}$$

$\varphi = 0.9$

$A_s = 1.2\ in^2 \quad 2(\#7\ bars)$

$f_y = 60\ ksi$

$d = 9.7\ in$

$f_c' = 4\ ksi$

$b = 12\ in$

Assuming a uniform lateral soil load distribution on the 6 ft of cantilevering wingwall shown in Figure 3.12, a 15.7 kip/ft tension demand was computed at the wingwall-pile cap connection.

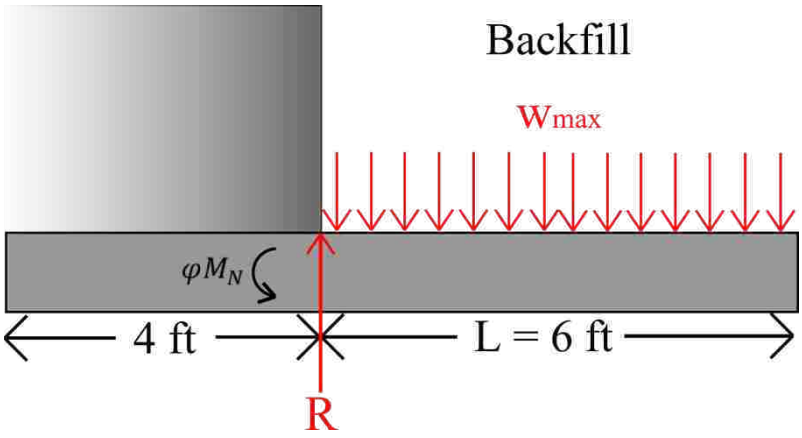

Figure 3.12. Uniform distributed load was used to approximate pullout force demand (*R*) at wingwall connection to pile cap.

Two lines of (5) 7/8-in-diameter ASTM A307 steel bolts spaced 3-ft-apart on centers were selected to resist the 15.7 kip/ft pullout force at the pile cap-wingwall connection. It was anticipated the line of bolts closest to the backfill would resist the majority of the pull-out force, while the second line of bolts aided in restraining movement. Tensile capacity of a 7/8-in-diameter ASTM A307 steel bolt is 20.9 kips when embedded 6 ¼ inches in 4000 psi concrete.

Bolts used to secure wingwalls in this study were embedded 7 inches and torqued to 200 ft-lb, which corresponds to a pretension of $T_b = 13.7\ kip/bolt$. Equation (3-3) was used to estimate the bolt torque-tension relationship.

$$T_b(lb) = \frac{Torque\ (ft \cdot lb)}{0.0167(bolt\ diameter\ (in))} \tag{3-3}$$

Steel square washers were inserted between the nut and concrete when torque was applied to bolts. In the event that the full passive resistance would develop at the tapered end of the wingwall during testing, it was estimated that slip demand at the connection would be 3.1 kip/bolt. Using Equation (3-4) the slip resistance (R_n) was estimated to be 4.6 kip/bolt, which is approximately 50% greater than the demand of 3.1 kip/bolt.

$$R_n = \mu D_u h_f T_b n_s \tag{3-4}$$

where,

$\mu = 0.3\ friction\ coefficient\ (conservative)$

$D_u = 1.13$

$h_f = 1.0\ for\ no\ fillers$

$T_b = 13.7\ kip/bolt\ (bolt\ pretension)$

$n_s = 1.0\ for\ one\ slip\ plane$

Where possible, threaded rods were cast in-place with the newly poured 45° wedge; otherwise Redhead® wedge anchors were installed into the existing abutment. Dimensions for the wingwall bolted connection are shown in Figure 3.13.

Figure 3.13. Wingwall bolt spacing used for large-scale testing.

Wingwall reinforcement details and concrete dimensions are illustrated in Figure 3.14. Horizontal reinforcement consisted of (9) #7 bars spaced vertically at 6 inches at the inside face

and the (4) #4 bars spaced at 12 inches at the outside face with #8 bars at the top and bottom. Horizontal reinforcement was tied together with #4 vertical loops spaced at 12 inches.

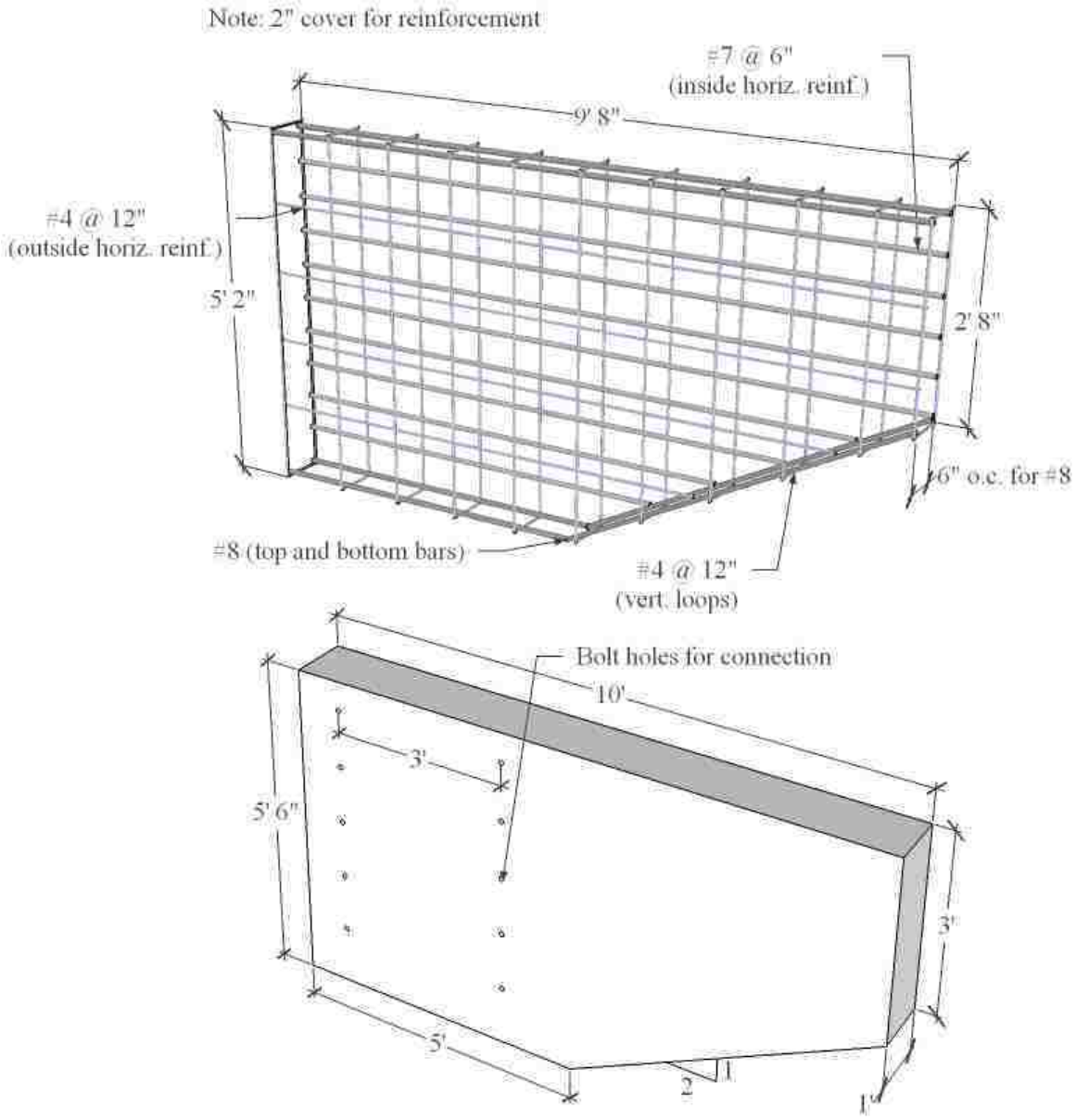

Figure 3.14. Wingwall design used in large-scale testing.

Wingwalls used for this study were 5.5-ft-high, 10-ft-long, and 1-ft-thick. At 5 ft out, the bottom of the wingwall tapered up at a 2H:1V slope. The tapered end was 3-ft high. Although the wingwalls were 10-ft-long, only 6 ft of wingwall extended into the backfill zone. The remaining 4 ft were used to connect the wingwall to the pile cap.

Wingwall reinforcement and forms before the concrete pour are shown in Figure 3.15. Cardboard mailing tubes, taped at both ends, occupied the space for the bolt holes during the concrete pour.

Figure 3.15. Wingwall reinforcement cages and forms.

Wingwalls were poured laying on their side, as shown in Figure 3.16. The same specified 6,000 psi concrete was used for the wingwalls and 45° skew wedge.

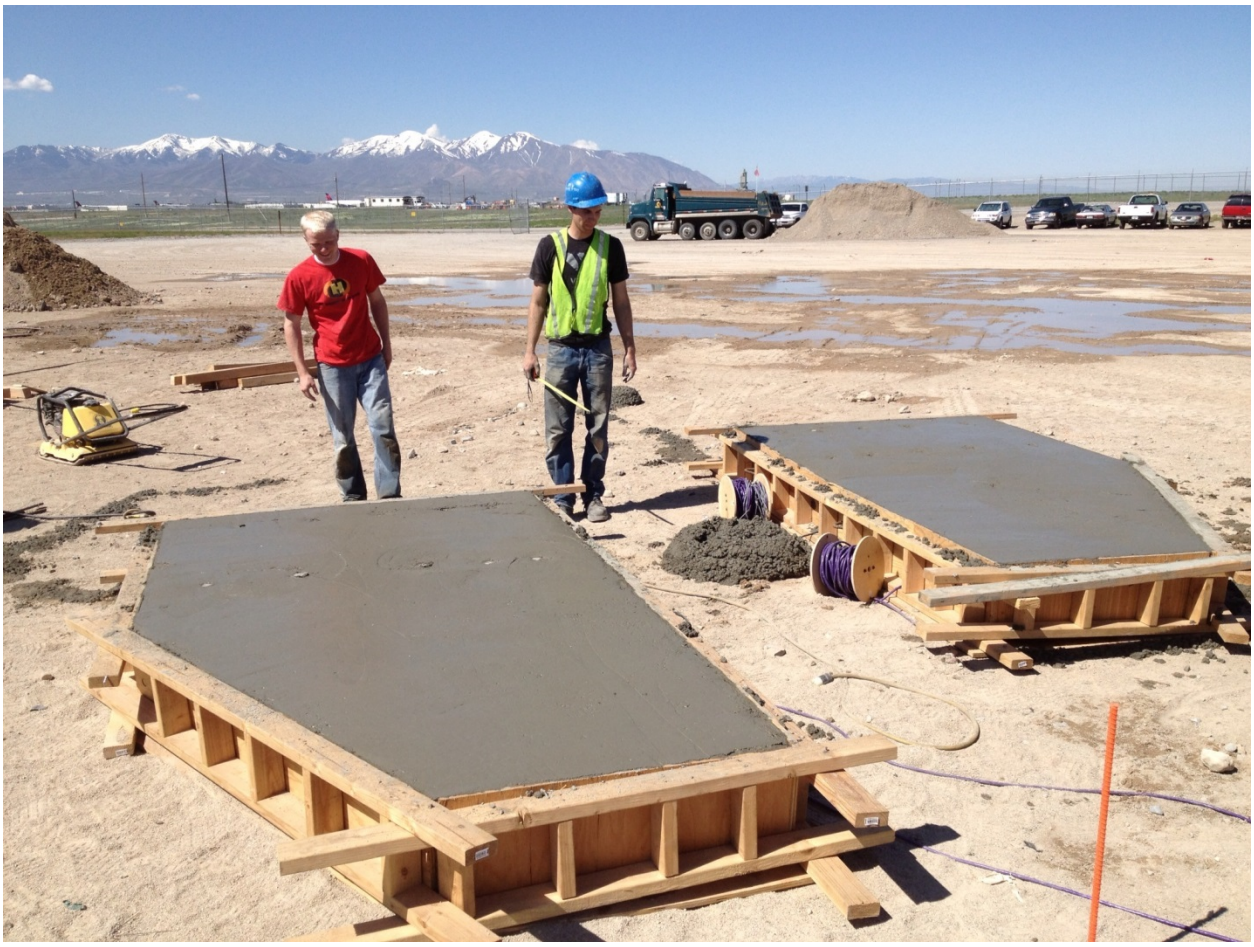

Figure 3.16. Concrete wingwalls poured lying flat.

The 45° skewed test abutment with reinforced concrete wingwalls is shown in Figure 3.17, which illustrates how the wingwalls extend into the backfill zone 6 feet, while the remaining 4 feet are used for the connection to the pile cap.

Figure 3.17. Large-scale 45° skewed abutment with reinforced concrete wingwalls.

3.3.5 Loading Apparatus

Loading of the abutment was accomplished through the use of two MTS actuators placed between the reaction foundation and the pile cap in a north-south direction as shown in Figure 3.18. The DYWIDAGs tying the reaction foundation together were used as the connection point between the actuators and the reaction system. The eight DYWIDAGs embedded in the pile cap, in addition to the two 4-foot (1.22 m) long extensions shown in Figure 3.18, provided the connection point between the actuators and the pile cap.

The abutment was loaded 0.05 in/min (1.27 mm/min) to target displacement intervals of approximately 0.25 in (6.35 mm). Each actuator had an extensional capacity of 600 kips (2.67 MN) (north direction) and a contractive capacity of 450 kips (2.00 MN) (south direction). Swivel heads were located at both the north and south ends of the actuators to provide a zero-moment connection between the actuators and pile cap. The actuators were installed level and were centered 2.75 feet (0.84 m) above the base of the 5.5-ft-high pile cap (0.5H).

Figure 3.18. 600-kip hydraulic actuators.

3.3.6 Backfill Zone

The backfill zone extended 24 ft behind the abutment backwall in the longitudinal direction and approximately 5 ft in the transverse direction on either side of the abutment. Within 8 ft from the abutment backwall, the backfill extended 1 ft below the base of the pile cap to allow for the potential log-spiral failure surface. Beyond 8 ft from the backwall, the backfill was approximately level with the base of the pile cap. The edges of the backfill tapered downward at a 2H:1V slope. Compacted backfills for 45° skew and 0° skew tests are shown in Figure 3.19 and Figure 3.20, respectively. The backfill was compacted to at least 95% of the modified Proctor value [111.5 pcf (17.52 kN/m^3)] with a vibratory drum roller and a walk-behind plate compactor in 6- to 8-in lifts until the backfill was level with the top of the abutment.

Figure 3.19. Densely compacted sand backfill with a 2H:1V slope at the edges for 45° skewed abutment.

Figure 3.20. Densely compacted sand backfill with a 2H:1V slope at the edges for non-skewed abutment.

3.3.7 Transverse Load-Deflection

A transverse load-deflection test was also performed on the 45° skewed abutment to gain a better understanding of the transverse resistance of the two pile rows relative to each other. Two 300-kip hydraulic jacks reacted against the east embankment to push the abutment in the transverse (west) direction, as seen in Figure 3.21. The reaction wall was comprised of 4-ft x 2-ft concrete blocks on densely compacted sand supported by railroad ties and steel plates and is more clearly shown in Figure 3.22.

Figure 3.21. Transverse load-deflection test setup.

The two hydraulic jacks were positioned 57 in (144.8 cm) below the top of the pile cap and 11½ in (29.2 cm) from either side of the centerline of the pile cap. Deflection was monitored using four string potentiometers at the top and bottom corners of the east side of the pile cap.

Figure 3.22. 300-kip hydraulic jacks.

3.4 Geotechnical Backfill Characterization

This section provides the soil gradation, relative density, relative compaction, and strength parameters associated with the backfill material used for this testing.

3.4.1 Backfill Soil and Compaction

Soil used for this series of tests consisted of approximately 250 tons (227 metric tons) of poorly graded sand (SP type soil according to the Unified Soil Classification System or an A-1-b type soil according to the AASHTO Classification System) at a moisture content of 7%. Pre- and post-testing gradation plots are shown in Figure 3.23. Contamination of the backfill material with native material located at the bottom and near the sides of the test pit may explain slight changes in the soil gradation; however, it may merely be a result of natural variation between soil samples. The grain-size distribution generally fell within the gradation limits of washed concrete sand (ASTM C33).

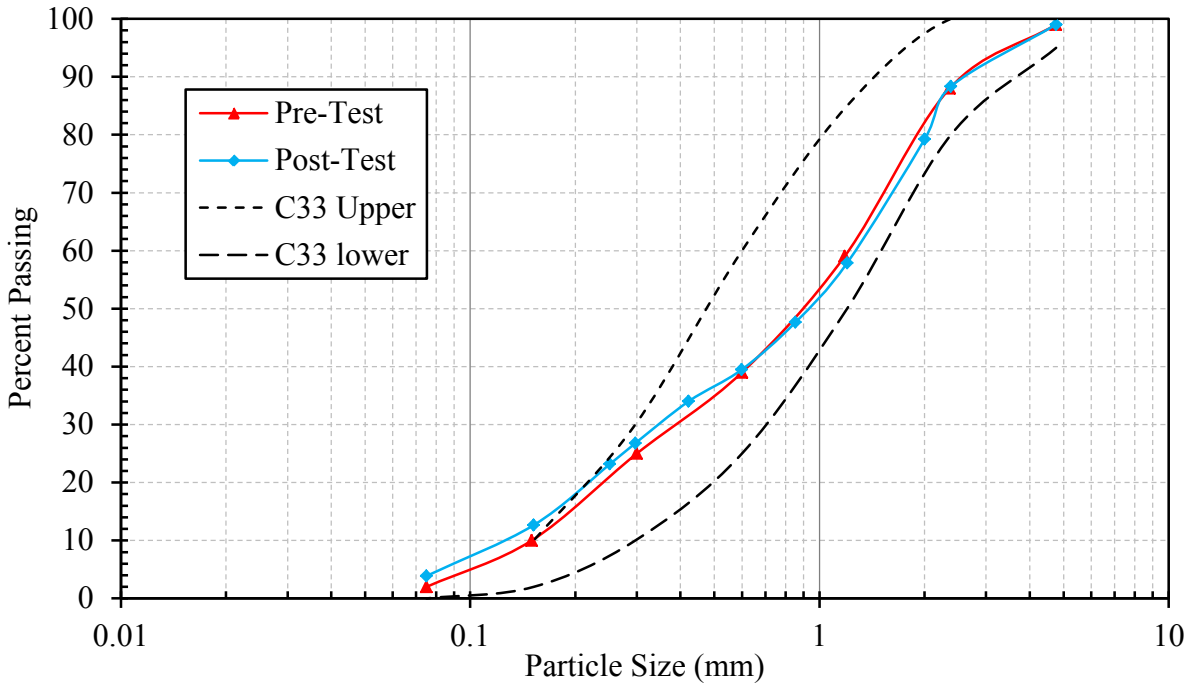

Figure 3.23. Pre- and post-test particle-size distribution of backfill soil, adapted from Franke (2013).

Although the additional fines accumulated during the testing process may have pushed the particle-size distribution slightly outside the gradation limits of washed concrete sand, this was not expected to significantly affect test results. Table 3.1 provides the soil gradation parameters for the soil particle-size analyses conducted before and after the skewed abutment tests.

Table 3.1. Soil Gradation Characteristics, Pre- and Post-Testing, adapted from Franke (2013)

Test	Sand (%)	Fines (%)	D_{60} (in) [mm]	D_{50} (in) [mm]	D_{30} (in) [mm]	D_{10} (in) [mm]	C_u	C_c
Pre-Test	98.0	2.0	1.22 [31.0]	0.9 [22.9]	0.4 [10.2]	0.16 [4.1]	7.6	0.8
Post-Test	96.1	3.9	1.26 [32.0]	0.92 [23.4]	0.34 [8.6]	0.13 [3.3]	9.7	0.7

Relative density (D_r) can be estimated using the empirical correlation between relative density and relative compaction (R) of granular soils (Lee and Singh 1971). From the measured field test data, this correlation [Equation (3-5)] was used to calculate the relative density from the relative compaction measured with a calibrated nuclear density gauge in the field. Table 3.2 shows average measured relative compaction and average relative density from the correlation.

$$R = 80 + 0.2D_r \quad (3\text{-}5)$$

where,

$R = Relative\ Compaction$ (%)

$D_r = Relative\ Density$ (%)

Table 3.2. Summary of Compaction and Moisture Content Data for Both Tests

Backfill Soil Properties	0º Skew Test	45º Skew Test	Average
Minimum Dry Unit Weight [pcf]	105.4	107.9	106.7
Maximum Dry Unit Weight [pcf]	109.9	111.5	111.4
Average Dry Unit Weight [pcf]	108.2	109.6	108.9
Relative Compaction	97.0%	98.3%	97.7%
Relative Density	85.0%	91.5%	88.3%
Moisture Content	7.2%	7.8%	7.5%

Dry unit weight, moisture content, and relative compaction were measured with a nuclear density gauge after each lift and are plotted with depth in Figure 3.24, Figure 3.25, and Figure 3.26 respectively. Dry unit weights were relatively consistent with depth. The largest deviation (2.2%) from the average dry unit weight was measured at a depth of 3 ft for the non-skewed abutment backfill.

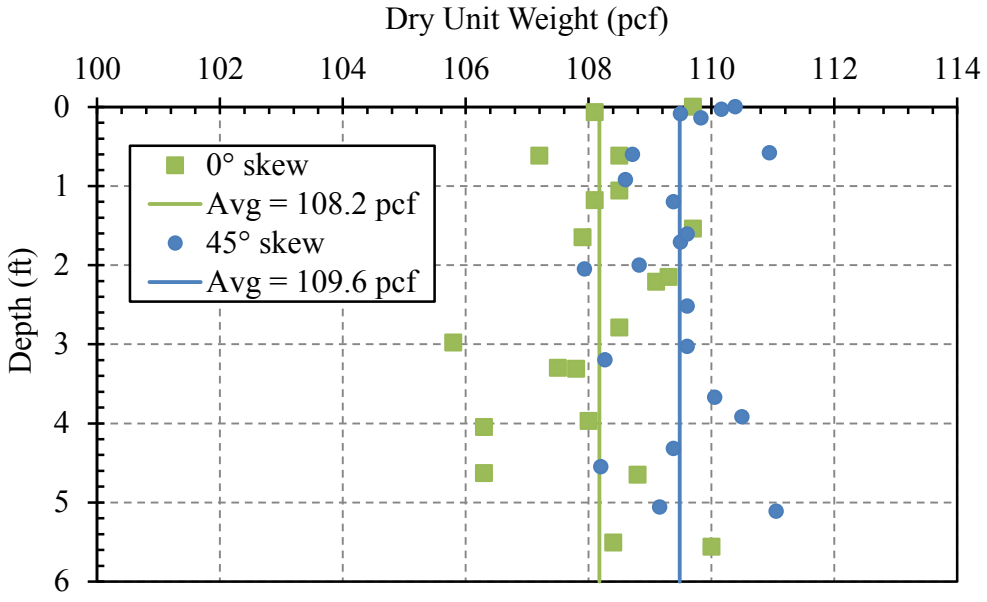

Figure 3.24. Backfill dry unit weight measurements with depth.

Backfills for both tests were compacted to approximately the same relative compaction. The average relative compaction of the backfill measured for the 45° skewed abutment was 1.2% higher than the non-skewed abutment.

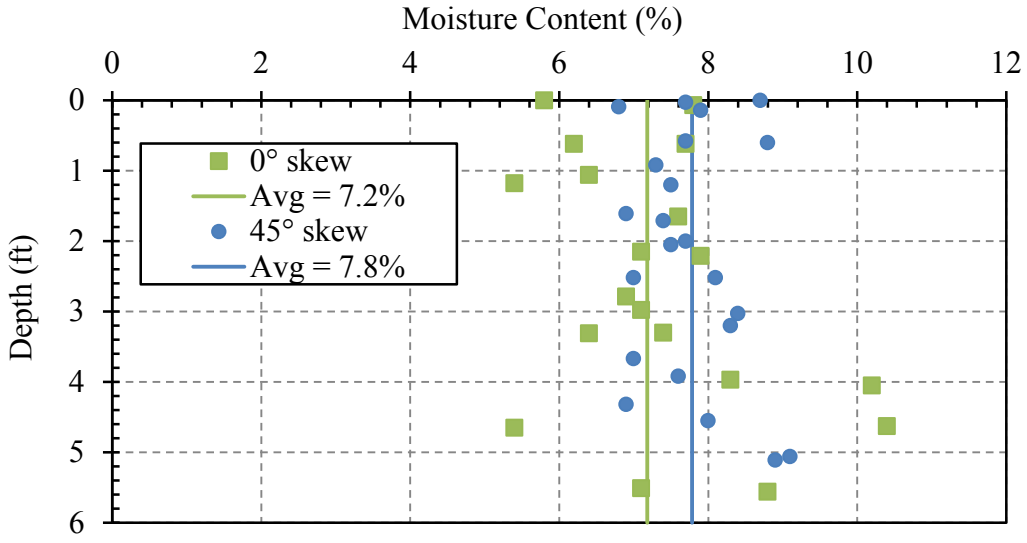

Figure 3.25. Backfill moisture content with depth.

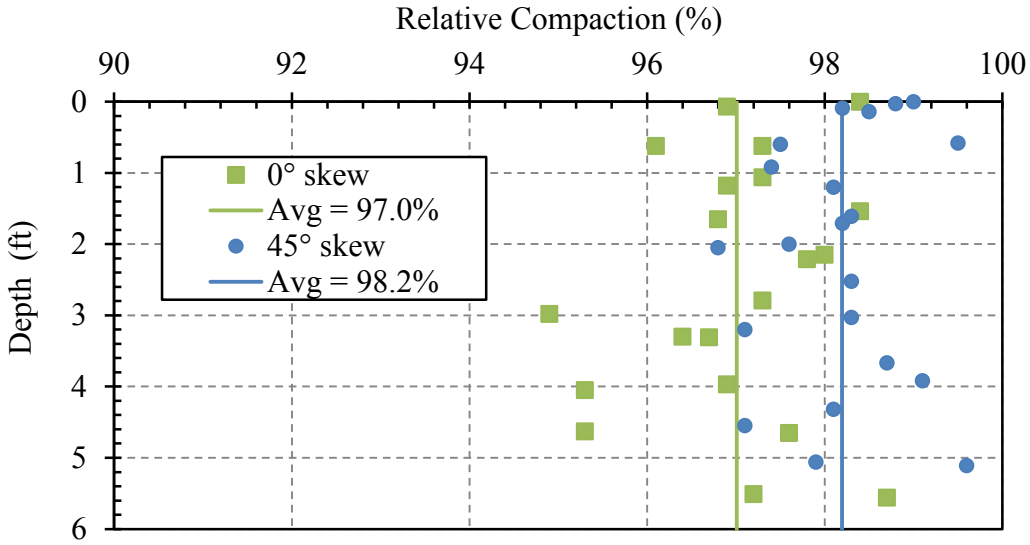

Figure 3.26. Backfill relative compaction with depth.

3.4.2 Backfill Soil Strength Parameters

The backfill friction angle (φ) and cohesion (c) were determined from direct shear tests performed in general accordance to ASTM D 3080, Standard Test Method for Direct Shear Test of Soils Under Consolidated Drained Conditions, in the Brigham Young University (BYU) soils laboratory (Franke 2013; Marsh 2013).

Normal stresses of 4.1, 8.2, 16.3, and 24.5 psi (28.1, 56.3, 112.5, and 168.8 kPa) were selected for testing to represent vertical stresses in field conditions. Dry tests were conducted in addition to tests at the compaction moisture content. Horizontal load-deflection plots for the dry and moist tests are shown in Figure 3.27 and Figure 3.28, respectively. Shear versus normal stress plots are shown in Figure 3.29 and Figure 3.30. Values for φ and c are listed in Table 3.3.

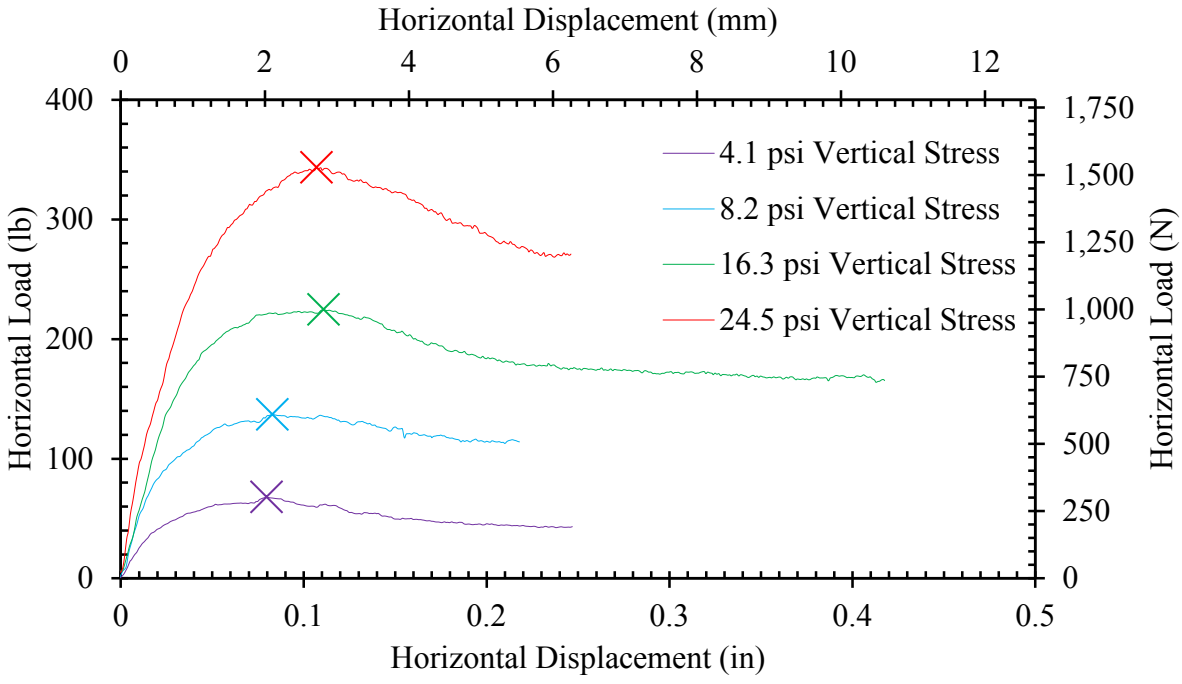

Figure 3.27. Horizontal load-deflection plot for dry direct shear tests.

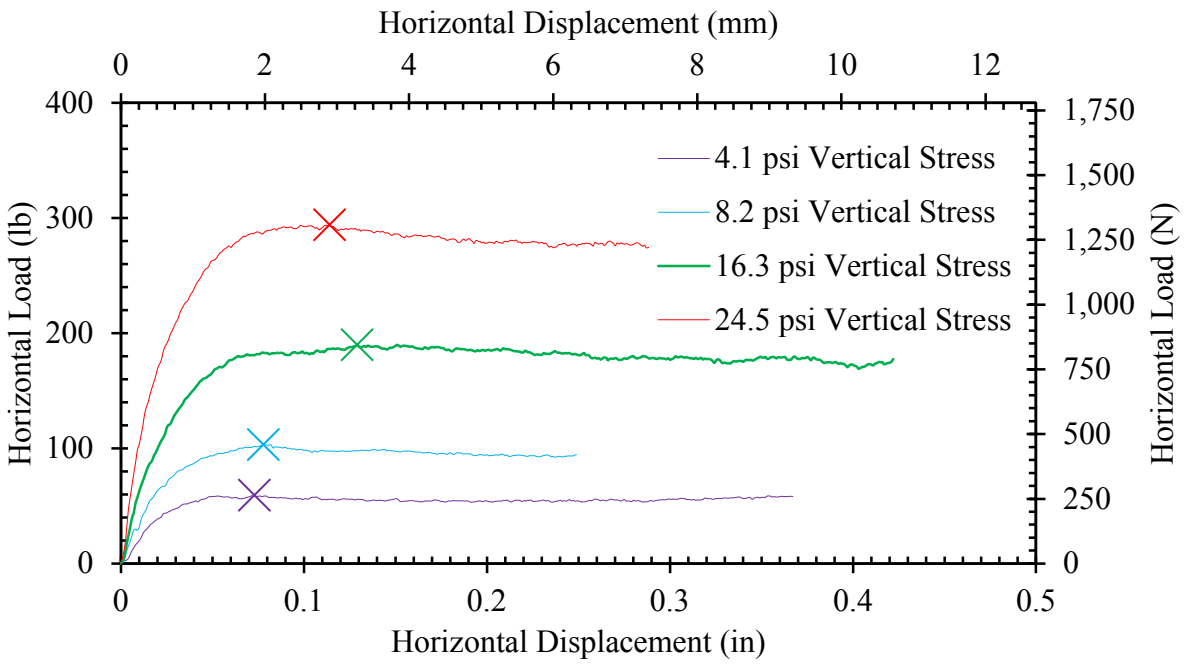

Figure 3.28. Horizontal load-deflection plot for direct shear tests at compaction moisture content.

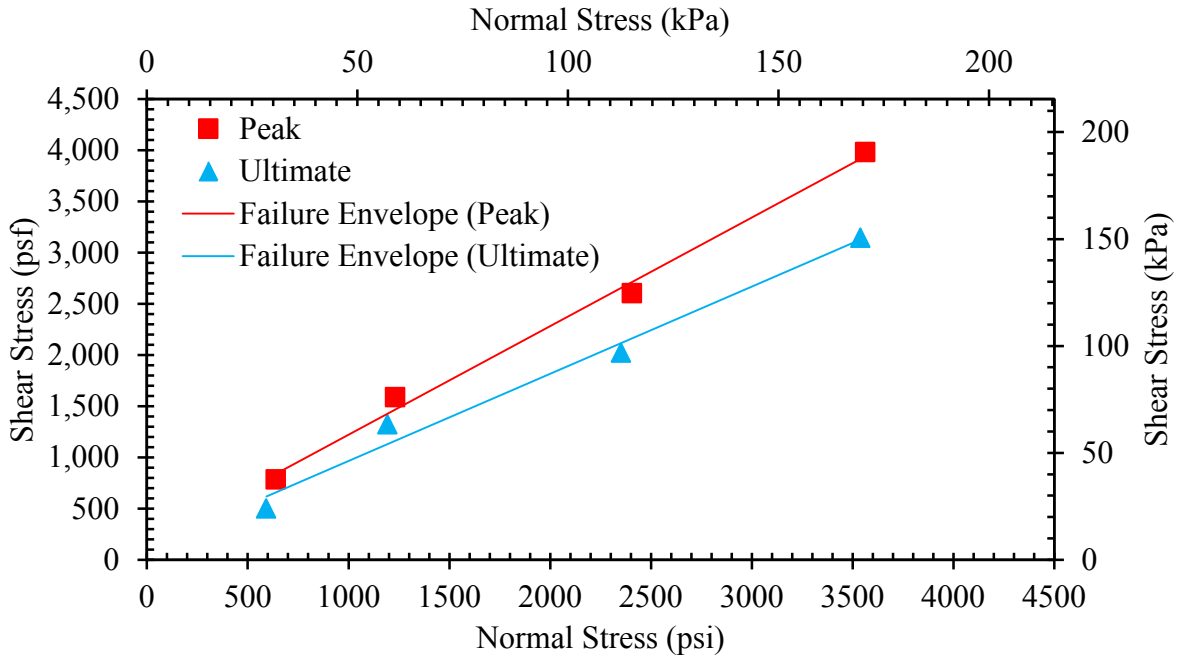

Figure 3.29. Normal stress-shear stress plot for dry peak and ultimate strength.

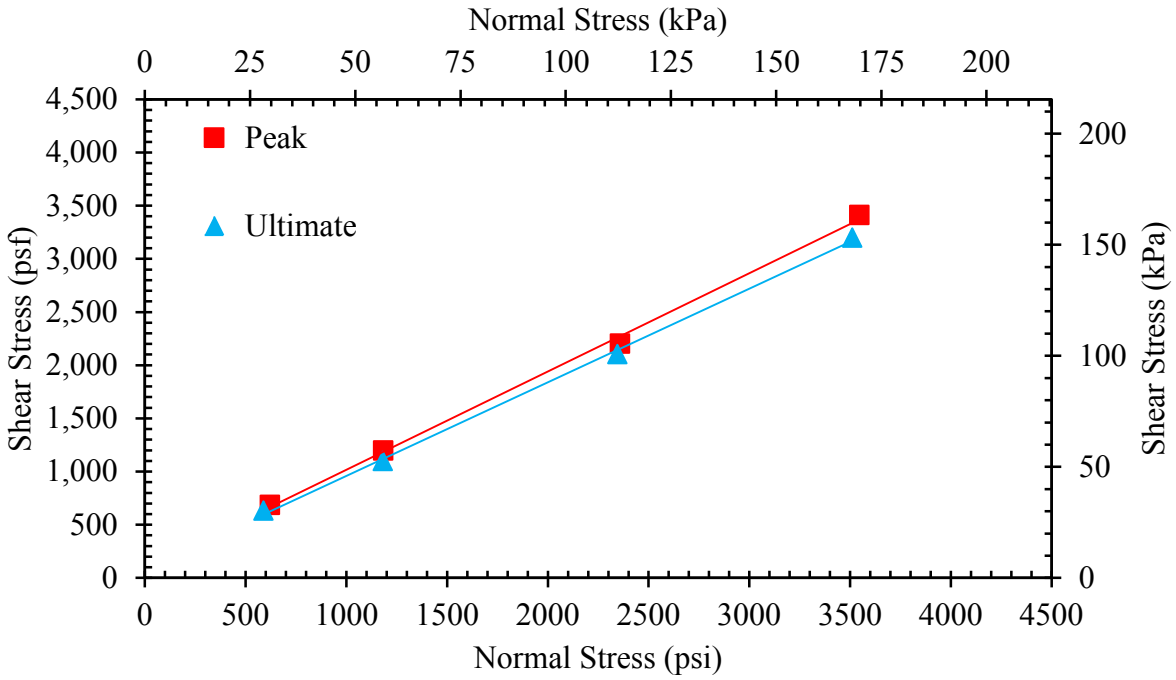

Figure 3.30. Normal stress-shear stress plot for peak and ultimate strength at compaction moisture content.

Table 3.3. Backfill Strength Parameters

Source of Test Result	Peak		Ultimate	
	ϕ (deg)	c (psf) [kPa]	ϕ (deg)	c (psf) [kPa]
Direct Shear (dry)	46.7	161.6 [7.74]	40.4	113.8 [5.45]
Direct Shear (dry, cohesionless)	48.3	0	41.8	0
Direct Shear (moist)	42.7	92.9 [4.45]	41.4	78.8 [3.77]
Direct Shear (moist, cohesionless)	43.8	0	42.3	0

In-situ direct shear tests were also performed on the sand backfill at the test site. The shear box used for the in-situ tests was 1.5-ft x 1.5-ft-wide and 8-in-high. A block of sand was formed by scraping sand from the edges of the shear box. The shear was gradually tapped further down the sand block until the sand was flush with the top of the box. The normal force was

applied by stacking 16-kg weights in the center of the box. Two tests were performed with 30 and 47 weights, respectively. The shear force was applied using a bottle jack. The test setup is shown in Figure 3.31. Although the in-situ test in Figure 3.31 was performed on gravel backfill, the test setup for sand was identical.

Figure 3.31. In-situ direct shear test setup.

Results from the in-situ direct shear tests suggest a friction angle of $\varphi = 41.9°$ and an apparent cohesion of $c = 191\, psf$, which are in good agreement with results from the laboratory direct shear tests.

3.5 Instrumentation and Measurements

This section describes the instrumentation used for data collection during large-scale field testing.

3.5.1 Abutment Movement

Longitudinal displacement of the abutment was monitored by four string potentiometers that were tied to an independent reference frame and attached to the four corners of the pile cap facing the actuators. Figure 3.32 provides a diagram of the independent reference frame, string potentiometers, and pile cap.

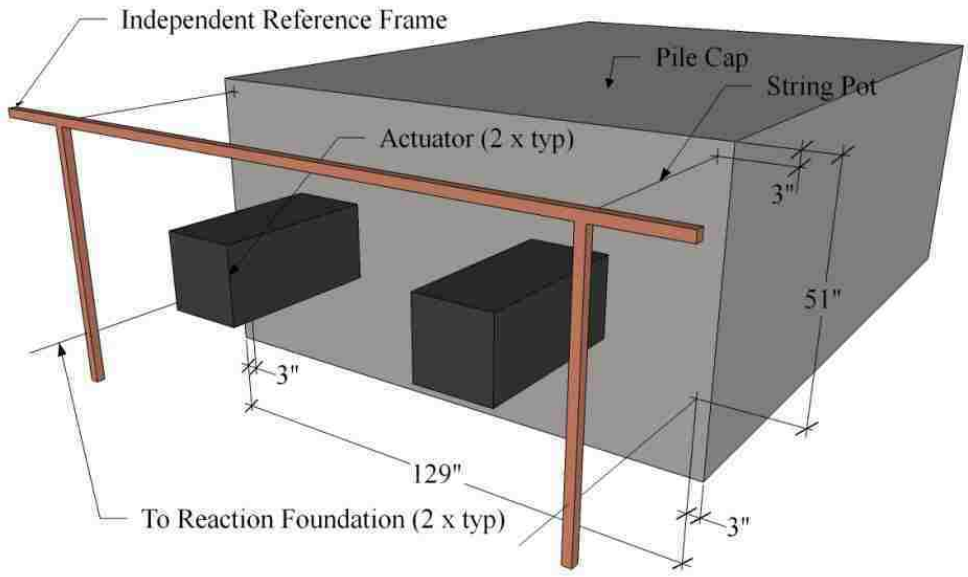

Figure 3.32. String potentiometer instrumentation for monitoring longitudinal displacement of abutment.

Transverse movement of the abutment was measured by inclinometers and shape accelerometer arrays in the center piles of the pile group and was also measured at the four

corners on top of the pile cap with a total station as depicted in Figure 3.33. In general, shape arrays provided more consistent measurements due to the automated nature of data collection compared with the manual operation of the total station. Because inclinometers and shape arrays were primarily measuring pile deflection with depth, instrumentation details are provided in section 3.5.3.

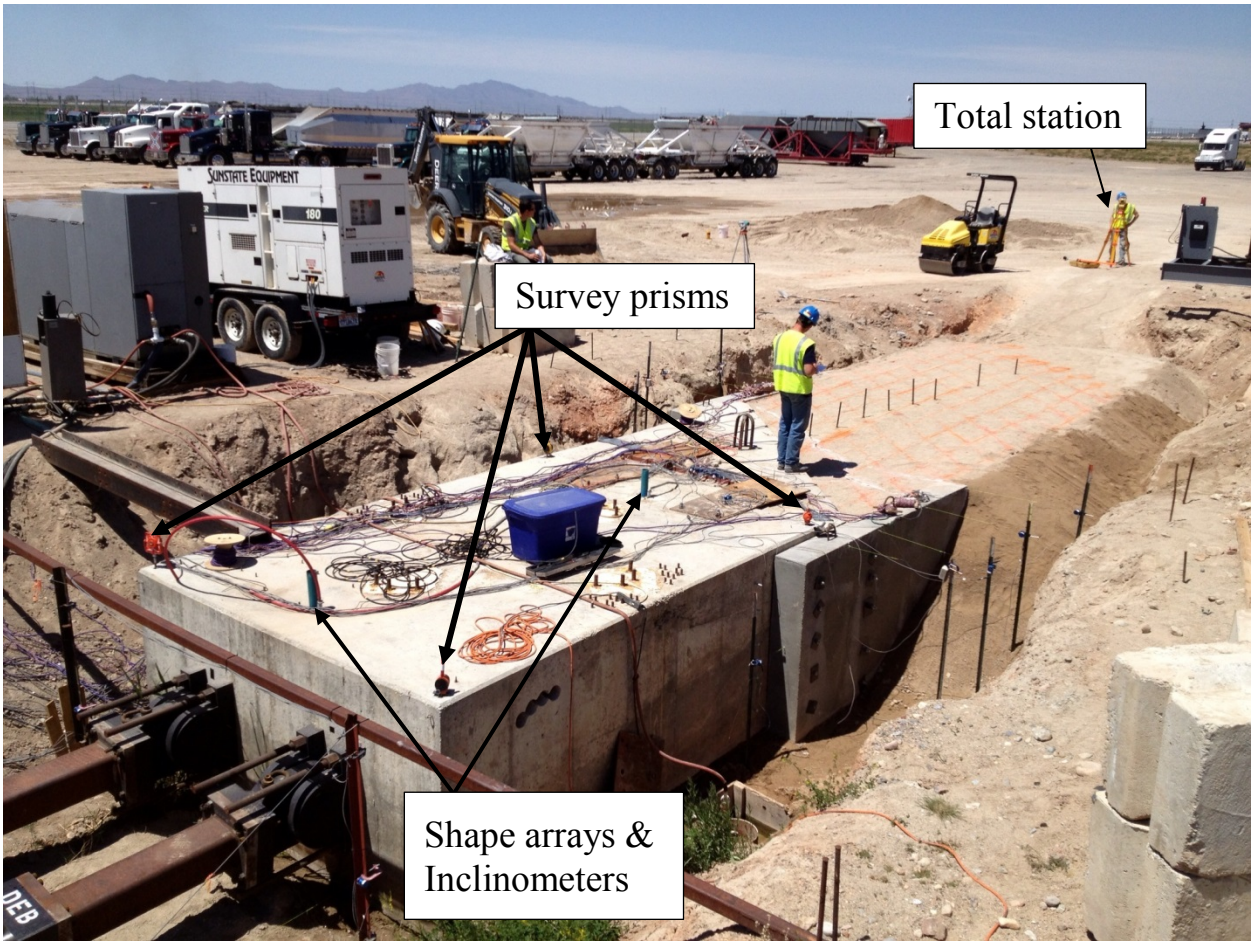

Figure 3.33. Instrumentation used to monitor transverse deflection of the abutment.

3.5.2 Passive Force

Passive resistance (P_p) of the soil backfill was measured by pressure transducers in the actuators and computed using Equations (3-6) and (3-7):

$$P_L = (P_{total} - P_{baseline}) \quad (3\text{-}6)$$

$$P_p = P_L cos\theta, \quad (3\text{-}7)$$

where P_{total} = total actuator load required to displace abutment into backfill, $P_{baseline}$ = actuator load required to displace abutment with no backfill, and θ = skew angle. Baseline resistance was attributed to the lateral resistance of the pile group.

Six Geokon® pressure cells on the 45° skewed abutment measured pressure distribution across the width of the pile cap and provided values for a comparison for passive force measurements from the actuators. All pressure cells were centered at 0.33H (22 inches) from the base of the pile cap where the resultant passive force was believed to act. Pressure cell locations are shown in Figure 3.34.

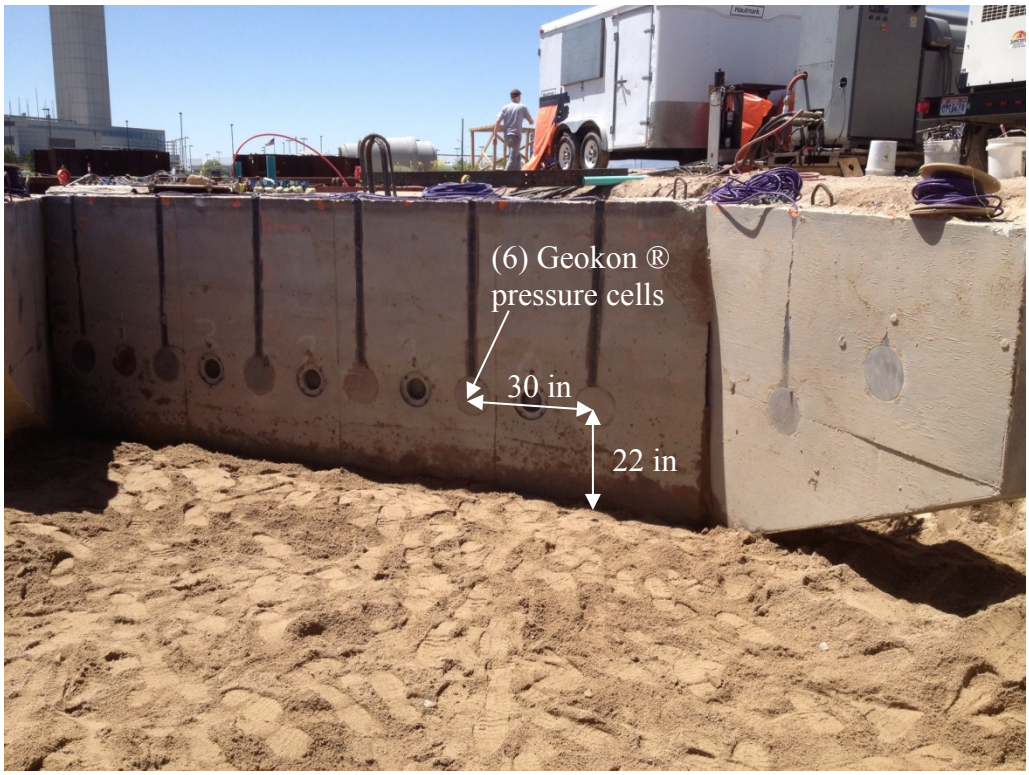

Figure 3.34. Pressure cell layout for 45° skewed abutment backwall.

3.5.3 Pile Deflection

Inclinometers and shape arrays (SAAR: ShapeAccelArray, Research model) in the center piles of both pile rows monitored longitudinal and transverse pile deflection with depth. Inclinometers were lowered down a 2.8-in (70-mm) outside diameter casing that was installed to a depth of 43 ft below the top of the pile cap. Measurements were taken at 2-ft intervals from 40-ft-depth to the top of the pile cap before and at the maximum deflection for each load-deflection test. Pile cap displacement was held relatively constant by the actuators during inclinometer measurements after testing. The limit of precision given for conventional inclinometers after eliminating all systematic errors is ± 0.049 in per 98.4 ft (± 1.24 mm per 30 m) (Mikkelsen 2003).

Shape arrays were fed through a 1-in (2.54-cm) inside diameter schedule 40 PVC electrical conduit that extended to a depth of 50 ft within the center piles. Pile deflections at the north and south end were recorded continuously during testing. The north shape array extended from the top of the pile cap to a 32-ft (9.8-m) depth and the south shape array extended from the top of the pile cap to a 24-ft (7.3-m) depth. A visual of the inclinometer and shape array at the north center pile is provided in Figure 3.35. Only data from the north shape array were used for reporting pile deflection; however, measurements from the south shape array were used for verifying pile cap deflection.

Figure 3.35. Inclinometer and shape array at the top of the pile cap.

3.5.4 Backfill Heave and Horizontal Displacement

Backfill heave and horizontal displacement were monitored by measuring movement at grid intersections on the backfill surface with a total station. A grid with 2-ft spacing across and parallel to the abutment skew was painted on the backfill surface for both 0° and 45° skew tests. The grid was refined to 1-ft spacing within the first 6-ft of backfill for the 0° skew test. Longitudinal, transverse, and elevation measurements were taken before and after load-deflection tests. For the 0° skew test targets were nailed to grid intersections within the first 12-ft of backfill and were monitored with a camera mounted above. Backfill instrumentation for the 45° and 0° skew tests are shown in Figure 3.36 and Figure 3.37.

Additional measurements of horizontal displacement were provided by string potentiometers that were mounted to the top of the pile cap and tied to stakes which were embedded several inches into the backfill. These stakes were placed within 2 ft on either side of the center of the pile cap as seen in Figure 3.36 and Figure 3.37. Measurements from this arrangement are useful in locating the length of the passive failure wedge. Relatively higher strains are expected near the abutment backwall and at the edge of the passive failure wedge where the shallow soil shear planes interact with the stakes as shown in Figure 3.38.

Figure 3.36. Orange spray-painted 2-ft grid on backfill surface for 45° skew.

Figure 3.37. Backfill surface grid for non-skewed abutment.

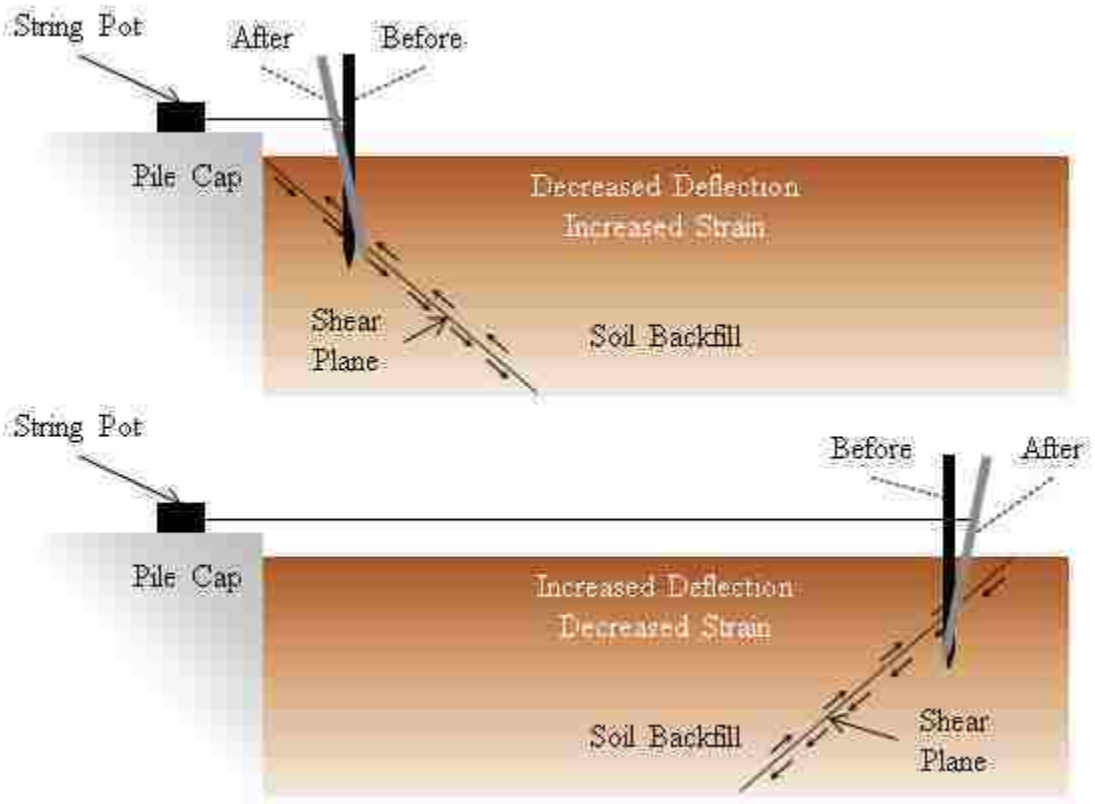

Figure 3.38. Stake-shear plane interaction, adapted from Bryan Franke (2013).

3.5.5 Shear Failure Surface

Red-dyed sand columns were compacted at locations shown in Figure 3.39 to capture the offset caused by the shear failure surface of the backfill. Holes were bored with 3-in-diameter hand augers to approximately 6-ft (1.8-m) depths within 8 ft (2.44 m) of the abutment backwall. Beyond 8 ft, shallower holes were bored in anticipation of the failure surface.

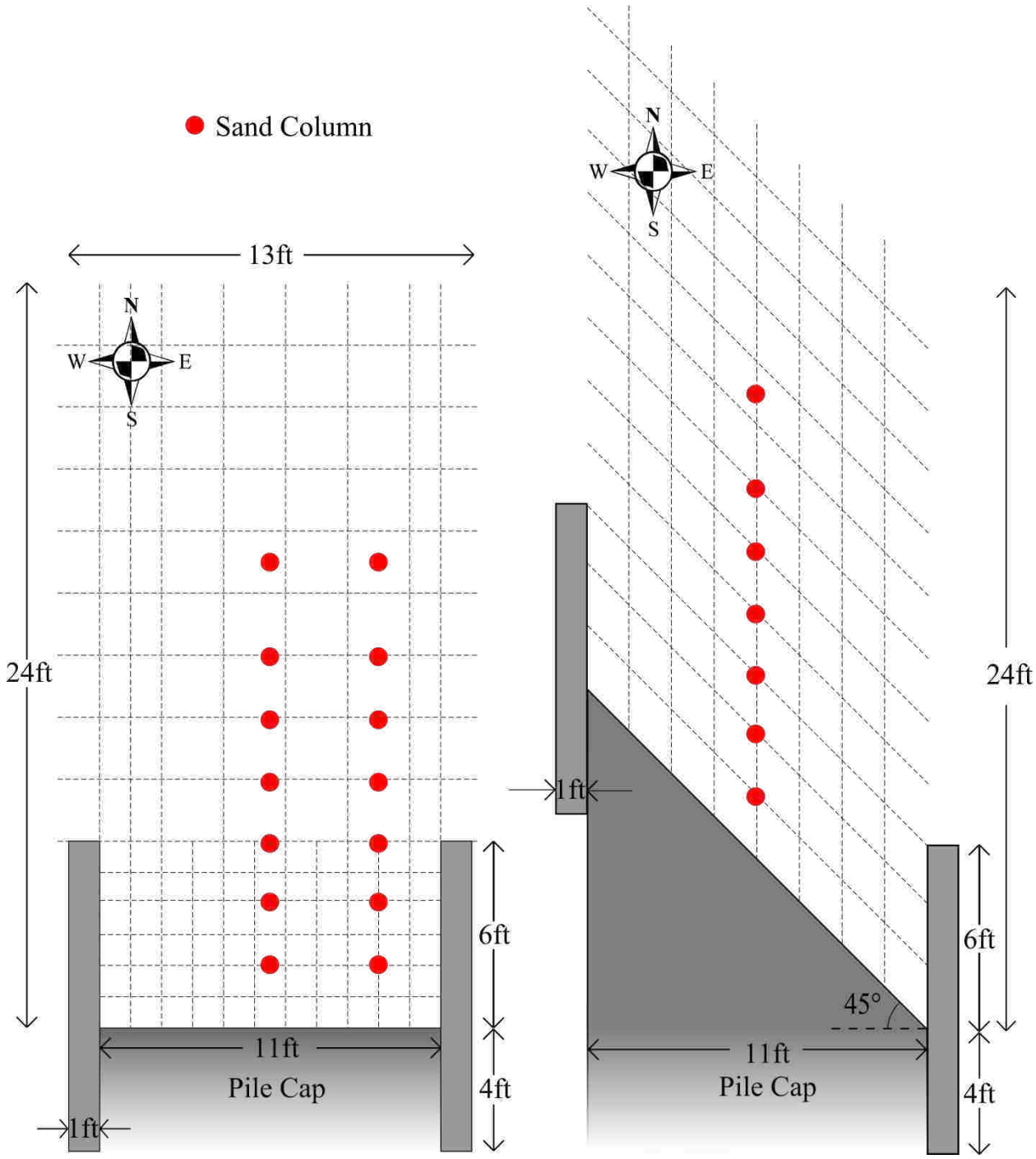

Figure 3.39. Red sand column locations.

3.5.6 Wingwall Instrumentation

Electrical resistance type strain gauges were bonded to the #7 reinforcing bars in wingwalls in a vertical line at 12-in (30.-cm) spacing at 3 ft (0.92 m) and 6 ft (1.8 m) from the tapered end of the wingwalls (see Figure 3.40). Strain on the side of the #7 reinforcement facing the backfill was measured continuously during load-deflection tests and used to back-calculate pressure and moments on the wingwalls. The strain at 6 ft (1.8 m) from the end was designed to give the maximum strain and moment at the interface with the abutment wall. Geokon® pressure cells were embedded flush with the wingwalls at locations shown in Figure 3.41. These cells were intended to provide some indication of the distribution of pressure along the wingwall.

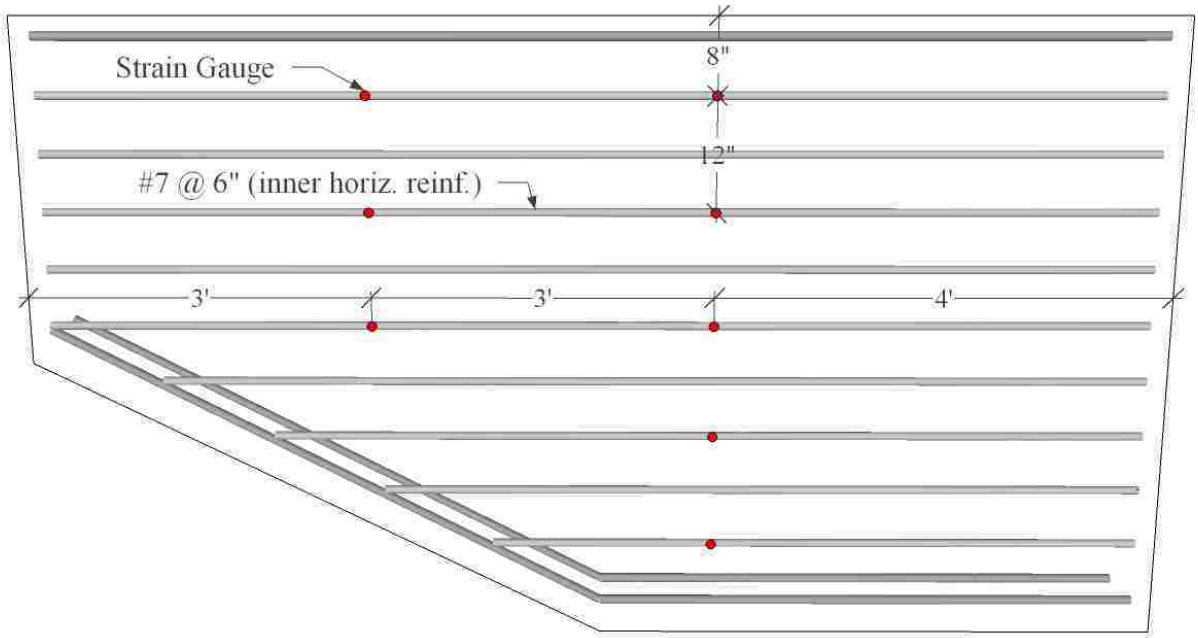

Figure 3.40. Wingwall strain gauge layout—same for both wingwalls.

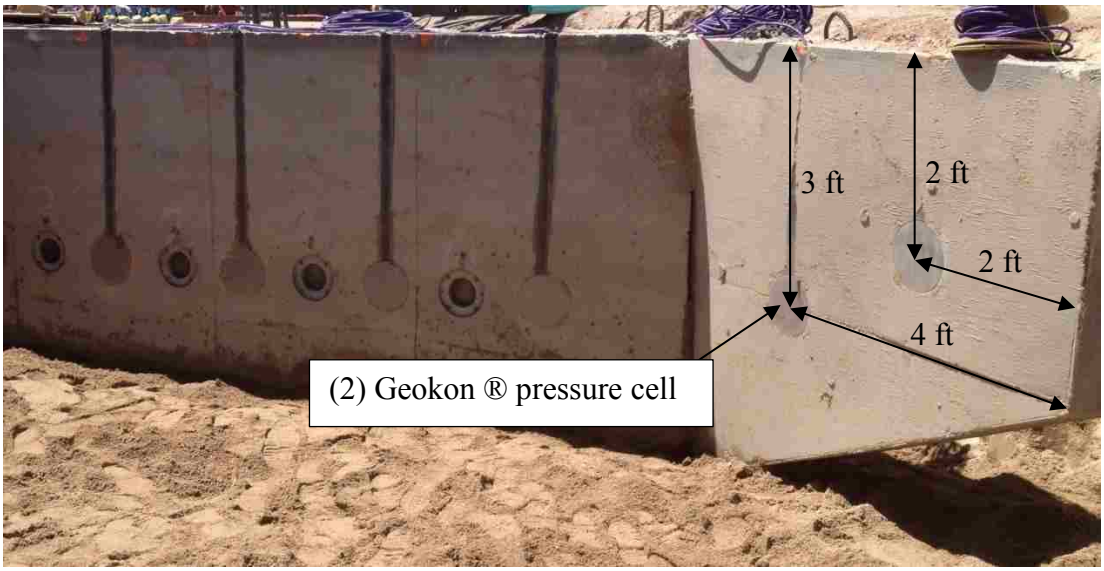

Figure 3.41. Wingwall pressure cell layout.

Transverse and longitudinal wingwall deflections were measured with string potentiometers and deflections at test completion are illustrated in Figure 3.42 String potentiometers were attached at the top of both wingwalls at 1-in (2.5 cm), 36-in (91 cm), 76-in (193), and 93-in (236 cm) from the tapered end. These sensors were intended to measure the deflected shape of the wingwall under loading. Additional string potentiometers were attached 3-ft from the base of both wingwalls at the ends facing the pile cap. These sensors were designed to measure any slippage of the wingwall in the longitudinal direction. The typical string potentiometer layout for monitoring wingwall deflection is depicted in Figure 3.42.

Figure 3.42. Wingwall string potentiometer instrumentation.

3.6 Testing Procedure

The backfill zone and sides of the abutment were excavated for placement of reinforced concrete wingwalls and backfill. Wingwalls were secured to abutment using (10) ASTM A307 steel bolts, which were torqued to 200 ft-lb (271 N-m). Before backfill was placed, a baseline load-deflection test was performed to measure the pile resistance of the abutment. A 2H:1V slope was implemented at the edges of the backfill, which is typical for reinforced concrete wingwall abutments. A 2-ft (0.61-m) grid (refined to 1-ft (0.305-m) spacing near abutment

backwall for 0° skew test) was spray-painted on the backfill surface and initial grid intersection coordinates were measured. Initial coordinates of the pile cap corners and initial inclinometer measurements were also recorded.

Following initial measurements, the abutment was loaded longitudinally into the backfill at 0.05 in/min (1.27 mm/min) to final displacements of approximately 3.0 in (7.6 cm) to 3.75 in (9.6 cm). Displacements larger than 3.75 in (9.6 cm) were avoided to prevent plastic deformation of piles. At 0.25-in (0.64-cm) displacement intervals, loading was held constant for about 2 minutes and force-deflection measurements were recorded and verified. Surface cracks were also recorded in a field book at 0.5-in (1.27-cm) displacement intervals. Pile deflection from shape arrays, strain in wingwall reinforcement, and pressure on the backwall and wingwalls were recorded continuously during testing. At test completion, backfill grid intersection coordinates and inclinometer readings were recorded.

The backfill material was completely excavated and re-compacted for each individual test. Two pumps on either side of the abutment were running constantly to keep the water table approximately 1 to 2 ft (0.305 to 0.61 m) below the base of the pile cap.

For the 45° skewed abutment only, cyclic loading was applied at 0.05 in/min (1.27 mm/min) before loading monotically to a deflection of 3.0 in (7.6 cm). The abutment experienced 20 cycles of being pushed to a deflection of 0.25 in (0.64 cm) and then pulled past its initial position to a deflection of -0.25 in (-0.64 cm).

4 FIELD TEST RESULTS

This chapter provides field test results for non-skewed and 45° skewed abutments with reinforced concrete wingwalls including passive force-deflection curves, backfill heave and displacement patterns, and the structural and geotechnical response of wingwalls. English units are the primary units used to present the results in this chapter.

4.1 Passive Force-Deflection

Baseline ($P_{baseline}$) and total longitudinal resistance (P_{total}) for non-skewed and 45° skewed abutments are plotted in Figure 4.1 and Figure 4.2. Longitudinal actuator load (P_L) resisted by the backfill was calculated using Equation (3-6).

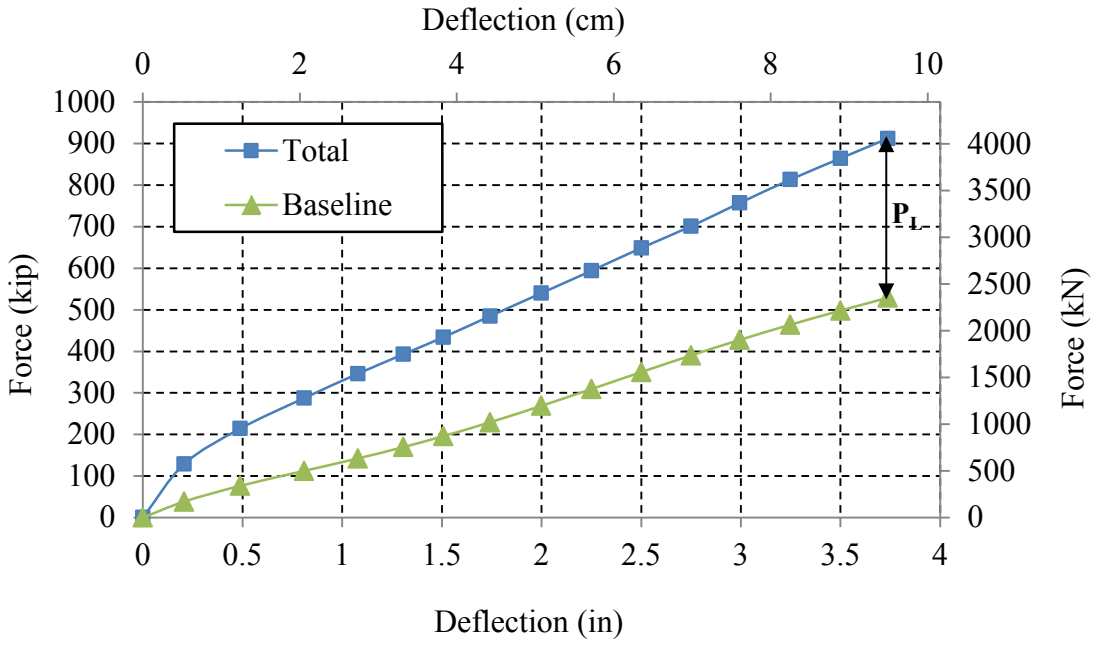

Figure 4.1. Total and baseline force-deflection curves for non-skewed abutment.

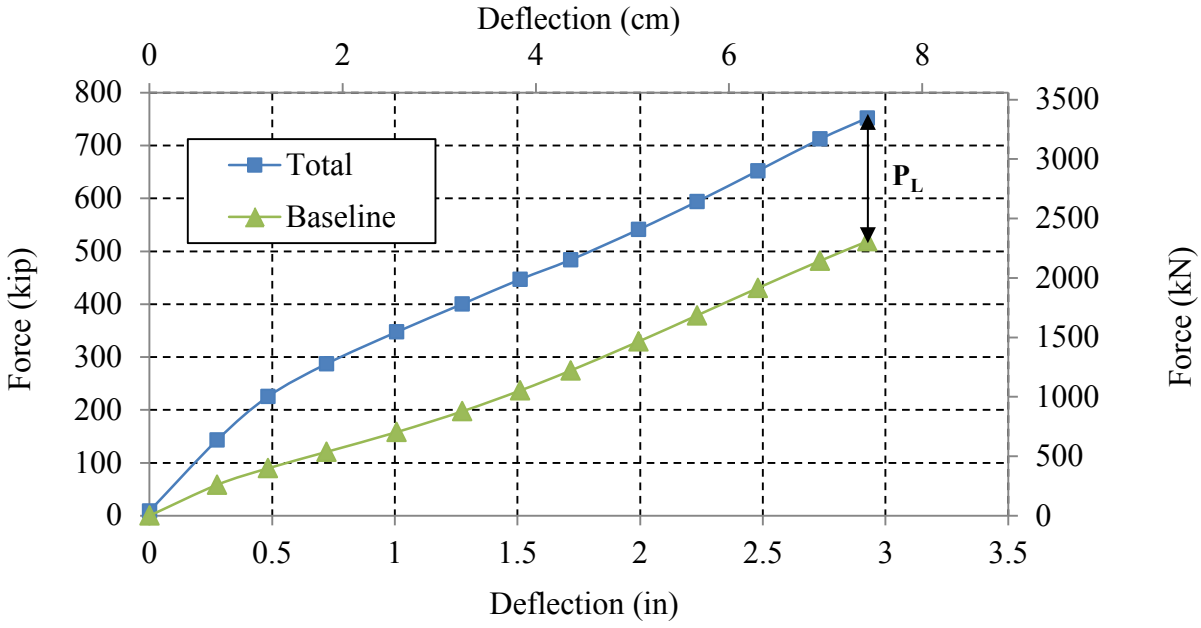

Figure 4.2. Total and baseline force-deflection curves for 45° skewed abutment.

Passive force-deflection curves are shown in Figure 4.3. Passive force (P_P) was calculated using Equation (3-7). Figure 4.3 clearly indicates a significant reduction in peak passive force for the 45° skew case. Labels reading 0.01H, 0.02H, etc. indicate deflections that are 1%, 2%, etc. of the backwall height.

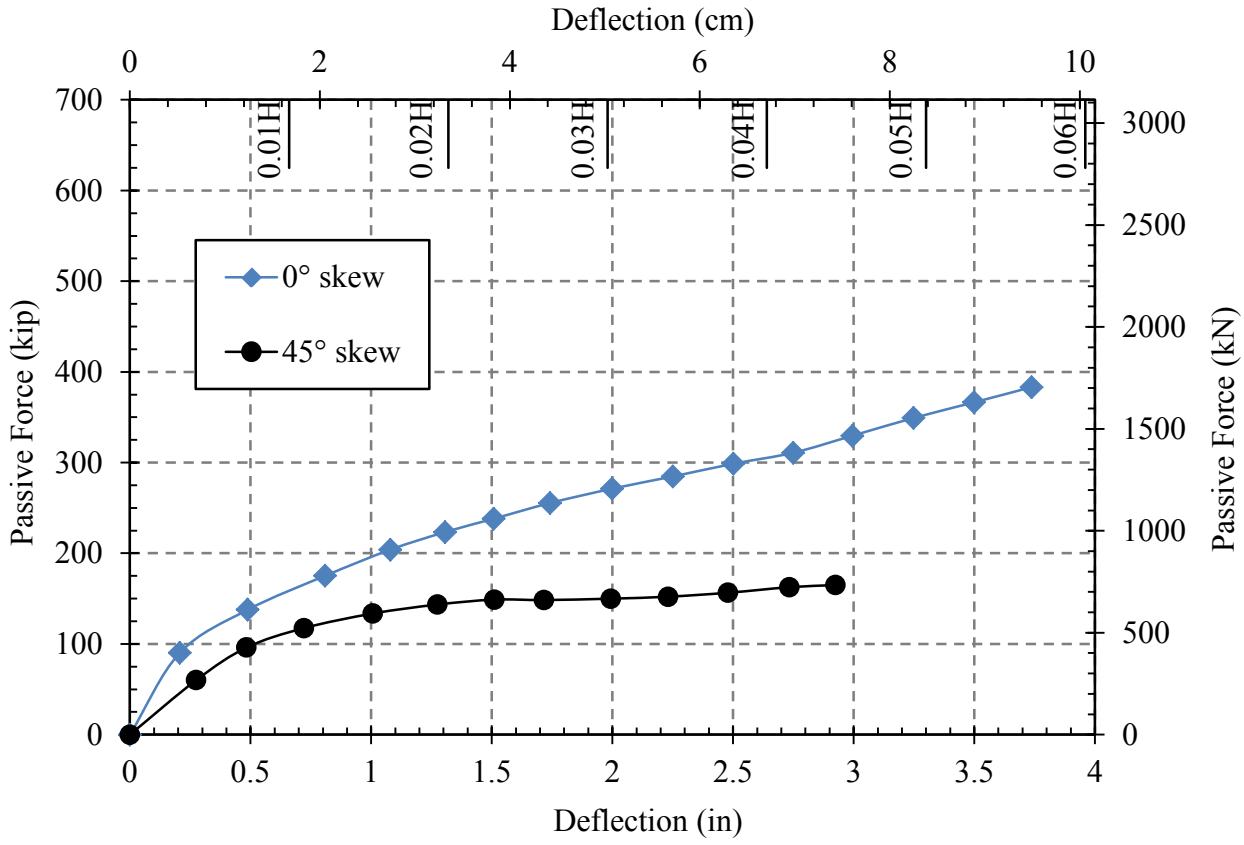

Figure 4.3. Passive force-deflection curves for 0° and 45° skewed abutments with reinforced concrete wingwalls.

While the reduction in passive force for the 45° skew case is clearly depicted in Figure 4.3, the steady accumulation of passive resistance for the non-skewed abutment at large deflections (nearly 6% of the backwall height) is inconsistent with previous studies. Results from previous large-scale testing on non-skewed abutments (without wingwalls) with densely compacted granular backfill indicate that the peak passive force is typically fully mobilized at

deflections 3 to 5% of the backwall height (Cole and Rollins 2006; Lemnitzer et al. 2009; Rollins and Sparks 2002). Large-scale tests on non-skewed abutment with RC wingwalls and densely compacted silty sand reported similar values to tests without wingwalls, indicating that peak passive resistance was achieved at deflections 2 to 3% of the backwall height (Bozorgzadeh et al. 2008). Based on the data plotted in Figure 4.3, the soil passive resistance behind the 45° skewed abutment appears to plateau at approximately 3% of the backwall height; however, passive force measurements were actually still increasing at the maximum deflection.

Passive force-deflection results in Figure 4.3 can be interpreted two ways. First, the steady increase in passive resistance for the non-skewed test and slight increase for the 45° skewed test at maximum deflections may be a result of not enough deflection to mobilize the peak passive force. This interpretation suggests that the peak passive force for both tests would have been achieved at a deflection greater than 5% of the backwall height, which is inconsistent with results from previous large-scale testing of abutments on dense granular backfill with and without wingwalls. Passive force-deflection plots from one study done by Romstad et al. (1996) show peak passive forces at deflections approximately 8% of the backwall height; however the higher values for the peak deflections were likely a result of the shear failure occurring in the Yolo Loam (clayey silt) embankment material. Because of the Yolo Loam, the results from the study by Romstad et al. (1996) do not provide an accurate comparison for this study which used densely compacted sand as the backfill material, extending 24 ft beyond the abutment backwall.

A second interpretation of the passive force-deflection results for this study suggests that peak passive forces were mobilized, but were not reflected in the data due to the baseline curves being unreliable at large deflections. The unreliability of the baseline curves at large deflections was likely caused by an increase in pile resistance between baseline tests and the tests with the

backfill. Baseline tests were conducted after previous load-deflection tests. After a load-deflection test, gaps are formed in the upper layers of the soil between the initial and final positions of the piles. As the backfill was compacted for the RC wingwall tests, vibrations from compaction likely caused the soil near the piles to fill in the gap, resulting in a higher pile resistance at larger deflections (as the piles are loaded into the soil that somewhat closed the gap) relative to the baseline test. In addition, the baseline curve used for the non-skewed abutment was approximately 20% softer at a deflection of 3.5 inches (8.9 cm) relative to the baseline curve used for the 45° skewed abutment. The softer baseline curve provides more evidence that the actual pile resistance was for the non-skewed test was underestimated, resulting in artificially increased values of passive resistance from the backfill.

This opinion is supported by hyperbolic passive force-deflection curves that are in good agreement with the data from this study until larger deflections (approximately 2.5 inches [6.4 cm]) as shown in Figure 4.4 and Figure 4.5. The higher passive force measurements at deflections greater than 2.5 inches (6.4 cm) are thought to be a result of an unreliable baseline resistance used to compute passive forces. Up to deflections of about 2.5 inches (6.4 cm), the hyperbolic curves follow the nonlinear passive force-deflection relationship so well that there is reason to doubt the accuracy of the baseline curve used in this study. The hyperbolic curves for the non-skewed and 45° skewed test achieve peak passive forces at deflections that are 5% and 2.2% of the backwall height, respectively. These peak deflection values are consistent with previous large-scale testing with and without wingwalls using densely compacted granular backfills. Hyperbolic curves were generated in a computer program called PYCAP (Duncan and Mokwa 2001). Parameters used to generate these curves are explained in section 6.3 entitled ‘PYCAP Parameters’ where the analysis done in PYCAP is explored.

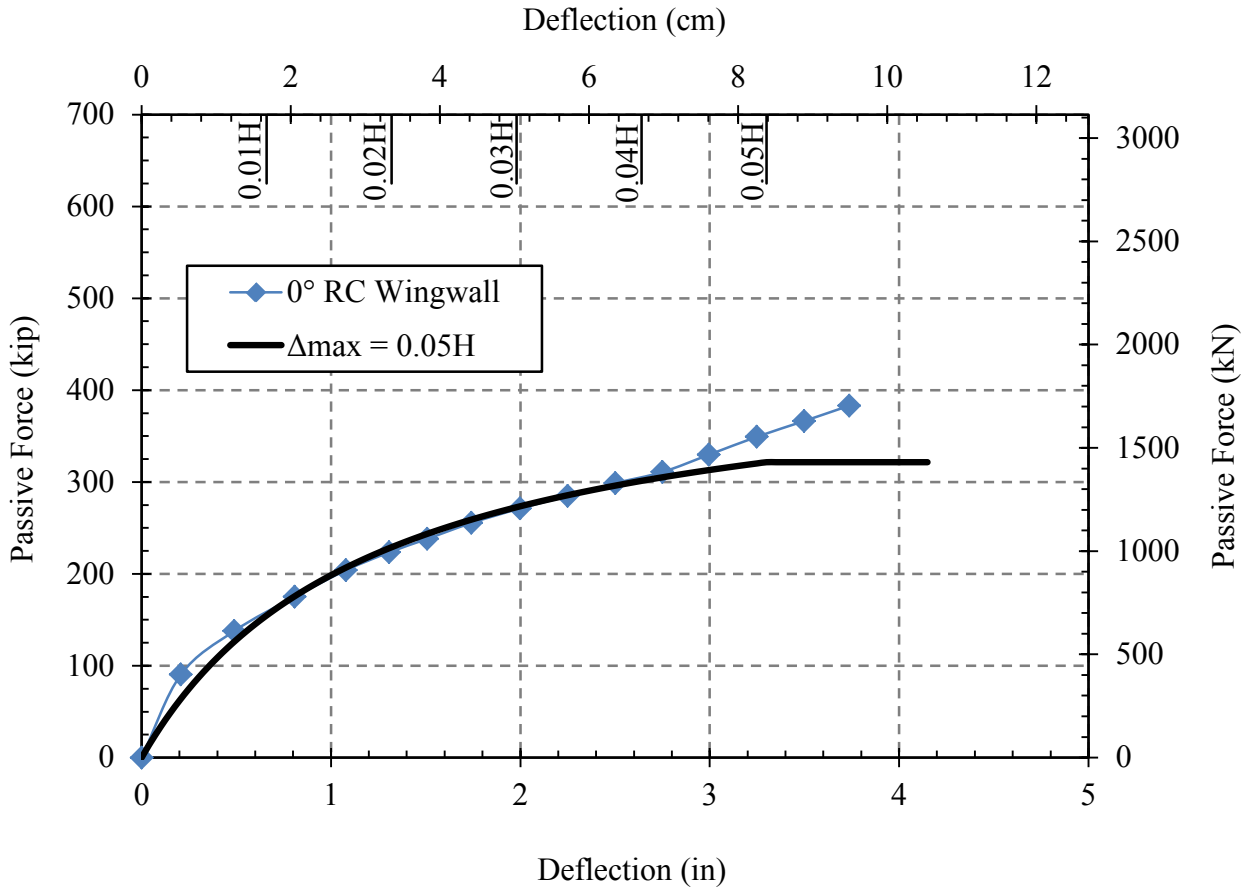

Figure 4.4. Non-skewed passive force-deflection curve compared with hyperbolic curve defined by $D_{max}/H = 0.05$.

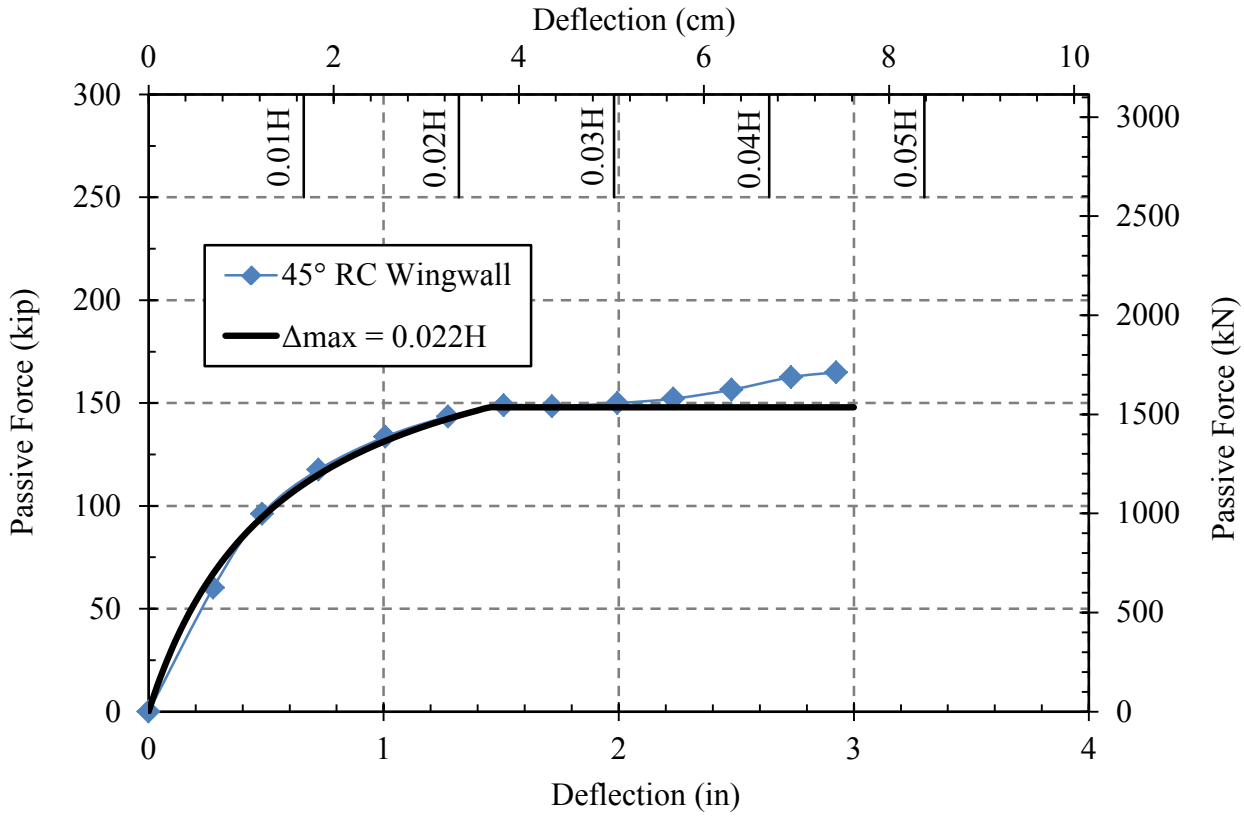

Figure 4.5. 45° skew passive force-deflection curve compared with hyperbolic curve defined by $D_{max}/H = 0.022$.

In Figure 4.4 and Figure 4.5, it is clear that only the last three to four test data points deviate from the hyperbolic passive force-deflection curve. The author believes that the hyperbolic passive force-deflection curves in Figure 4.4 and Figure 4.5 more accurately represent what actually occurred during testing; however, skew reduction factors and passive force analyses were completed for both the measured data and the hyperbolic curves.

Using the measured test data, the peak passive force for the 45° skewed abutment, approximately 165 kips (739 kN) is 43% of the peak passive force for the non-skewed abutment, approximately 383 kips (1716 kN). The hyperbolic curves suggest lower peak passive forces of approximately 322 kips (1443 kN) and 148 kips (663 kN) for the 0° and 45° skewed abutments,

respectively, which results in a reduction factor of 46%. The hyperbolic curves suggest a slightly higher reduction factor (46%) for the 45° skew case compared to the recorded test data (43%). Both reduction factors from test data and hyperbolic curves are plotted on the reduction curve proposed by Rollins and Jessee (2012) along with the laboratory tests and numerical model results by Shamsabadi et al. (2006) in Figure 4.6.

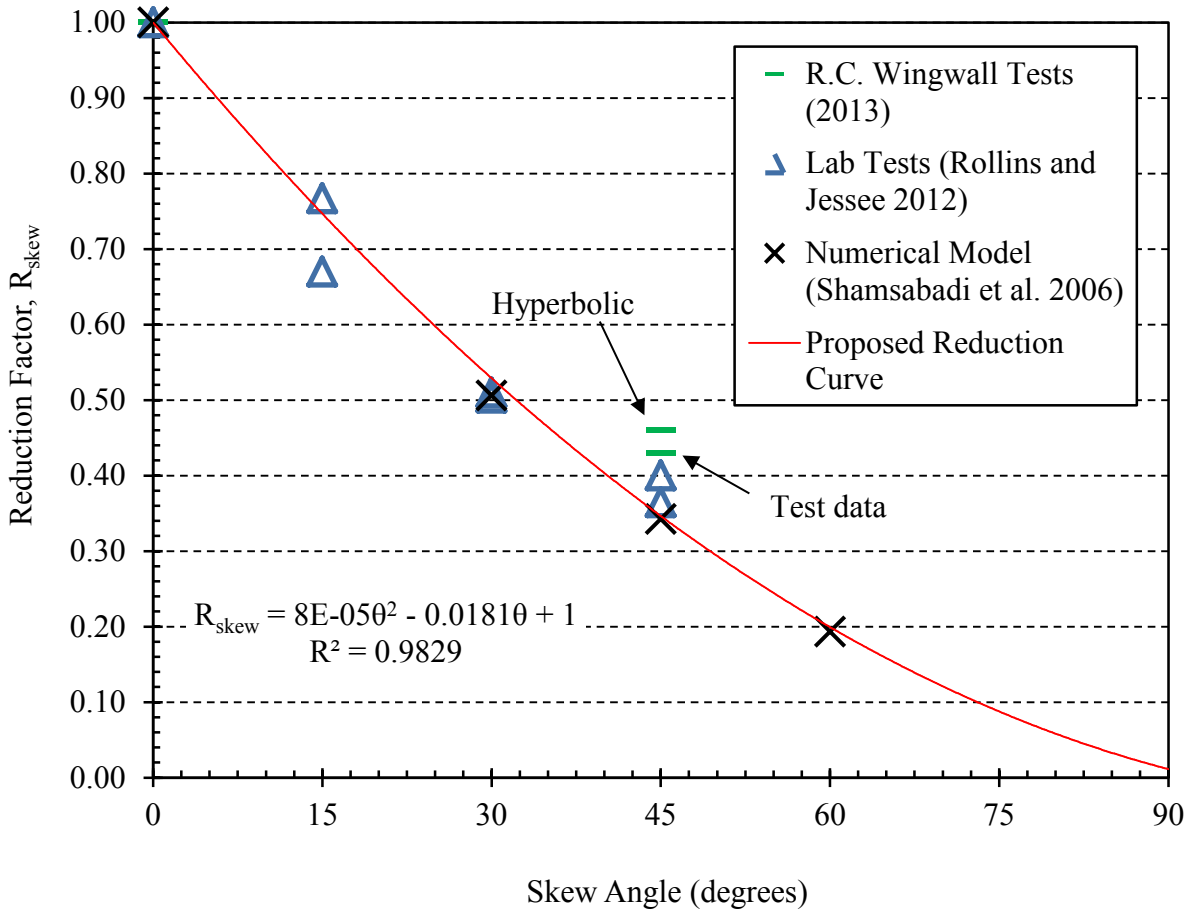

Figure 4.6. Reduction factor, R_{skew} (passive force for a given skew angle normalized to non-skewed passive force) plotted versus skew angle based on lab tests (Rollins and Jessee 2012), numerical analyses (Shamsabadi et al. 2006) and results from field tests in this study.

The reduction curve proposed by Rollins and Jessee (2012) recommends a reduction factor of 35% for a 45° skew, which is 8 to 11% lower than the 43% and 46% computed from the test data and hyperbolic curves. One possible explanation for the discrepancy may be increased friction on the RC wingwalls relative to the laboratory tests. For example, the laboratory tests (Rollins and Jessee 2012) used to develop the reduction curve employed the use of plastic lining between the backfill and sidewalls to minimize frictional resistance along the sidewalls. Frictional resistance was relatively equal for laboratory tests at all skews because of the plastic lining. However, in the large-scale field tests for this study, backfill was directly in contact with the concrete wingwalls allowing for varying amounts of frictional resistance to develop along the wingwalls. Calculations of increased friction are further explored in section 4.6.1 after the soil pressure distributions on the wingwalls are presented.

Because of the plastic lining between backfill and sidewalls, Rollins and Jessee's (2012) reduction curve is more appropriate when effects from increased sidewall friction between tests are minimal. The peak passive force for the 45° skewed abutment drops 5% when increased frictional resistance is considered based on both strain gauge and pressure cell data. This drop in peak passive force lowers the reduction factor from 2 to 3% closer to the value from the 45° skew laboratory tests obtained by Rollins and Jessee (2012).

The additional 5 to 8% discrepancy is possibly due to increased 3D effects relative to the zero skew case, which is explored further in Chapter 6. Passive force-deflection curves from this study suggest that the skew reduction curve proposed by Rollins and Jessee (2012) overestimates the reduction in peak passive force by 8 to 11% for a 45° skew with RC wingwall geometry.

4.2 Cyclic Loading

Total actuator force-deflection results from 20 cycles of cyclic loading on the 45° skewed abutment are shown in Figure 4.7. The abutment started at an initial deflection of 0 inches, pushed to a deflection of approximately 0.25 inches (0.64 cm), and then relaxed to a deflection of approximately -0.25 inches (0.64 cm). This cycle was repeated 20 times. Total force is plotted in Figure 4.7 instead of passive force as the baseline curve was only calibrated for positive deflections. Because the abutment experienced negative deflections during cyclic loading, passive force calculations are only accurate for positive deflections into the backfill.

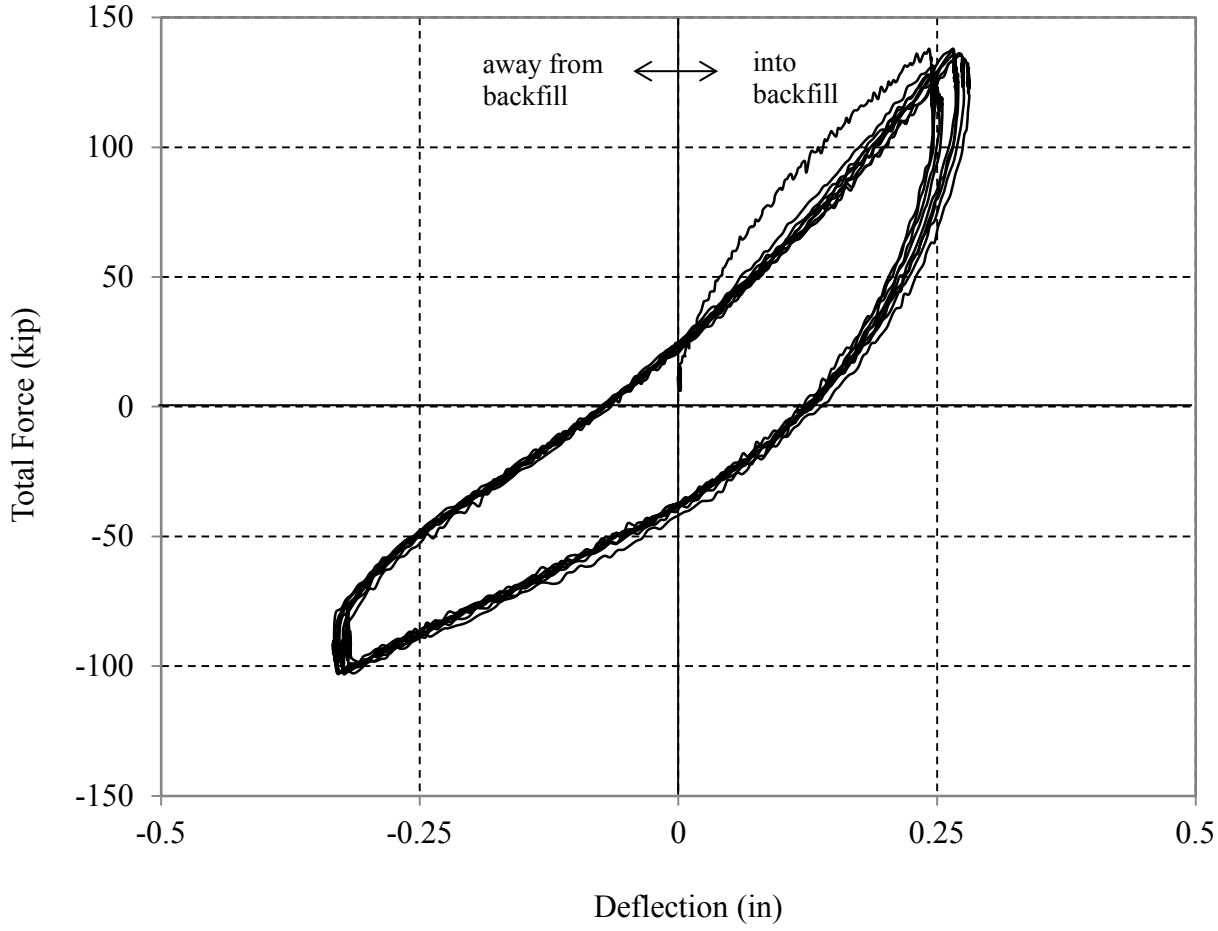

Figure 4.7. Hysteresis loop showing total actuator force vs. deflection (20 cycles).

The total force in Figure 4.7 represents the resistance from both the piles and the backfill. As expected, when the abutment was pushed into the backfill (positive deflection), more resistance was measured compared to the resistance as it was pulled away from the backfill (negative deflection). Figure 4.7 indicates a 35% increase in resistance when the abutment was pushed into the backfill compared to being pulled away from the backfill. A relatively large decrease in initial soil stiffness was also observed after just one cycle. Very little degradation was observed with continued cycles.

Total cyclic loads associated with positive deflection (into the backfill) were converted to passive forces and plotted in Figure 4.8 with the full passive force-deflection curve for the 45° skewed abutment. The decreased initial soil stiffness for the full passive force-deflection curve matches well with the soil stiffness after cyclic loading.

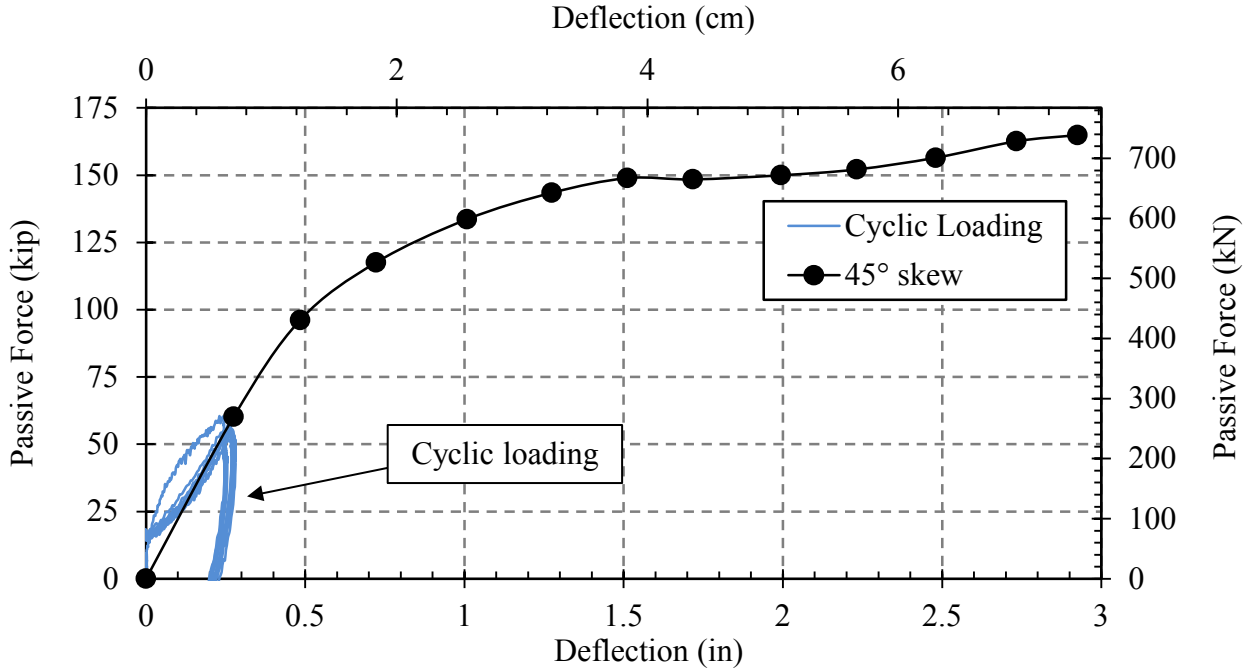

Figure 4.8. Cyclic loading in relation to full passive force-deflection curve.

4.3 Transverse Deflection and Rotation of Abutment

Average transverse deflection is plotted versus longitudinal deflection in Figure 4.9 for the non-skewed and the 45° skewed abutments based on shape array measurements at a depth of 0.75 ft (0.23 m) below the top of the abutment. The 45° skewed abutment experienced four times the transverse deflection relative to the non-skewed abutment. At the largest measured longitudinal displacement, the 45° skewed abutment had moved 0.34 in (0.86 cm) to the west, in contrast to the non-skewed abutment which moved only 0.09 in (0.22 cm) to the west. Though deflections are small, the effect of skew angle is apparent.

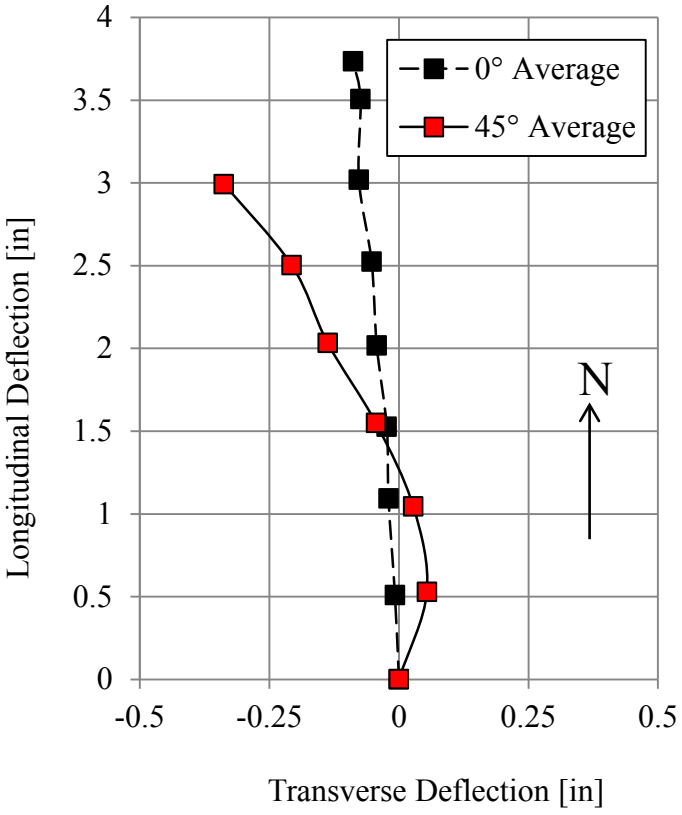

Figure 4.9. Average transverse deflection for non-skewed and 45° skewed abutments.

The difference in transverse deflection between the north and south ends of the abutments is shown in Figure 4.10 and indicates the tendency for the skewed abutment to rotate. The north

end of the abutment is in contact with the backfill. Figure 4.10 illustrates that the north end of the 45° skewed abutment deflected 0.1 inches (0.25 cm) more than the south end, which indicates that the abutment is rotating such that the obtuse side is being pushed into backfill while the acute side is pulling away. This observation is in good agreement with field observations and 3D PLAXIS modeling by Shamsabadi et al. (2006) which both indicate that skewed abutment backwalls tend to be pushed primarily at the obtuse corner during lateral loading.

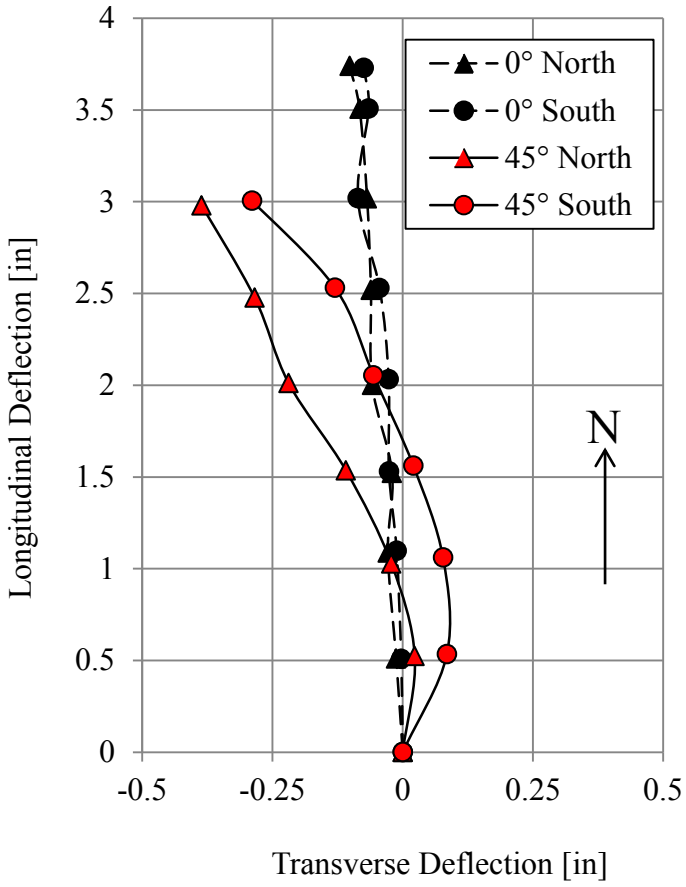

Figure 4.10. North and south transverse deflection for non-skewed and 45° skewed abutments.

Rotation of non-skewed abutment is negligible compared to the 45° skewed abutment. As the non-skewed abutment was longitudinally loaded, north and south ends generally experienced equal amounts of transverse deflection.

To better understand the transverse resistance of the piles, a transverse baseline load test was performed on the 45° skewed abutment. Figure 4.11 displays the pile resistance as a function of transverse deflection. The abutment was loaded by two hydraulic jacks and both contributed approximately 73 kips (327 kN) each. The north and south pile transverse pile resistance in Figure 4.11 was developed based on force and moment equilibrium for the transverse load-deflection test.

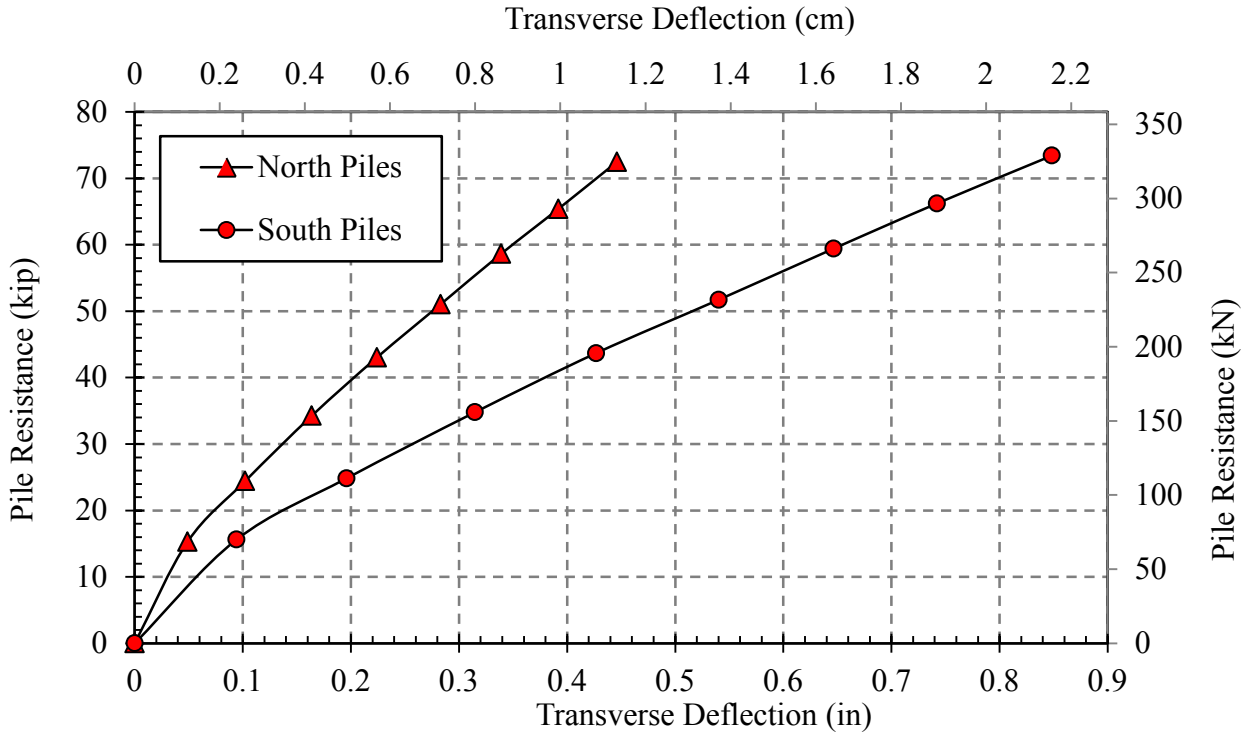

Figure 4.11. Transverse pile resistance from transverse baseline load test.

The results shown in and Figure 4.11 indicate that at maximum deflections for the north and south ends of the 45° skewed abutment test [0.39 inches (1.0 cm) at the north end and 0.29 inches (0.74 cm) at the south end], the north row of piles experienced approximately 60 kip (269 kN) in the transverse direction compared to 33 kip (149 kN) for the south row of piles. For the non-skewed test, the north row of piles experienced roughly 24 kips (108 kN) of resistance compared to approximately 14 kips (63 kN) of resistance from the south row of piles. In both cases, the north row of piles provided close to twice the amount of transverse resistance relative to the south row of piles. The total transverse pile resistance, from the north and south piles combined, was nearly 2.5 times higher for the 45° skewed abutment relative to the non-skewed abutment.

4.4 Backfill Response

Results for backfill horizontal displacement, vertical heave, and shear failure surface geometry are provided in this section. These results offer insight on the effects of skew angle on the geometry of the passive soil wedge.

4.4.1 Backfill Horizontal Displacement and Strain

Final and initial longitudinal and transverse measurements at grid intersections on the backfill surface were used to generate displacement vectors using Visual Basic code written in Microsoft Excel by Franke (2013). Displacement vectors for the non-skewed and 45° skewed abutments are illustrated in Figure 4.12. For the non-skewed test, the backfill appeared to displace generally parallel to the loading direction, with an average direction of 87° measured counterclockwise from the positive transverse axis or pile cap face. For the 45° skewed test, the average direction of backfill displacement was 101° relative to the positive transverse axis,

indicating more westward movement of the backfill when compared to the non-skewed backfill. The westward movement of the backfill for the 45° skewed test is in good agreement with the larger westward transverse deflection of the entire abutment, approximately 0.34 in (0.86 cm).

Displacement vectors from the non-skewed test suggest that the soil confined within the wingwalls generally moved longitudinally as one mass with relatively consistent displacement vectors. Beyond the wingwalls, the soil displaced outward relative to the edge of the wingwalls. In contrast, for the 45° skewed test, the overall lack of confinement seemed to allow the soil within 6 ft of the backwall to displace more freely when compared to the non-skewed test, especially on the west side of the abutment. Soil closest to the backwall moved in a northwest direction whereas soil further back from the wall moved more parallel to direction of loading. Larger displacements were observed at the obtuse end of the abutment, which once again suggests that the abutment was rotating into the backfill on obtuse side.

Figure 4.12 also offers insight on why a higher reduction factor was measured for the 45° skewed abutment with RC wingwalls compared to the proposed reduction curve. Backfill behind the 45° skewed abutment was more confined at the obtuse side of the abutment relative to the acute side. This increased confinement and friction along the wingwall led the enclosed soil near the east wingwall to move, more or less, as a rigid block relative to the soil near the west wingwall. The soil that moved as a rigid block may have effectively decreased the skew angle of the abutment from 45° to approximately 35°, which corresponds to a reduction factor of $R_{skew} \approx 0.46$. Surface crack patterns for the 45° skew in Figure 4.16 of the following section provide evidence of the location of the soil that displaced as a rigid block. The surface cracks near the backwall suggest that the rigid block of soil extended to the midpoint of the wingwall, 3ft (0.9 m) out from the backwall, which corresponds to an abutment skew angle of approximately 35°.

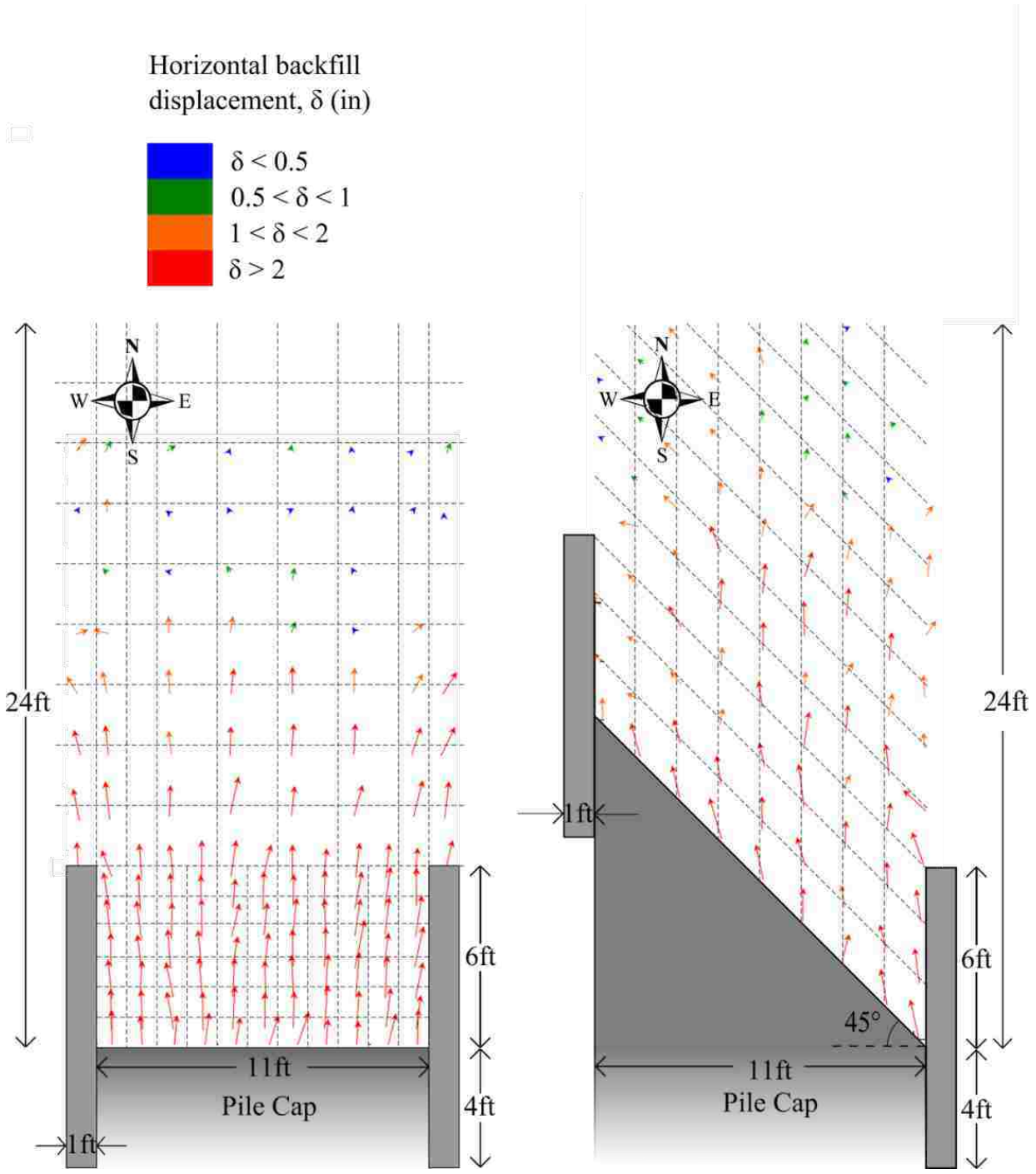

Figure 4.12. Horizontal backfill displacement for 0° and 45° skew at test completion (2ft grid in vertical direction and parallel to abutment skew—refined to 1ft grid within 6ft of pile cap for 0° skew test).

Additional displacement and soil strain plots were developed from the string potentiometers tied to stakes in the backfill (see section 3.5.4). Backfill displacement versus distance from the abutment backwall is shown for the non-skewed and 45° skewed abutment in Figure 4.13 and Figure 4.14, respectively. At all intervals of abutment deflection for both tests, higher backfill displacement was measured closer to the abutment backwall and decreased with increasing distance from the backwall.

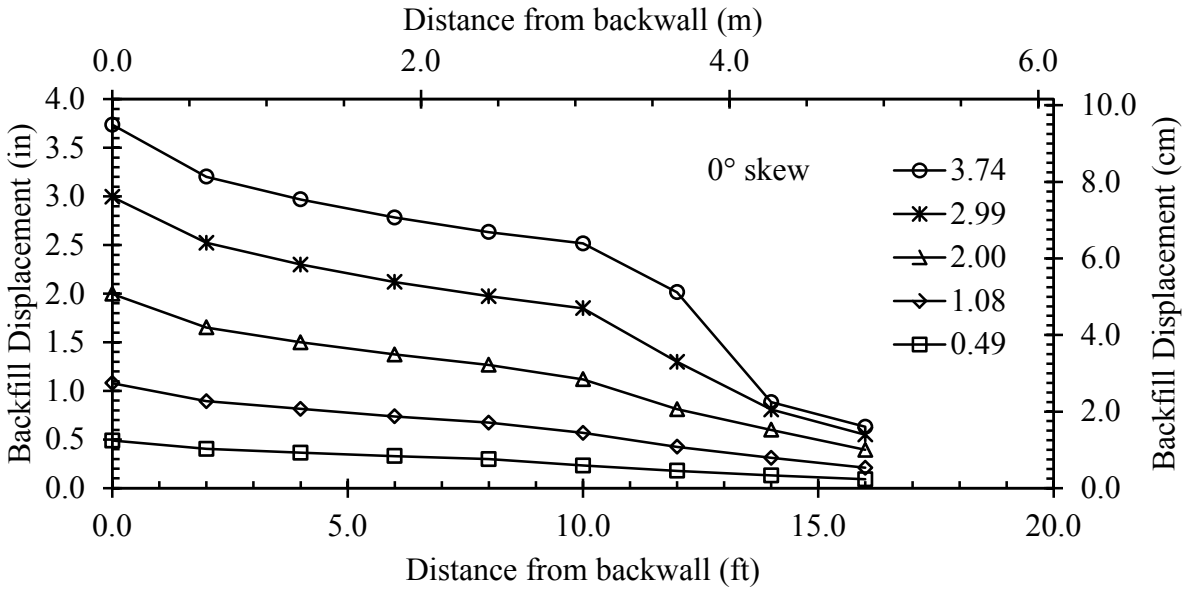

Figure 4.13. Non-skewed abutment—backfill displacement versus distance from backwall at increasing abutment deflection intervals.

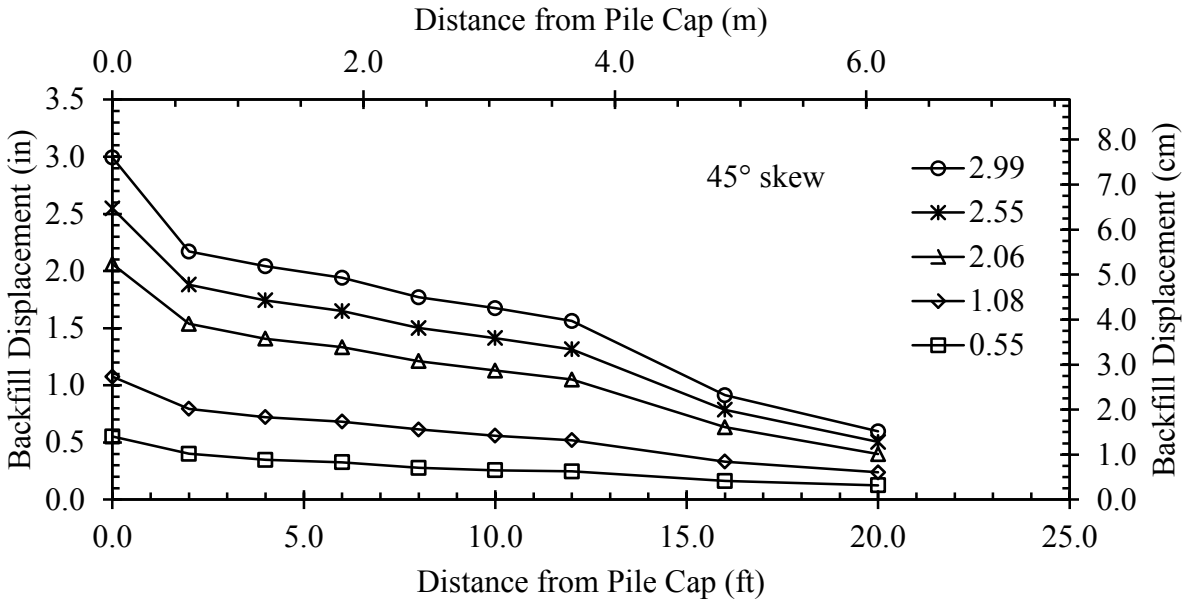

Figure 4.14. 45° skewed abutment—backfill displacement versus distance from backwall at increasing abutment deflection intervals.

Compressive soil strain was computed based on the maximum backfill displacements. Figure 4.15 shows the compressive soil strains versus distance from the backwall for both tests. High compressive strains were measured for both tests near the backwall. At greater distances from the backwall the compressive strain decreased until about 10 ft (3.1 m) where the compressive strain increased and reached a peak at approximately 13 to 14 ft (4.0 to 4.3 m). The high compressive strains near the backwall and at 13 to 14 ft (4.0 to 4.3 m) from the backwall reflect the shallow shear planes interacting with the stakes (see Figure 3.38). The relatively higher strains at approximately 14 ft (4.3 m) are consistent with surface manifestations of the passive failure wedge observed at maximum deflection for the both tests. For the non-skewed test, surface cracks were observed at approximately 14 ft (4.3 m) from the backwall. Based on previous large-scale testing, surface shear cracks were associated with 0.4 to 0.6 inches (1.0 to

1.5 cm) of heave (Franke 2013; Marsh 2013). At 14 ft (4.3 m) from the 45° skewed abutment backwall heave was approximately 0.5 to 0.75 inches (1.3 to 1.9 cm), which is consistent with the relatively higher strain.

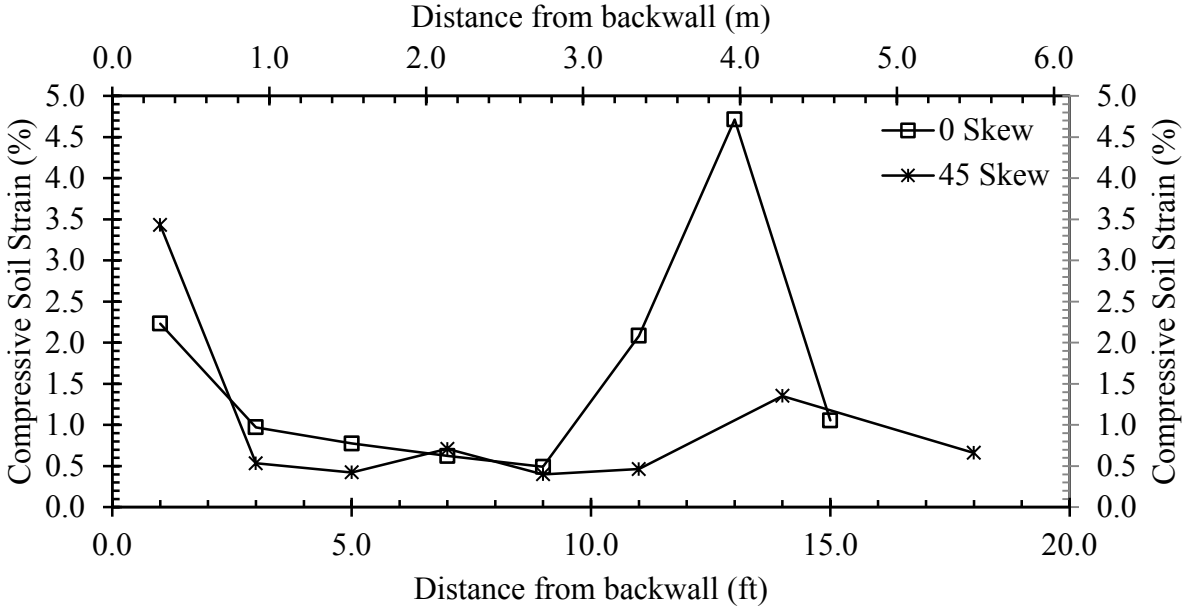

Figure 4.15. Comparison of compression soil strain for non-skewed and 45° skewed abutments.

4.4.2 Backfill Vertical Heave

Backfill vertical heave contours were generated in ArcMap and are illustrated in Figure 4.16. Heave from the non-skewed test was fairly symmetrical. The maximum heave for the non-skewed test was 2.3 in (5.8 cm), 3.5% of the backwall height (0.035H), at approximately 4 ft (1.2 m) out from the center of the pile cap face. Surface cracks extended outward from the tapered end of both wingwalls and converged at a central point 14.5 ft (4.4 m) from the center of the pile

cap face. The cracks identifying the location of the failure surface were roughly associated with a heave between 0.5 and 0.75 inch (1.3 to 1.9 cm), which is consistent with previous large-scale tests (Franke 2013; Marsh 2013).

Heave for the 45° skewed test was slightly asymmetrical with greater heave near the tapered end of the wingwall at the obtuse end of the abutment. Maximum heave for the 45° skewed test was only 1.4 in (3.6 cm), 2.1% of the backwall height (0.021H), located approximately 6 ft (1.8 m) from the abutment backwall face spanning 8 ft (2.4 m) in the middle of the backfill. Long surface cracks formed during cyclic loading, before the abutment was pushed 3.0 inches (7.6 cm) into backfill. The development of these surface cracks suggests that the soil near the backwall behaved as a rigid block with the abutment, likely due to soil and wall friction. As mentioned earlier, if the rigid block of soil is included in measuring the skew angle, a skew angle of approximately 35° is measured compared to the 45° skew of the pile cap alone. Shear cracks extending from the edge of the wingwalls seemed to extend to a greater width than for the non-skewed wall. Shear cracks identifying the back edge of the failure surface did not develop; however, if shear cracks are associated with a heave of 0.5 to 0.75 inches (1.3 to 1.9 cm) the location of the failure surface would have been about 14 ft (4.3 m) back from the face of the backwall. This distance to the back edge of the failure surface is comparable to that for the non-skewed backfill.

Because the backfill tapered downward at a 2H:1V slope on both sides of the abutment, heave was not recorded beyond the abutment width.

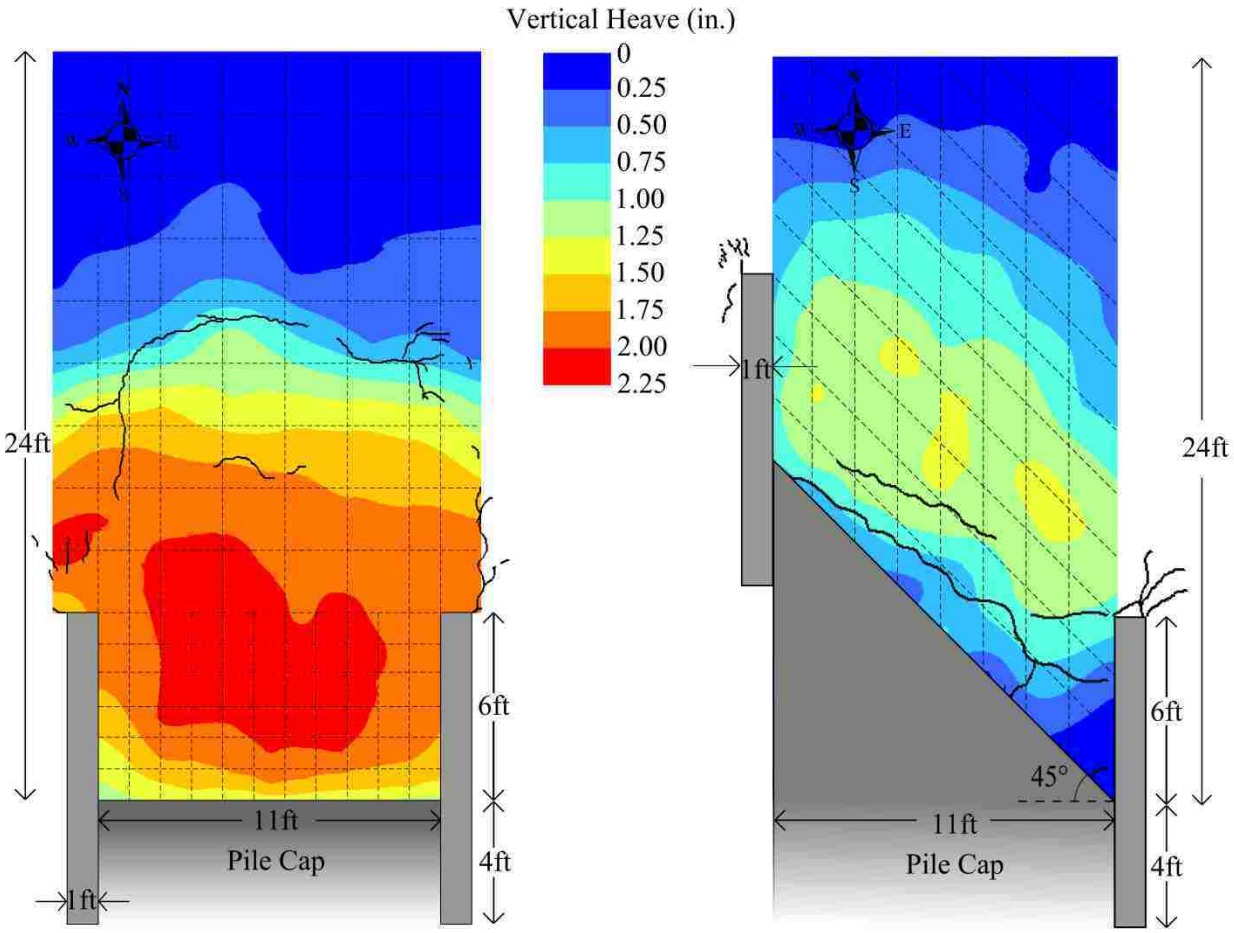

Figure 4.16. Heave contours and surface cracks for 0° and 45° skew at test completion (2ft grid in vertical direction and parallel to abutment skew—refined to 1ft grid within 6ft of pile cap for 0° skew test).

Heave contours indicate that the shear failure surface was somewhat restricted by the wingwalls. This was expected with a narrow abutment (11-ft-wide [3.4 m]) and is consistent with predictions by Shamsabadi et al. (2006). Based on surface cracks and heave measurements between 0.5 and 0.75 inch (1.3 to 1.9 cm), failure surface effective widths were estimated to be approximately 13.5 ft (4.1 m) for both cases, slightly wider than the abutment width, and are illustrated in Figure 4.17.

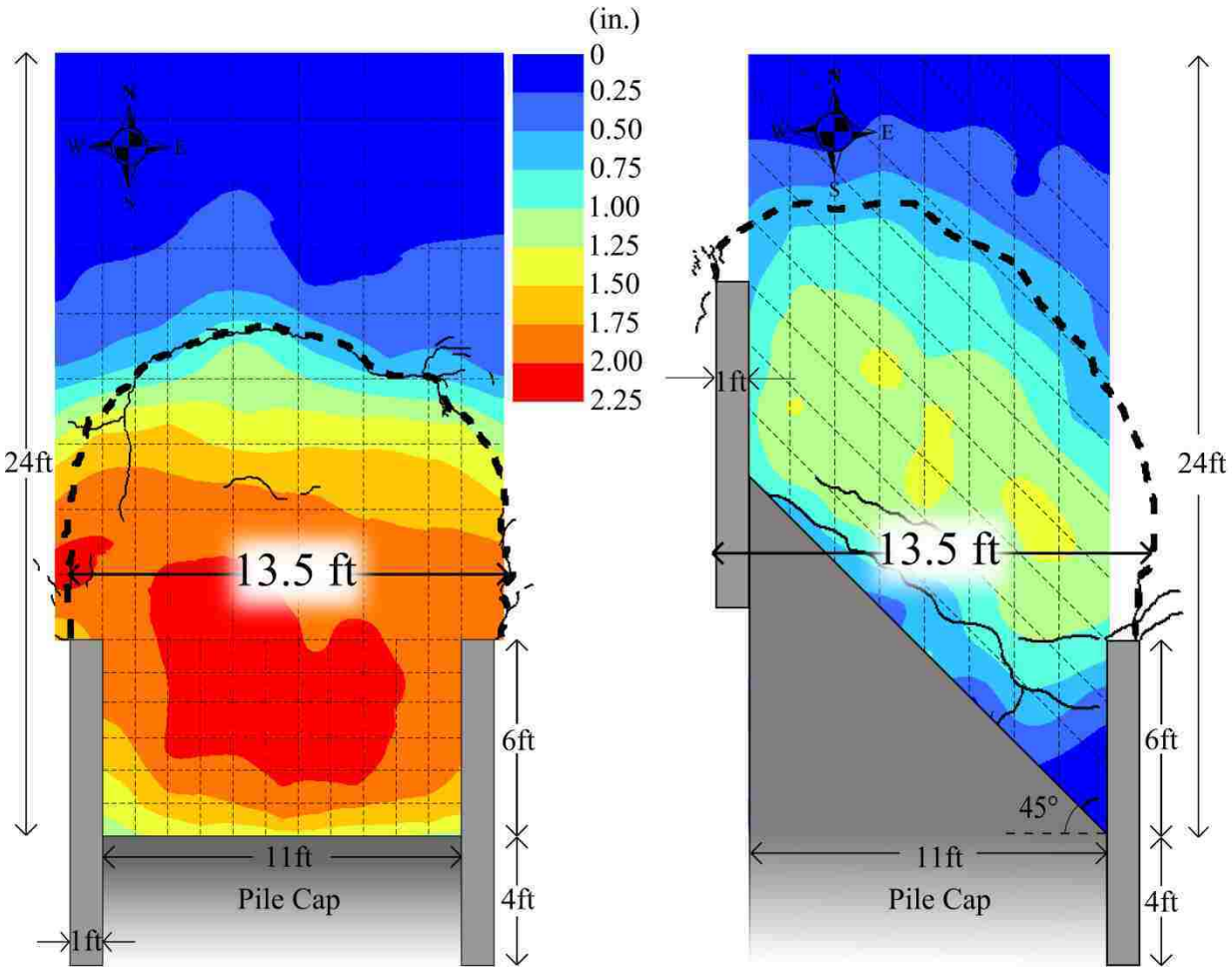

Figure 4.17. Failure surface effective widths based on surface cracks and heave measurements between 0.5 and 0.75 inch.

4.4.3 Shear Failure Surface

Shear failure surfaces were estimated from observations of offsets in the red soil columns compacted in the backfill. Figure 4.18 shows an offset in a red soil column due to the mobilized shear surface in the soil. Offsets are connected at four consecutive locations with white spray paint in Figure 4.19.

Figure 4.18. Offset in red soil column from shear failure surface.

Figure 4.19. Estimate of shear failure surface from four consecutive soil columns.

Estimated failure surfaces are illustrated in Figure 4.20 and Figure 4.21. Both failure surfaces behind the non-skewed and 45° skewed abutments closely resemble a log spiral shear surface. For the non-skewed abutment, surface cracks were observed at approximately 13 ft (4.0 m) and 14.5 ft (4.4 m) from the backwall face, and were in good agreement with the estimated subsurface shear planes. The equation for the angle of inclination of the linear failure surface is shown in Figure 4.20.

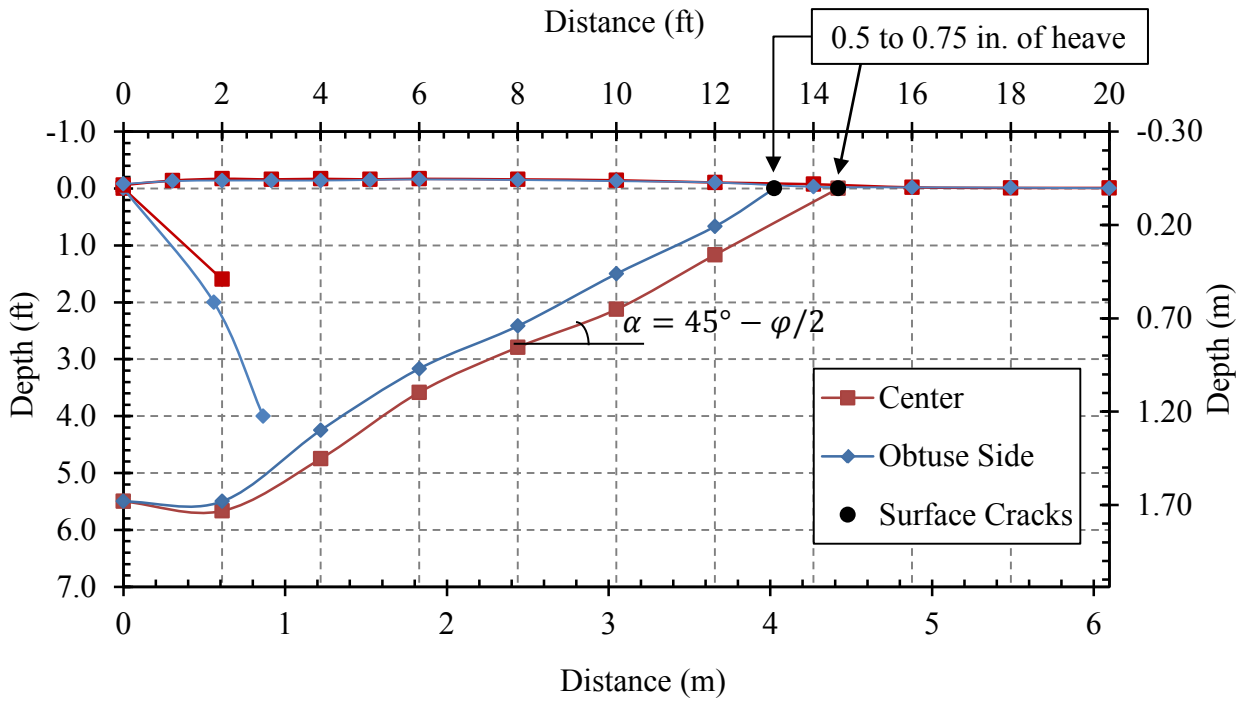

Figure 4.20. Backfill shear failure surface for non-skewed abutment.

For the 45° skewed abutment, offsets in the red sand columns were more difficult to identify. Only one offset was clearly identified at 2 ft (0.61 m) from the backwall. Although no surface cracks formed, indicating the length of the passive failure surface, heave measurements of 0.5 to 0.75 inches (1.3 to 1.9 cm) were used to estimate the passive failure surface length. A

linear failure surface was estimated from the sand column offset identified at 2 ft (0.61 m) to the ground surface at 14 ft (4.3 m) from the backwall where 0.5 to 0.75 inches (1.3 to 1.9 cm) of heave were measured.

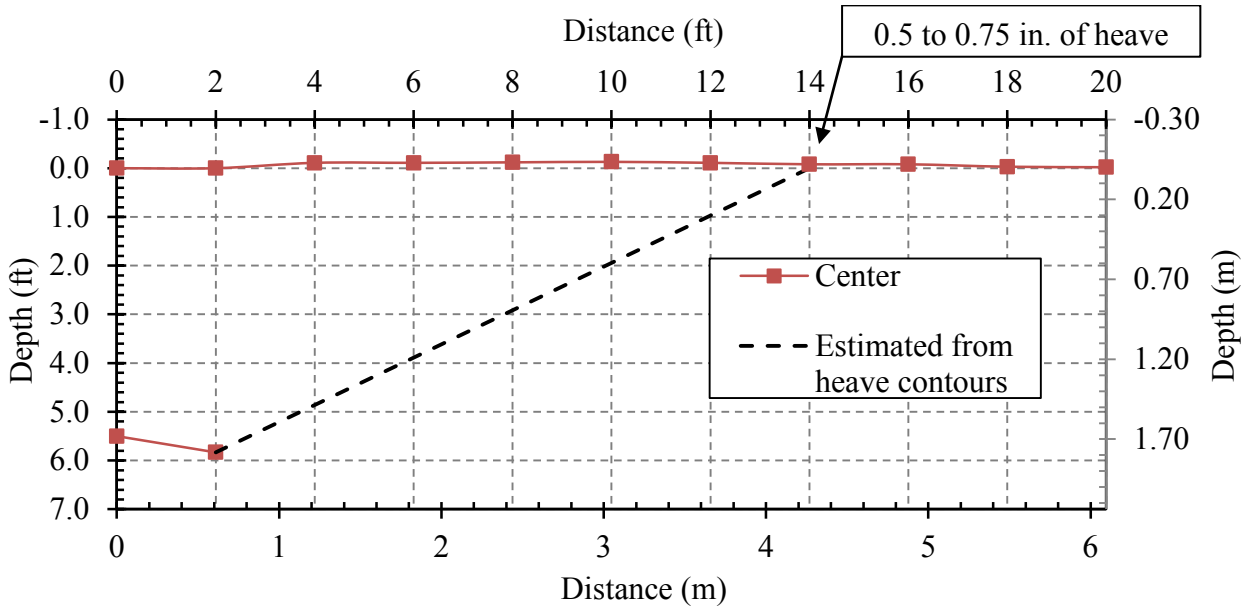

Figure 4.21. Backfill shear failure surface for 45° skewed abutment.

Friction angle (φ) estimates were back-calculated using Equation (4-1).

$$\alpha = 45° - \varphi/2 \tag{4-1}$$

where, $\alpha = Angle\ of\ inclination\ of\ the\ linear\ failure\ surface$

Back-calculated friction angles are listed in Table 4.1. Values of α and φ for the non-skewed test are averages of the shear surfaces at the center and obtuse side of the abutment. A friction angle of $\varphi = 39.5°$ estimated from the non-skewed backfill shear surfaces is in good agreement with direct shear test results (see Table 3.3). When approximating the linear failure

surface based on heave measurements for the 45° skew test, a friction angle of $\varphi = 38.1°$ is obtained, which is consistent with the non-skewed test.

Table 4.1. Friction Angles (φ) Back-calculated From Angles of Inclination (α)

Abutment skew	α degrees	φ degrees
0°	25.3	39.5
45°	25.9	38.1

4.5 Structural Wingwall Response

The wingwall deflection and bending moment distribution along the height of the wingwalls are presented in this section.

4.5.1 Wingwall Deflection

The total deflection measured by the string potentiometers positioned transverse to the wingwalls (see Figure 3.42) was corrected for longitudinal deflection to get transverse deflection (ΔT) as shown in Figure 4.22. Transverse deflection was calculated using Equations (4-2), (4-3), and (4-4). Variables used in these equations are illustrated in Figure 4.22.

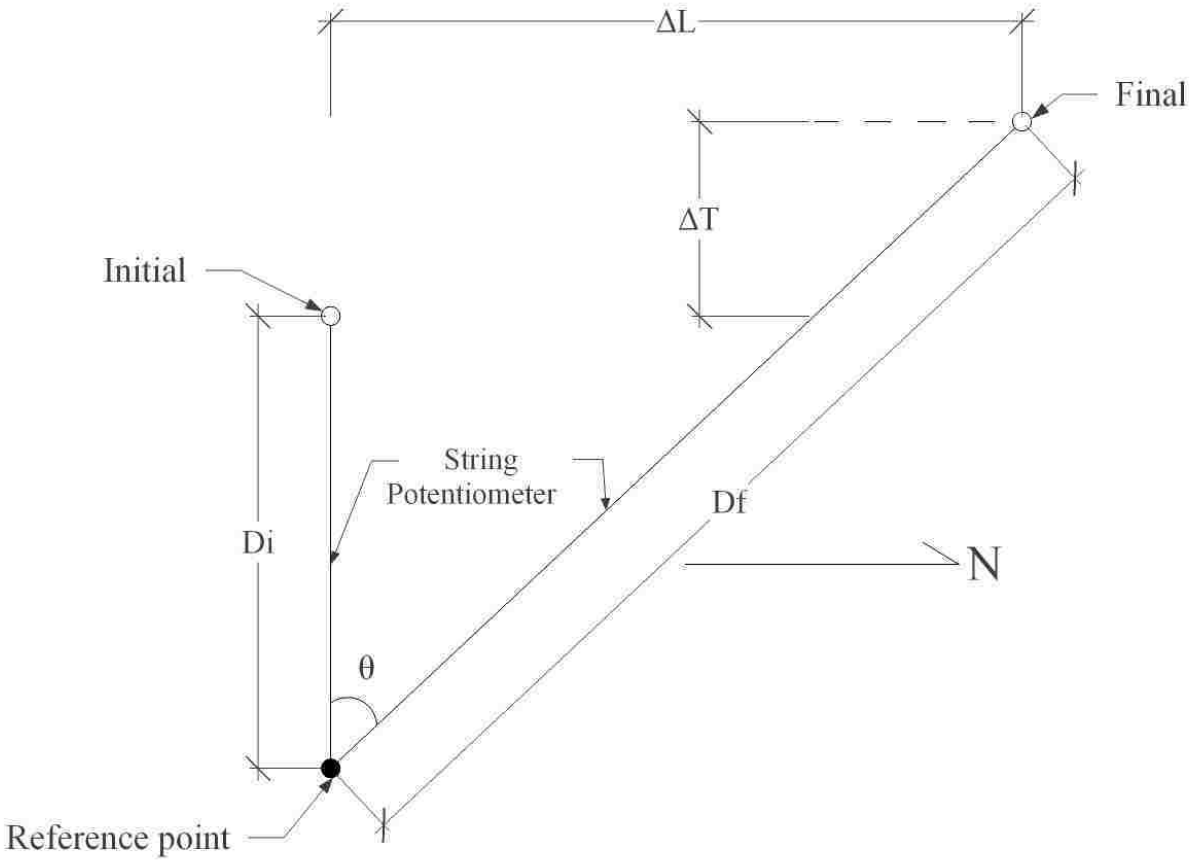

Figure 4.22. Wingwall transverse deflection calculated as transverse component (ΔT) of string potentiometer extension.

The length of the string due to only longitudinal movement, removing any effects from transverse movement, was calculated using Equation (4-2).

$$D_{long} = \sqrt{{D_i}^2 + \Delta L^2} \tag{4-2}$$

The additional length of the string attributed to transverse movement was calculated using Equation (4-3).

$$\Delta D = D_f - D_{long} \tag{4-3}$$

Transverse deflection (ΔT) was calculated using Equation (4-4).

$$\Delta T = \Delta D cos(\theta) \quad (4\text{-}4)$$

The deflected shape of wingwalls from both tests in Figure 4.23 did not resemble the typical deflected shape of a cantilever beam subject to a uniform distributed load as conceptualized in Figure 3.12 (see section 3.3.4). The curvature suggests the soil at the tapered end of the wingwall provided sufficient confinement to slightly induce axial compression in addition to the distributed load along the inside wingwall face. Axial compression of the wingwall was likely caused from the passive force of the soil. Assuming that sufficient deflection of the wingwall mobilized the peak passive resistance of the soil, a triangular pressure distribution at the tapered end of the wingwall was used to approximate the passive pressures at each strain gauge depth in the wingwall. Because the wingwall thickness was 1 ft (0.305 m) and tributary height of the #7 reinforcing bars was 0.5 ft (0.15 m), pressures were multiplied by a 0.5 ft^2 (0.05 m^2) tributary area to approximate the passive forces experienced at each strain gauge depth. Passive forces are listed in Table 4.2.

Table 4.2. Approximate Passive Forces at Strain Gauge Depths

Number	Strain gauge depths (in)	Strain gauge depths (ft)	Pressure (psf)	Force (kip) over 0.5 ft^2 trib. area
1	8	0.67	1373	0.7
2	20	1.67	2863	1.4
3	32	2.67	4352	2.2
4	44	3.67	5841	2.9
5	56	4.67	7331	3.7

As is typical in beam-column structural design, combined axial and distributed loads result in first and second order moments and are much more complex compared to simple

distributed loads on a cantilever beam; however, for simplicity, the loads were only approximated as distributed loads, neglecting any second order effects from the axial loads.

For the non-skewed abutment, the bulging shape with larger transverse deflections in the middle portion of the cantilever wingwall reflect some amount of axial compression from the soil passive resistance at the tapered end. Maximum transverse wingwall deflection for the non-skewed abutment was measured on the tapered end of the west wingwall and was approximately 0.3 in (0.76 cm).

Wingwall deflection for the 45° skewed abutment reflects the westward movement of the abutment during lateral loading. Both wingwalls deflected in the same general direction, which seemed to be in response of being forced into the soil on the west side of both wingwalls. Because the soil on the west side of the west wingwall sloped downward, there was less resistance to westward movement in comparison with the east wingwall where the soil on the west side of the wingwall had a constant height. Maximum wingwall deflection was approximately 0.5 in (1.27 cm) and was measured at the tapered end of the east wingwall. Larger deflections on the wingwall on the obtuse side of the 45° skewed abutment correspond with larger moments computed from strain gauge data.

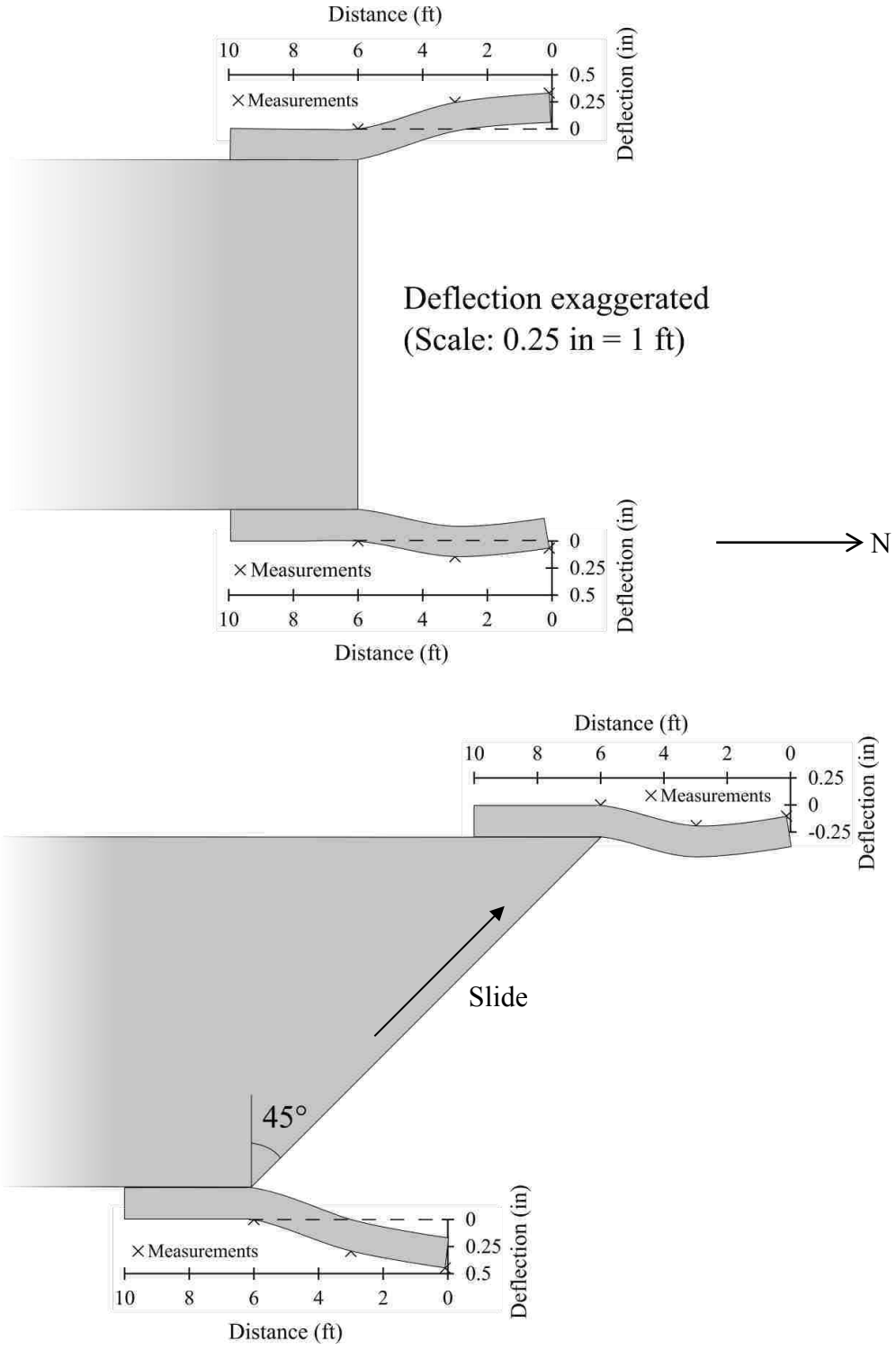

Figure 4.23. Transverse wingwall deflection at test completion for non-skewed and 45° skewed abutments (Deflection exaggerated 1 ft = 0.25 in).

4.5.2 Moment Distribution

Moment distributions were calculated from strain gauge measurements which measured in units of micro-strain (μ). Strain was not large enough during testing to yield the reinforcement. The strain of the wingwall reinforcement monitored during load testing increased in a systematic fashion with increasing load. Although strain gauge measurements appeared to be consistent, moments were much lower than the design moment $\left(\varphi M_N = 47.6\ kip \cdot \frac{ft}{ft}\ [65.0\ kN \cdot \frac{m}{m}]\right)$ calculated using Equation (3-1). Two explanations are proposed for the inconsistencies between the measured moments and the design moment: (1) some amount of rotation may have occurred at the wingwall bolted connection, which would relieve the moment experienced by the reinforcement where the strain gauge was located, and (2) insufficient transverse displacement of the wingwalls occurred to mobilize passive pressure along the wingwall. Consequently, the bending moments on the wingwall during testing were less than the bending moment that would occur had the full passive force been mobilized at larger displacements. In addition, the wingwalls did not experience a simple distributed load during testing, which was the load case used to approximate design soil pressures. The deflection of the wingwalls illustrated in Figure 4.23 indicates that the wingwalls were probably also loaded in axial compression due to the passive resistance of the soil in addition to a nonuniform distributed load across the wingwall face.

Because monolithic wingwalls were beyond the scope of this study, each wingwall was connected with (10) 7/8-in-diameter ASTM A307 steel bolts, which were torqued to 200 ft-lb (271 N-m). Bolt holes at the connection were 2.25-in (5.72-cm) in diameter and on average allowed for approximately 0.75 in (1.91 cm) of slipping relative to the pile cap during testing. String potentiometers tied to the wingwalls indicate that wingwalls slipped in the direction

opposite to the direction of loading, which was likely caused by soil passive forces acting on the tapered end of the wingwalls. Rotation at the bolted connection was not measured, but it is believed that a small amount of rotation occurred.

The strain measured by the strain gauges was a combination of positive strain due to bending and negative strain due to axial compression. Strain gauges were bonded to inner side of the wingwall tension reinforcement (#7 bars), facing the backfill, at 3ft (0.92 m) and 6 ft (1.8 m) from the tapered end (see Figure 3.40). Strain gauges located 6 ft (1.8 m) from the tapered end are roughly at the pile cap face. As the wingwalls bended away from the pile cap, the strain gauges that were roughly in line with the pile cap face experienced tension, which was measured as positive strain. At the same time, the reinforcement was likely experiencing axial compression as the soil passive force developed from the wingwall being pushed into the backfill. Compression was measured as negative strain, effectively decreasing the strain (and moment) measured by the strain gauge. The elastic stress-strain relationship $\sigma = \varepsilon E$, and the principle of equilibrium were employed to calculate bending moments from micro-strain measurements. Micro-strain in #7 bars was converted to tensile force using Equation (4-5).

$$F = \varepsilon E A \tag{4-5}$$

where,

$$F = tensile\ force$$

$$\varepsilon = \frac{\mu}{1{,}000{,}000} = strain \tag{4-6}$$

$$\mu = microstrain$$

$$E = 29{,}000{,}000\ psi\ for\ steel$$

$$A = 0.60\ in^2\ for\ \#7\ rebar$$

According to equilibrium, the force in the tension reinforcement must be equal to the force in the compression reinforcement. The equal tension and compression forces create a moment couple, where the moment arm is the distance between tension and compression reinforcement on centers. The cross section of the reinforced concrete wingwall in Figure 4.24 shows the moment arm distance $\left(d = 6\frac{5"}{16}\right)$. The moment at each strain gauge location was calculated as $M = Fd$. In general, strain in the tension reinforcement increased with increasing actuator load and maximum strain was measured at maximum loading, which occurred at the maximum deflection for both tests.

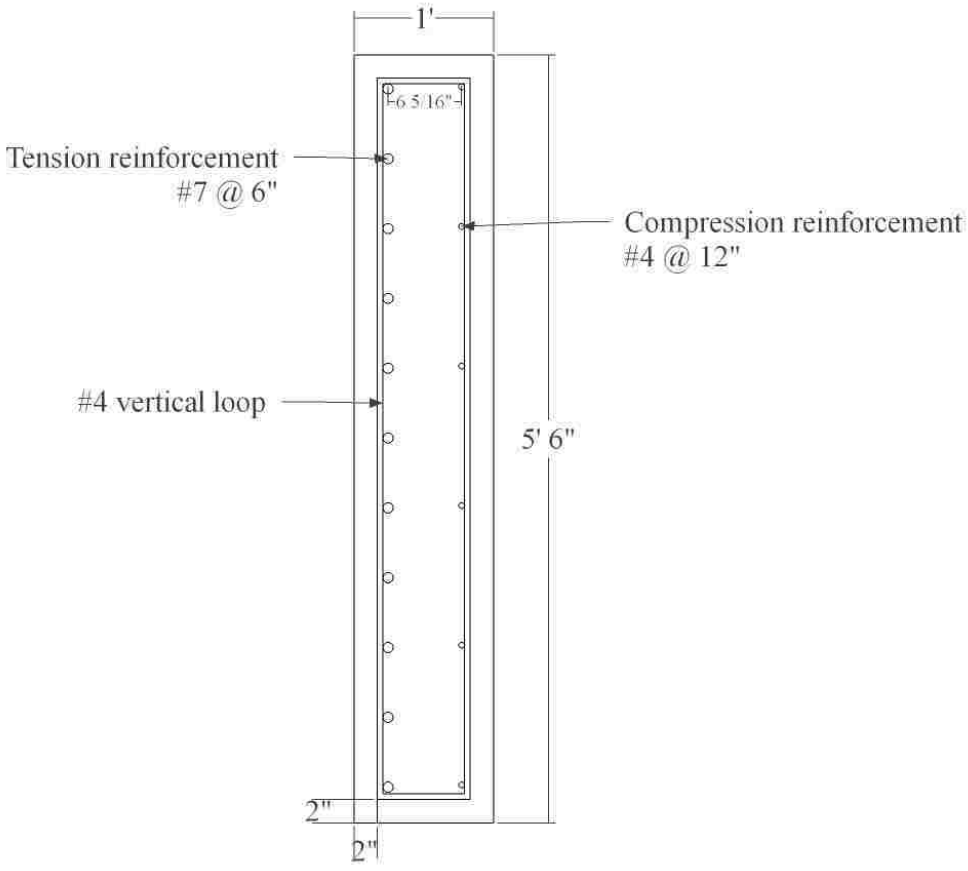

Figure 4.24. Reinforced concrete wingwall section.

The bending moment distributions at test completion for wingwalls on non-skewed and 45° skewed abutments are shown in Figure 4.25 and Figure 4.26. Although moment magnitudes may be unreliable for design with monolithic wingwalls, the comparison between non-skewed and 45° skewed abutments is insightful. The general shape of the moment distribution is also helpful in locating the depth of the maximum moment.

Relatively small bending moments developed in the wingwall reinforcement on the non-skewed abutment, although bending moments were generally larger near the pile cap. Negative moments 3-ft from the tapered end correspond with the compression bending observed from the deflected shape (see Figure 4.23).

At the corner of the east wingwall (obtuse side) and the pile cap the maximum moment was seven times larger for the 45° skewed abutment compared to the non-skewed abutment, which is in good agreement with backfill displacement results. For the 45° skewed abutment, the maximum wingwall moment was fourteen times larger on the obtuse side of the abutment compared to the acute side. In general, maximum bending moments occurred at the strain gauge that was 20 in (50.8 cm) below the top of the wingwall, which is about the midpoint of the 3-ft (0.92 m) tapered end. The depth of the maximum moment appears to be caused by the upward taper of the wingwall.

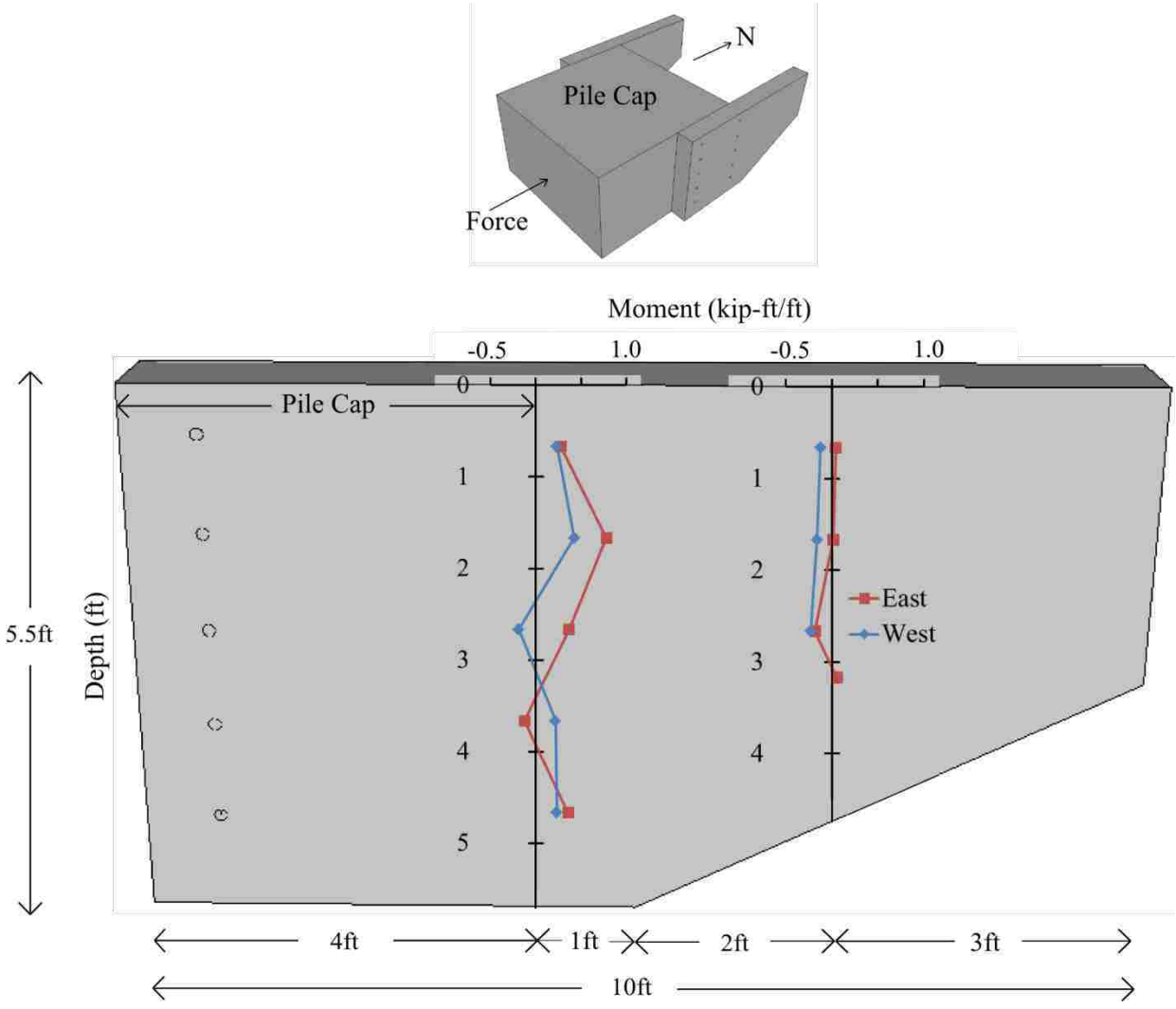

Figure 4.25. Winwgall moment distribution at test completion for non-skewed abutment.

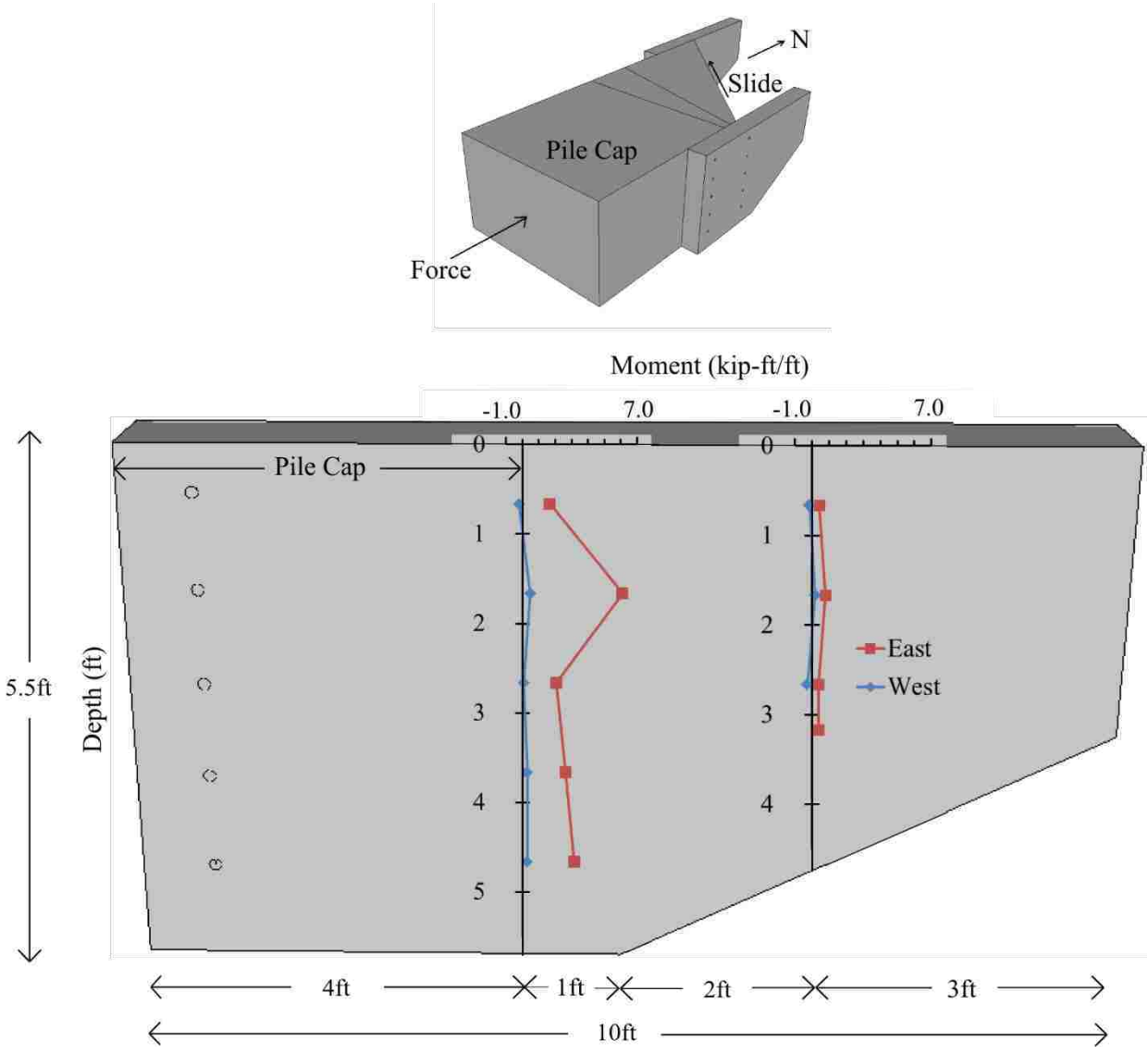

Figure 4.26. Wingwall moment distribution at test completion for 45° skewed abutment.

Moment distributions from non-skewed and 45° skewed tests are compared in Figure 4.27.

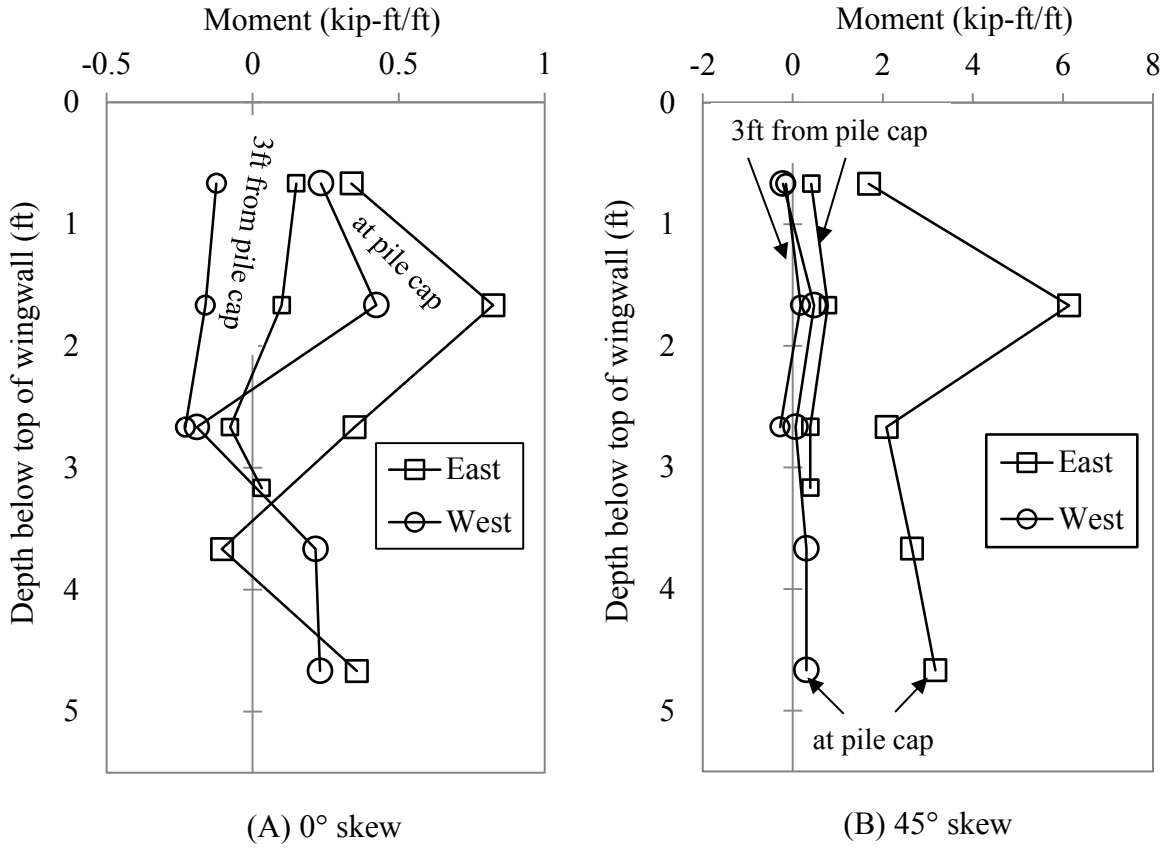

Figure 4.27. Moment distributions in wingwalls at maximum deflection: (A) 0° skew. (B) 45° skew.

Bending moments were also computed using pressure cell data. Pressure measured from the Geokon® pressure cells was uniformly distributed over respective tributary areas. The bottom pressure cell on the west wingwall did not record any data; thus, the pressure measured by the top pressure cell was distributed across the entire west wingwall. Bending moments were approximated by computing one resultant force on each wingwall from the pressure measurements that acted at the centroid of the wingwall (1.9 ft [0.58 m] from the backwall).

Average bending moments (kip-ft/ft) based on pressure cell measurements were consistently higher compared with moments calculated from strain gauge data and are shown in Table 4.3.

Table 4.3. Average Moments (kip-ft/ft) on Wingwalls at Maximum Deflection

Skew	Moment (kip-ft/ft)	
	West	East
0°	5.7	8.9
45°	5.4	12.3

Bending moments approximated from pressure cell data do not consider axial compression caused by the passive resistance of the soil at the tapered end of the wingwall. For a more accurate comparison between strain gauge and Geokon® pressure cell data, bending moment distributions were recalculated from strain gauge measurements that were modified for axial compression due to the passive resistance of the soil using Equation (4-7).

$$M = \left(F_{measured} + P_{pwing}\right)d \tag{4-7}$$

where,

$M = moment$

$F_{measured} = tensile\ force\ measured\ by\ strain\ gauge$

$P_{p,wing} = peak\ passive\ resistance\ of\ soil\ associated\ with\ strain\ gauge\ depth$

$d = 6\frac{5}{16}\ inches\ (moment\ arm)$

Because axial compression due to $P_{p,wing}$ acting at the end of the wingwall would decrease the tensile force experienced by the reinforcing bars, the effect was reversed by adding $P_{p,wing}$ to the $F_{measured}$. The value $\left(F_{measured} + P_{p,wing}\right)$ was used to approximate the tensile

force in the reinforcement in response only to the soil pressure (or distributed load) along the inner face of the wingwall. Values of $P_{p,wing}$ were approximated using a traditional triangular pressure distribution with depth and are shown in

Table 4.4. The effect of the taper was neglected. Values of $K_{p\varphi} = 12.84$ and $K_{pc} = 5.0$ were obtained from PYCAP (Duncan and Mokwa 2001) and used in Equation (4-8) to compute the horizontal soil pressure $(\sigma_{h,wing})$ at each depth.

$$\sigma_{h,wing} = K_{p\varphi}\gamma D + 2c\sqrt{K_{pc}} \quad (4\text{-}8)$$

where,

$\sigma_{h,wing} = horizontal\ soil\ pressure$

$D = depth\ of\ strain\ gauge$

$K_{p\varphi} = lateral\ earth\ pressure\ coefficient\ associated\ with\ the\ friction\ angle\ and\ weight\ of\ the\ soil$

$K_{pc} = lateral\ earth\ pressure\ coefficient\ associated\ with\ the\ apparent\ cohesion\ of\ the\ soil$

$\gamma = 116\ pcf\ (unit\ weight\ of\ the\ soil)$

$c = 85\ psf\ (apparent\ cohesion)$

Table 4.4. Peak passive force $(P_{p,wing})$ acting on the tapered end of the wingwall at strain gauge depths

Strain gauge depths (in)	Strain gauge depths (ft)	$\sigma_{h,wing}$ (psf)	$P_{p,wing}$ (kip) over 0.5 ft^2 trib. area
8	0.67	1373	0.7
20	1.67	2863	1.4
32	2.67	4352	2.2
44	3.67	5841	2.9
56	4.67	7331	3.7

Because the wingwall width was 1 ft (0.305 m) and the reinforcing bars were spaced 6 inches (15.2 cm) apart, $\sigma_{h,wing}$ was applied over 0.5 ft^2 (0.05 m^2) tributary area to approximate $P_{p,wing}$.

Figure 4.28 shows the bending moment distributions along the height of the wingwalls with the effects of axial compression removed. Moments in Figure 4.28 (effects of axial compression removed) are higher relative to moments in Figure 4.27 which are based on the total strain that includes the effects from axial compression; however, a significant increase was not obtained relative to the design moment of $\varphi M_N = 47.6\ kip \cdot \frac{ft}{ft}$ ($65.0\ kN \cdot \frac{m}{m}$).

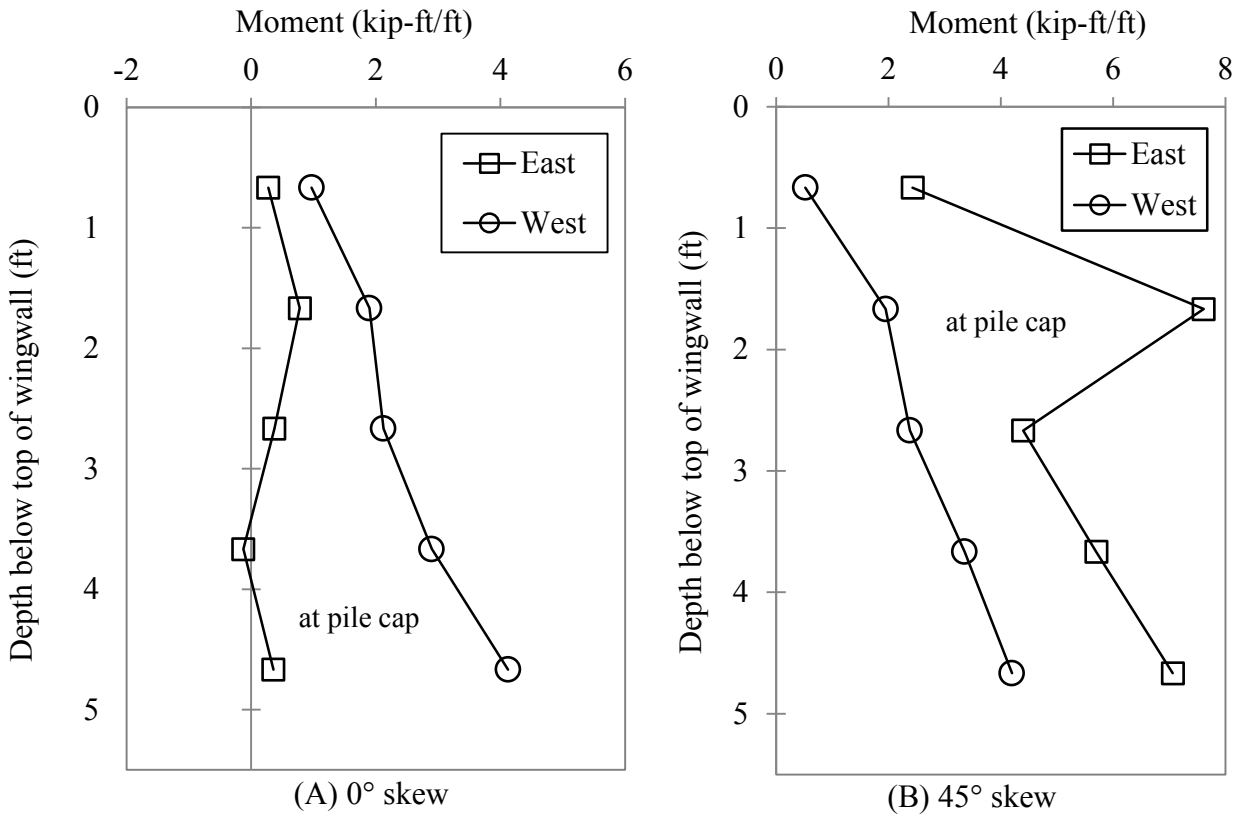

Figure 4.28. Moment distributions in wingwalls at maximum deflection with axial compression removed: (A) 0° skew. (B) 45° skew.

4.6 Geotechnical Wingwall Response

Soil pressures and lateral earth pressure coefficients were computed based on moment calculations.

4.6.1 Soil Pressure Distribution

Soil pressure distributions along the wingwalls on both non-skewed and 45° skewed abutments are illustrated in Figure 4.29 and Figure 4.30. Soil pressures were approximated using the moments calculated with the strain gauge data and, therefore, follow a similar trend. Significantly higher pressures were observed on the 45° skewed abutment east (obtuse side) wingwall compared to pressures computed on the west wingwall and both wingwalls on the non-skewed abutment. Maximum pressure experienced by the east (obtuse side) wingwall on the 45° skewed abutment, approximately 2400 psf (115 kPa) was six times as large as the maximum pressure experienced by non-skewed wingwalls, approximately 400 psf (19.2 kPa).

Soil pressures were multiplied by tributary areas to compute the total normal force acting on the wingwalls. For the non-skewed test, both east and west wingwalls experienced approximately 3 kips (13.4 kN) of normal force, based on results shown in Figure 4.29. Wingwall normal forces for the 45° skewed test were computed from results shown in Figure 4.30. For the 45° skewed abutment, the east wingwall experienced 19 kips (85 kN) compared to 2 kips (9.0 kN) experienced by the west wingwall.

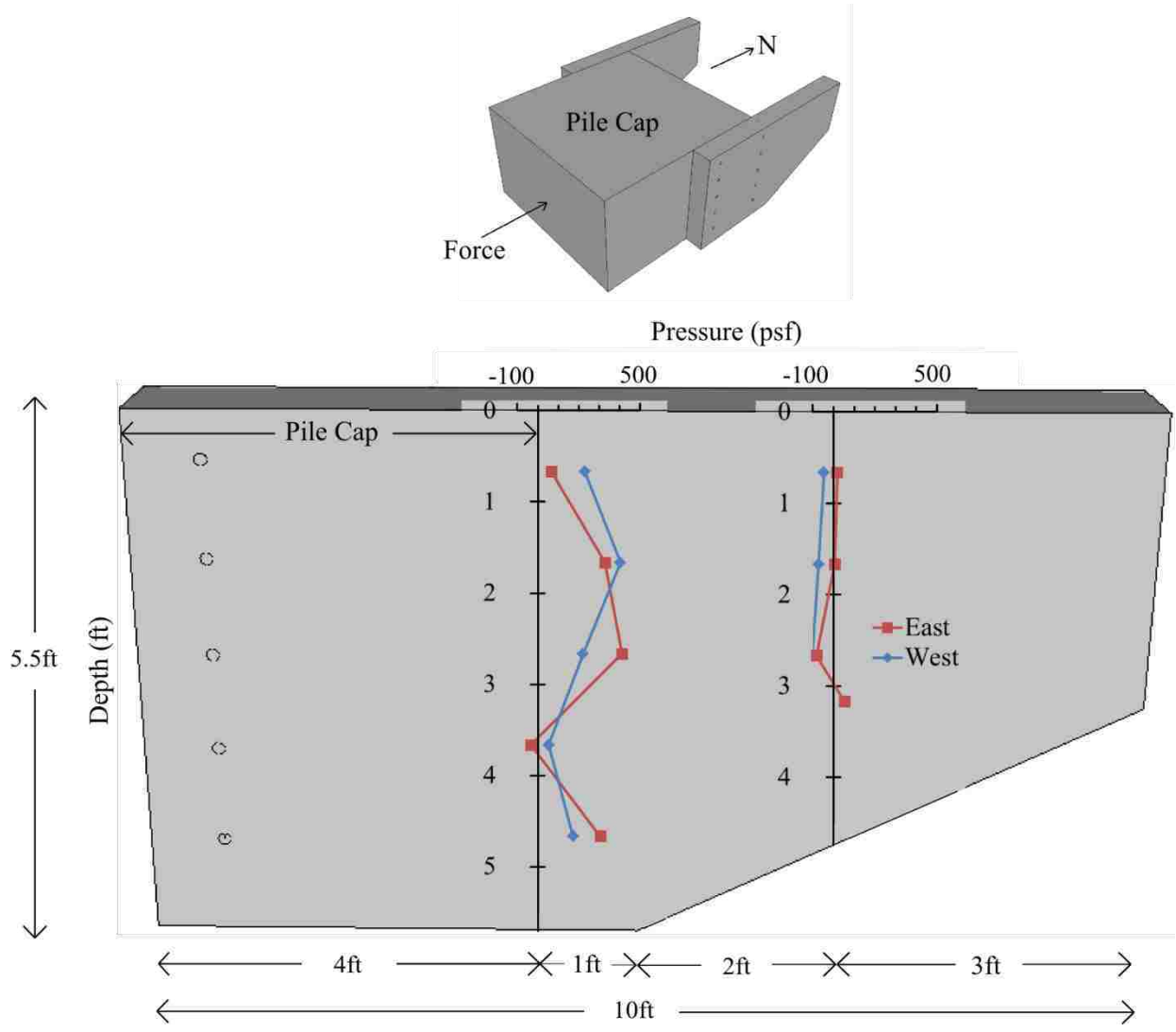

Figure 4.29. Horizontal pressure distribution along wingwall height at test completion for non-skewed abutment.

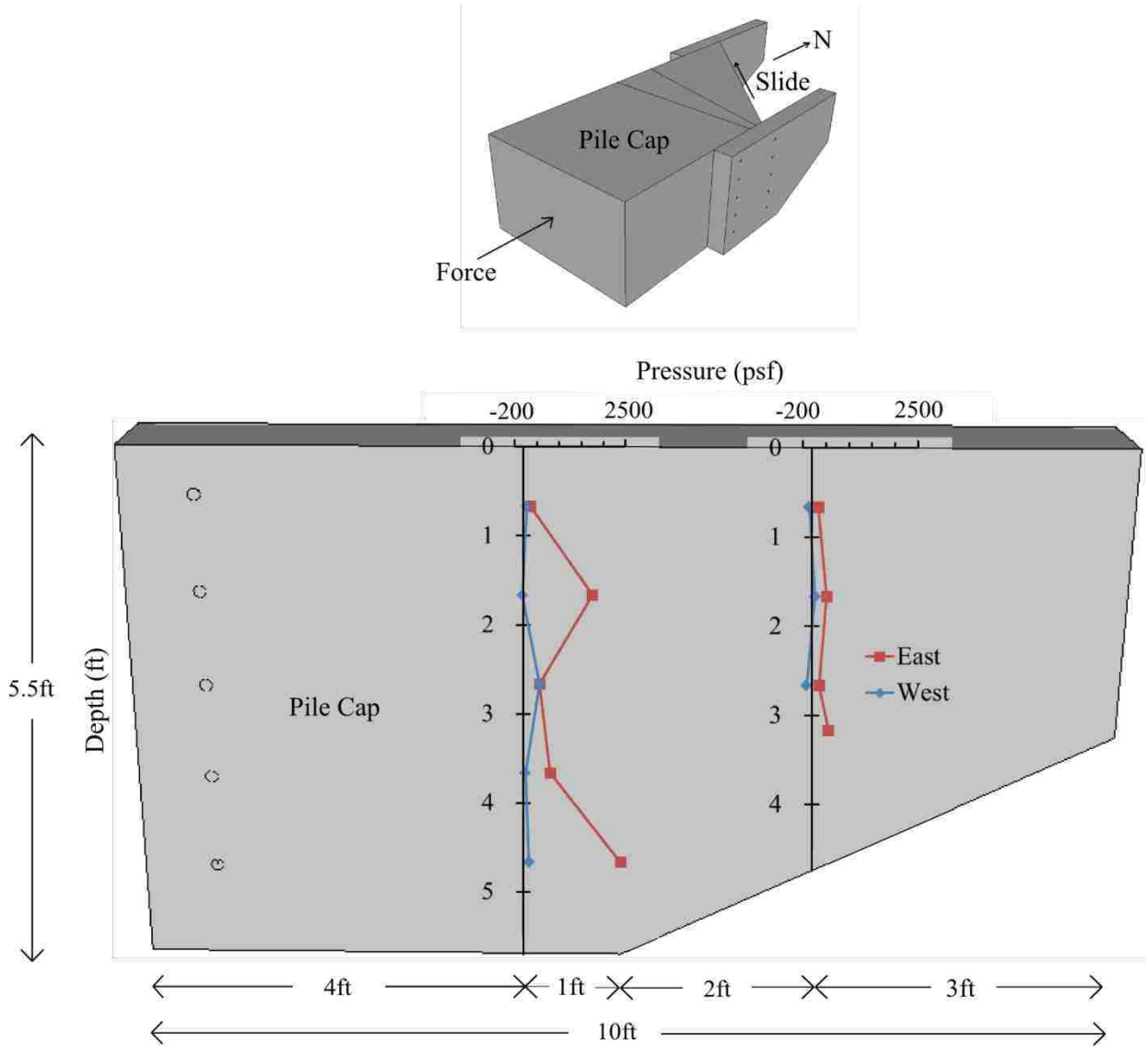

Figure 4.30. Horizontal pressure distribution along wingwall height at test completion for 45° skewed abutment.

Figure 4.31 illustrates the cantilever model used to approximate the pressure distribution along the wingwall. Two distributed loads (w_1 and w_2) were used to approximate lateral soil pressures on wingwalls and were applied along the wingwall at distances corresponding to moments calculated at strain gauge locations.

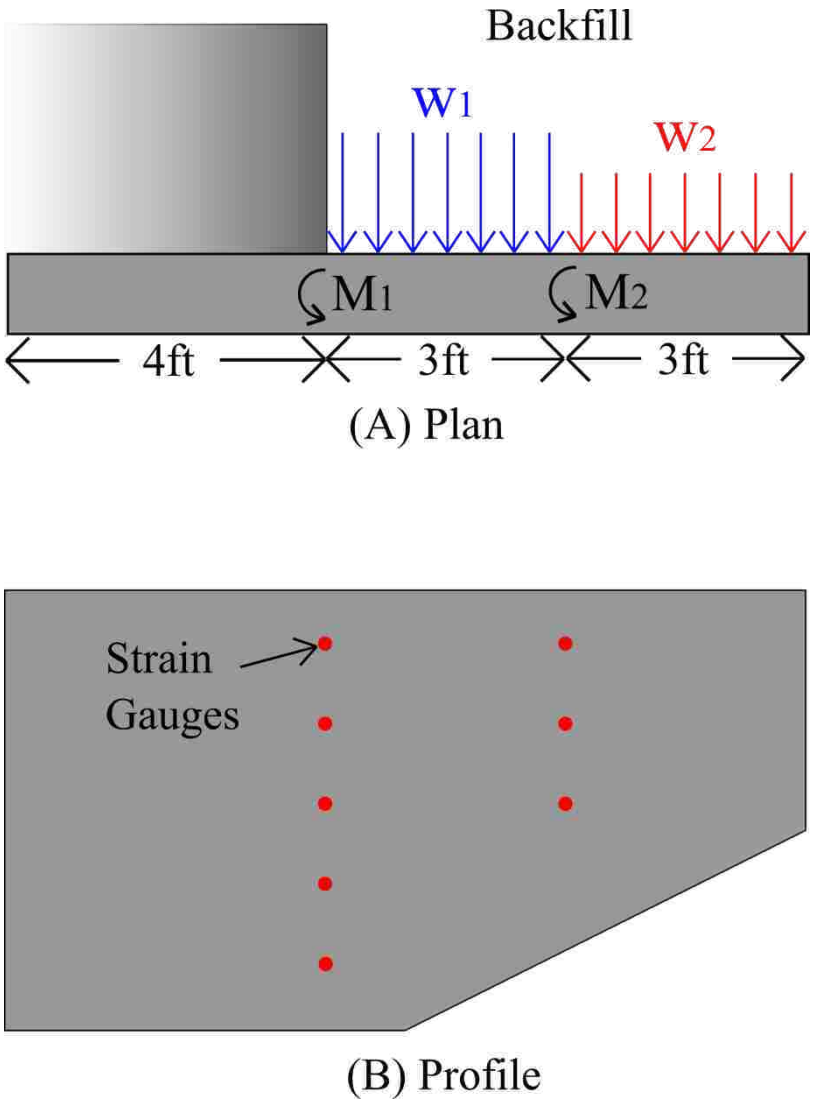

Figure 4.31. Conceptual model for approximating distributed loads along the length of the wingwall.

Values for w_1 and w_2 were back-calculated from the bending moment that was calculated at each strain gauge location (see section 4.5.2). Load distributions w_1 and w_2 were computed for the upper three levels of strain gauges using Equations (4-9), (4-10), (4-11), and (4-12).

$$M_2 = \frac{w_2(3ft)^2}{2} \tag{4-9}$$

$$w_2 = \frac{2M_2}{(3ft)^2} \tag{4-10}$$

$$M_1 = w_2(3ft)(4.5ft) + \frac{w_1(3ft)^2}{2} \tag{4-11}$$

$$w_1 = \frac{2[M_1 - w_2(3ft)(4.5ft)]}{(3ft)^2} \tag{4-12}$$

For the lower two levels of single strain gauges, only one distributed load was used to approximate the soil pressure distribution across the appropriate length.

A comparison of lateral soil pressures experienced by the non-skewed and 45° skewed abutments is provided in Figure 4.32.

The significantly higher pressures experienced by the east (obtuse side) wingwall on the 45° skewed abutment, resulted in higher frictional resistance along the face of the east wingwall compared to the non-skewed abutment. Frictional resistance was calculated with Equation (4-13).

$$Friction = N * tan\delta \text{ ,} \tag{4-13}$$

where,

$N = Normal\ force\ acting\ on\ wingwall$

$\delta = 0.7\varphi$

$\varphi = soil\ friction\ angle$

$\delta = wall\ friction\ angle$

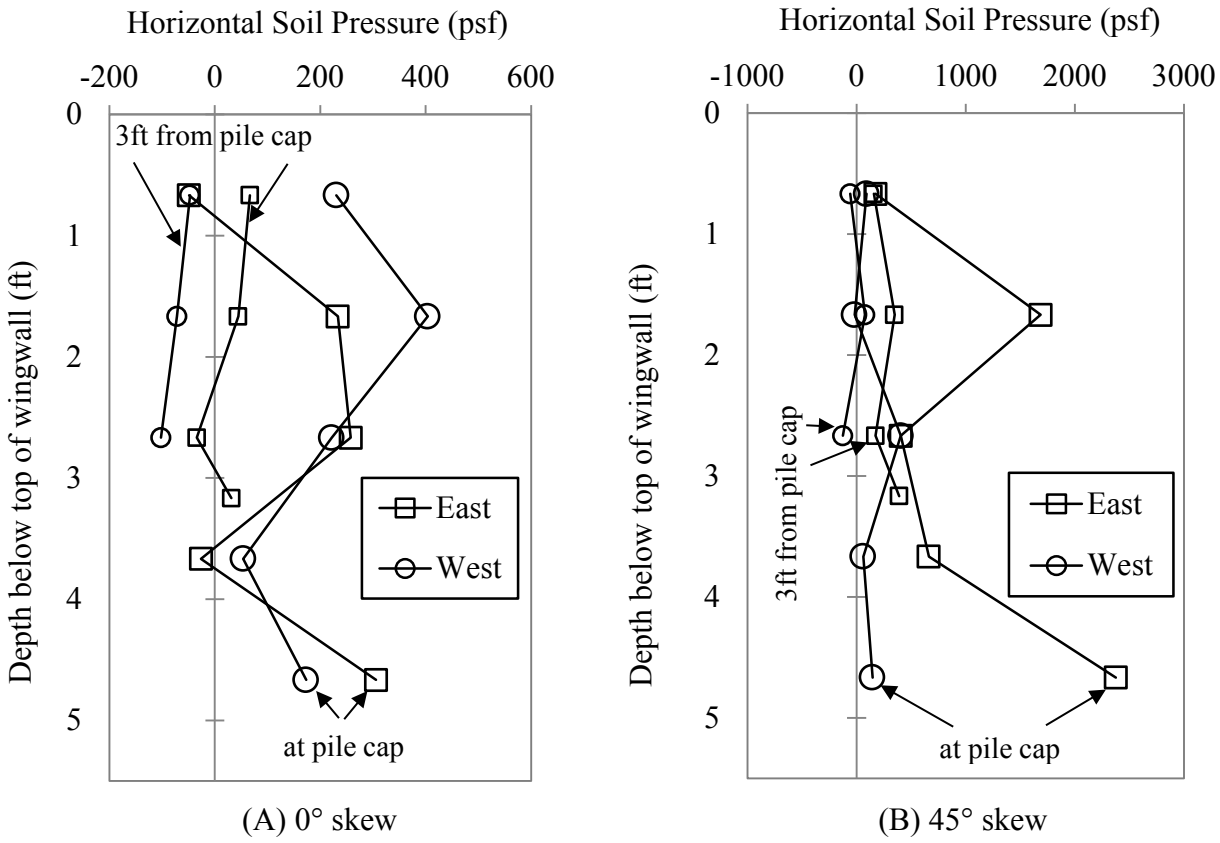

Figure 4.32. Soil pressure distributions on wingwalls at test completion: (A) 0° skew. (B) 45° skew.

A significant increase in normal force was observed on the east wingwall for the 45° skewed abutment at maximum deflection compared to the non-skewed abutment. This increase in normal force was due to increased pressures on the wingwall at the obtuse end of the abutment from 0.3 in (0.76 cm) more deflection than the non-skewed abutment in the westward (transverse) direction. Because frictional resistance is a function of normal force, a significant increase in frictional resistance was provided by the east wingwall (at the obtuse end of abutment) on the 45° skewed abutment compared to the non-skewed abutment. Table 4.5 and Table 4.6 provide values of increased normal force (ΔN) and increased friction (ΔF_f) along the east wingwall (wingwall on obtuse end of abutment) of the 45° skewed abutment, based on strain

gauge and Geokon® pressure cell data. Values for ΔN and ΔF_f were computed using Equations (4-14) and (4-15).

$$\Delta N = Normal\ Force_{45^\circ} - Normal\ Force_{0^\circ} \quad (4\text{-}14)$$

$$\Delta F_f = Friction_{45^\circ} - Friction_{0^\circ} \quad (4\text{-}15)$$

The reduction factors (R_{skew}) shown at the bottom of Table 4.5 and Table 4.6 are the ratio of the peak passive resistance of the 45° skew test, when friction is considered, to the peak passive resistance of the non-skewed test. Reduction factors shown in these tables use actual test data (not hyperbolic approximation) and are computed using Equation (4-16).

$$R_{skew} = \frac{\left(P_{p,skew} - \Delta F_f\right)_{max}}{P_{p,non-skew}} \quad (4\text{-}16)$$

$$P_{p,skew} = Passive\ force\ for\ 45^\circ\ skew$$

$$P_{p,non-skew} = Peak\ passive\ force\ for\ 0^\circ\ skew\ (383\ kips)$$

Data from both strain gauges and pressure cells suggest that friction along the obtuse side wingwall on the 45° skewed abutment contributed 5% of the total passive resistance which raises the reduction factor by 2% ($R_{skew} = 0.41\ to\ R_{skew} = 0.43$).

The soil pressure distributions from Figure 4.32 exhibit very similar patterns to soil pressure distributions obtained by Bozorgzadeh et al. (2008) from lateral load tests on a non-skewed test abutment with reinforced concrete wingwalls in a silty sand backfill. Bozorgzadeh et al. (2008) plotted soil pressure versus depth at the west side and center of the test abutment shown in Figure 4.33 and Figure 4.34. Although soil pressure was measured on the abutment wall (not on wingwalls), the pressure distribution shape closely resembles those for the

Table 4.5. Increased Frictional Resistance on East Wingwall for 45° Skewed Abutment (from strain gauge data)

Deflection in	ΔN kip	ΔF_f kip	Passive - Friction kip
0.00	0.8	0.0	0
0.28	0.6	0.3	60
0.48	0.5	0.2	96
0.72	0.9	0.5	117
1.01	1.7	0.9	133
1.27	4.0	2.1	141
1.51	6.8	3.6	145
1.72	8.0	4.3	144
1.99	9.4	5.0	145
2.23	10.5	5.6	147
2.48	12.0	6.4	150
2.73	14.1	7.5	155
2.93	15.8	8.4	156
	Reduction Factor (R_{skew}) =		**0.41**

Table 4.6. Increased Frictional Resistance on East Wingwall for 45° Skewed Abutment (from Geokon® pressure cell data)

Deflection in	ΔN kip	ΔF_f kip	Passive - Friction kip
0.00	3.3	1.7	0
0.28	13.4	7.1	53
0.48	17.6	9.4	87
0.72	4.3	2.3	115
1.01	17.2	9.2	124
1.27	15.8	8.4	135
1.51	14.4	7.6	141
1.72	10.0	5.3	143
1.99	12.0	6.4	144
2.23	5.4	2.9	149
2.48	14.6	7.8	149
2.73	12.3	6.5	156
2.93	19.4	10.3	155
	Reduction Factor (R_{skew}) =		**0.41**

wingwalls in this study. The position of actuators that applied loading for Figure 4.33 and Figure 4.34 is shown in Figure 4.35. The positioning of the loading apparatus used by Bozorgzadeh et al. (2008) for the large-scale test was different from positioning used for this study; however, it appears that the resultant force acted near mid-height of the abutment backwall for both studies.

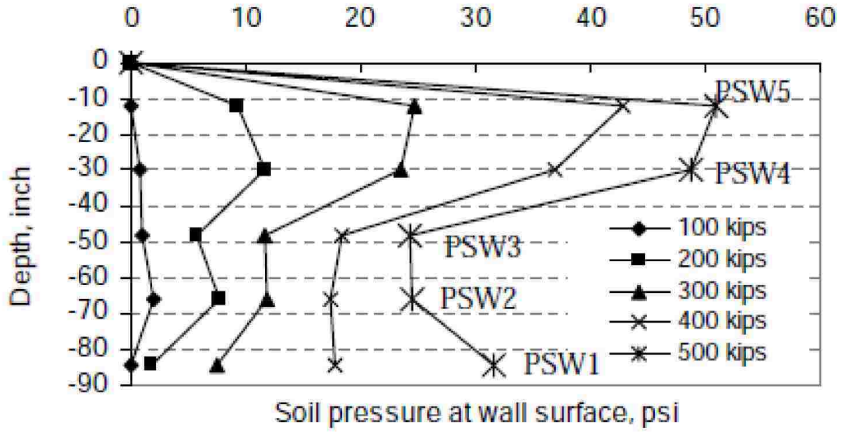

Figure 4.33. Soil pressure at west end of abutment wall versus depth (Bozorgzadeh et al. 2008).

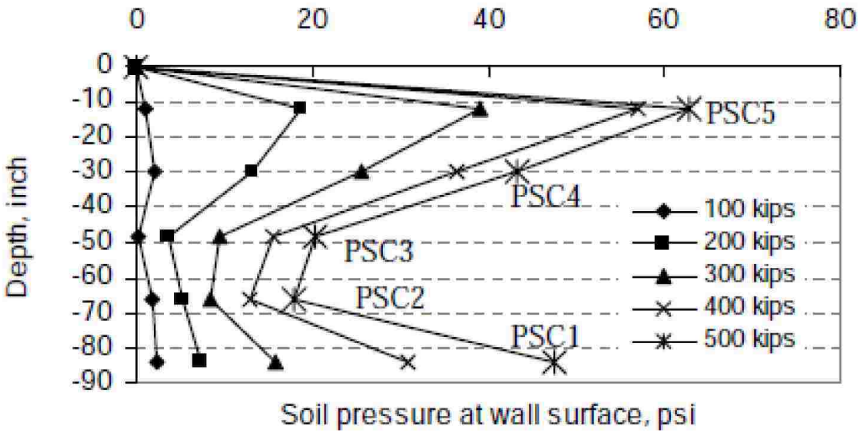

Figure 4.34. Soil pressure at center of abutment wall versus depth (Bozorgzadeh et al. 2008).

Figure 4.35. Position of applied load (Bozorgzadeh et al. 2008).

Wingwall normal forces were also computed based on measurements from Geokon® pressure cells shown in Figure 4.36. Pressures were applied to the tributary areas shown in Figure 4.36 to compute the total normal force acting on the wingwalls. The lower pressure cell on the west wingwall did not record pressure measurements; therefore, the pressure measured from the upper pressure cell was applied to the entire wingwall area in contact with the soil for the west wingwall. For the zero skew test, the pressure cells suggest normal forces of 23 kips (103 kN) and 12 kips (54 kN) on east and west wingwalls, respectively, at maximum

longitudinal deflection. For the 45° skew test, normal forces of 35 kips (157 kN) and 13 kips (58 kN) were estimated for east and west wingwalls, respectively.

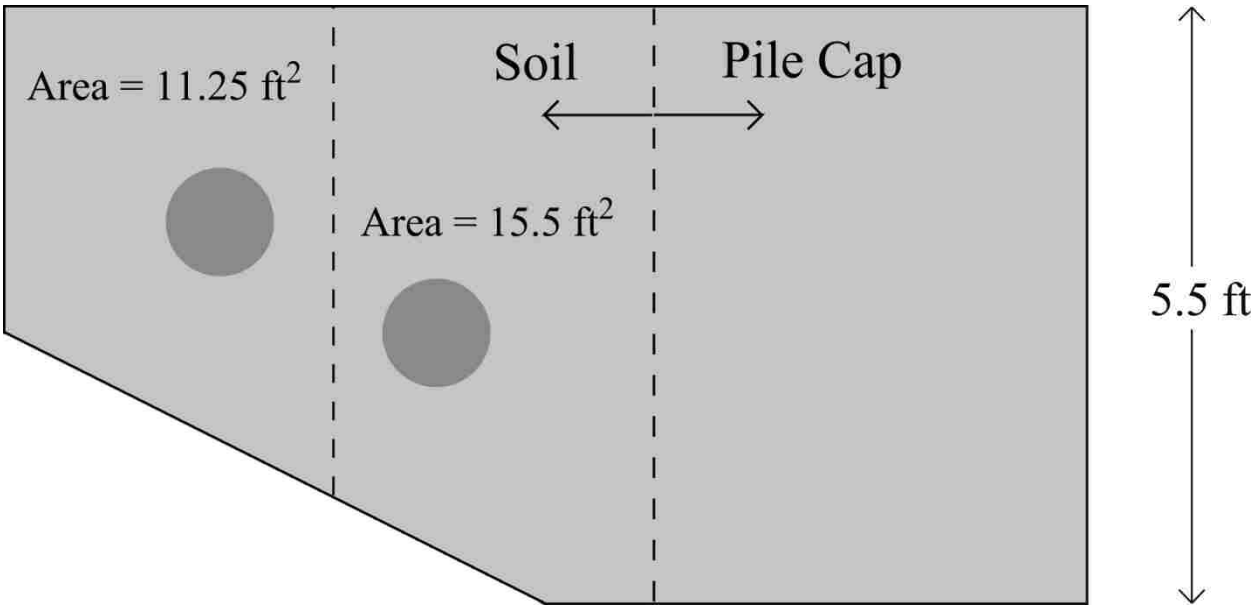

Figure 4.36. Pressure cells on wingwalls with respective tributary areas.

Forces that developed on the east wingwall on the 45° skewed abutment were the largest relative to all other wingwall forces. This is likely due to the larger westward movement of the abutment during the 45° skew test. The north end of the 45° skewed abutment, closest to the wingwalls, moved approximately 0.4 inches (1.0 cm) in the westward direction compared to 0.1 inches (0.25 cm) for the non-skewed abutment, which explains the higher passive forces measured on the east wingwall on the 45° skewed abutment.

An analysis was done for the east wingwall (45° skew) to determine the reliability of estimating the passive force development on the wingwall using the abutment backwall passive force-deflection curves. Passive force-deflection curves for non-skewed and 45° skewed abutments were both used for comparison.

For this analysis, the wingwall was divided into three 2-ft (0.61-m) wide segments, shown in Figure 4.37. Average deflections in the westward direction (into the backfill) were computed for each segment as the difference between the total abutment movement in the westward direction [0.4 inches (1.0 cm) at the north end] and the deflection at each segment in the eastward direction (see Figure 4.23). Wingwall deflection was computed in this fashion to more accurately represent the actual pressure distribution along the length of the wingwall (see Figure 4.30). Higher pressures were measured near the pile cap with lower pressures near the tapered end. The net deflections into the backfill (Δ) for each wingwall segment are shown in Figure 4.37. An average height (H_{av}) was calculated for each segment and was used to compute the ratio of deflection to wall height Δ/H_{av}, also shown in Figure 4.37.

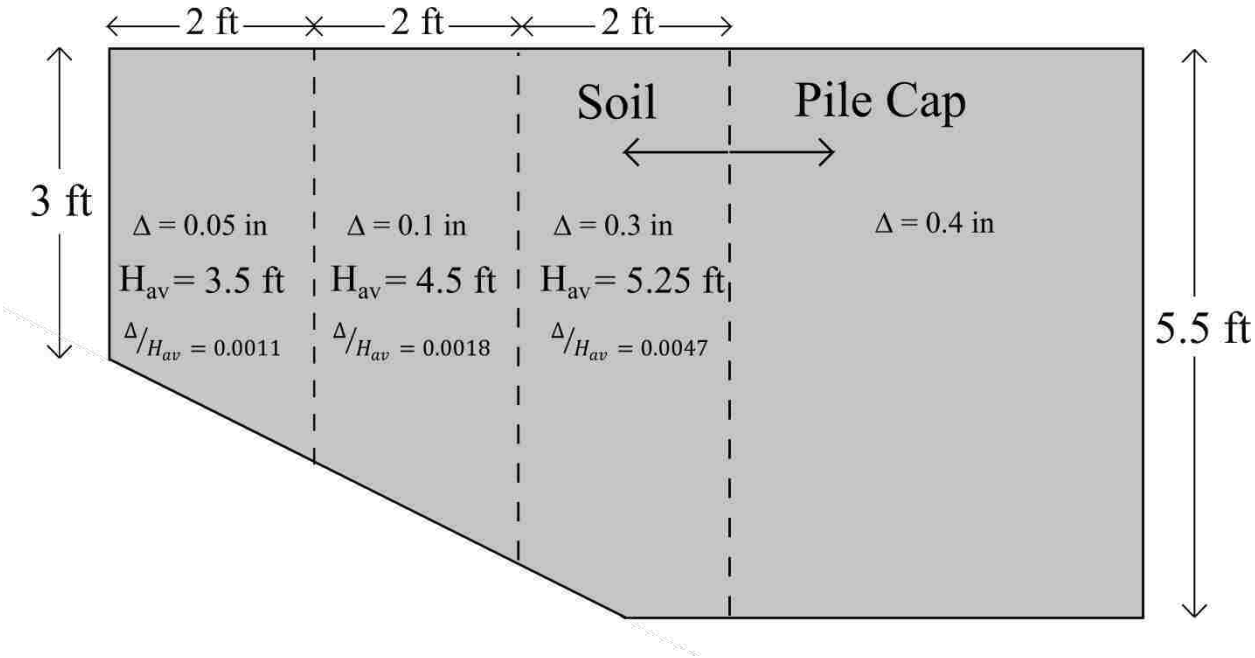

Figure 4.37. Contact area between soil and wingwall divided into three segments.

Values of Δ/H_{av} were plotted with the normalized passive force-deflection curves in Figure 4.38 to estimate the percentage of passive force that developed on the wingwall. The normalized passive force-deflection curves in Figure 4.38 are based on the hyperbolic approximations of passive force development. The peak passive force per unit width for both non-skewed and 45° skewed tests are shown near their respective curves.

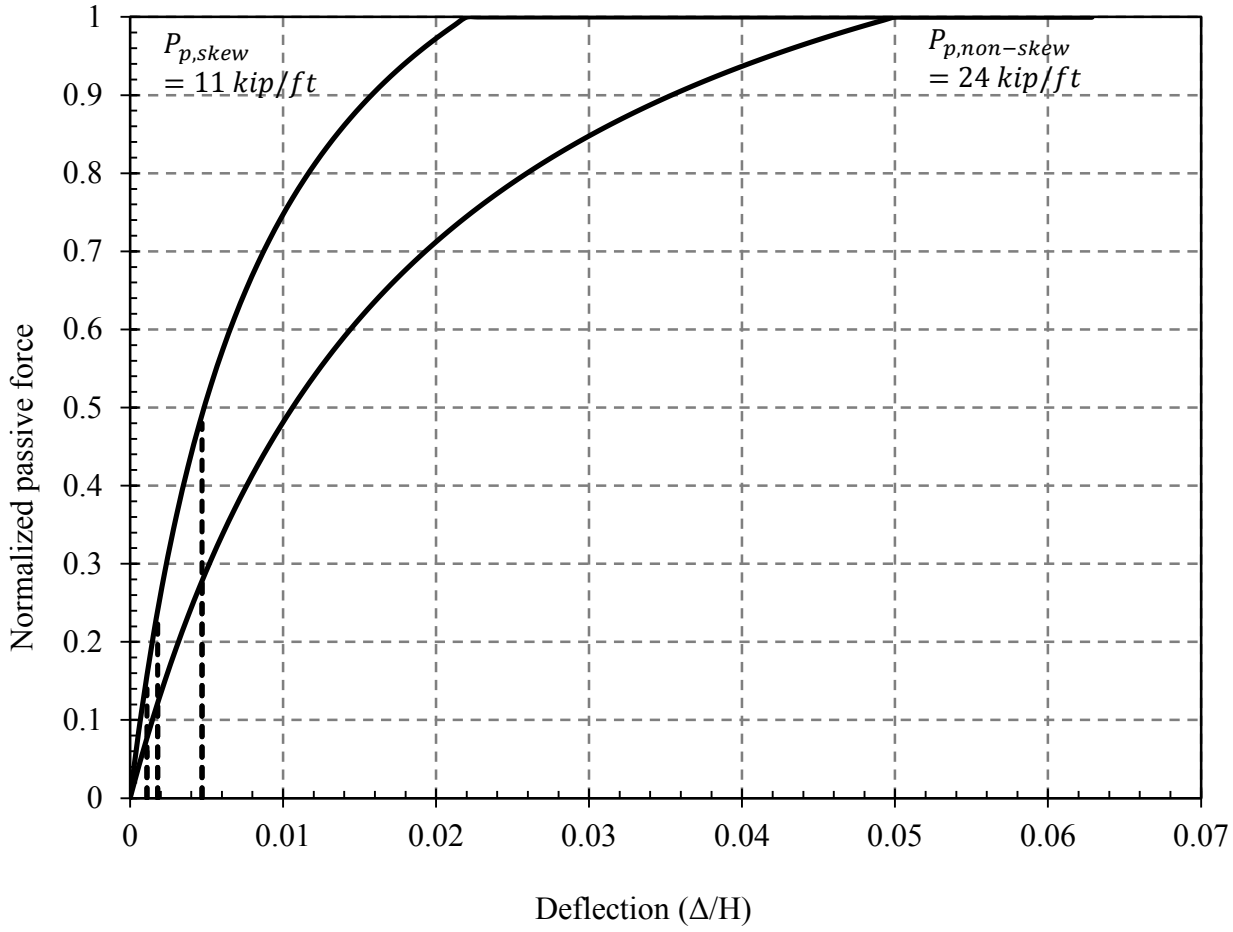

Figure 4.38. Normalized passive force versus deflection-height ratio (Δ/H).

The passive force distribution from this analysis is illustrated in Figure 4.39, which provided passive forces based on both non-skewed and 45° skewed passive force-deflection

curves. The total passive force acting on the wingwall was computed as the sum of the forces from the three segments.

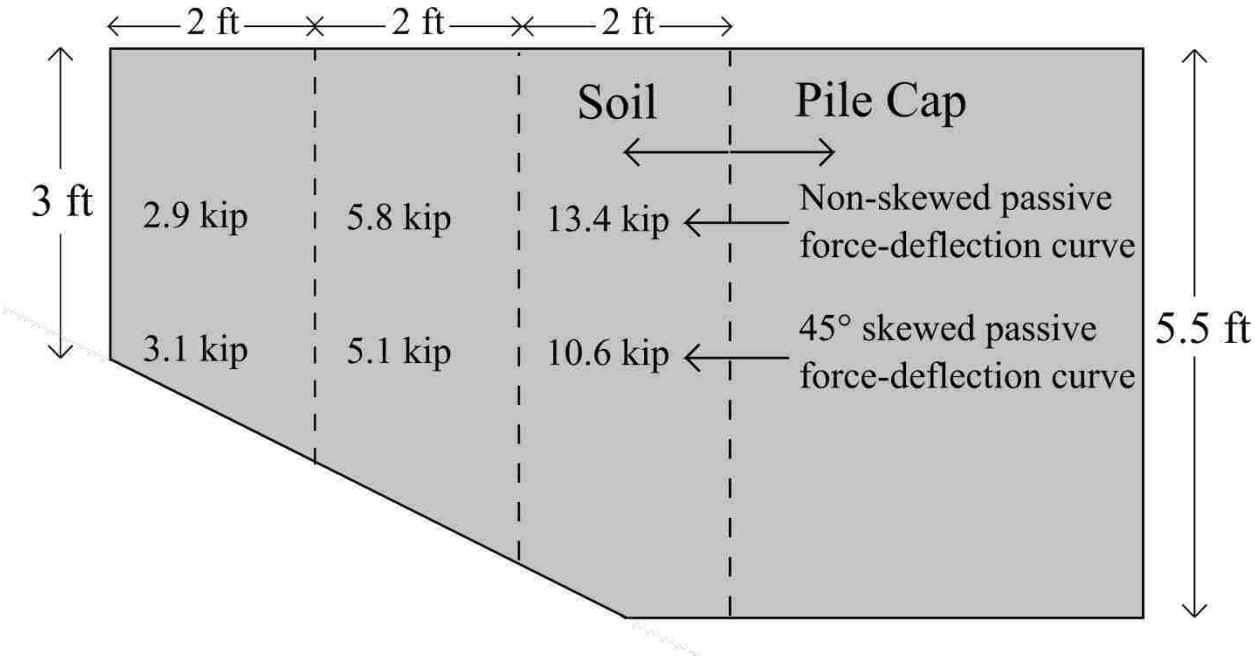

Figure 4.39. Passive force distribution along wingwall segments.

Using the 45° skew passive force-deflection curve, the total estimated passive force on the east wingwall (45° skew) was 19 kips (85 kN), which is within 1% of the computed passive force from the strain gauge measurements [19 kips (85 kN)]. Using the non-skewed passive force-deflection curve, a total passive force of 22 kips (99 kN) was estimated, which overestimates the passive force from strain gauge measurements by 16%. Total passive forces from this analysis underestimate the passive forces obtained from the Geokon® pressure cells [35 kips (157 kN)] by 46% when using the 45° skew passive force-deflection curve, and by 37% when using the non-skewed passive force-deflection curve. This analysis largely confirms measurements from strain gauges and suggests that the passive force acting normal to the

wingwall may be reasonably estimated from the design passive force-deflection curve for the abutment backwall and the anticipated transverse wingwall deflection.

4.6.2 Lateral Earth Pressure Coefficients

Lateral earth pressure coefficients (k) at the soil-wingwall interface were calculated using Equation (4-17).

$$k = \frac{\sigma_h'}{\sigma_{vo}'} \tag{4-17}$$

Plots of the lateral earth pressure coefficients (based on strain gauge data) with depth are shown in Figure 4.40 for the non-skewed and 45° skewed abutments. The majority of k values at the soil-wingwall interface for the non-skewed abutment are less than 1.0, suggesting at-rest conditions. On the 45° skewed abutment, however, the east (obtuse) wingwall is clearly experiencing higher lateral earth pressures with k values as high as 8.6 near the pile cap at a 20-in (50.8-cm) depth. The lateral pressures on the west (acute) wingwall are similar to the non-skewed case.

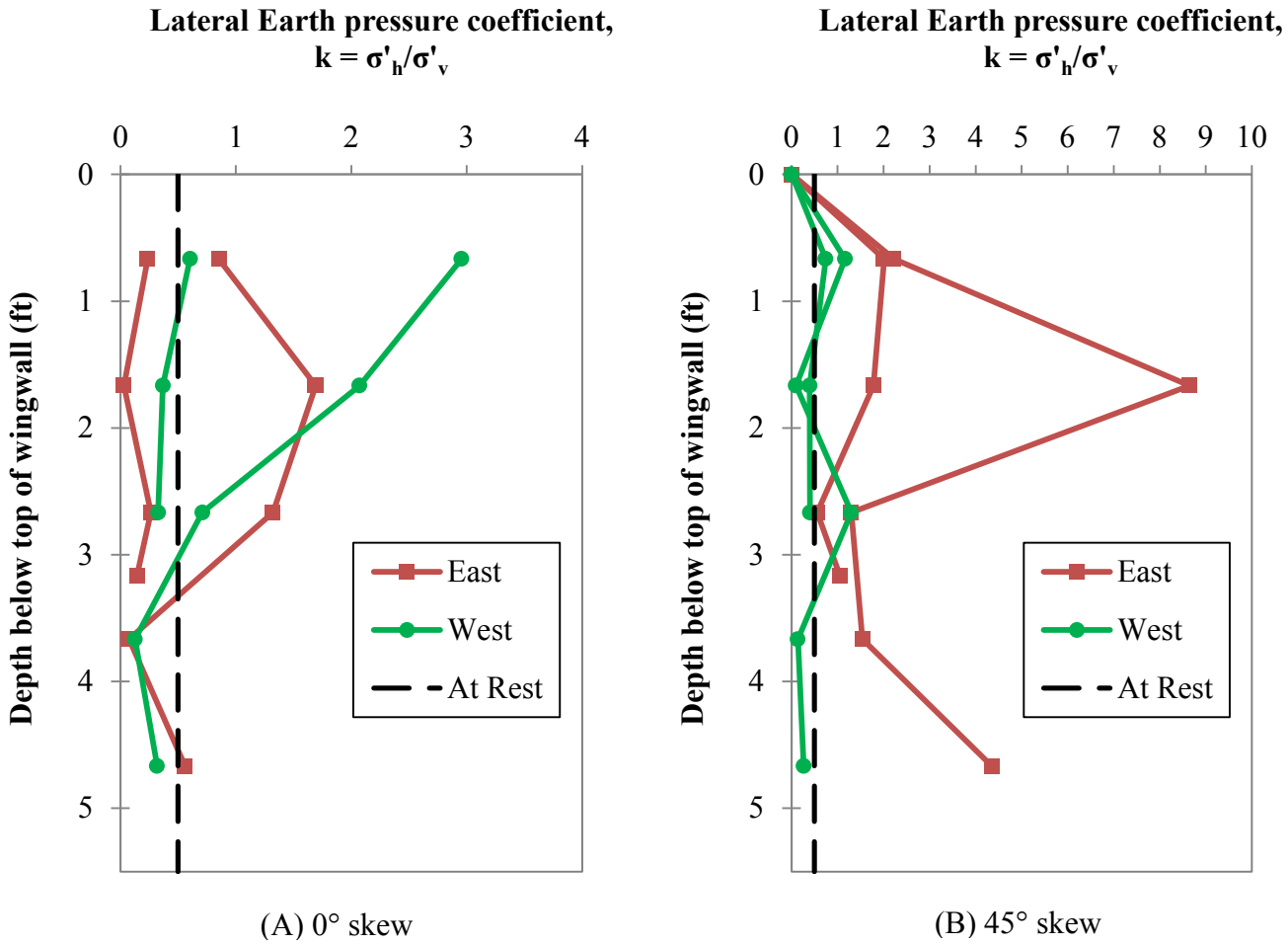

Figure 4.40. Lateral earth pressure coefficients with depth along wingwalls based on strain gauge data for (A) 0° skew test and (B) 45° skew test

Lateral earth pressure coefficients based on pressure cell measurements are shown in Figure 4.41 and show relatively good agreement with coefficients in Figure 4.40.

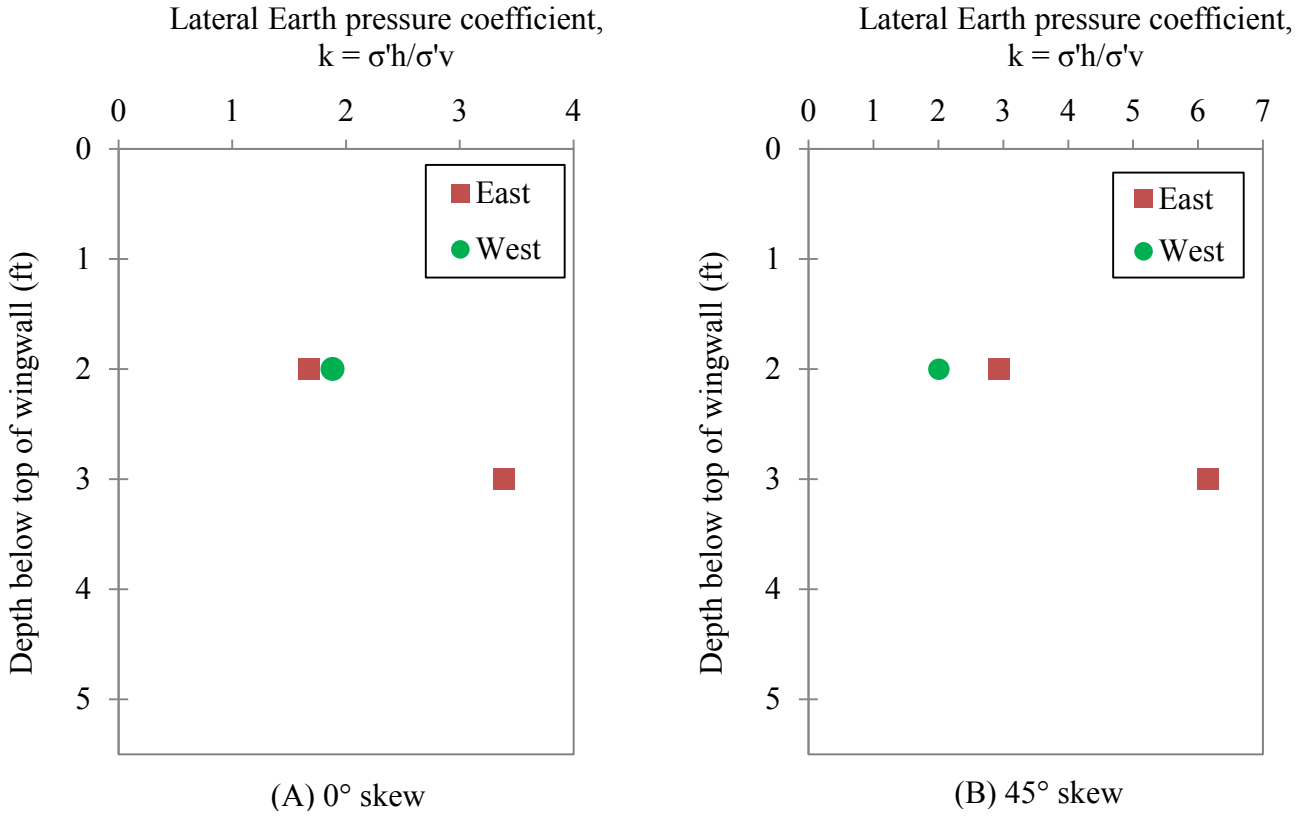

Figure 4.41. Lateral Earth pressure coefficient with depth along wingwalls based on pressure cell data for (A) 0° skew test and (B) 45° skew test.

4.7 Pile Deflection with Depth

Longitudinal deflection of the north center pile with depth is plotted for non-skewed and 45° skewed abutments at maximum longitudinal deflection in Figure 4.42 and Figure 4.43. Data are plotted from the north shape array, inclinometer, and average string potentiometer measurements at top and bottom of the pile cap. In general, deflection measurements from the three instrumentation systems were in good agreement.

The percent difference between the inclinometer and shape array profiles from the top of the cap to a depth of 15 ft (4.6 m) ranges between 0.3 and 7.0% with an average of 2.5% for the

0° skew test and 0.2% and 4.6% with an average of 1.9% for the 45° skew. The displacements below a depth of 15 ft (4.6 m) are very small and the error values in this zone are less than 0.02 inch and not particularly meaningful.

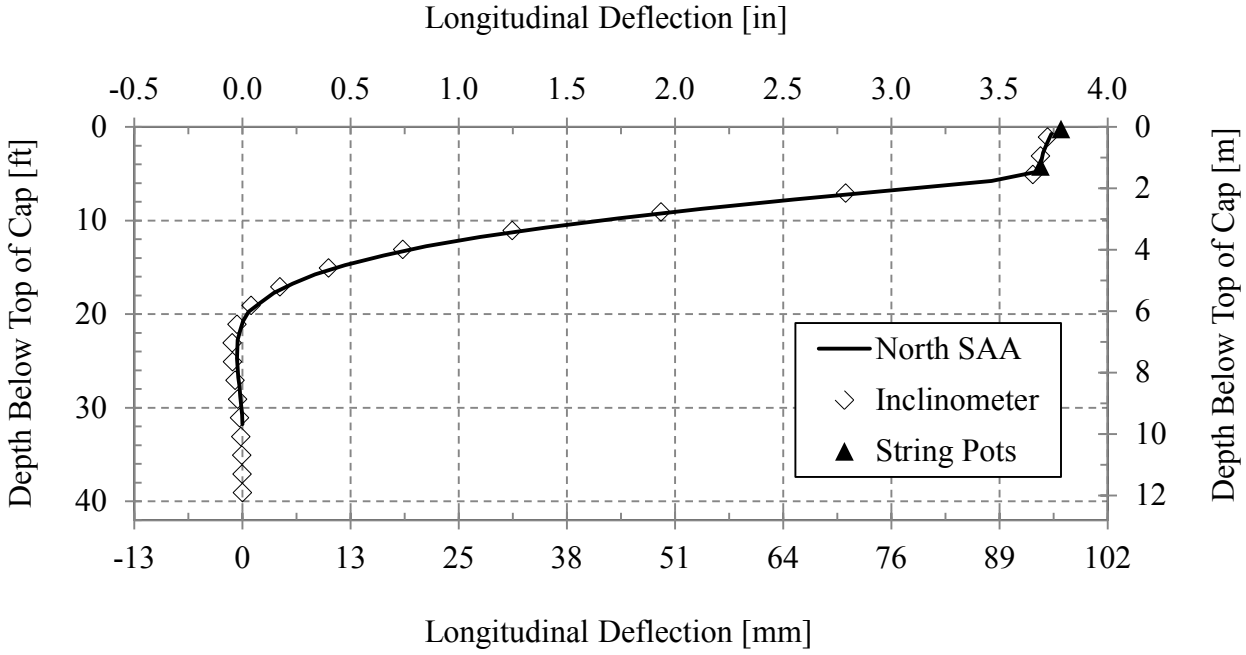

Figure 4.42. Longitudinal pile deflection with depth for non-skewed abutment at test completion.

The measurements indicate a relatively linear deflection profile within the pile cap. Below the base of the cap, the piles deflect in a non-linear fashion with the deflections reaching a point of counterflexture at depth of approximately 21 ft (6.3 m) and a point of fixity at about 31 ft (9.45 m). Agreement between the north and south inclinometers was generally very good. Transverse deflection versus depth profiles for the pile cap, recorded by shape array and inclinometer, are also plotted in Figure 4.44 and Figure 4.45. Plotted on a smaller scale, the percent error seems larger than the longitudinal error although the magnitude difference is small.

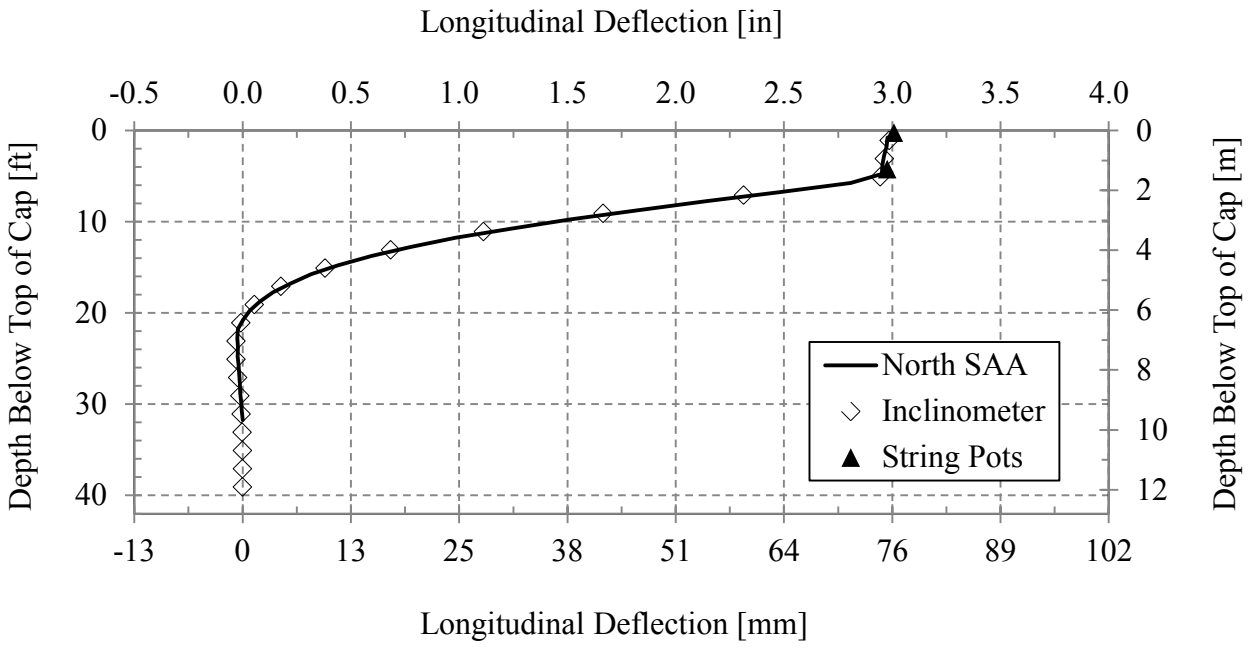

Figure 4.43. Longitudinal pile deflection with depth for 45° skewed abutment at test completion.

However, as observed for the deflections below 20 ft (6 m) in the longitudinal test, the percent difference is exaggerated due to the smaller scale. The percent difference is within the error thresholds of each instrument (±1.5 mm/30 m for shape array, and ±1.24 mm/30m for inclinometer (Rollins et al. 2009). Results are similar for the tests at other skew angles. Once again, the shape of the deflection profile indicates essentially linear deflection in the pile cap and very small rotations. The deflection in the piles is non-linear and decreases to zero at a deflection of about 20 ft (6 m). For the non-skewed test, the readings throughout the depth of the shape array are likely due to the small transverse movement and the inaccuracy of the instrument under small deflections.

Although the inclinometer readings were only taken at the maximum deflection for each load test, shape array profiles in the longitudinal and transverse directions were obtained at each deflection increment (0.25 in) for both tests. Figure 4.46 and Figure 4.47 show profiles of

longitudinal deflection with depth for each deflection increment. As the deflection level increases the deflection of the pile cap remains linear but the rotation progressively increases while the depth to the point of fixity increases. Similar curves were obtained in the transverse direction. At smaller deflection levels there are some variations associated with the small measurement errors; however at larger deflections, the data was accurate and useful in visualizing the pile movement.

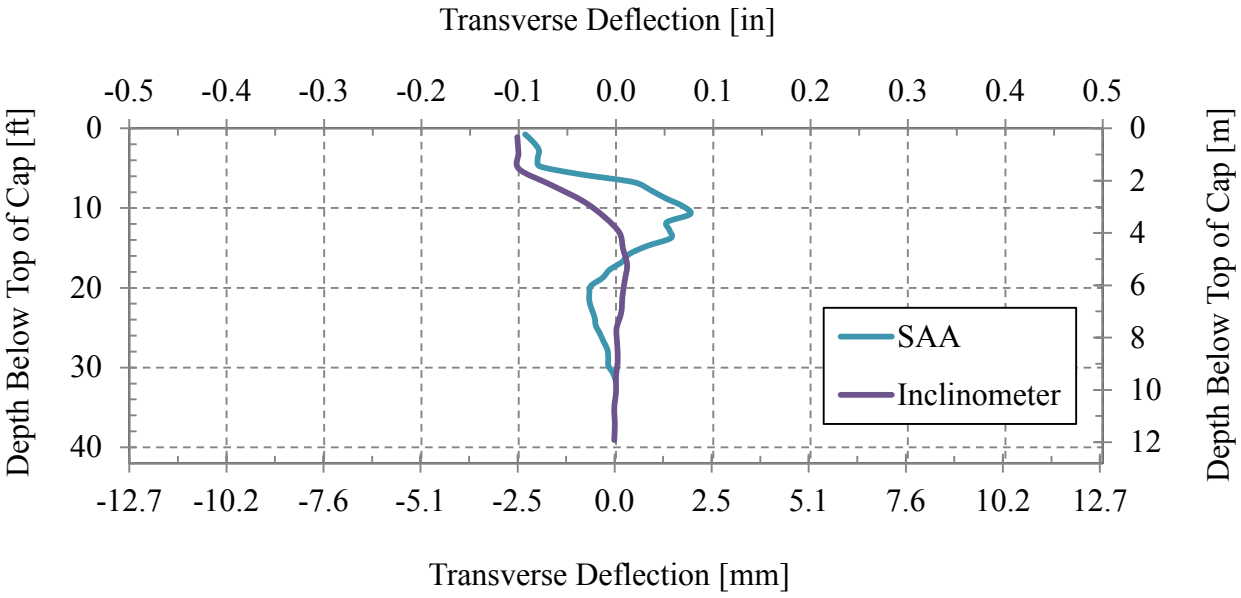

Figure 4.44. Transverse pile deflection with depth for non-skewed abutment at test completion.

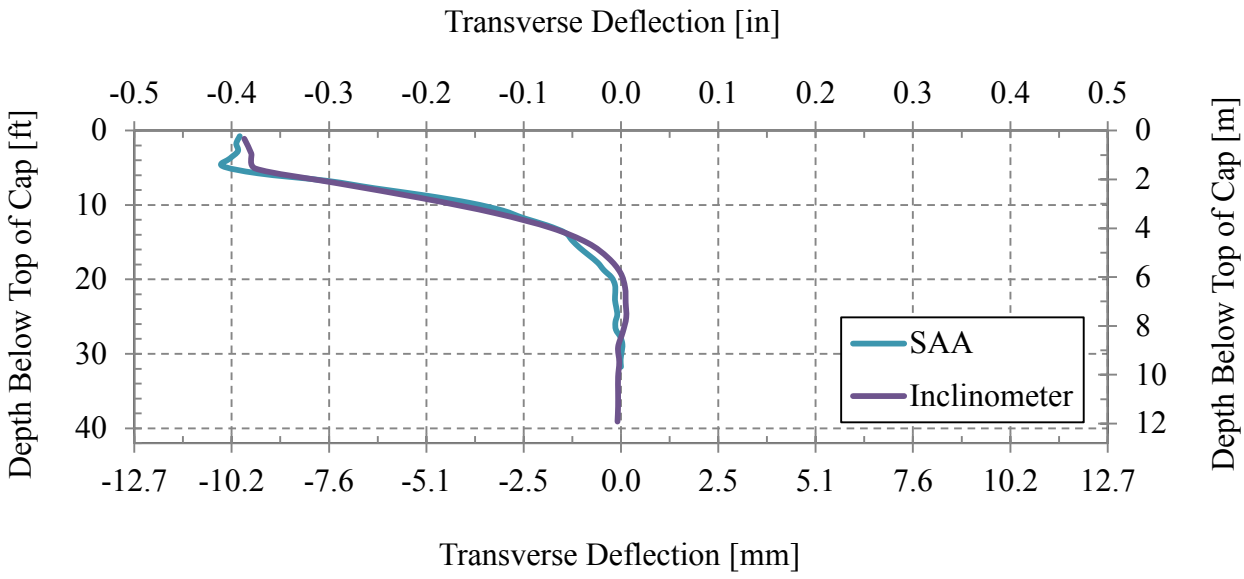

Figure 4.45. Transverse pile deflection with depth for 45° skewed abutment at test completion.

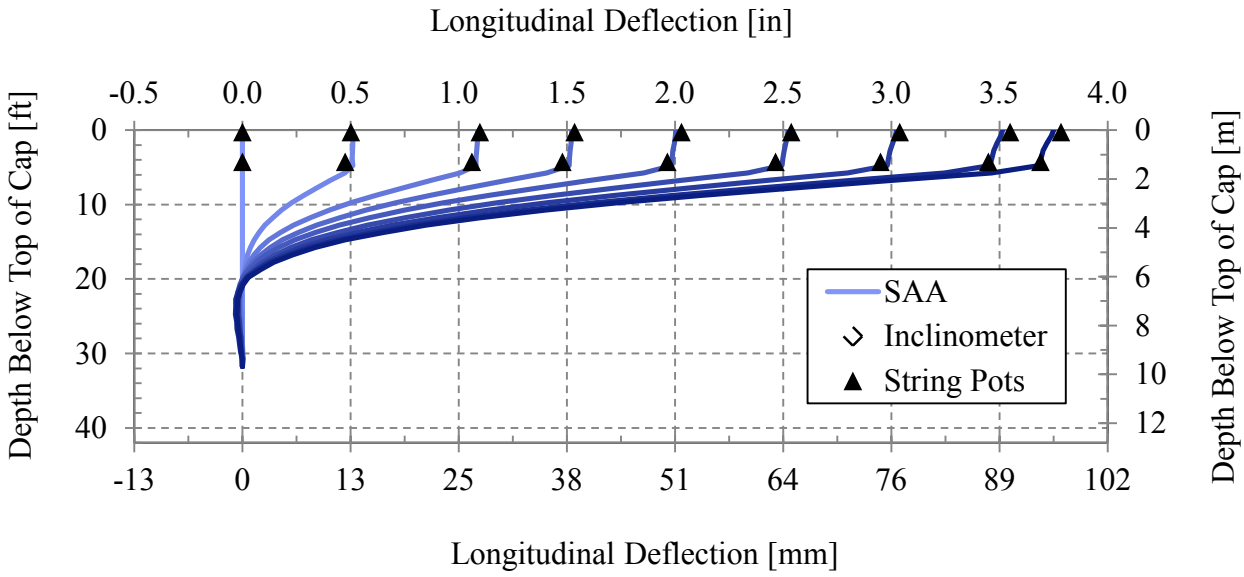

Figure 4.46. Incremental longitudinal pile deflection with depth for non-skewed abutment.

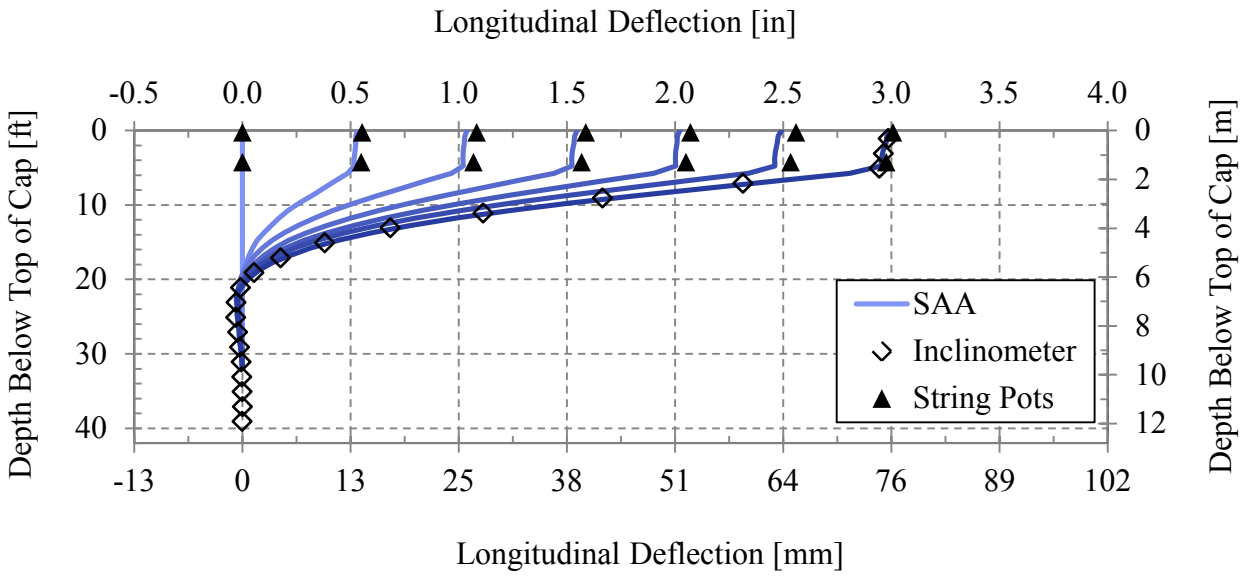

Figure 4.47. Incremental longitudinal pile deflection with depth for 45° skewed abutment.

4.8 Pressure Distribution Across the Backwall

Pressure was measured by Geokon® pressure cells at six locations across the width of the 45° skewed abutment backwall. These pressure cells were centered 22.5 in (57 cm) or a third of the backwall height (0.33H) from the base of the pile cap. Measurements from the pressure cells are shown in Figure 4.48.

Pressure measurements across the backwall are consistent with previous large-scale tests; however, these results are inconsistent with field observations by Shamsabadi et al. (2006) who observed that skewed abutments typically rotate such that the obtuse side of the abutment is pushed into the backfill more than the acute side. The high pressures at the acute end are likely caused by end effects. Figure 4.48 indicates that after deflections of 1.5 inches (3.8 cm) the pressure increased significantly more on the east side compared to the west side, which is in good agreement with the pressure build up measured on the east wingwall.

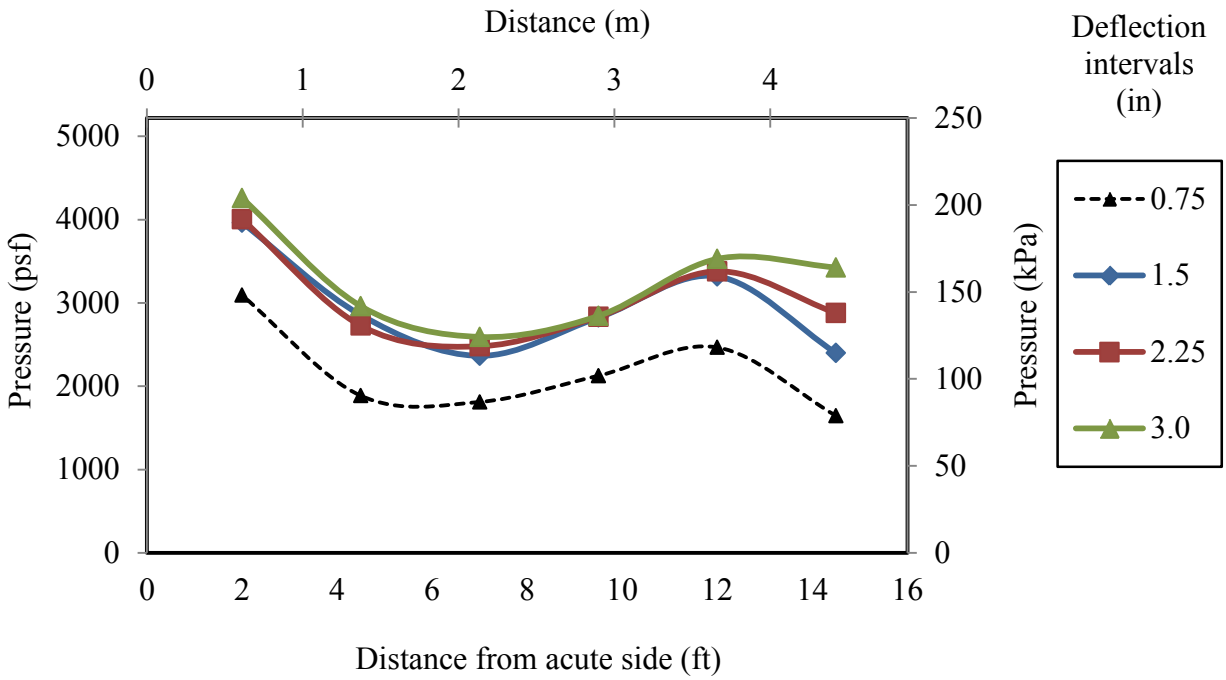

Figure 4.48. Pressure distribution across 45° skewed abutment.

5 ANALYSIS OF PASSIVE FORCE-DEFLECTION RESULTS

5.1 Comparison of Passive Earth Pressure Predictions

Passive earth pressure coefficients (K_p) were computed in PYCAP (Duncan and Mokwa 2001) using Rankine, Coulomb, and log spiral methods. For the log spiral method K_p is separated into $K_{p\varphi}$ and K_{pc} to differentiate passive resistance contributed by friction angle (φ) and by cohesion (c). Peak passive resistance (P_p) in this section represents the peak passive force in the horizontal direction only and is calculated using Equations (5-1) and (5-2).

$$P_p = P_{p,ult}\cos(\delta) \tag{5-1}$$

where,

$$P_{p,ult} = \left(\frac{1}{2}K_P\gamma H^2 + 2\sqrt{K_P}cH\right)W \tag{5-2}$$

$H = 5.5\ ft\ (abutment\ backwall\ height)$

$W = 13\ ft\ (abutment\ width)$

$c = 100\ psf\ (cohesion)$

$\varphi = 40°\ (friction\ angle)$

$\delta = 28°\ (wall\ friction)$, where $\frac{\delta}{\varphi} = 0.70$

$\gamma = 116.0\ pcf\ (moist\ unit\ weight\ of\ soil)$

The 13-ft (4.0-m) abutment width includes the 1-ft (0.305-m) width of the wingwalls on either side of the 11-ft (3.3-m) wide pile cap. This assumes that passive pressure develops on the projected height of the wingwalls with no reduction due to the taper in the wingwall height.

Values for K_p from the Rankine and Coulomb theories and $K_{p\varphi}$ and K_{pc} from the Log Spiral method are listed in Table 5.1. As expected, the Rankine K_p value is much lower than the Coulomb K_p value and the Log Spiral $K_{p\varphi}$ value is in between the value computed by Rankine and Coulomb methods.

Table 5.1. Comparison of Lateral Earth Pressure Coefficients (K_p)

	Rankine	Coulomb	Log Spiral
K_p	4.60	20.88	-
$K_{p\varphi}$	-	-	12.84
K_{pc}	-	-	5.00

The peak passive force (P_p) was initially computed using the Rankine, Coulomb and Log Spiral methods with a width of 13 ft (4.0 m), neglecting any 3D width corrections. In addition, the Log Spiral method was used to compute P_p with the Brinch-Hansen (1966) 3D correction factor to increase the effective width of the abutment. Predictions for peak passive force are compared with peak passive forces from the non-skewed and 45° skewed test data (which may be unreliable at large deflections due to unreliable baseline curve) in Table 5.2 and Table 5.3. Peak passive force predictions are also compared with the log spiral hyperbolic approximations in Table 5.4 and Table 5.5, which may more accurately represent the soil behavior. The Rankine,

Coulomb, and Log Spiral methods do not account for a reduction in P_p due to skew angle; consequently, all three methods predict the same value for P_p regardless of skew angle.

Table 5.2. Non-skewed Peak Passive Force (P_p) Predictions Compared With Test Data

	Test Data (Non-skew)	Rankine	Coulomb	Log Spiral	Log Spiral with Brinch-Hansen 3D effects
P_p (kip)	**383**	120	474	322	539
Error	-	-69%	+24%	-16%	+41%

Table 5.3. 45° Skewed Peak Passive Force (P_p) Predictions Compared With Test Data

	Test Data (45° skew)	Rankine	Coulomb	Log Spiral	Log Spiral with Brinch-Hansen 3D effects
P_p (kip)	**165**	120	474	322	539
Error	-	-27%	+187%	+95%	+227%

For the non-skewed abutment, the Log Spiral method without the 3D correction factor provided the most accurate peak passive force prediction, underestimating the actual value by 16%. However, using the 3D correction factor led to a 41% overestimate of the resistance. For the 45° skewed abutment, the low estimate from the Rankine method most accurately predicted the peak passive force with an error of -27%.

The accuracy of the peak passive force predictions, based on the same methods, compared with the hyperbolic approximation of the peak passive force is presented in Table 5.4 and Table 5.5. Because the hyperbolic approximation of the peak passive force is computed using the log spiral method, there is 0% error for the non-skewed test.

Table 5.4. Non-skewed Peak Passive Force (P_p) Predictions Compared With Hyperbolic Approximation

	Hyperbolic Approximation (Non-skew)	Rankine	Coulomb	Log Spiral	Log Spiral with Brinch-Hansen 3D effects
P_p (kip)	**322**	120	474	322	539
Error	-	-63%	+47%	0%	+67%

Table 5.5. 45° Skewed Peak Passive Force (P_p) Predictions Compared With Hyperbolic Approximation

	Hyperbolic Approximation (45° skew)	Rankine	Coulomb	Log Spiral	Log Spiral with Brinch-Hansen 3D effects
P_p (kip)	**148**	120	474	322	539
Error	-	-19%	+220%	+118%	+264%

If the passive force-deflection curve is modeled as a hyperbola, the Rankine value for peak passive force is the most accurate for the 45° skewed abutment with an error of only -19%.

5.2 Caltrans and AASHTO Design

The measured passive force-deflection curves and the hyperbolic approximations are compared with the Caltrans design curves in Figure 5.1 and the AASTHO design curves in Figure 5.2 and Figure 5.3. Parameters used for Caltrans and AASHTO design methods are listed in Table 5.6 and Table 5.7. Caltrans parameters were computed using Equations (2-2), (2-3), (2-4), and (2-5). The backfill material, which is granular with low fines content, meets Caltrans standards for a stiffness of 50 kip/in; however, curves are presented for both stiffness values for comparison.

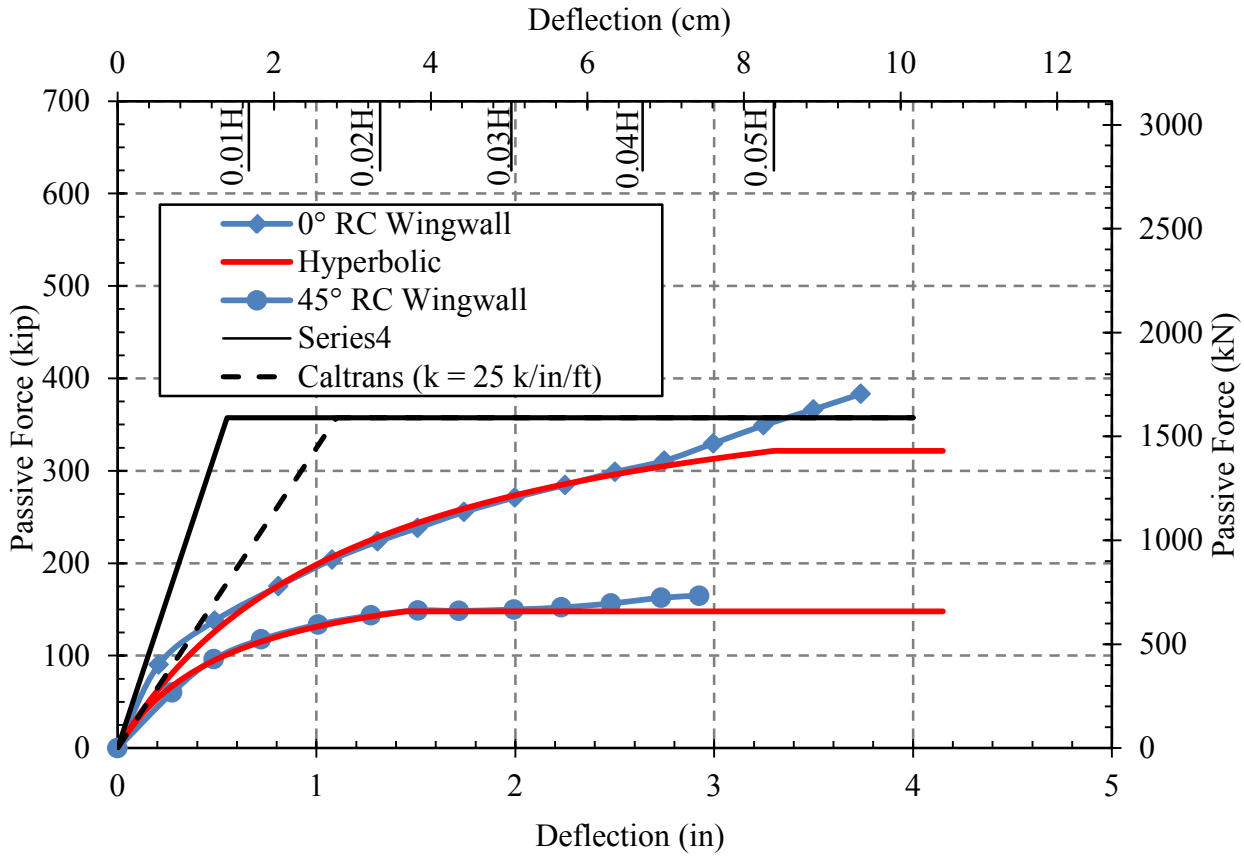

Figure 5.1. Caltrans design curves compared with test data and hyperbolic approximations.

Figure 5.1 illustrates the inadequacy of the current Caltrans design method to accurately predict the passive force-deflection relationship for either the non-skewed or 45° skewed abutments with RC wingwalls. The Caltrans design method overestimates the passive resistance for the non-skewed abutment from $0\ in < \Delta < 3.25\ in$ ($0\ cm < \Delta < 8.3\ cm$, with values passive resistance values that are 2.7 times the actual resistance at displacement of $\Delta =$ $0.5\ in$ ($1.27\ cm$). Even with the lower stiffness value, the agreement is relatively poor until large displacements. Despite excessively high passive force measurements at intermediate deflection values, the design peak passive force proposed by Caltrans is within 11% of the hyperbolic

approximation and 7% of the measured peak. In comparison with the curves for the 45º skewed abutment the predicted curves are even more unconservative.

For the AASHTO design curves P_{ult} was computed in accordance with design guidelines in section 3.11.5.4—Passive Lateral Earth Pressure Coefficient, k_p (p. 3-105) of *AASHTO LRFD Bridge Design Specifications* (2010). Figure 3.11.5.4-2 was employed to graphically estimate $k_p \approx 17$. A reduction factor $(R = 0.783)$ obtained from a ratio of $-\frac{\delta}{\varphi} = -0.7$ was applied to the value of k_p estimated from Figure 3.11.5.4-2 to result in $Rk_p = 13.3$. AASHTO recommends a $\frac{\Delta_{max}}{H}$ value between 0.01 and 0.05 for dense granular backfill (section C3.11.5.4, AASHTO 2010). AASHTO design curves with $\frac{\Delta_{max}}{H}$ ranging from 0.01 to 0.05 are compared with test data and hyperbolic approximations in Figure 5.2. Values of $\frac{\Delta_{max}}{H}$ equal to 0.03 and 0.04 provided the best match and are more clearly shown in Figure 5.3.

The AASTHO design curves with $\frac{\Delta_{max}}{H}$ equal to 0.03 and 0.04 provide a more accurate passive force-deflection relationship compared with the Caltrans method for this study. The curve with $\frac{\Delta_{max}}{H} = 0.03$ slightly overestimates the passive resistance at a deflection of 2 inches where it rises above the measured curve, while the curve with $\frac{\Delta_{max}}{H} = 0.04$ provides more of a lower bound estimate of passive force as it generally predicts lower passive forces at all deflections. The peak passive force proposed by AASHTO underestimates the hyperbolic peak passive force by only 4.5%. The measured peak passive force is underestimated 20%. Like the Caltrans design curves, AASHTO design curves are also very unconservative for a 45° skewed abutment, overestimating the passive resistance by more than double at large deflections.

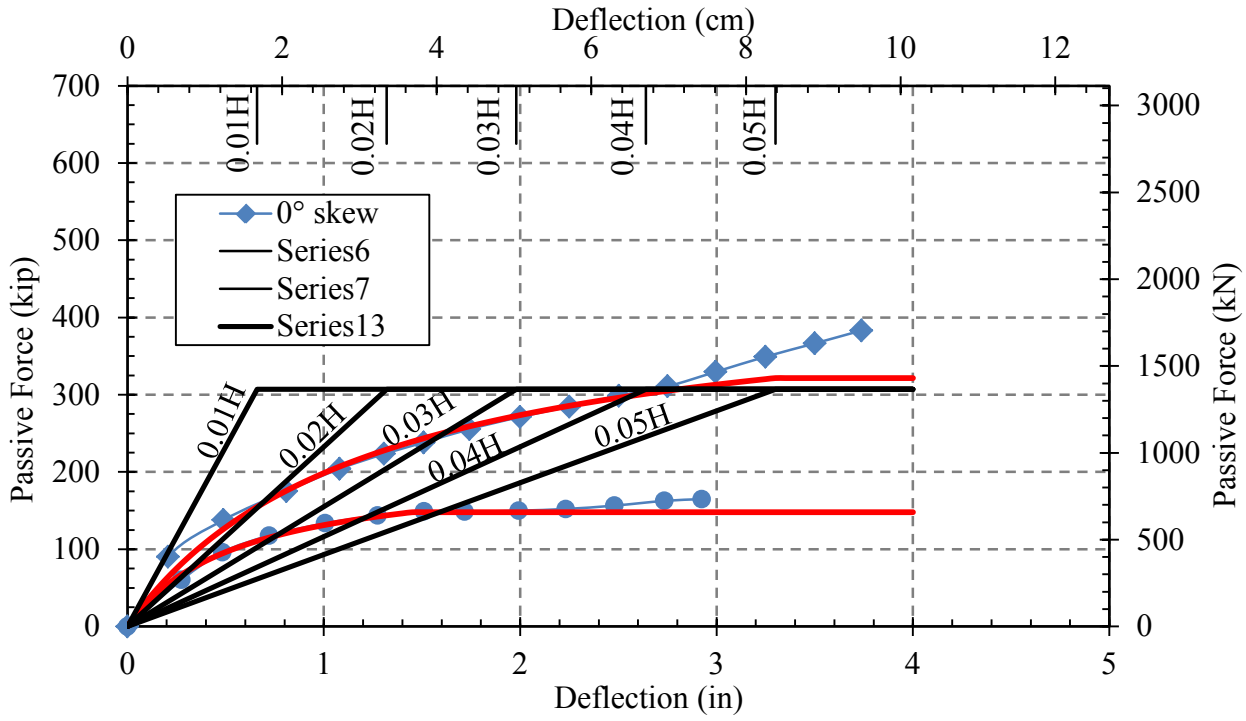

Figure 5.2. AASHTO design curves compared with test data and hyperbolic approximations.

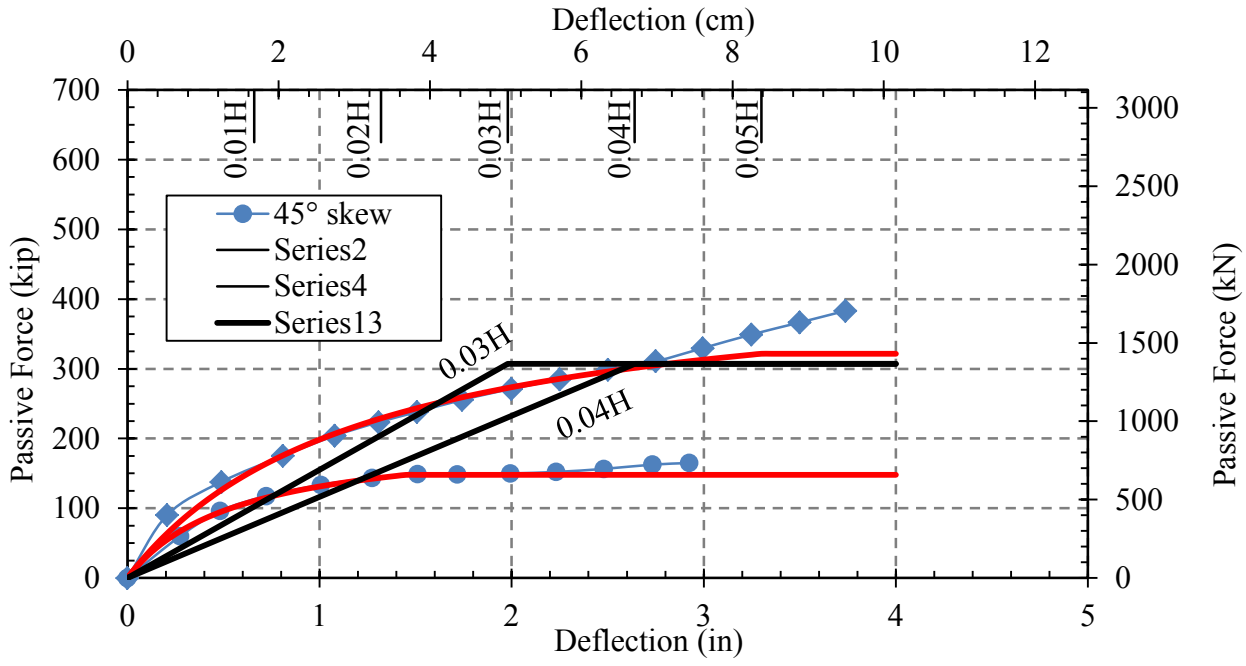

Figure 5.3. Best-fit AASHTO design curves (0.03H and 0.04H)

Table 5.6. Caltrans Design Parameters

Meet Specifications	H ft	W ft	K_i kip/in/ft	K_{abut} kip/in	A_e ft^2	P_{ult} kip
Yes	5.5	13.0	50.0	650.0	71.5	357.5
No	5.5	13.0	25.0	325.0	71.5	357.5

Table 5.7. AASHTO Design Parameters

Trial	Δ_{max}/H	Δ_{max} in	P_{ult} kip
1	0.01	0.66	307
2	0.02	1.3	307
3	0.03	1.98	307
4	0.04	2.64	307
5	0.05	3.3	307

The hyperbolic design curves are further explored in Chapter 6 where PYCAP analysis results are presented.

6 COMPARISON WITH DIFFERENT ABUTMENT GEOMETRIES

In this chapter, passive force-deflection curves for reinforced concrete wingwall abutments are compared with curves for similar large-scale tests involving MSE wingwalls and unconfined backfill geometries. The non-skewed tests with MSE wingwall and unconfined geometries were performed by Brigham Young University in 2012 (Franke 2013; Marsh 2013). All 45° skewed tests were conducted in 2013 as part of the test series for this study. The skew reduction factor results are also compared. Finally, comparisons are made between measured and computed passive force-deflection relationships using the computer program PYCAP (Duncan and Mokwa, 2001).

6.1 Total Passive Force Comparison

Total passive force-deflection curves for non-skewed and 45° skewed abutments are plotted in Figure 6.1 and Figure 6.2 for the three abutment geometries: unconfined, MSE wingwall, and RC wingwall. The results for Figure 6.1 and Figure 6.2 are plotted at the same scale and a comparison clearly indicates a substantial decrease in passive resistance at a skew angle of 45º. For both the zero and 45º skew cases, the unconfined geometry produced the highest passive force for a given deflection. For the zero skew case the RC wingwall produced the lowest passive force while for the 45º skew case, the MSE wall yielded the lowest passive forces.

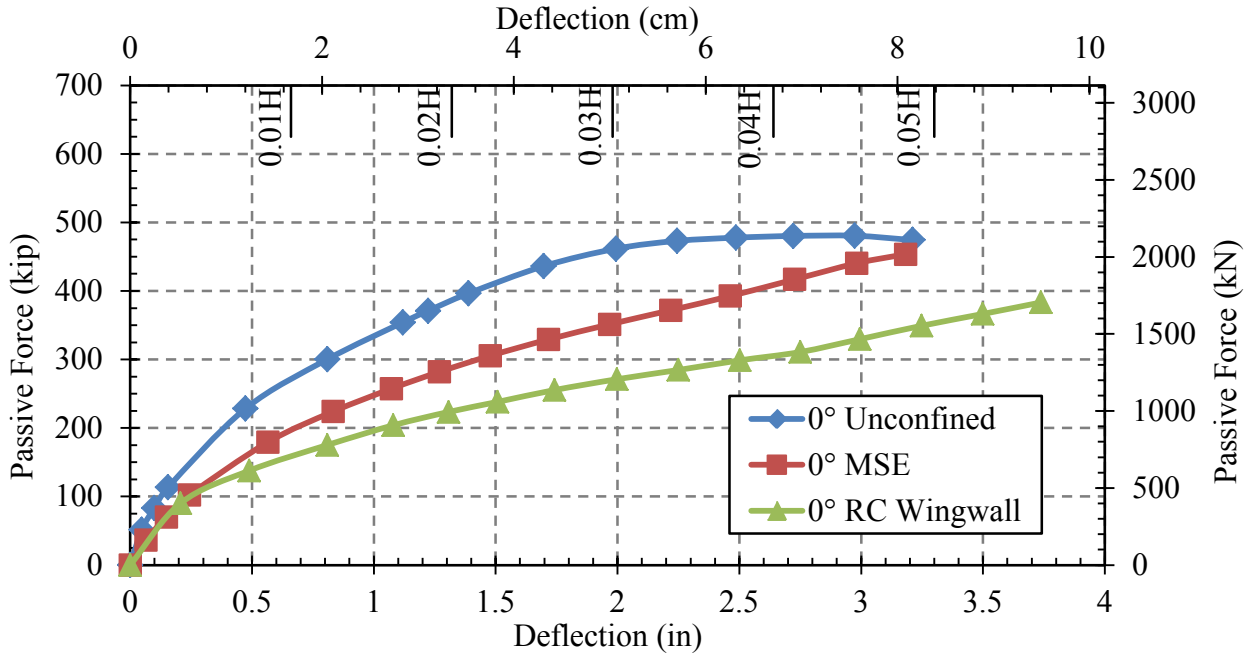

Figure 6.1. Total passive force-deflection curves for non-skewed unconfined, MSE wall, and RC wingwall abutment geometries.

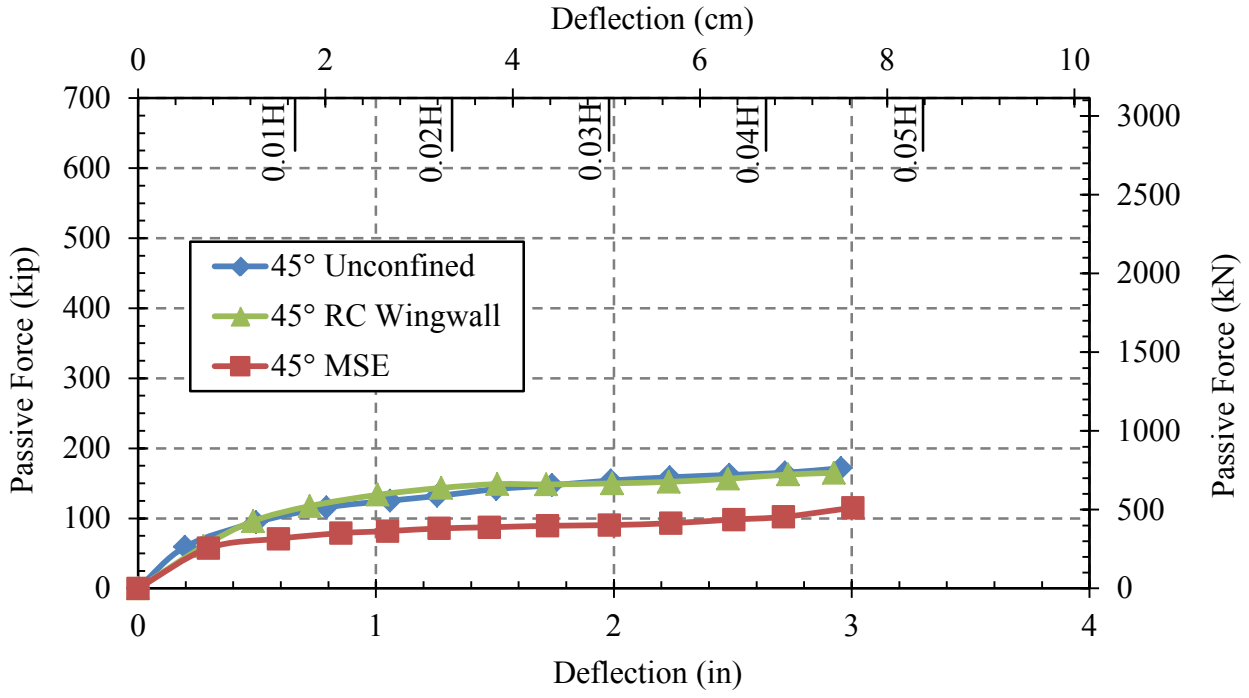

Figure 6.2. Total passive force-deflection curves for 45° skewed unconfined, MSE wall, and RC wingwall abutment geometries.

Figure 6.3 demonstrates how all three test geometries compare at a 45° skew angle.

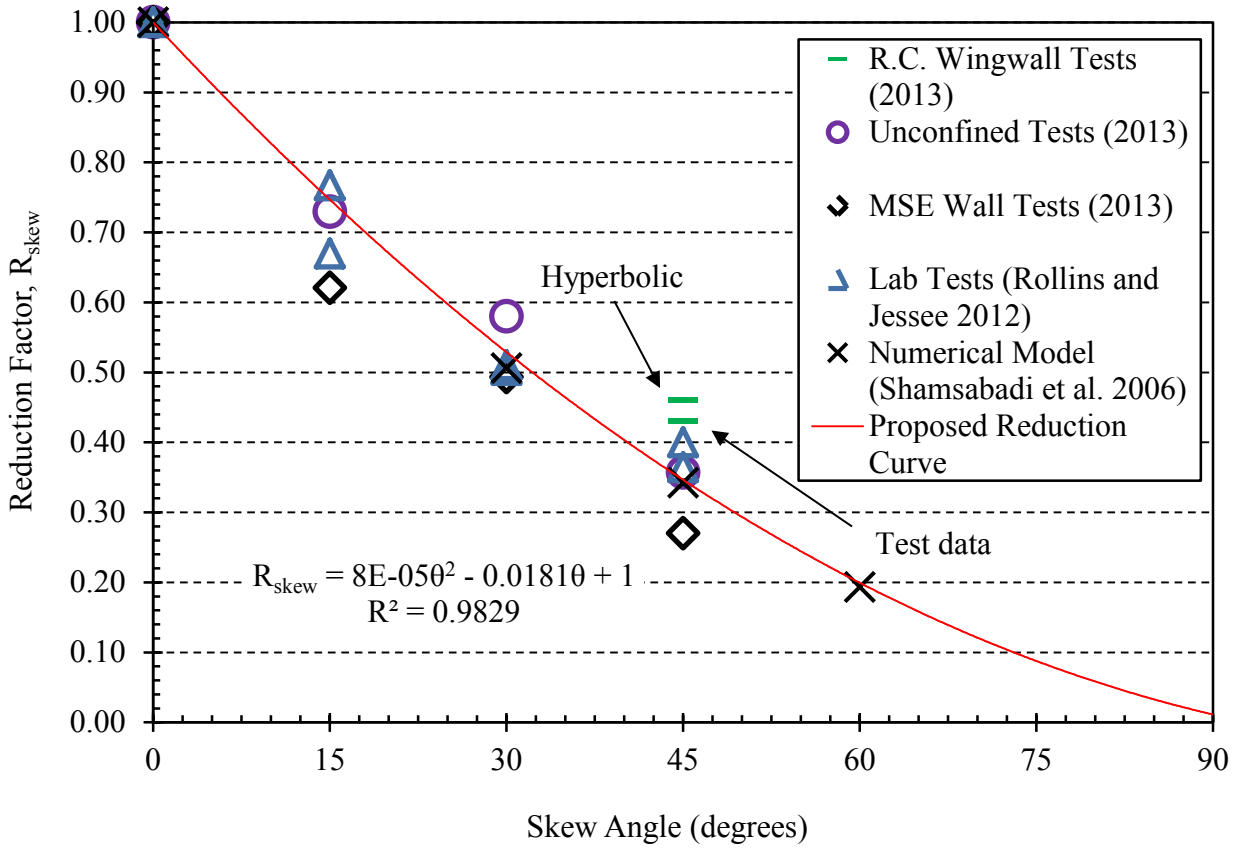

Figure 6.3. Reduction factors for RC wingwall, MSE wall, and unconfined abutment geometries in relation to proposed reduction curve.

For the 45° skew case, the reduction in peak passive resistance for the unconfined geometry is most accurately predicted by the reduction curve. The reduction for MSE wall geometry lies below the curve, while the reduction factor for RC wingwall geometry lies above. At other skew angles, the test results also scatter about the curve proposed by Rollins and Jessee (2013) based on small scale laboratory tests; however, the results for the MSE wall tests tend to plot somewhat below the curve.

6.2 Passive Force per Width

Comparisons using total passive force are inadequate for evaluating soil strength because the effective width of the soil failure surface differs with abutment geometry. Effective widths for all the three geometries at both skew angles were estimated based on the location of surface cracks and heave measurements between 0.5 and 0.75 inch (1.3 to 1.9 cm). Effective widths for the non-skewed and 45° skewed geometries are illustrated using a dashed line in Figure 6.4 and Figure 6.5, respectively. For 45° skewed unconfined and RC wingwall geometries, projected widths and widths parallel to the skewed backwall are shown for comparison purposes. Projected widths are used as the effective widths.

The unconfined backfills produced the widest effective widths (21 ft [6.4 m] for non-skewed and 17.8 ft [5.5 m] for 45° skewed abutments) compared to MSE and RC wingwall geometries. The passive failure surfaces for the MSE wingwall tests were constrained by the wingwalls, resulting in an effective width of 11.5 ft (3.5 m) (the distance between the walls) for both tests. The surface cracks and heave contours suggest that the RC wingwall passive failure surfaces exhibit characteristics of both the unconfined and MSE wingwall geometries. Effective widths were estimated to be 13.5 ft (4.1 m) for both skew angles. Although shear failure surfaces extend beyond the abutment width (including the wingwalls), the effective widths are only 4% larger than the width of the abutment. The soil at the sloped embankment portion of the backfill could not be compacted as densely as the level backfill within the abutment width because of the presence of the slope, and this may contribute to the narrower failure surface. Because the effective widths for the RC wingwall geometry are essentially equal to the abutment width, the passive failure surface may be better approximated with a 2D geometry rather than a 3D geometry.

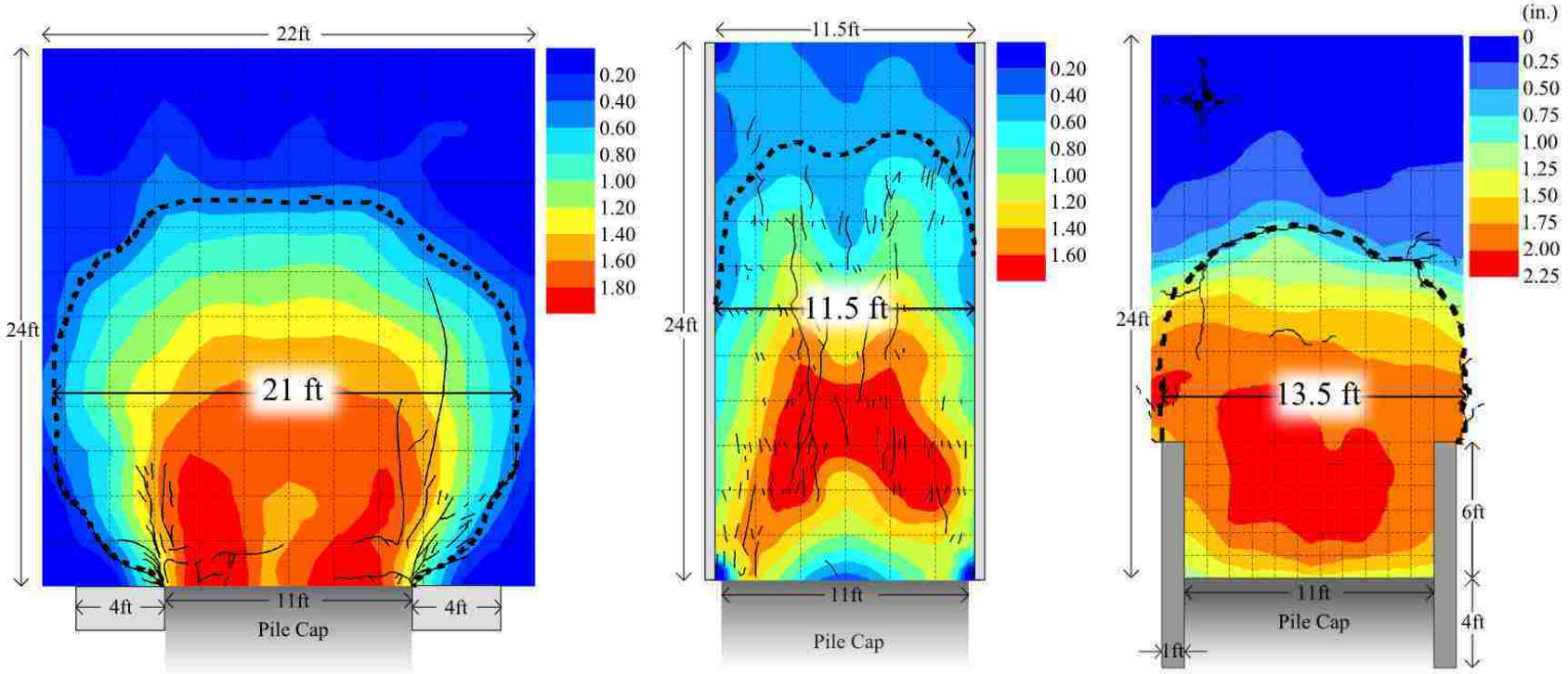

Figure 6.4. Comparison of effective widths for non-skewed test geometries.

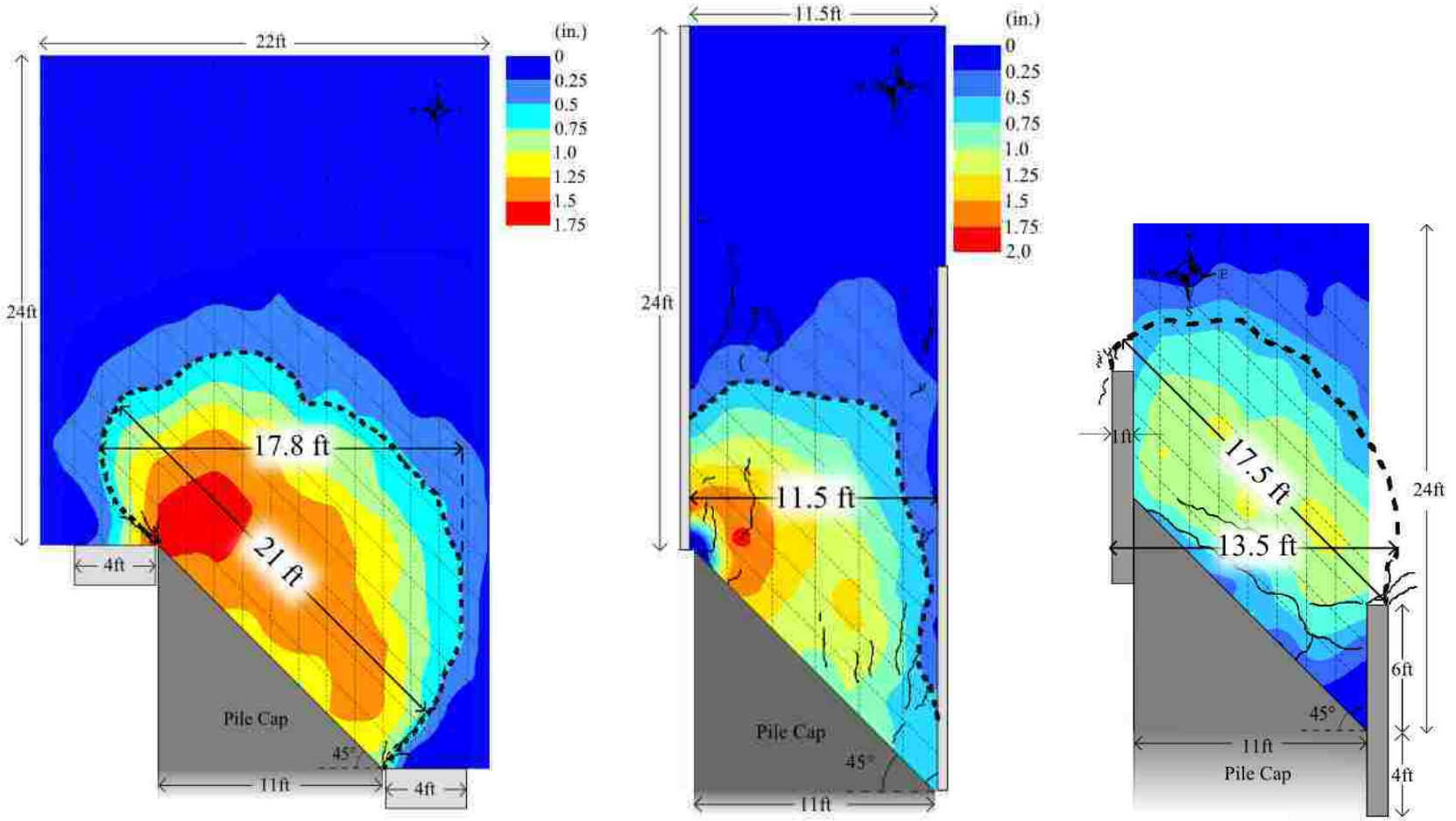

Figure 6.5. Comparison of effective widths for 45° skewed test geometries.

Passive force per width was calculated for all deflection increments using Equation (6-1).

$$Passive\ force/width = \frac{Total\ Passive\ Force}{Effective\ Width} \quad (6\text{-}1)$$

The measured effective widths in Figure 6.4 and Figure 6.5 were used in Equation (6-1). Passive force/width-deflection curves for non-skewed and 45° skewed abutments are shown in Figure 6.6 and Figure 6.7, respectively.

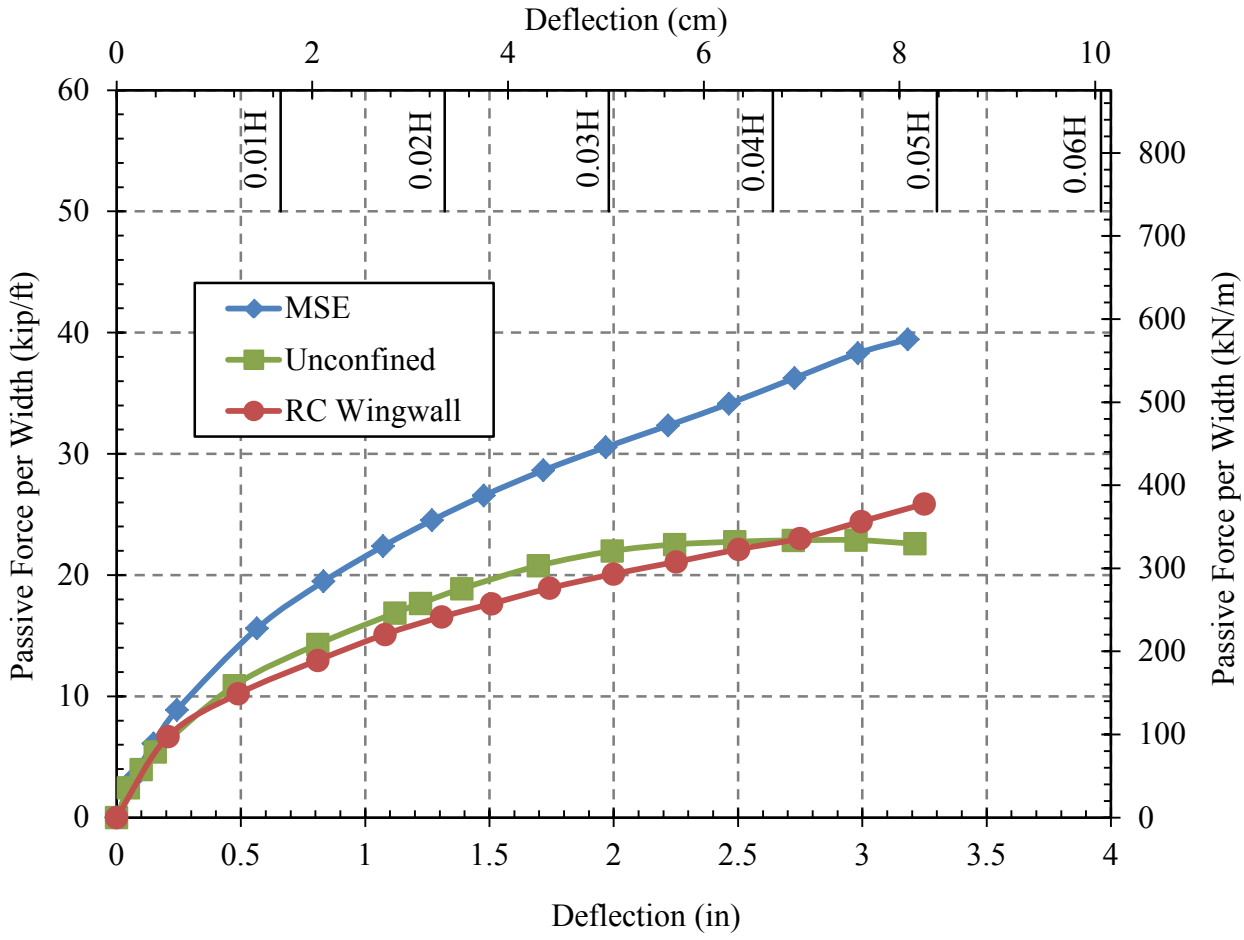

Figure 6.6. Passive force/width-deflection curves for non-skewed abutments.

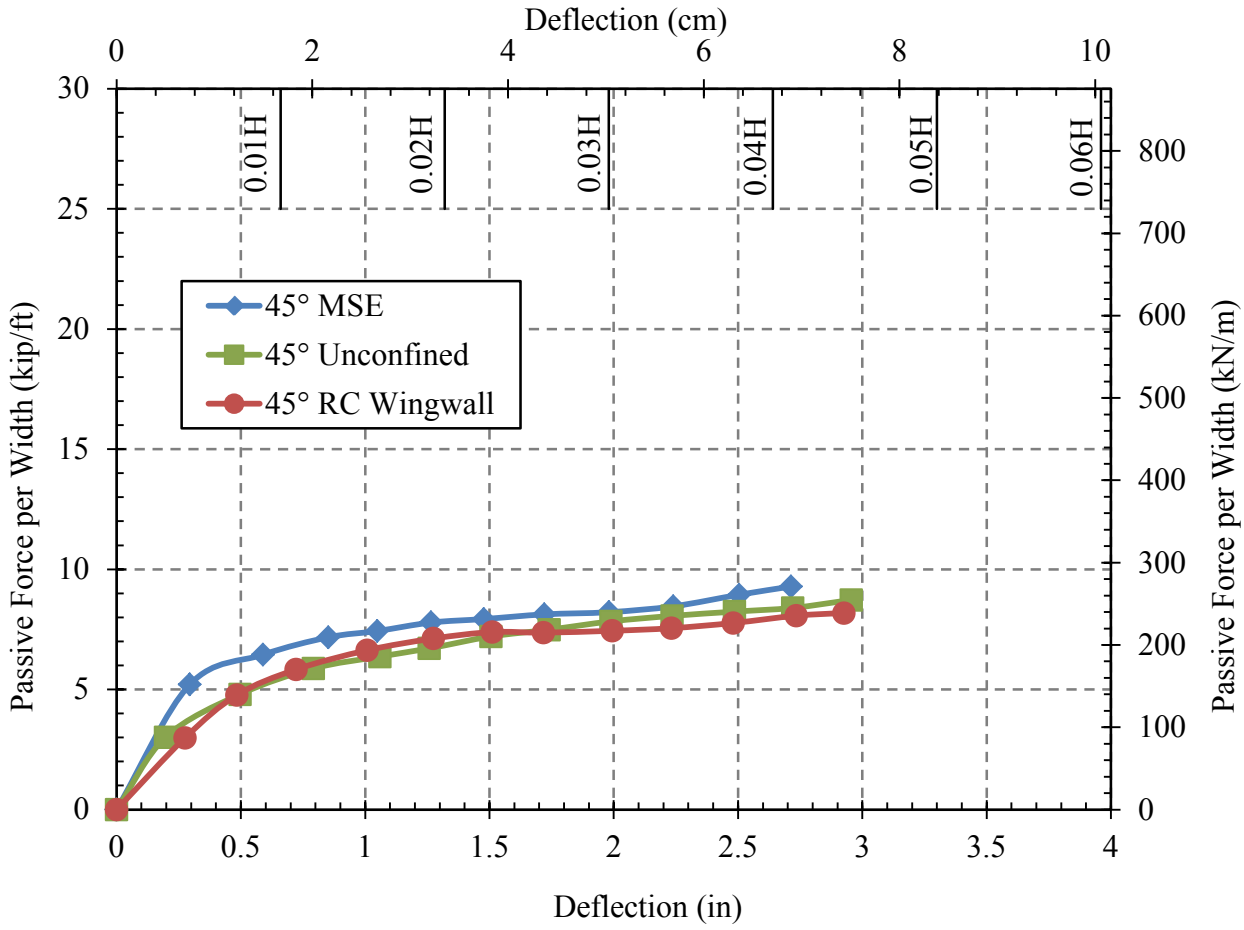

Figure 6.7. Passive force/width-deflection curves for 45° skewed abutments.

For the non-skewed case, the MSE wingwall geometry provides an additional 60% passive resistance per width compared to RC wingwall and unconfined geometries. The increased passive resistance is attributed to the smaller effective width from MSE wingwall confinement, the added resistance from grid reinforcements, and the higher plane-strain friction angle (φ_{ps}) of the soil appropriate for this condition. Kulhawy and Mayne (1990) observed that φ_{ps} is on average 12% higher than the triaxial friction angle (φ_T) for densely compacted material.

At a 45° skew angle, a maximum passive force per width of approximately 8 to 9 kip/ft (117 to 132 kN/m) is achieved regardless of abutment geometry. MSE wingwalls appear to have little effect on passive resistance per width at a 45° skew. At both 0° and 45° skew angles, abutments with RC wingwall geometry provided similar passive resistance per width as the unconfined backfill geometry.

6.3 PYCAP Parameters

Passive force-deflection predictive hyperbolic curves were computed in PYCAP (Duncan and Mokwa, 2001) for unconfined, MSE and RC wingwall geometries at zero and 45° skew angles. Two sets of parameters were used to generate passive force-deflection curves. First, parameters were selected that are consistent with previous large-scale testing and also accurately represent the effective widths measured in this study, shown in Table 6.1. Two separate values of skew reduction factors (R_{skew}) for 45° skew were evaluated to compare with the recommendation by Rollins and Jesse (2012). In addition, reasonable alternative values for friction angle (φ) and the 3D factor were selected in combination with the reduction factor proposed by Rollins and Jessee ($R_{skew} = 0.35$) for the 45° skew RC wingwall case. This analysis was done to investigate the effects of increased friction along the east wingwall and increased 3D effects relative to the non-skewed RC wingwall abutment, which led to a higher reduction factor ($R_{skew} = 0.43\ to\ 0.46$).

An additional set of parameters was chosen to investigate the changes required to obtain a best-fit curve for MSE and RC wingwall tests, which both exhibited increasing passive resistance at maximum deflection. A better fit was not obtained using different parameters for the MSE wingwall tests; therefore, the hyperbolic approximations using parameters from Table 6.1 are

considered the best-fit curves. Best-fit parameters for the RC wingwall case are listed in Table 6.2. Parameter symbols are explained below.

$b = abutment\ width$

$H = abutment\ backwall\ height$

$c = cohesion$

$\varphi = friction\ angle$

$\delta = wall\ friction$

$E_i = initial\ soil\ modulus$

$\gamma_m = moist\ unit\ weight\ of\ soil$

$D_{max}/_H = movement\ required\ to\ develop\ full\ passive\ resistance$

$Note$: $3D\ correction\ factor\ is\ given\ the\ parameter$ "R" $in\ PYCAP$

Poisson's ratio (v) of the soil was approximated using Equation (6-2) recommended by Duncan and Mokwa (2001).

$$v = \frac{1 - sin\varphi}{2 - sin\varphi} \tag{6-2}$$

Identical values for H, c, and γ_m were entered for all three abutment geometries for both sets of parameters to maintain consistency and isolate other parameters that are more effected by abutment geometry. Average field values for γ_m were 116.6, 117.3, and 116.0 for unconfined, MSE wingwall, and RC wingwall abutment geometries, respectively. The same parameters used for calibrating non-skewed passive force-deflection curves were evaluated on the 45° skewed

Table 6.1. PYCAP Parameters That Are Consistent With Previous Studies And With Failure Surface Geometries In This Study

Figure No.	Abutment Type	b (ft)	H (ft)	c (psf)	φ (deg)	δ = 0.7φ (deg)	ν	E_i (ksf)	γ_m (pcf)	D_{max}/H 0°	D_{max}/H 45°	3D factor 0°	3D factor 45°	R_{skew} 45°
6.8	Unconfined	11	5.5	100	40	28	0.26	475	117	0.04	0.04	1.79	1.79	0.35
6.9	MSE wingwall	11.5	5.5	100	44.8	31.4	0.23	300	117	0.05	0.05	1	1	0.27
6.10	MSE wingwall	11.5	5.5	100	44.8	31.4	0.23	300	117	0.05	0.05	1	1	0.35
6.11	RC wingwall	13	5.5	100	40	28	0.26	200	117	0.05	0.022	1	1	0.46
6.12	RC wingwall	13	5.5	100	40	28	0.26	200	117	0.05	0.022	1	1	0.35
6.13	RC wingwall	13	5.5	100	40	28	0.26	200	117	-	0.022	-	1.15	0.35
6.14	RC wingwall	13	5.5	100	40	28	0.26	200	117	-	0.022	-	1.15	0.35

Table 6.2. PYCAP Best-Fit Parameters

Figure No.	Abutment Type	b (ft)	H (ft)	c (psf)	φ (deg)	δ = 0.7φ (deg)	ν	E_i (ksf)	γ_m (pcf)	D_{max}/H 0°	D_{max}/H 45°	3D factor 0°	3D factor 45°	R_{skew} 45°
6.15	RC wingwall	13	5.5	100	42.3	29.6	0.25	200	117	0.07	0.07	1	1	0.46

abutment test data, with the exception of $^{D_{max}}/_{H}$ (for RC wingwalls only) and skew reduction factor (R_{skew}) for all 45° skew tests.Because it was found that the reduction curve proposed by Rollins and Jessee (2012) underestimates the reduction factor for a 45° skew with RC wingwalls, two reduction factors are shown for comparison between recommendations from this study (for RC wingwalls only) and from Rollins and Jessee (2012). A reduction of $R_{skew} = 0.46$ is recommended by this study, whereas $R_{skew} = 0.35$ was recommended by Rollins and Jessee (2012). Similarly, for the MSE wingwall abutment a reduction factor of $R_{skew} = 0.27$ was found to be more accurate compared to $R_{skew} = 0.35$ (Franke, 2013).

It appears consistent for all skews that E_i decreases by 40 to 60% for RC and MSE wingwall abutments compared to unconfined abutments. Initial stiffnesses (E_i) of 200 to 300 ksf (9.6 to 14.4 MPa) were observed for RC wingwall and MSE wall geometries compared to $E_i \approx 500\ ksf$ (25.0 MPa) for unconfined geometries. Based on measurements from large-scale tests, peak passive forces were measured consistently at approximately 0.04H for unconfined geometries compared to RC and MSE wingwall abutment passive force-deflection curves that did not necessarily exhibit a peak passive force within 0.05H.

6.4 PYCAP Analysis—Consistent With Previous Studies

The predictive hyperbolic curves in this section are based on parameters in Table 6.1.

6.4.1 Unconfined

Parameters used in generating the hyperbolic curves for abutments with unconfined geometry similar to parameters used by Marsh (2013). An initial soil modulus of $E_i = 475\ ksf$ (22.9 MPa) was employed for this analysis compared to $E_i = 520\ ksf$ (25.0 MPa)

used by Marsh (2013). This change is acceptable as it only affects the initial slope of the curve. A cohesion value of $c = 100\ psf$ $(4.8\ kPa)$ was used compared to $c = 85\ psf$ $(4.1\ kPa)$ used by Marsh (2013). The increase of 15 psf only increased the peak passive force by 3% and was thought to be more consistent with the laboratory and in-situ direct shear tests. The Brinch-Hansen 3D correction factor was employed for the unconfined abutment and was computed as $R = 1.79$ based on the abutment geometry, same as Marsh (2013). Soil and wall friction angles were identical to those used by Marsh (2013). The peak passive force was approximated at a deflection 4% of the backwall height (0.04H). Both passive force-deflection curves in Figure 6.8 generated in PYCAP for non-skewed and 45° skewed abutments show great agreement with the actual test data, and are therefore considered to be best-fit curves as well.

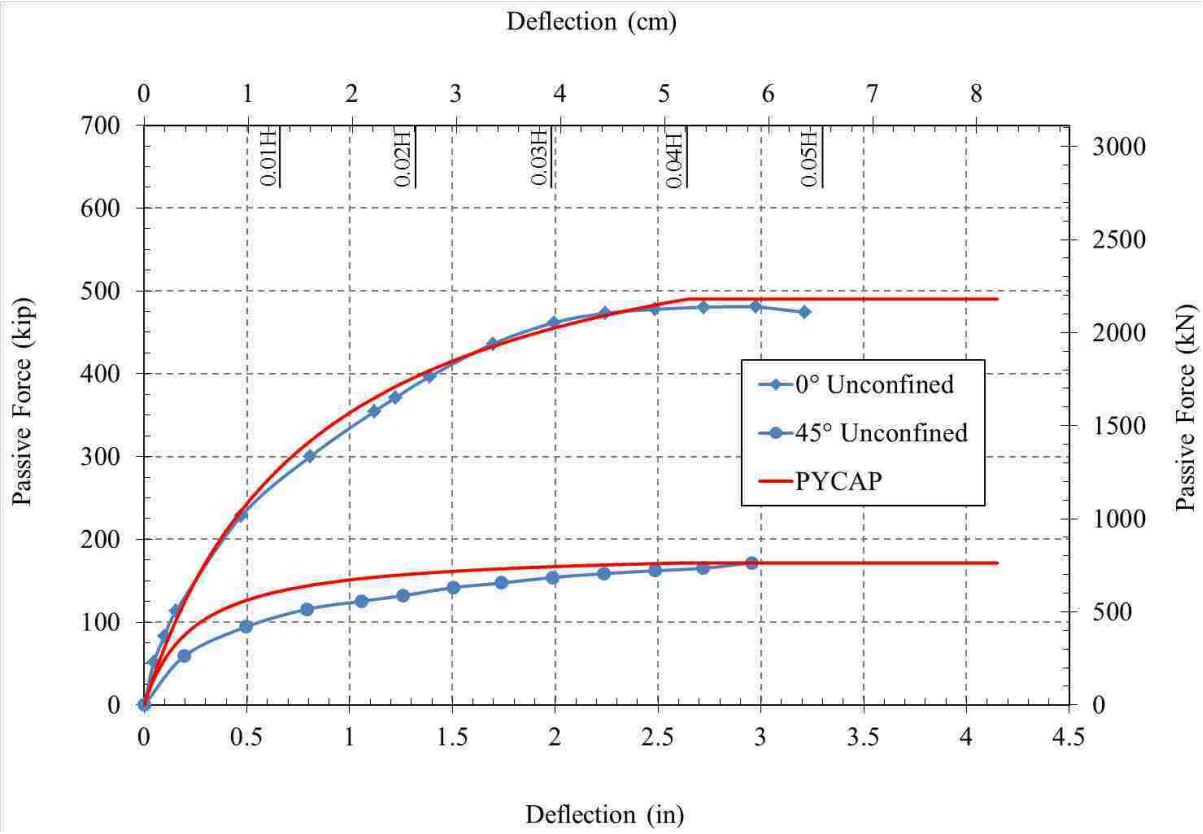

Figure 6.8. PYCAP hyperbolic approximations for unconfined geometry.

PYCAP curves estimate the peak passive force within 2% and 0.05% of the zero and 45° skew tests, respectively.

6.4.2 MSE Wingwall

For developing the hyperbolic curve for the MSE wall geometry, the plane-strain friction angle (φ_{ps}) was used to account for the plane-strain (2D) conditions provided by the MSE wingwall confinement. A plane-strain friction angle of $\varphi_{ps} = 44.8°$ was used and is approximately 12% higher than the ultimate friction angle (φ), which is consistent with results by Kulhawy and Mayne (1990). Wall friction was still set as $\delta = 0.7\varphi$. Because MSE wingwalls were spaced 11.5 ft (3.5 m) apart, $b = 11.5\,ft$ $(3.5\,m)$ was used effective abutment width. Initial soil stiffness was lower compared with the unconfined geometry. To reflect the decrease in initial soil stiffness, the initial soil modulus was decreased to $E_i = 300ksf$ $(14.4\,MPa)$. Because the MSE wingwall confinement limited the passive failure wedge from extending beyond the abutment width, the 3D correction factor was set to $R = 1.0$ to represent no 3D effects. PYCAP hyperbolic curves for MSE wingwall geometry are shown in Figure 6.9 and Figure 6.10. Reduction factor values of $R_{skew} = 0.27$ and $R_{skew} = 0.35$ were used to generate the 45° skew curves in Figure 6.9 and Figure 6.10, respectively.

Although intermediate values of passive resistance are slightly overestimated by PYCAP, the values for peak passive force are within 1% and 0.5% for the zero and 45° skew case, respectively.

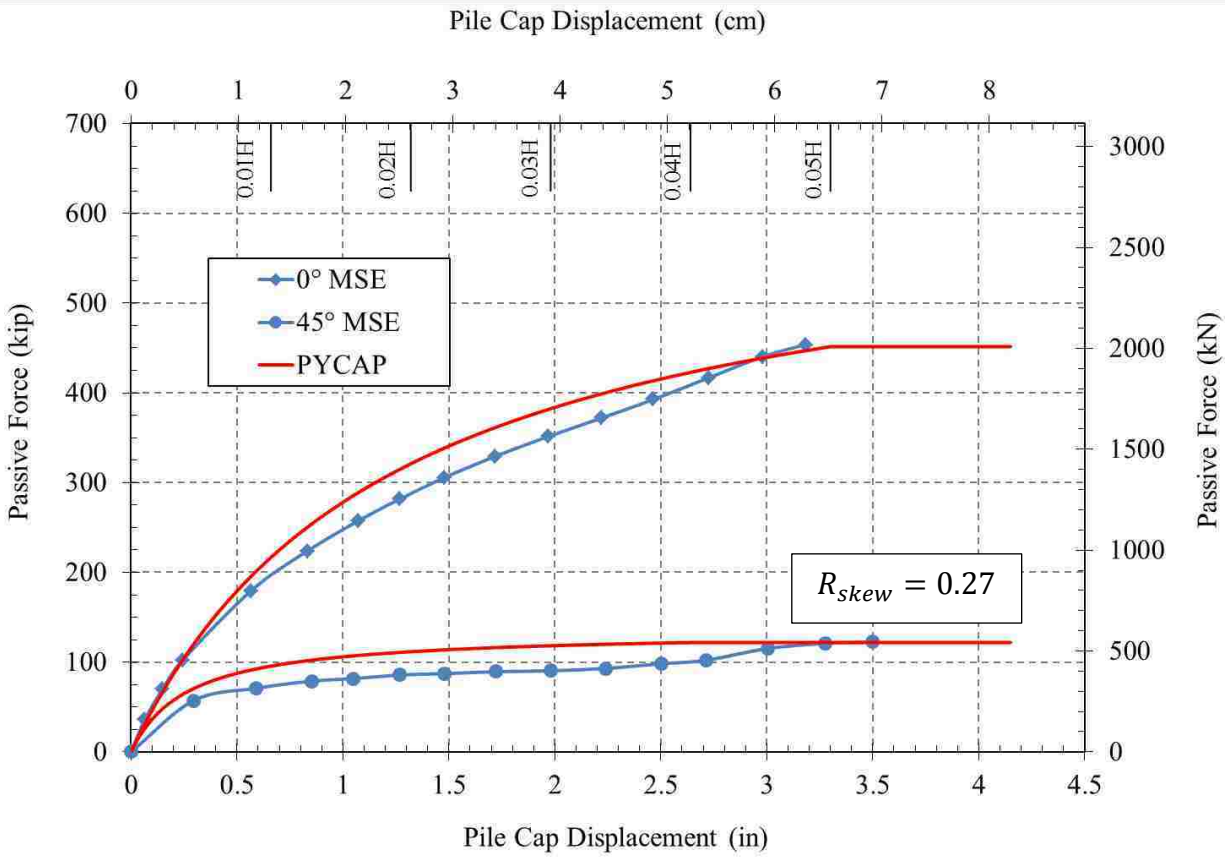

Figure 6.9. PYCAP hyperbolic approximations for MSE wingwall geometry ($R_{skew} = 0.27$ for 45° skew)

When the reduction factor recommended by Rollins and Jessee (2012) is use ($R_{skew} = 0.35$), the peak passive force for the 45° skew is overestimated by 30% (see Figure 6.10).

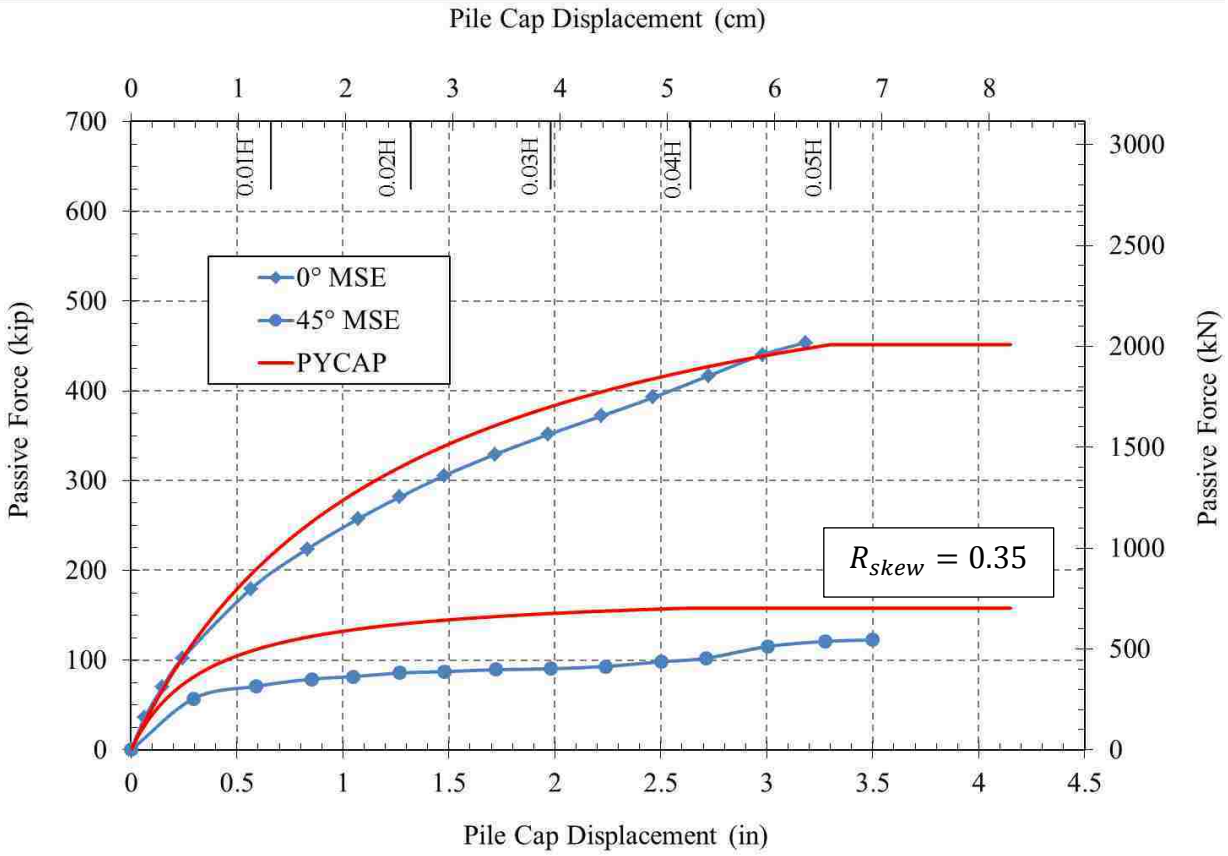

Figure 6.10. PYCAP hyperbolic approximations for MSE wingwall geometry ($R_{skew} = 0.35$ for 45° skew)

6.4.3 RC Wingwall

For the RC wingwall case, hyperbolic curves were generated using a 2D failure geometry to represent little to no 3D effects observed in the backfill; however, the plane-strain friction angle was not used. A friction angle of $\varphi = 40°$ was used, as was the case for the unconfined abutment geometry. The abutment width of $b = 13\ ft$ $(4.0\ m)$ includes the 1-ft (0.305-m) wide wingwalls on either side of the abutment. PYCAP hyperbolic approximations are shown in Figure 6.11 and Figure 6.12. The 45° skew approximation in Figure 6.11 uses $R_{skew} = 0.46$, while Figure 6.12 uses the recommendation from Rollins and Jessee (2012) $R_{skew} = 0.35$.

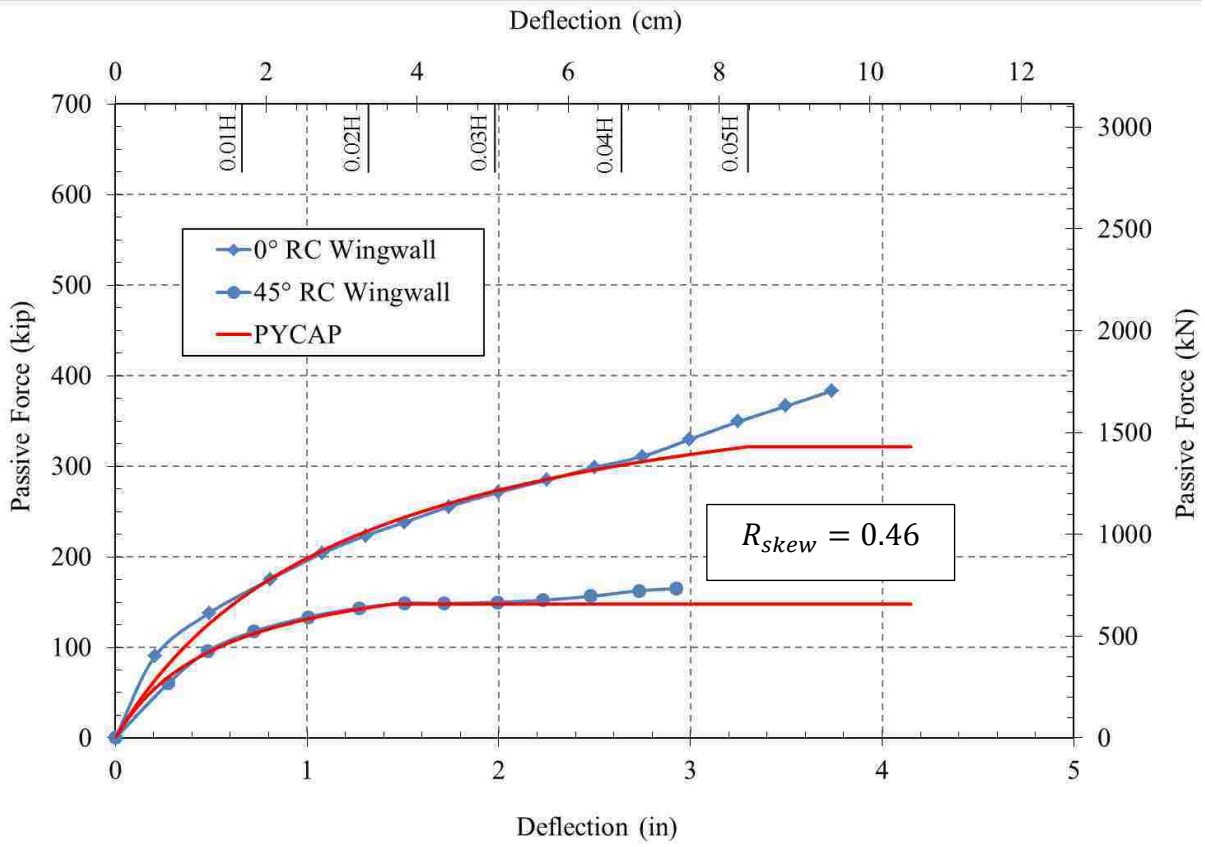

Figure 6.11. PYCAP hyperbolic approximations for RC wingwall geometry ($R_{skew} = 0.46$ for 45° skew).

In Figure 6.11, peak passive forces predicted by PYCAP are within 16% and 10% of the measured values from the zero and 45° skew tests. The discrepancy between the predicted and measured values is thought to be a result of an unreliable baseline curve at large deflections. This thought was prompted by the good agreement between the PYCAP and measured curves (in Figure 6.11) up to a deflection of approximately 2.5 inches (6.4 cm). The PYCAP curves generated in Figure 6.11 are based on parameters that are consistent with results from previous large-scale tests and with effective width measurements in this study.

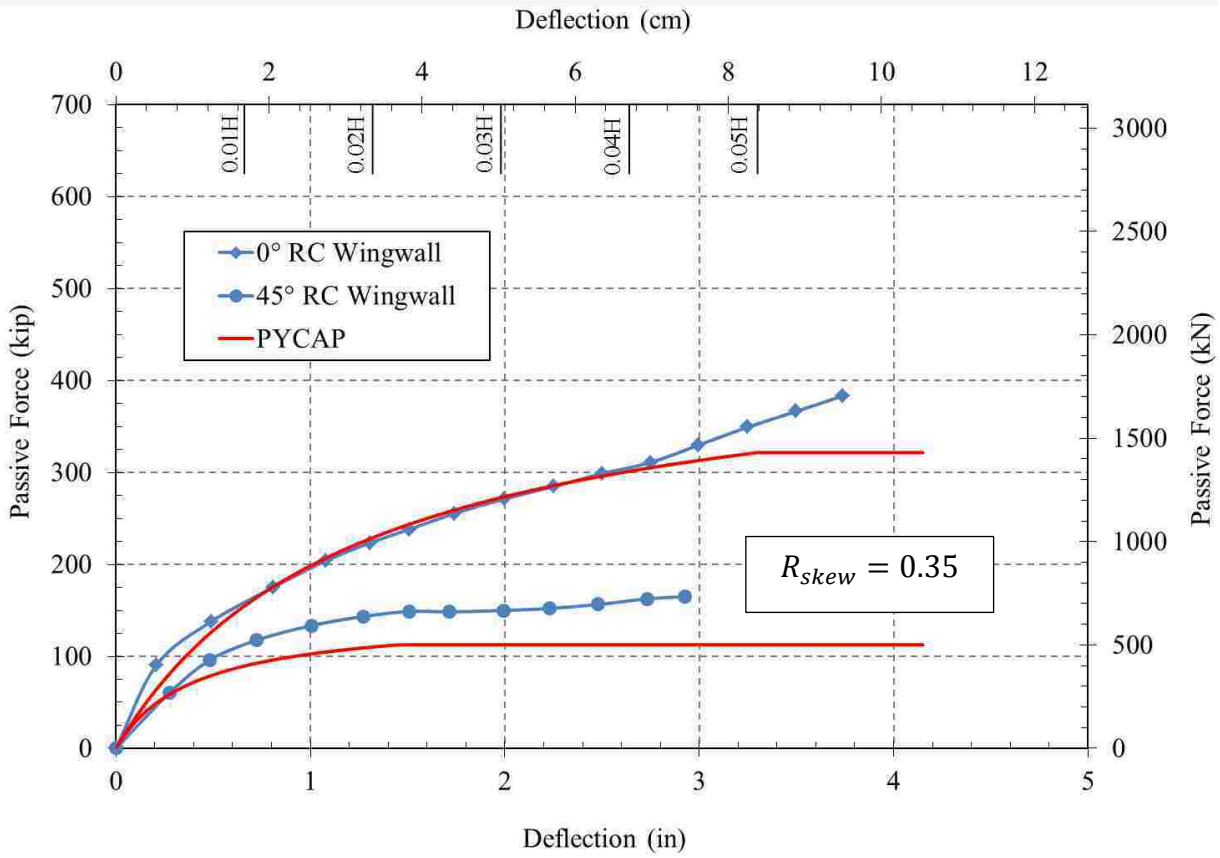

Figure 6.12. PYCAP hyperbolic approximations for RC wingwall geometry ($R_{skew} = 0.35$ for 45° skew).

When the reduction factor of $R_{skew} = 0.35$ is used, proposed by Rollins and Jessee (2102) for the 45° skew case, and all other parameters are kept the same, the peak passive force is underestimated by 32%.

Factors that contribute to the increased reduction factor ($R_{skew} = 0.43\ to\ 0.46$) for the 45° skew case are investigated in Figure 6.13 and Figure 6.14 by increasing the 3D factor and including increased passive resistance from increased friction along the east wingwall. Increased 3D effects are investigated in Figure 6.13. Heave contours in Figure 6.5 were used to estimate a larger effective width. This approach is limited due to the lack of heave data beyond the abutment width because of the embankment slope; however, due to the lack of a better method a

maximum probable effective width of 15 ft was justified by extrapolation of the heave contours. An effective width of 15 ft (4.6 m) corresponds to a 3D factor of 1.15, which was the value used in Figure 6.13.

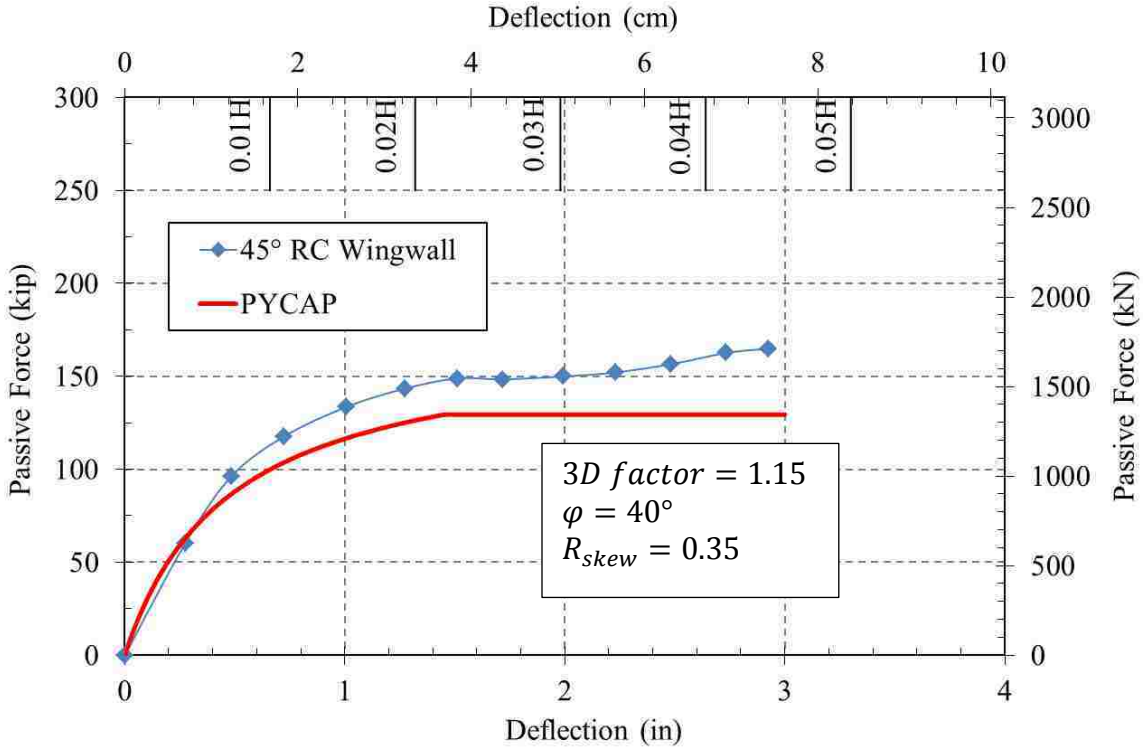

Figure 6.13. 45° skew wingwall with increased 3D effects relative to zero skew case.

Increased 3D effects alone bring the peak passive force within 13% of the measured passive force at a deflection of 0.022H.

A combination of increased 3D effects and increased friction along the east wingwall is portrayed in Figure 6.14. The increased frictional resistance along the wingwall was accounted for by adding an additional 6 kips (26.9 kN) of passive resistance to the peak passive force at a deflection of 2.2% the backwall height. Recall that pressure measurements indicated higher pressures on the east wingwall for the 45° skew test relative to the zero skew test. The predicted

passive force at a deflection of 2.2% the backwall height is within 9% of the measured passive force.

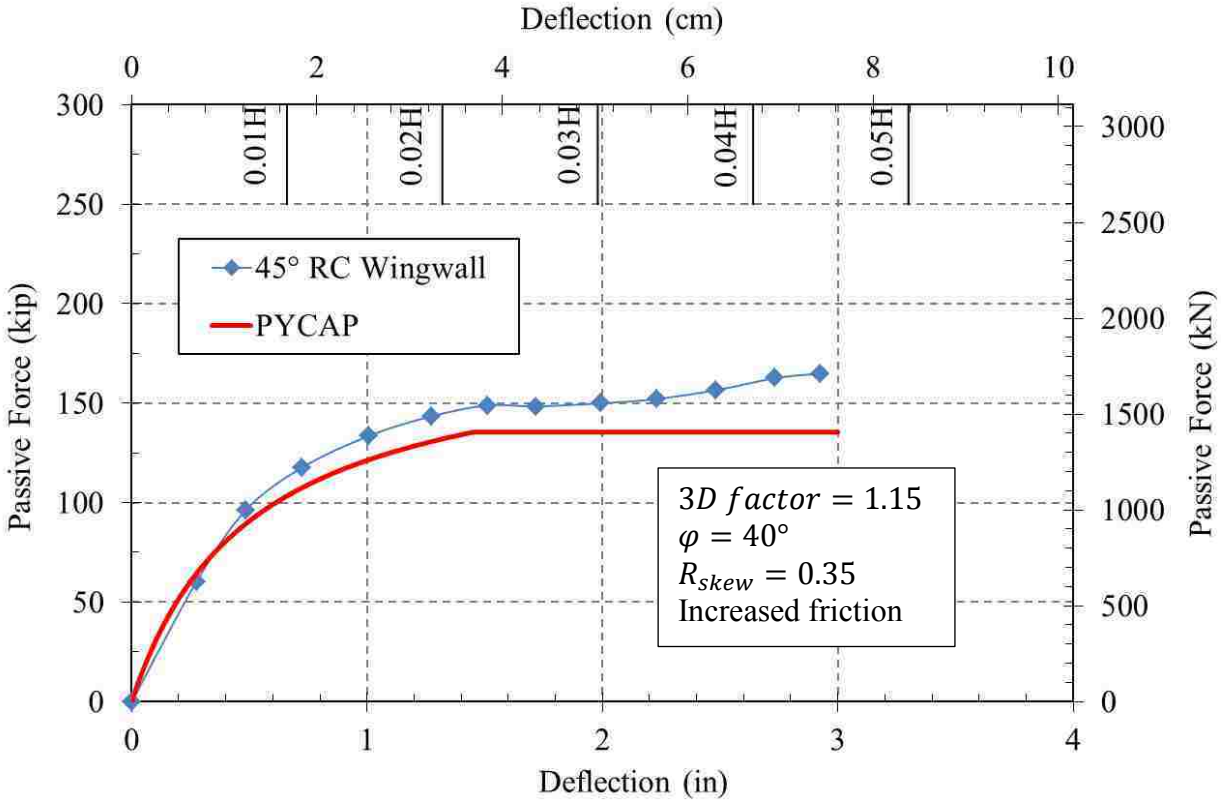

Figure 6.14. 45° skew wingwall with increased 3D effects and increased friction angle relative to zero skew case.

Reasonable increases in friction angle and the 3D factor help to explain the discrepancy between the measured reduction factor of $R_{skew} = 0.43\ to\ 46$ for the 45° skew RC wingwall case and recommended reduction factor of $R_{skew} = 0.35$ for a 45° skew (Rollins and Jessee 2012).

6.5 PYCAP Best-Fit Analysis for RC Wingwall Geometry

The best-fit hyperbolic curves in this section are based on parameters in Table 6.2, which aim to model the increasing passive resistance at large deflections.

6.5.1 RC Wingwalls

Changes were made, within reason, in the soil parameters for the RC wingwall tests to investigate a best-fit hyperbolic curve for both non-skewed and 45° skew cases. Best-fit PYCAP curves were generated for both skew angles using the same modified parameters and are shown in Figure 6.15. The soil friction angle was increased by approximately 6% to a value of $\varphi = 42.3°$, which increased the wall friction angle to $\delta = 29.6°$. In addition, the peak deflection value was increased to ${D_{max}}/{H} = 0.07$, which is higher than the typical value but still less than ${D_{max}}/{H} = 0.08$ reported by Romstad et al. (1996).

For the non-skewed case, at a deflection of 3.75 inches the measured passive force is underestimated by 2%. For the 45° skew case, the passive force at 3.0 inches (7.6 cm) of deflection is overestimated by 4%. While the error decreased for the non-skewed passive force prediction at 3.75 inches (9.5 cm), the passive force predictions at deflections less than 3.75 inches (9.5 cm) are less accurate compared to hyperbolic curves using a peak deflection that is more consistent with previous testing (5% of the backwall height).

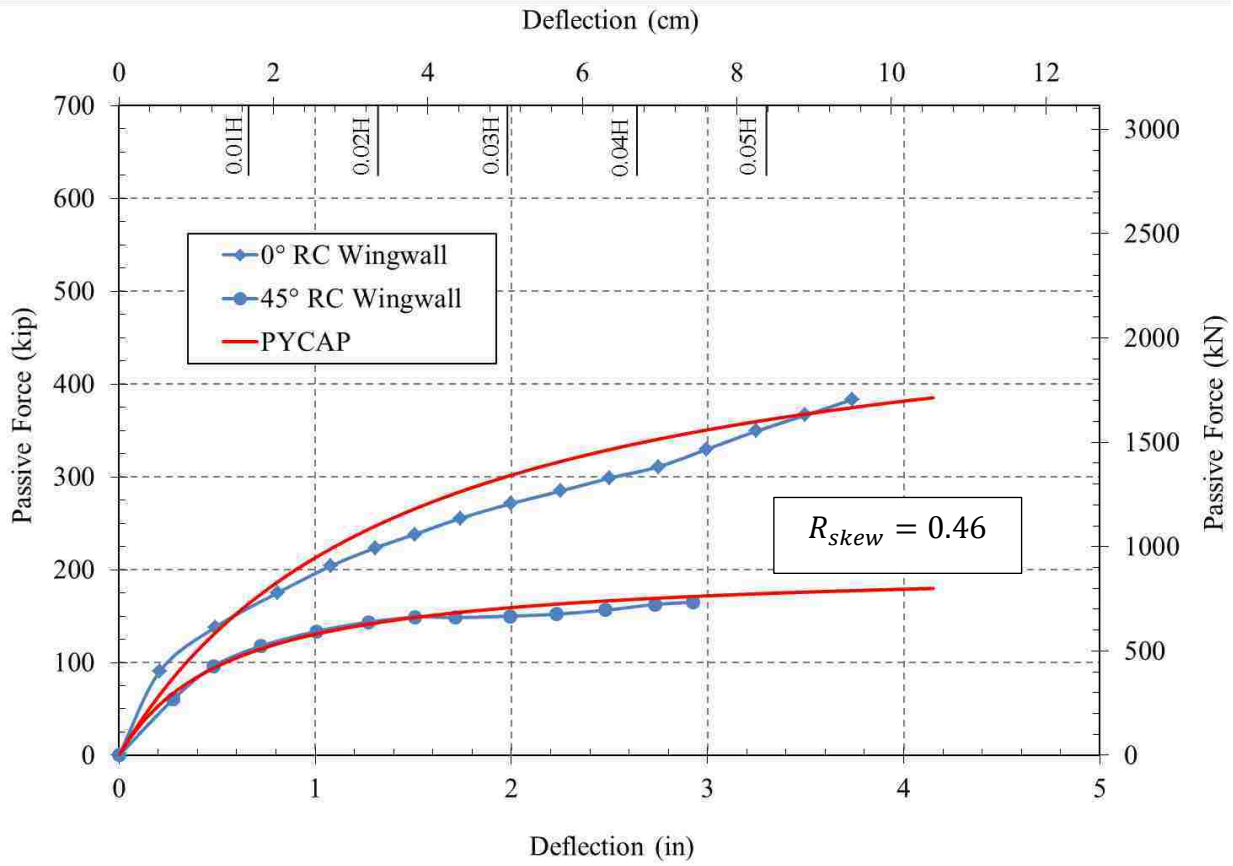

Figure 6.15. PYCAP best-fit curves for RC wingwall geometry.

6.6 Comparison of Failure Surface Geometry

Based on the 3D correction factors used in PYCAP, effective widths were back-calculated and compared to those that were measured from surface cracks and heave measurements. Comparisons of measured and PYCAP effective widths are provided in Table 6.3 and Table 6.4 for non-skewed and 45° skewed abutments.

Table 6.3. Effective Width Comparison For Non-skewed Abutments

Abutment Type	Abutment Width ft	3D Factor	Effective Width PYCAP ft	Measured ft	Error
Unconfined	11	1.79	19.7	21	6%
MSE Wall	11.5	1.0	11.5	11.5	0%
RC Wingwall	13	1.0	13.0	13.5	4%

Table 6.4. Effective Width Comparison For 45° Skewed Abutments

Abutment Type	Abutment Width ft	3D Factor	Effective Width PYCAP ft	Measured ft	Error
Unconfined	11	1.79	19.7	17.8	11%
MSE Wall	11.5	1.0	11.5	11.5	0%
RC Wingwall	13	1.0	13.0	13.5	4%
RC Wingwall	13	1.15	15	13.5	11%

The relatively low error suggests that appropriate 3D factors were used when estimating peak passive forces in PYCAP.

The predicted log spiral surface generated in PYCAP is illustrated in Figure 6.16. PYCAP predicted a log spiral passive wedge that daylighted 18.5 ft (5.6 m) from the backwall face for both non-skewed and 45° skewed abutments. Field measurements suggest that a passive wedge 18.5 ft (5.6 m) in length overestimates the actual length of the passive wedge by approximately 22%, which was closer to 15 ft (4.6 m).

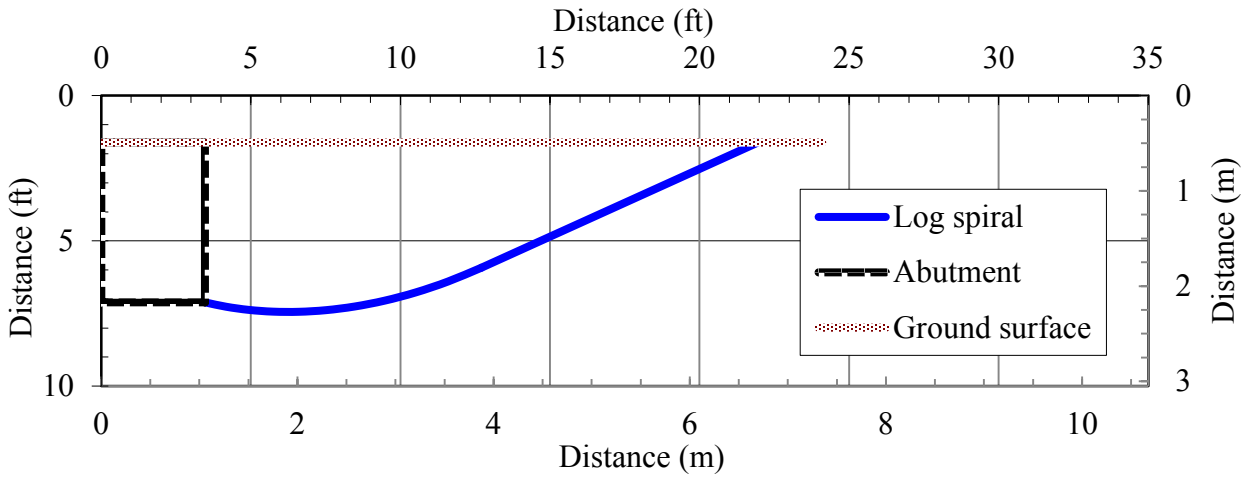

Figure 6.16. Predicted log spiral shear failure surface generated in PYCAP (Duncan and Mokwa 2001).

7 CONCLUSIONS

Conclusions are based on large-scale lateral load tests on abutments with longitudinal reinforced concrete (RC) wingwalls.

1. Large-scale field test results tests largely confirm previous results obtained from numerical models developed by Shamsabadi et al. (2006) and small-scale lab tests by Jessee (2012) showing a significant reduction in peak passive force as skew angle increases (57% reduction for 45° skew).
2. The reduction in peak passive force is overestimated by 8 to 11% for a 45° skew with RC wingwalls using the reduction curve proposed by Rollins and Jessee (2012). A 54 to 57% reduction ($R_{skew} = 43\ to\ 46\%$) was measured compared to the recommended 65% reduction ($R_{skew} = 35\%$) for 45° skew. The higher reduction factor (R_{skew}) for a 45° skewed abutment with RC wingwalls is attributed an increase in friction on the obtuse side wingwall and an increase in 3D effects relative to the non-skewed abutment with RC wingwalls.
3. Passive force-deflection curves based on large-scale tests did not exhibit a clear result for peak passive force due to limitations involving the baseline resistance; however, the peak passive resistance was estimated to fully develop at 0.05H for the non-skewed abutment and at 0.022H for the 45° skewed abutment based on hyperbolic models. These values for

peak deflections are consistent with previous large-scale tests which indicate that peak passive resistance is mobilized at deflections under 5% of the backwall height.

4. In general, the initial stiffness (K_{max}) of the backfill was 40% lower for RC wingwall and MSE wall geometries compared with unconfined geometries. Cyclic loading (20 cycles $\pm$0.25 in.) seemed to reduce the initial soil stiffness (K_{max}) by 50%.
5. The passive failure surface for the RC wingwall case appears to develop a failure geometry that closely resembles a 2D, log-spiral failure geometry, similar to failure surface observed for MSE wingwall case. A skew dependent 3D correction that is lower than the Brinch-Hansen value may be appropriate for the RC wingwall case.
6. The maximum bending moment acting on RC wingwalls was measured at the strain gauge 20 in (50.8 cm) below the top of the wingwall nearest to the backwall. For the 45° skewed abutment the maximum wingwall bending moment was 14 times larger on the obtuse side of the abutment compared to the acute side and 7 times larger compared to the maximum bending moment from the non-skewed abutment.
7. Lateral soil pressures were significantly higher on the obtuse side wingwall compared to the wingwall on the acute side for the 45° skewed abutment. Higher pressures on the obtuse side wingwall contributed an additional 5% to the longitudinal resistance of the 45° skewed abutment. Soil pressure distributions acting on non-skewed wingwalls were similar in magnitude to those on the acute side wingwall on the 45° skewed abutment.
8. Based on large-scale tests and estimates of effective widths, abutments with MSE walls provide up to 60% more passive resistance per width compared to non-skewed unconfined and RC wingwall geometries. At a 45° skew, little difference was observed in passive resistance per width for unconfined and MSE and RC wingwall geometries.

REFERENCES

AASHTO (2010). *AASHTO LRFD Bridge Design Specifcations*, AASHTO, Washington, DC.

AASHTO (2011). *Guide Specifications for LRFD Seismic Bridge Design*.

Apirakvorapinit, P., Mohammadi, J., and Shen, J. (2012). "Analytical Investigation of Potential Seismic Damage to a Skewed Bridge." *Practice Periodical on Structural Design and Construction*, 17(1), 5-12.

Apirakyorapinit, P., Mohammadi, J., and Shen, J. (2012). "Analytical Investigation of Potential Seismic Damage to a Skewed Bridge." *Practice Periodical on Structural Design and Construction*, 16(1), 5-12.

Bozorgzadeh, A., Ashford, S. A., Restrepo, J. I., and Nimityongskul, N. (2008). "Experimental and Analytical Investigation on Stiffness and Ultimate Capacity of Bridge Abutments." University of California, San Diego.

Burke Jr., M. P. (1994). "Semi-Integral Bridges: Movements and Forces." 1-7.

Caltrans, C. D. o. T. (2010). "Seismic Design Criteria, Version 1.6, November 2010." Division of Engineering Services, Office of Structure Design, Sacramento, California.

Christensen, D. S. (2006). "Full Scale Static Lateral Load Test of a 9 Pile Group in Sand." Master of Science, Brigham Young University, Provo, Utah.

Clough, G. W., and Duncan, J. M. (1991). *Foundation engineering hand-book*, Chapman and Hall, New York.

Cole, R., and Rollins, K. (2006). "Passive Earth Pressure Mobilization during Cyclic Loading." *Journal of Geotechnical and Geoenvironmental Engineering*, 132(9), 1154-1164.

Douglas, D. J., and Davis, E. H. (1964). "The Movement of Buried Footings due to Moment and Horizontal Load and the Movement of Anchor Plates." *Geotechnique, London*, 14(2), 115-132.

Duncan, J., and Mokwa, R. (2001). "Passive Earth Pressures: Theories and Tests." *Journal of Geotechnical and Geoenvironmental Engineering*, 127(3), 248-257.

Duncan, J. M., and Chang, C. Y. (1970). "Nonlinear Analysis of Stress and Strain in Soils." *Journal of the Soil Mechanics and Foundations Division*, 96(5), 1629-1653.

Elnashai, A. S., Gencturk, B., Kwon, O.-S., Al-Qadi, I. L., Hashash, Y., Roesler, J. R., Kim, S. J., Jeong, S.-H., Dukes, J., and Valdivia, A. (2010). "The Maule (Chile) Earthquake of February 27, 2010: Consequence Assessment and Case Studies."

Elnashai, A. S., Gencturk, B., Kwon, O., Al-Qadi, I. L., Hashash, Y., Roesler, J. R., Kim, S. J., Jeong, S., Dukes, J., and Valdivia, A. (2010). "The Maule (Chile) Earthquake of February 27, 2010: Consequence Assessment and Case Studies." Department of Civil and Environmental Engineering, University of Illinois at Urbana-Champaign, 190.

Franke, B. (2013). "Passive Force on Skewed Abutments with Mechanically Stabilized Earth (MSE) Wingwalls Based on Large-Scale Tests." M.S., Brigham Young University, Provo, Utah.

Gadre, A. D., and Dobry, R. (1998). *Centrifuge modeling of cyclic lateral response of pile-cap systems and seat-type abutments in dry sand*, MCEER, Multidisciplinary Center for Earthquake Engineering Research, Troy, N.Y.

Jessee, S. J. (2012). "Skew Effects on Passive Earth Pressures Based on Large-Scale Tests." M.S., Brigham Young University, Provo, Utah.

Johnson, S. R. (2003). "Static Lateral Load Testing of a Full-Scale Pile Group Spaced at 5.65 Pile Diameters."M.S. Thesis, Brigham Young University, Provo, UT.

Kulhawy, F. H., and Mayne, P. W. (1990). "Manual on estimating soil properties for foundation design." Medium: X; Size: Pages: (298 p).

Lee, K. L., and Singh, A. (1971). "Relative Density and Relative Compaction." *Journal of Soil Mechanics and Foundations Design*, 97(7), 1049-1052.

Lemnitzer, A., Ahlberg, E., Nigbor, R., Shamsabadi, A., Wallace, J., and Stewart, J. (2009). "Lateral Performance of Full-Scale Bridge Abutment Wall with Granular Backfill." *Journal of Geotechnical and Geoenvironmental Engineering*, 135(4), 506-514.

Marsh, A. (2013). "Evaluation of Passive Force on Skewed Bridge Abutments with Large-Scale Tests." Master of Science, Brigham Young University, Provo, Utah.

Mikkelsen, P. E. (2003). "Advances in Inclinometer Data Analysis." *Symposium of Field Measurements in Geomechanics*, FMGM 2003, Oslo, Norway, 13 pp.

Nichols (2012). D. K. Rollins, ed.

Ovesen, N. K. (1964). *Anchor slabs, calculation methods and model tests*, Akademiet for de tekniske Videnskaber, Copenhagen.

Potyondy, J. G. (1961). "Skin Friction Between Various Soils and Construction Materials." *Geotechnique, London*, 11(1), 339-353.

Rankine, W. J. M. (1857). "On the Stability of Loose Earth." *Philosophical Transactions of the Royal Society of London*, 147(ArticleType: research-article / Full publication date: 1857 /), 9-27.

Rollins, K., and Sparks, A. (2002). "Lateral Resistance of Full-Scale Pile Cap with Gravel Backfill." *Journal of Geotechnical and Geoenvironmental Engineering*, 128(9), 711-723.

Rollins, K. M., and Cole, R. T. (2006). "Cyclic Lateral Load Behavior of a Pile Cap and Backfill." *Journal of Geotechnical & Geoenvironmental Engineering*, 11.

Rollins, K. M., Gerber, T., Cummins, C., and Herbst, M. (2009). "Monitoring Displacement vs. Depth in Lateral Pile Load Tests with Shape Accelerometer Arrays." *Proceedings of 17th International on Soil Mechanics & Geotechnical Engineering*, 3, 2016-2019.

Rollins, K. M., Gerber, T. M., and Heiner, L. (2010). "Passive Force-Deflection Behavior for Abutments With MSE Confined Approach Fills." Brigham Young University Department of Civil & Environmental Engineering, Salt Lake City, UT, 83.

Rollins, K. M., and Jessee, S. J. (2012). "Passive Force-Deflection Curves for Skewed Abutments." *Journal of Bridge Engineering*, 17(5).

Romstad, K., Kutter, B., Maroney, B., Vanderbilt, E., Griggs, M., and Chai, Y. H. (1996). "Longitudinal Strength and Stiffness Behavior of Bridge Abutments." University of California, Davis, California.

Sandford, T. C., and Elgaaly, M. (1993). "Skew Effects on Backfill Pressures at Frame Bridge Abutments." *Transportation Research Record: Journal of the Transportation Research Board*, 1-11.

Shamsabadi, A., Kapuskar, M., and Zand, A. (2006). "Three-Dimensional Nonlinear Finite-Element Soil-Abutment Structure Interaction Model for Skewed Bridges." *Fifth National Seismic Conference on Bridges & Highways*San Francisco, CA, 14.

Shamsabadi, A., Kapuskar, M., and Zand, A. (2006). "Three-Dimensional Nonlinear Finite-Element Soil-Abutment Structure Interaction Model for Skewed Bridges." *5th National Seismic Conference On Bridges and Highways*, FHWA, ed.San Francisco, CA, 1-10.

Shamsabadi, A., Rollins, K. M., and Kapuskar, M. (2007). "Nonlinear Soil-Abutment-Bridge Structure Interaction for Seismic Performance-Based Design." *Journal of Geotechnical & Geoenvironmental Engineering*, 133(6), 14p.

Six, J. (2013). D. K. Rollins, ed.

Steinberg, E., Sargand, S., and Bettinger, C. (2010). "Forces in Wingwalls from Thermal Expansion of Skewed Semi-Integral Bridges." Ohio University Department of Civil Engineering, Athens, Ohio.

Strassburg, A. N. (2010). "Influence of Relative Compaction on Passive Resistance of Abutments with Mechanically Stabilized Earth (MSE) Wingwalls." Master of Science, Brigham Young University, Provo, Utah.

Taylor, A. J. (2006). "Full-Scale-Lateral-Load Test of a 1.2 m Diameter Drilled Shaft in Sand."M.S. Thesis, Brigham Young University, Provo, Utah.

Toro, F., Rubilar, F., Hube, M. A., Santa-Maria, H., and Cabrera, T. (2013). "Statistical Analysis of Underpass Damaged During 2010 Chile Earthquake." *Proc. 7th National Seismic Conference of Bridges and Highways (7NSC)*Oakland, CA.

Unjohn, S. "Repair and Retrofit of Bridges Damaged by the 2010 Chile, Maule Earthquake." *Proc., International Symposium on Engineering Lessons Learned from the 2011 Great East Japan Earthquake*.